VNIVERSITAT
DE VALÈNCIA

Departamento de Física Atómica, Molecular y Nuclear

Design and implementation of PET detectors based on monolithic crystals and SiPMs

PhD Thesis
Programa de doctorado en Física

Andrea González Montoro

Instituto de Instrumentación para la Imagen Molecular,
(Centro Mixto CSIC — UPV)

Under the supervision of
Antonio Javier González Martínez

Valencia, November 2018

VNIVERSITAT
DE VALÈNCIA

Departamento de Física Atómica, Molecular y Nuclear

Design and implementation of PET detectors based on monolithic crystals and SiPMs

PhD Thesis
Programa de doctorado en Física

Andrea González Montoro

Instituto de Instrumentación para la Imagen Molecular,
(Centro Mixto CSIC — UPV)

Under the supervision of
Antonio Javier González Martínez

Valencia, November 2018

Antonio Javier González Martínez, Científico Titular del Consejo Superior de Investigaciones Científicas (CSIC), y

Facundo Ballester Pallarès, Catedrático del Departamento de Física Atómica Molecular y Nuclear de la Universidad de Valencia,

Certifican:

Que la presente memoria, *"Design and implementation of PET detectors based on monolithic crystals and SiPMs"* ha sido realizada bajo su dirección en el Instituto de Instrumentación para la Imagen Molecular, centro mixto de la Universidad Politécnica de Valencia y del CSIC, por **Andrea González Montoro**, y constituye su Tesis para optar al grado de Doctor en Ciencias Físicas.

Y para que así conste, en cumplimiento de la legislación vigente, presenta en el Departamento de Física Atómica, Molecular y Nuclear de la Universidad de Valencia la referida Tesis Doctoral, y firman el presente certificado.

Valencia, a 26 de Octubre de 2018,

Fdo.: Antonio Javier González Martínez, Director de la Tesis Doctoral

Fdo.: Facundo Ballester Pallarès, Tutor de la Tesis Doctoral

Contents

Acknowledgements

Los años invertidos en el desarrollo de esta tesis han sido un continuo vaivén de emociones. Confeccionar una tesis doctoral es como un viaje en una montaña rusa, hay días en los que crees que todo es imposible, que nunca vas a conseguir sacar ese resultado que tanto necesitas. Pero de repente, das con la clave y consigues ese resultado, en ese momento la felicidad que llena tu cuerpo es inmensa. No obstante, cuando miro atrás y pienso en los años invertidos en el Instituto de Instrumentación para la Imagen Molecular (I3M), no solo recuerdo las medidas y los resultados, sino también a toda esa gente que hacen que esto sea posible, que sea real. Necesitaría muchos folios más para dar cabida a los reconocimientos que se merecen, pero me ceñiré a los estándares.

En primer lugar, me gustaría agradecer el esfuerzo a mi director de tesis, Antonio J. González. La mayor parte de oportunidades que se me han brindado han surgido gracias a él, así que nunca podré estar lo suficientemente agradecida. Me sigue asombrando su capacidad para transmitir tanto entusiasmo científico y unas ganas brutales por seguir progresando, por descubrir y por aprender. Agradezco mucho su disponibilidad para aconsejarnos continuamente y su predisposición para entrar en el laboratorio y medir con nosotros, guiándonos cuando más perdidos estamos. Y es que ningún proyecto sería posible sin su contribución y guía. Él desde el primer momento confió en mi, me ha enseñado la cultura del esfuerzo y me ha hecho crecer científicamente. Han sido muchos los momentos y las horas que hemos pasado juntos, las inquietudes y nervios compartidos, por lo que su influencia trasciende lo puramente profesional. Gracias también por abrirnos las puertas de tu casa e introducirnos a tu familia, que sin duda forman parte del *"PETeam"*. En resumen, por ser para mi un ejemplo no solo como científico sino también como persona, de nuevo, gracias (infinitas).

También recalcar la contribución del director del Instituto, el Profesor José María Benlloch, el cual a pesar de la inmensidad de tareas que realiza siempre encuentra un hueco para escucharnos, aconsejarnos y ayudarnos. Continuando con científicos de relevancia, agradecerle su apoyo a Filomeno Sánchez. Son incontables las conversaciones inspiradoras en las que es capaz de hacerte plantearte cosas que jamás hubieses pensado, consiguiendo que llegues siempre un paso más lejos en la investigación. Gracias por ofrecernos tu apoyo incondicional, tu visión, una mirada crítica y consejos únicos.

Por supuesto, gran parte de los resultados obtenidos y de mi felicidad durante estos años se la debo a mis compañeros de laboratorio: Koldo, Liczandro, Gabi, Albert, Efthimis, Marta, John y José María Monzó. Es curioso cómo han conseguido que ir a trabajar deje de ser una obligación y se convierta en un *hobbie*, han sido capaces de conseguir que los lunes sean menos duros, que los viernes lleguen antes y que las jornadas se pasen volando. Y es que es increíble la complicidad que tenemos, hemos reído, bailado salsa, buscado cristales y piezas, en definitiva, momentos únicos. Por supuesto han dejado de ser compañeros para convertirse en mucho más, en mi familia. Trabajando así, la investigación es un placer.

No menos importante han sido los compañeros de las otras líneas de investigación del I3M: Juan Pablo, Edu, José Manuel, Miquel, Sergio (Turís y Ultra-Sonidos), Juanjo, Laura, María José, Fran, Michael y Amadeo. Gracias por las comidas, los almuerzos (que aún hay algunos pendientes), las cenas (de esto hay muchas pendientes), las risas, las carreras, las anécdotas, la fiesta y las conversaciones de pasillo. He disfrutado mucho.

Agradecer también a Facundo y a Javier su colaboración. Gracias por iniciarme en este mundo y por haber podido contar siempre con vosotros.

Continuando con la gente que he conocido en el ámbito laboral, mencionar y agradecer a todo el equipo de Oncovisión su contribución a mi formación, en especial a Julio Barberá que siempre está dispuesto a ayudar. También a la gente de Bruker, sobretodo a Carlos Correcher ya que me resulta imposible describir todo lo que he aprendido de él. I would like to also thanks Peter Bruyndonckx for his help, it has been a great pleasure counting and collaborating with you during this period.

I would like to also highlight the international stays conducted during this thesis. They have been very important periods in my life in which I have learned, enjoyed other cultures and broadened my horizons. I have been very lucky to have met such special people at these stages. Special mention deserves the group of Radiology at the University of Washington, which welcomed me as one more of the group, introduced to me the American culture and taught me many things. To all of them, Adrienne, William, Larry, Sandra, Nate and Geng. Especially thanks to Dr. Robert Miyaoka and Professor Paul Kinahan, for trusting me and helping me in everything. It has been also a great time my stay at the Kilinikum Rechts der Isaar in Munich, it has been very productive and inspiring. Thanks to Dr. Jorge Cabello, who spent time in my training, advised me and helped me in everything. It would be an honor to continue collaborating with you in the future.

Por supuesto, pasarán los años y siempre estaremos juntos, a mis mejores amigos: Sofía, Jose (sin duda el más especial), Sergio, Carlitos, Alex y María. Y no menos importantes, mis amigos de la carrera, al final va a ser verdad eso que dicen y los amigos de la carrera son para toda la vida. Os debo muchas “fisicosas”, risas y todo lo que aún nos queda por vivir. A vosotros, Andrés, Lydia, Paula, Miguel, Iván, Dani, Pablo, Chimeno y Yago. También va por los chicos del “Burjapiso”, Gomis, Quique y Héctor. Por favor, no cambiéis nunca.

Y por último a las personas más importantes de mi vida, a mi familia. A mis padres, Joaquín y Pilar, por aguantar mi genio, mis lloros y mis preocupaciones, por estar siempre conmigo, por apoyarme incondicionalmente y luchar por mí y por mis hermanos con todas sus fuerzas. Sin vosotros nada sería posible. A mis hermanos, Borja y Adrián, porque son mi alegría, mi motor, y a pesar de ser la hermana mayor aprendo casi yo más de ellos que ellos de mí. Me lo dan todo, me quieren y siempre serán lo más importante de mi vida. A mi yaya Fina, por ser una persona tan especial, por preocuparse por todos y por vivir con tanta intensidad nuestros logros. No me imagino mi vida sin ella, sin ir a verte y comer chocolate juntas o que le cuentes a todo el barrio lo mucho que nos quieres, pero que sepas que yo te quiero más (si es posible). A mi Terry, mi cachorro, el mejor perro del universo, que siempre se sentaba a mi lado cuando estudiaba, nunca te olvidaré. Sin lugar a dudas, soy la persona más afortunada del mundo con una familia como esta, no tengo palabras suficientes porque incluso el más largo de los libros se queda corto para describir mis sentimientos y agradecerles todo lo que se merecen.

A Miguel, mi Miguelico, mi media naranja (o mi medio limón), te quiero. Te incluyo en familia porque para mi eso es lo que eres. Hemos estado juntos en tu tesis, en la mía y en muchísimas otras cosas. Estos años han sido muy duros para ti, pero tu fuerza y tu manera de seguir adelante son un ejemplo a seguir. Me encanta cómo valoras la familia, como sabes cuidar a los tuyos y cómo eres capaz de ser la persona más tierna de mi mundo. Gracias por apoyarme, por compartir tu vida conmigo y por aguantarme (aunque a veces sea difícil). Sin duda tu madre, Antonia, hizo un buen trabajo contigo, estoy en deuda con ella y por eso parte de esta tesis va por ella, por cuidarnos mientras pudo. También a tu familia, en especial a tu tita Inma, gracias. Me muero de ganas por compartir nuestras vidas y que como en los cuentos comamos perdices.

Esta tesis es merito mío y de todos vosotros, de nuevo, gracias infinitas ∞.

List of Publications

This PhD thesis is based on the following peer-reviewed publications:

[1] **Performance Study of a Large Monolithic LYSO PET Detector with Accurate Photon DOI Using Retroreflector Layers**

A. González-Montoro, A. Aguilar, G. Cañizares, P. Conde, L. Hernández, L.F. Vidal, M. Galasso, A. Fabbri, F. Sánchez, J. M. Benlloch and A.J. González.

DOI: 10.1109/TRPMS.2017.2692819
IEEE TRANSACTION ON RADIACTION PLASMA MEDICAL SCIENCES, Volume 1, No. 3, pp. 229 – 237, 2017.

[2] **Initial Results of the MINDView PET Insert Inside the 3T mMR**

A. J. Gonzalez, **A. Gonzalez-Montoro**, J. Barbera, L. F. Vidal, L. Moliner, F. Sanchez, C. Correcher, E. J. Pincay, G. Cañizares, E. Lamprou, S. Sanchez, J. V. Catret, S. Jiménez-Serrano, S. Aussenhofer, J. Cabello, M. Schwaiger, A. Iborra, D. Visvikis, T. Merlin and J. M. Benlloch
DOI: 10.1109/TRPMS.2018.2866899

IEEE TRANSACTION ON RADIACTION PLASMA MEDICAL SCIENCES, Available online 23 August 2018.

[3] **Detector block performance based on a monolithic LYSO crystal using a novel signal multiplexing method**

A. González-Montoro, F. Sanchez, R. Marti, L. Hernández, A. Aguilar, J. Barbera, J.V. Catret, G. Cañizares, P. Conde, E. Lamprou, F. Martos, S. Sanchez, L.F. Vidal, J. M. Benlloch, and A.J. González.
DOI:10.1016/j.nima.2017.10.098

NUCLEAR INSTRUMENTS AND METHODS IN PHYSICS RESEARCH SECTION A, Available online 12 February 2018.

[4] **Highly improved operation of BGO-PET blocks**

A. González-Montoro, F. Sanchez, S. Majewski, S. Zanettini, J. M. Benlloch, and A.J. González.
DOI: 10.1088/1748-0221/12/11/C11027
JOURNAL OF INSTRUMENTATION, Volume 12, 2017.

[5] **A scintillatior geometry suitable for very small PET gantries**

A.J. González, **A. González-Montoro**, A. Aguilar, G. Cañizares, R. Marti, S. Iranzo, E. Lamprou, S. Sanchez, F. Sanchez, and J. M. Benlloch.

DOI: 10.1088/1748-0221/12/12/C12018
JOURNAL OF INSTRUMENTATION, Volume 12, 2017

[6] **Pilot tests of a PET detector using the TOF-PET ASIC based on monolithic crystals and SiPMs**

A. Aguilar, **A. González-Montoro**, A.J. González, L. Hernández, J.M. Monzó, R. Bugalho, L. Ferramacho and J. M. Benlloch.

DOI: 10.1088/1748-0221/11/12/C12033
JOURNAL OF INSTRUMENTATION, Volume 11, 2016.

List of Figures

List of Tables

List of Abbreviations

ADC	Analog to Digital Converter
ASL	Arterial Spin Labelling
APD	Avalanche Photodiodes
BPF	Back Projection-Filtering
COG	Center of Gravity
CRT	Coincidence Resolving Time
CT	Computed Tomography
CTW	Coincidence Time Window
DAQ	Data Acquisition
DCR	Dark Count Rate
DOI	Depth of Interaction
dSiPM	Digital Silicon Photomultipliers
ENF	Excess Noise Factor
FBP	Filtered Back Projection
fMRI	Functional Magnetic Resonance Imaging
FORE	Fourier Rebinning
FOV	Field of View
FPGA	Field-Programmable Gate Array
LD	Light Distribution
LIOB	Laser Induced Optical Barriers
LOR	Line of Response
LS	Least Square
ML	Maximum Likelihood

MLEM	Maximum Likelihood Expectation Maximization
MRI	Magnetic Resonance Imaging
MRS	Magnetic Resonance Spectroscopy
MSRB	Multi-Slice Rebinning
NMRI	Nuclear Magnetic Resonance Imaging
NN	Neural Networks
OSEM	Ordered Subsets Expectation Maximization
PDE	Photon Detection Efficiency
PET	Positron Emission Tomography
PMT	Photomultiplier Tube
PSD	Pulse Shape Discrimination
QE	Quantum Efficiency
RF	Radiofrequency
RR	Retroreflector
RTP	Raising to the Power
SiPM	Silicon Photomultiplier
SNR	Signal to Noise Ratio
SPAD	Single-Photon Avalanche Diode
SPECT	Single Photon Emission Computed Tomography
SSRB	Single Slice Rebinning
TBI	Traumatic Brain Injury
TDC	Time to Digital Converter
TOF	Time of Flight
3DRP	3D Reprojection algorithm
18F-FDG	18F-Fluoro-deoxy-glucose

Preface

This doctoral thesis focuses on both the design and experimental validation of gamma-ray detector blocks for Positron Emission Tomography (PET) scanners. Components compatible with magnetic fields and therefore, suitable for their simultaneous use with Magnetic Resonance Imaging (MRI) systems have been selected. The present work makes use of detectors based on large and thick monolithic scintillation crystals and SiPMs photosensors.

During the course of this thesis, the physical principles underlying PET technology have been studied. A theoretical model for the scintillation light distribution in monolithic blocks has been also derived. Experimentally, high performance detector blocks based on thick LYSO monolithic blocks and retroreflector layers have been designed and validated, providing accurate characterization of the gamma-ray impact coordinates in the crystal, including the Depth of Interaction (DOI) information. It has been possible to characterize events in the entire crystal volume. Due to the good achieved detector performance, the designed detector blocks have been used in two dedicated brain PET systems. One design has been installed in the MR compatible MINDView insert which is a European Union (EU) project leaded by i3M and founded through the FP7 program. Another detector design is currently use in the CareMiBrain PET scanner, which is a project founded through the EU Horizon 2020 research and innovation program. Moreover, during the thesis, several relevant studies have been carried out such as the characterization of a large variety of SiPMs arrangements, the performance of both dual staggered-layers and monolithic BGO blocks, the characterization of nanopattern structures to increase the extraction of the scintillation photons, and a hybrid approach using both monolithic and pixelated crystals in one detector. Special emphasis has been given to the characterization and implementation of the DOI within monolithic blocks.

This thesis is organized as follows: Chapter 1 introduces the Medical Imaging techniques, including a description of both morphological and functional imaging, and their fusion producing multimodal imaging.

In Chapter 2, since PET imaging is the focus of the thesis, an extensive description of the PET imaging technique is outlined. The chapter starts with a brief history of PET, its physical principles, and a summary of the most relevant reconstruction methods and corrections that are used. In addition to the basic concepts, the role of Time of Flight (TOF) and DOI in PET are described in this chapter.

Chapter 3 deals with the methods and materials required for PET imaging, making special emphasis in the ones used for the development of the scientific articles included in the thesis. This chapter contains a summary of the most relevant positioning algorithms used in monolithic blocks, a discussion of the influence of the crystal surface treatments, and a description of the PET detector block and its main components. Moreover, in order to further support the concepts that are presented, the chapter describes some calculations and experimental validations that are not included in the published articles. Finally, a brief description of the systems that have motivated the performed studies is presented.

Since this thesis is based on a compendium of the most relevant articles published during the course of the PhD studies, Chapter 4 presents a copy of those research articles, as published in the different per-reviewed journals, including a brief introduction highlighting the main results.

In particular, my contribution in these studies has been the design and implementation of the detector blocks, including extensive investigations regarding the use of new treatments to the scintillation crystal surface, such as retroreflector layers or nanopattern structures, with the overall aim of improving the detector performance. In addition to the acquisition and analysis of the data, software tools (C++, ROOT and MATLAB) used for the data processing and 3D impact coordinates estimation (in particular of the DOI coordinate) have been developed. Regarding the implementation of the MINDView brain PET insert, the calibration of the detector modules and its installation at the Klinikum Recht der Isaar, are part of this thesis. An active participation in the data processing of those tests was carried out.

A final conclusion summarizing the main scientific results is presented in Chapter 5. See this chapter for an overview of the main objectives and general motivations of this thesis.

Chapters 6 and 7 outline, both in Spanish and Valencian, respectively, the objectives, motivation, materials, methods, results and conclusions of this doctoral thesis. The complete list of all the per-reviewed articles (including the selected for the compendium) and the conference proceedings published during the development of this thesis can be found in Appendix A.

1. Medical Imaging

Medical Imaging refers to all the non-invasive techniques and processes that are used to generate visual representations of the human body in order to diagnose, monitor or treat different medical conditions.

Medical Imaging technologies allow us to provide images of internal structures and to visualize the functionality of organs and tissues, establishing a database of normal anatomy and physiology and therefore, making it possible to identify abnormalities.

As a discipline, Medical Imaging is a part of biological imaging and includes a large number of different technologies, providing each one distinct but complementary information. For example: X-rays are mainly used to observe bone structures while Positron Emission Tomography (PET) systems are used to evaluate a radio-tracer uptake by an organ. The main application field of Medical Imaging is radiology which uses X-ray, ultrasound and nuclear medicine techniques. Images are obtained using ultrasounds or different energies of the electromagnetic spectra, including radiofrequency (RF) in Magnetic Resonance Imaging (MRI), X-rays in radiography and Computerized Tomography (CT) and γ-rays in Nuclear Medicine techniques. It is necessary to use a type of radiation able to penetrate through the tissues and to interact with them. If not, as it occurs with visible light, its use is limited to certain areas, such as dermatology, gastroenterology and obstetrics (endoscopy).

The diagnostic utility of Medical Imaging techniques lies both on the technical quality of the process and on the conditions of its acquisition. Therefore, the quality of the obtained image establishes a compromise between the maximum possible technical aspects and the minimum potential risks for the patient and the medical personnel.

Depending on the type of information provided, Medical Imaging techniques can be therefore organized in two main groups, namely functional (molecular information) and morphological (anatomical information) imaging. In order to improve the quality of the diagnostic, in most cases both anatomical and functional images are merged providing insights of the internal structures and the metabolic processes *in vivo*. Figure 1 shows a scheme summarizing the most important techniques included in each group.

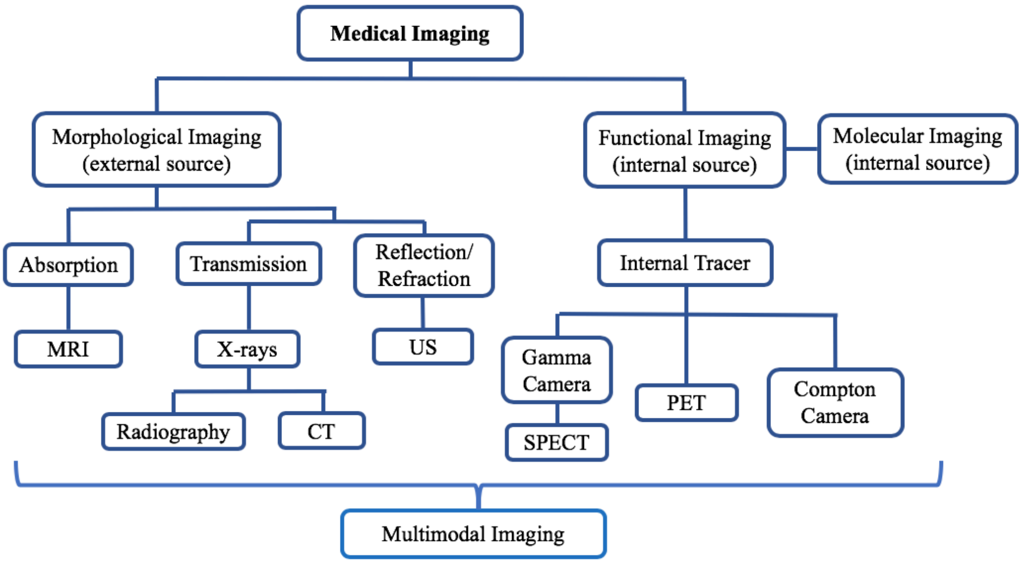

Figure 1. Diagram summarizing the most relevant Medical Imaging techniques and the type of emission sources used.

1.1. Morphological Imaging

Morphological techniques enclose all imaging types that provide information of the internal structures of the body, such as bones, organs or tissues. To produce these images, it is necessary to use an external source and a detector device able to collect the radiation emitted by this source. In this case, it is mandatory to use particles with an energy able not only to penetrate through the tissues, but also able to interact with them. If not, the detected energy will not contain information of the internal structures. Radiography, Computed Tomography [7], Magnetic Resonance Imaging [8] and Ultrasound [9] are the most common morphological techniques. Moreover, other imaging techniques are rising up, such as Elastography, that maps the elastic properties of soft tissues [10].

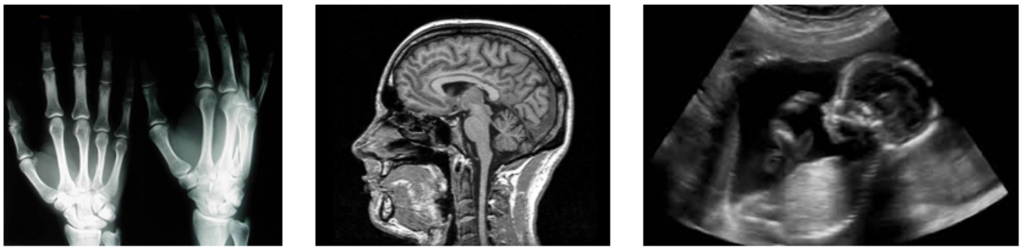

Figure 2. Images obtained using different morphological imaging techniques. Left, radiographic image of human hands. Center, MR image of a human head. Right, ultrasonographic image of a human fetus.

1.1.1. Radiography

Radiography is a transmission imaging technique in which the contrast of the image is provided by the differential absorption of X-rays among different tissues generating planar images. Its origin is based on the discovery of the X-rays in 1895 by Roentgen [11]. To generate the image, the beam of ionizing radiation, i.e., X-rays, is produced and projected towards the subject of study. Part of the beam is absorbed by the object depending on its density and composition, for example, soft tissue absorbs small amounts of radiation whereas bone absorbs larger amounts, as a result soft tissues appear darker than bones in the final image. The rest of the beam passes through the object reaching the detector, which can be either a photographic film or a digital detector. There are three main radiographic applications of X-rays:

i. *Projectional radiography* generates two-dimensional images that are often used to identify fractures or pathological changes in some organs. Contrast medias are generally used to more accurately diagnose ulcers or certain types of cancer. Figure 2 left shows a radiographic image of human hands.
ii. *Mammography* is based on the use of low energy X-rays (to increase the contrast in the image) for the examination of the human breast. This technique is used for both diagnosis and screening.
iii. *Fluoroscopy* consists on obtaining real-time images of internal structures, acquiring numerous X-ray images in a time frame. This technique employs a constant input of X-rays but a lower dose rate. It is used in image-guided procedures, such as positioning catheters, and also to visualize the physiology of internal organs.

1.1.2. Computed Tomography

Computed Tomography is an X-ray imaging procedure based on rotating a narrow beam of X-rays simultaneously with a detector matrix around the subject of study. During the rotations, images are acquired at different angles

[12]. As more as 400 to 600 X-ray radiographies are acquired during a CT exploration. The information is collected and processed generating cross-sectional images (slices) of the subject. Once the acquisition is completed, the system stacks all the slices together generating a 3D image of the subject that provides more detailed information than conventional X-ray procedures.

1.1.3. Magnetic Resonance Imaging

Magnetic Resonance Imaging, also known as Nuclear Magnetic Resonance Imaging (NMRI), is a technique used to obtain images of the anatomy and in some cases of the physiological processes occurring in the body. This modality constitutes one of the most important anatomical imaging techniques being very useful in localizing lesions in the whole body. Physiological processes are studied using functional MRI (fMRI), that measures changes in brain metabolism as a function of the changes associated to the blood flow allowing to localize and measure the resulting brain activation. For this purpose, Blood Oxygen Level Dependent (BOLD) contrast [12] or Arterial Spin Labeling methods (ASL) [13] are used.

The MRI operation principle is based on using powerful magnets to polarize and excite the hydrogen nuclei of water molecules present in the human tissue. Excitation of other nuclei is also possible. MRI scanners use three magnetic fields:

i. Static field (B_0).
ii. Gradient field.
iii. Radio-frequency field (B_1).

In MRI scanners a very strong static field (main field, B_0) first polarizes the hydrogen nuclei. Since B_0 is constant, all the hydrogen nuclei have the same resonance frequency and therefore, the emitted signals do not provide any spatial information on where the resonance took place (making it impossible to obtain an image). In order to obtain spatial information, gradient fields are applied producing different spatial encodings on the nuclear spins. Then, radio frequency antennas (RF coils) that emit a radio frequency pulse at the resonant frequency of the hydrogen nucleus are used. The RF pulse is absorbed by protons and their direction with respect to the B_0 field changes. When the RF pulse is turned off, the direction of the protons comes back to its original position (aligned with the main field) emitting radio-waves. These radio-waves are detected by the receiver coil (most scanners have transmitter-receiver coils, TR coil) and are used to generate an image. A schematic description of these processes is shown in Figure 3.

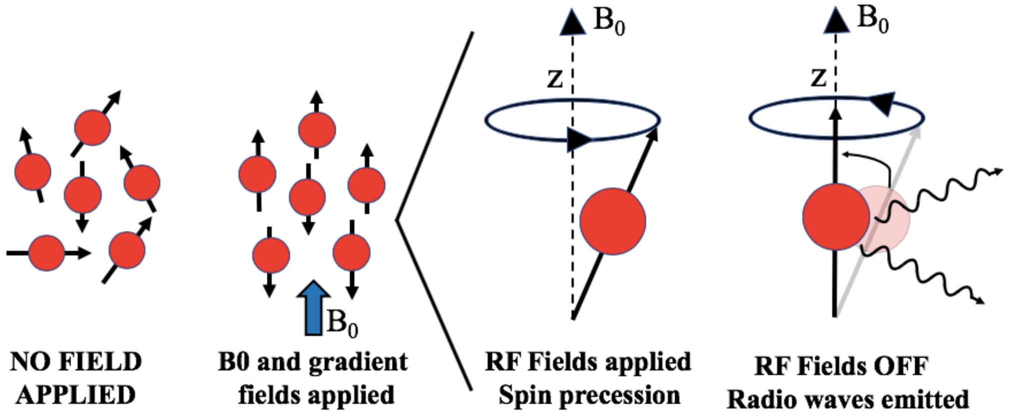

Figure 3. Schematic process of the MRI principle. From left to right, hydrogen nuclei spins are randomly oriented, when the main field is applied (B_0) the spins aligned parallel or antiparallel with the field. RF pulses are applied and the spins direction changes. When the pulses stop the spins come back to their original orientation emitting radio-waves.

Different pulse sequences can be used depending on the characteristics of the study. It is possible to combine these sequences in order to differentiate tissue characteristics or cancer types [14][15]. It is worth mentioning, that MRI scanners are not only used for imaging purposes but also for other clinical aspects, such as spectroscopy. This technique is called Magnetic Resonance Spectroscopy (MRS) and consists on the evaluation of chemical abnormalities in tissue.

As CT scanners, MRI systems provide cross-sectional images on the internal structures. The main advantage of MRI is that provides higher contrast images for soft tissues without making use of ionizing radiation. Figure 2 center shows an MRI image of a human head.

1.1.4. Ultrasonography

Medical Ultrasonography (US) uses high frequency acoustic waves (2.000 to more than 20.000 Hz) that are reflected by tissues to produce images. This modality is based on the transmission and reception of acoustic waves [9]. The emitted signal is reflected due to a change in the tissue composition as a result of a variation in the mechanical impedance within the medium, as for example occurs between the placenta and the muscles. Therefore, as the media changes at different depth in the body, the reflected acoustic wave reaches the detector (which is also the emitter) at different time intervals. This technique is less expensive than CT or MRI and quick to perform, being an appropriate approach to observe and study the function of moving structures in real time (useful for biopsy or drainage procedures), including the imaging of the abdominal organs, heart, tendons, muscles and veins. Furthermore, this technique does not use ionizing radiation making it the perfect one to image fetus in pregnant women, as for instance shown in the right panel of Figure 2. Modern US scanners include Doppler capabilities allowing to assess the blood flow in arteries and veins. As a drawback, ultrasounds provide in general less anatomical detail than alternative techniques such as CT or MRI scanners.

1.2. Functional Imaging

Functional (nuclear) imaging techniques include all the gammagraphic techniques that provide images of a radio-tracer distribution inside the body, allowing to track physiological and biochemical processes in vivo. To obtain these images it is necessary to use compounds in which one or more atoms are substituted by single photon or positron-emitting radionuclides. These compounds are called radio-tracers and can be injected, inhaled or administrated via oral to the patient. After its administration, the compound is distributed in the organism emitting radiation as a result of the radioisotope decay. This radiation is externally collected, and used to generate 3D images. There are four main nuclear imaging systems techniques: Gamma Cameras, Single Photon Emission Computed Tomography (SPECT), Positron Emission Tomography (PET) and Compton Imaging.

Molecular Imaging

Molecular Imaging techniques have their origins in the field of nuclear medicine and provide detailed images *in vivo* of the processes happening inside the subject under study at the molecular and cellular levels [16]. Its goal is acquiring a broad knowledge of the diseases improving the diagnose and treatment.

Molecular Imaging, uses molecular probes (biomarkers) that are sent to specific biological targets or pathways. Biomarkers chemically interact with targets allowing to study biological processes without modifying their natural environment. Therefore, molecular imaging provides information, at a molecular level, with non-invasive, safe and pain-less techniques that is inaccessible with other imaging technologies or that would require more invasive procedures (surgery or biopsy). This information allows to identify diseases in its earliest stages and to determine its severity. Molecular Imaging helps physicians to select the most effective therapy based on the molecular properties of the abnormality and the biological characteristics of the patient. After the therapy treatment, molecular imaging techniques can also be used to determine the response to the treatment and to assess its effectiveness. If the treatment is not appropriated, can be quickly changed by observing the response in cellular activity [17].

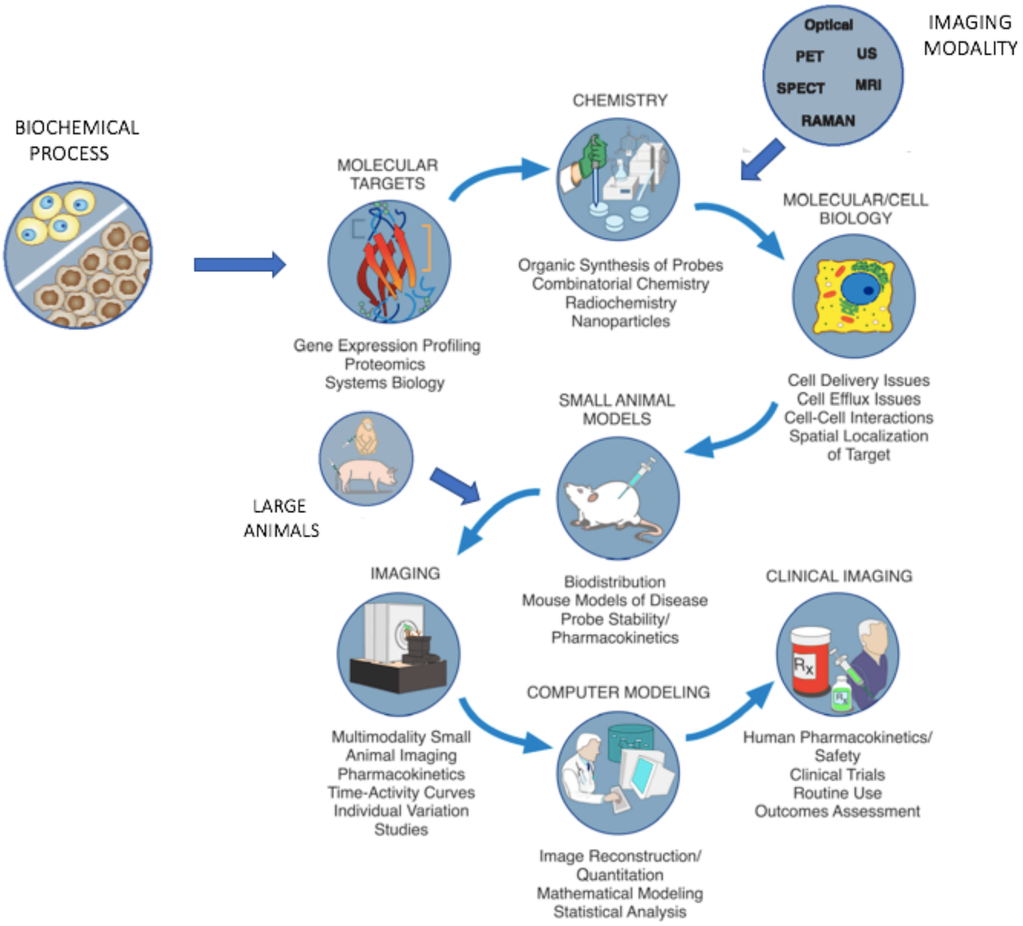

Figure 4. Schematic figure summarizing the most important process followed during a molecular image study (Original images extracted from [18] and [19]).

There are several processes involved in a molecular imaging study. It all starts with the identification of a pathological abnormality and the subsequent investigation and synthetization of a biological target for the observation of relevant molecular processes. The next step is to select an adequate image technique (PET, SPECT…). Up to this point, the model is transferred to the preclinical area and animal models (small and large animals) are used to evaluate the specificity and selectivity of the biomarker and the selected imaging technique. Finally, if tests with animals are successful, computer modeling of the process is performed and the methodology is translated into the clinical site. Figure 4 summarizes the most important steps in a molecular imaging study.

The development and application of these new imaging techniques intend to increase the understanding of disease mechanism allowing for an early detection and better diagnose. Moreover, it allows to characterize and analyze the therapeutic effects of drugs at the molecular level, almost immediately after the start of the treatment and therefore, the optimization of medicines and genetic therapies.

Molecular imaging techniques are multiple and diverse, including PET, SPECT, digital autoradiography, fMRI, MRS, optical bioluminescence, optical fluorescence or ultrasound.

1.2.1. Gamma Camera

Gamma camera systems are the simplest nuclear imaging devices [20]. In imaging procedures using gamma cameras, the patient is injected with a single gamma ray emitting tracer, such as ^{99m}Tc. The emitted gamma-rays are detected by the camera providing information about the metabolic processes.

A gamma camera is composed of a scintillator crystal optically coupled to a photosensor. The scintillation block is preceded by a physical collimator (lead or tungsten) to ensure that only gamma-rays coming from a certain point are collected [21]. Recently, solid state designs such as those based on Cadmium Zinc Telluride (CZT) are more popular due to their higher energy resolution that for instance helps when using multi-isotopes. The selection of the collimator mainly depends on the application. Figure 5 shows the most commonly used collimator types that are briefly described below:

i. Parallel-hole collimators, consist of a plate of dense material containing holes separated by lead or tungsten septa. They are used for low energy radio-tracers, such as ^{99m}Tc, and medium energy radio-tracers, such as ^{111}In, ^{131}I or ^{67}Ga. This collimator type allows one for a homogeneous sensitivity across the Field of View (FOV) [22].
ii. Converging hole collimators, are used when the object is smaller than the detector area. The holes converge toward a focal line parallel to the axis of the source improving the spatial resolution [23].
iii. Diverging hole collimators, are used when the object to be imaged is large. Its use makes it possible to enlarge the FOV and still obtain a sufficiently high resolution image [24].
iv. Pinhole collimators consist of a small pinhole aperture in a plate of lead or tungsten. Pinhole collimators are often used to image small-organs and in small-animal imaging because they allow for high magnification so that submillimeter resolution can be achieved.
v. Multi pinhole collimators are based on many pinhole collimators. This approach is a tradeoff between spatial resolution and sensitivity.

Since gamma cameras operate in single gamma mode, the scintillation crystal used should not contain natural radioactivity. For this purpose, NaI, CsI (Na or Tl doped), BGO or GAGG crystals are used.

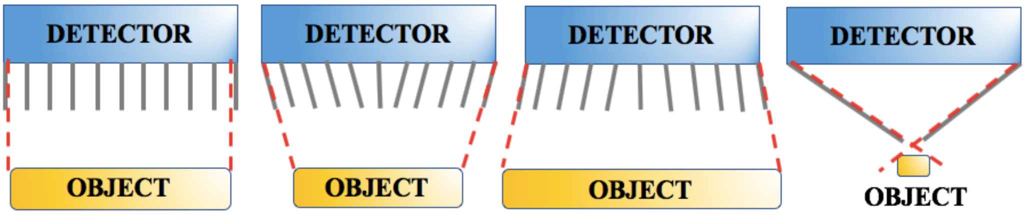

Figure 5. Most commonly used collimator types in gamma cameras, from left to right: parallel hole, convergent hole, divergent hole and pinhole collimators.

1.2.2. SPECT

SPECT systems are composed by multiple gamma cameras that rotate around the patient acquiring the single photons emitted in the radiotracer decay process for each different angular position [25]. Typically, the angular step between consecutive image projections varies from 3 to 6 degrees covering the entire FOV. Figure 6 shows a scheme of an SPECT system.

The detector blocks composing a SPECT system are similar to those used in gamma cameras. A scintillator material is optically coupled to a photodetector, typically using a light guide between them. As in gamma cameras, several types of collimators, scintillators and photosensor (including CZT technology) are used.

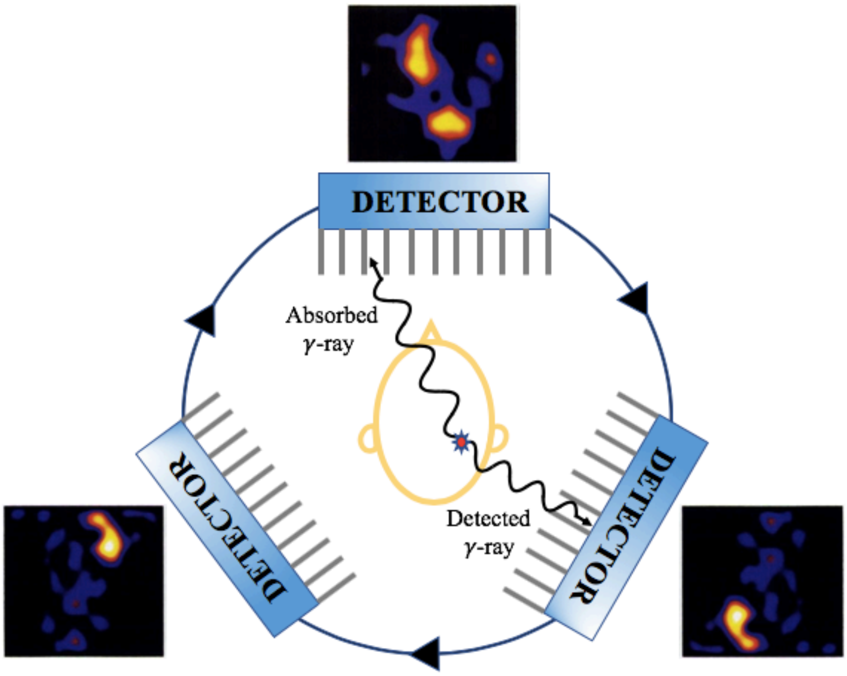

Figure 6. Scheme of a SPECT system, the gamma cameras (detectors) rotate around the patient acquiring cross-sectional images.

In contrast to gamma cameras, SPECT scanners provide 3D images. 2D projections are combined and reconstructed in order to obtain such tomographic 3D images. It is common to use SPECT scanners together with CT in order to combine both functional and anatomical information, respectively. There is a broad variety of available radiotracers, making possible a high number of SPECT applications such as brain functional studies, heart, bone or lung analysis, to name but a few. For instance, best known SPECT applications in brain imaging are blood perfusion to study dementia, epilepsy or TBI (Traumatic Brain Injury).

1.2.3. Compton Camera Imaging

Compton imaging is a non-invasive technique based on the Compton scattering of X-rays and γ-rays [25]-[27]. This technique is a variety of the SPECT in which mechanical collimators are replaced by electronic collimation methods. Compton cameras are based on different layers of detectors (two or three) working in coincidence mode and therefore, allowing for electronic collimation processes. A radioactive element also injected to the patient, emits γ-rays that interact in the first layer of detectors (usually low-Z element absorber) by photoelectric or Compton scattering. For Compton interactions, photons are scattered and interact in the second layer of detectors (high-Z element absorber) via photoelectric interaction. Determining the photon interaction coordinates in both detectors allows one to reconstruct a cone, which apex corresponds to the interaction (Compton scattering) position in the detector and its axis corresponds to the propagation directions of the scattered photon. The intersection of different cones (from different events) provides information relative to the source position. Therefore, Compton imaging techniques are able to obtain directional information of an incoming single gamma ray. Figure 7 provides a description of the process. The spatial resolution of the camera is a function of the spatial resolution of both the scatter and abortion detectors, and on their separation distance [28].

Compton cameras are used for the visualization of γ-rays sources and have application not only in the medical area but also in astrophysics [29][30] or semiconductor detector developments [31]. Concerning medical research, they are used to image and distinguish tumors from surrounding tissue [32] and to track the incident ions used in hadrontherapy [25], among others. In order to provide more accurate images, researchers are proposing to combine PET and Compton cameras [33].

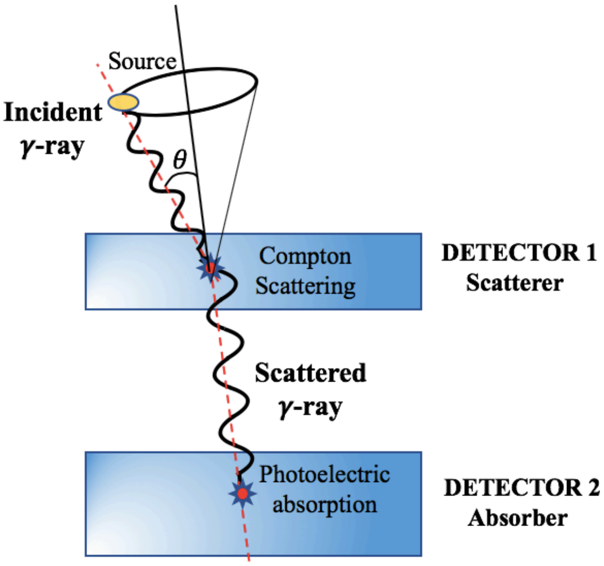

Figure 7. Schematic representation of a Compton detector. Photons of unknown propagation direction reach the first (scatterer) detector and are Compton scattered, then low energy gammas are fully absorbed in the second (absorption) detector.

1.2.4. PET

PET scanners are based on the coincidence principle with the simultaneous detection of two 511 keV photons. PET detector blocks are similar to those used in gamma cameras and SPECT, however no physical collimation is used. To obtain the image, patients are injected with positron emitter radioisotopes that decay inside the patient body emitting a positron that subsequently annihilates with a core electron of the patient body emitting two opposite 511 keV photons. PET scanner detectors are optimized for the specific energy of 511 keV and their operation principle is based on opposed detectors measuring in coincidences the two emitted photons. After a complex image reconstruction processes a tomographic emission image is generated.

PET, as well as other nuclear imaging techniques, is both a medical and a research tool. Its main clinical application is oncology (imaging of tumors and metastases), and the clinical diagnosis of certain brain diseases such as those causing various types of dementias. Figure 8 shows three examples of a brain PET image with different pathologies. PET is also an important research tool to map normal human brain and heart function, and to support drug development. PET is also used in pre-clinical studies with animals.

As in the SPECT modality, PET scanners provide tomographic functional images that can be combined with CT or MRI systems. However, given the lack of the physical collimator in PET scanners, their sensitivity is significantly higher than in the case of SPECT.

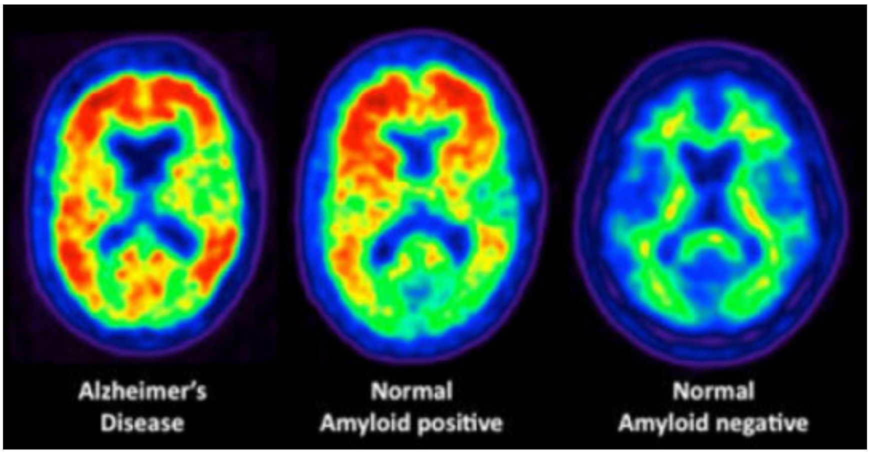

Figure 8. PET images of the human brain. PET scans reveal amyloid plaques, which appear as warm colors such as red and orange. The middle scan is from a person with no symptoms of cognitive problems, but with evident levels of amyloid plaque in the brain [34].

Since PET is the focus of this thesis, a more extensive description of its physical principles, gamma-ray detection processes and image formation, will be carried out in the following chapter (see Chapter 2).

1.3. Multimodal Imaging

Over the last few decades many efforts have been performed in order to improve tomographic imaging technologies. Regarding anatomical techniques, both CT and MRI have improved their capabilities, not only from the technological point of view, but also concerning new software algorithms that improve the final imaging quality [35][36].

As earlier described, nuclear imaging techniques, PET and SPECT, are the most sensitive methods for clinical use [37] and provide hig hly quantitative images for the study of biochemical and functional abnormalities. However, the absence of background anatomical information make them difficult to interpret the radio-tracers distributions, leading sometimes to misinterpretations of the images. To deal with this problem, many algorithms co-register and merge the functional PET and SPECT images with prior anatomical images provided by means of CT or MRI systems [38][39]. This works well for static organs such as the brain. However, most human organs and tissues are in continuous motion leading to an image mismatch [40]. Physical movements can also occur between the acquisition leading to attenuation artifacts and diagnostic inaccuracies. As a result, the image quality is degraded. Gating techniques have been developed in order to improve cardiac or respiratory movements in sequential imaging acquisitions [41].

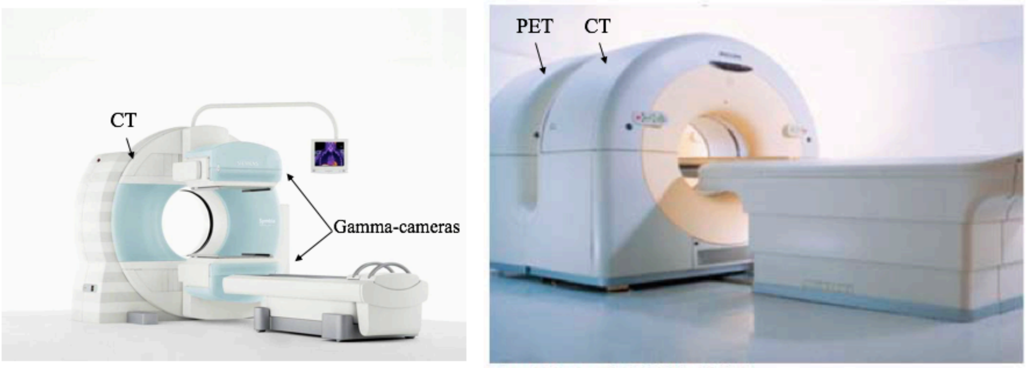

Figure 9. Left, commercial SPECT/CT scanner Symbia T-series manufactured by Siemens Healthineers. Right, commercial PET/CT scanner Gemini TF 64 manufactured by Philips.

Precise co-registered PET or SPECT images with CT data increase diagnostic accuracy compared to independent acquisitions. To improve the images co-registration, SPECT/CT and PET/CT combined acquisitions started to be sequentially carried without moving the patient from the bed and thus, significantly reducing differences concerning positioning and organ motions [42]-[44].

Hybrid SPECT/CT scanners are based on a multi-slice CT system and multi-headed gamma camera SPECT. Advancements in medical imaging allowed to integrate all the detectors (including their electronics) in one element and to control both modalities with the same software interface. Nowadays, CT and SPECT studies are performed sequentially by moving the bed, Figure 9 left shows the commercial SPECT/CT Symbia T-Series (Siemens). The main drawback of this approach is the large footprint required to install both systems.

Concerning hybrid PET/CT, the images are also acquired sequentially. Both scanners are in a tandem configuration, PET and CT FOV are separated (20-60 cm) in the axial direction, see the right photograph of Figure 9.

It is common to use CT scanners to provide attenuation maps in order to correct emission data. Figure 10 provides an example of an adenocarcinoma of the colon. Top and bottom panels show axial and coronal images from PET (left), CT (center) and fused PET/CT (right). Nevertheless, SPECT/CT and PET/CT acquisitions cannot be performed simultaneously due to technical challenges and therefore, there is always some uncertainty in the positioning. Adding the CT modality has the drawback of increasing the dose to the patient [45], limiting the number of studies that can be done.

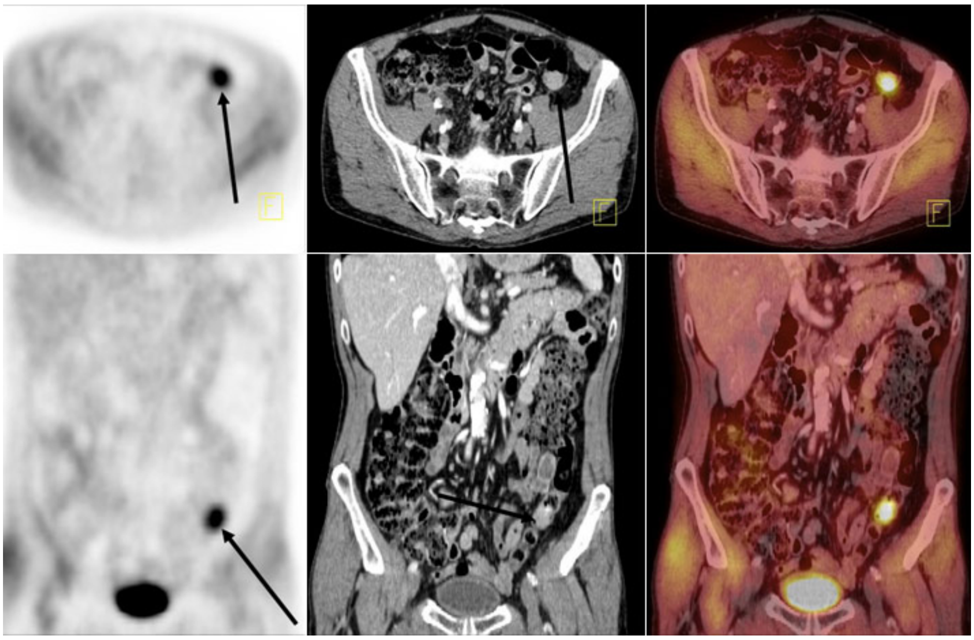

Figure 10. Axial (top) and coronal (bottom) images from a PET/CT scan. PET images are on the left, CT images in the center, and PET/CT fusion images on the right [46].

Alternatively to combining PET or SPECT with CT, those were suggested to be fussed with MRI. Concerning simultaneous SPECT/MRI and PET/MRI, their progress was slower as a result of technical operation challenges with the detectors used in PET and SPECT due to the influence of the magnetic fields of the MR in the photosensor technology [47]. Despite the technical difficulties, PET/MRI and SPECT/MRI have exhibited a higher interest to the medical community.

The detector blocks of most commercially available SPECT and PET scanners are composed by Photomultiplier Tubes (PMTs) that are highly sensible to magnetic fields and therefore, cannot work within the MRI scanner FOV. There have been two different approaches to overcome this problem. The first one was to shield the PMTs and place the PET and MRI systems in a tandem mode, allowing the displacement of the bed from the MRI to the PET FOV. In the second solution, only the PET scintillation blocks were placed inside the MRI FOV, and the scintillation light was transferred by means of optical fibers or light guides to the PMTs that were placed outside the MRI FOV, where there is a weaker influence of the magnetic field [48]. However, the introduction of MR compatible photosensors based on solid-state technology, first Avalanche Photodiodes (APD) and later Silicon Photomultipliers (SiPM), have allowed including the photosensors in the magnetic field region simplifying the system design. This technology has increased the interest for simultaneous PET/MR and SPECT/MR acquisitions [49].

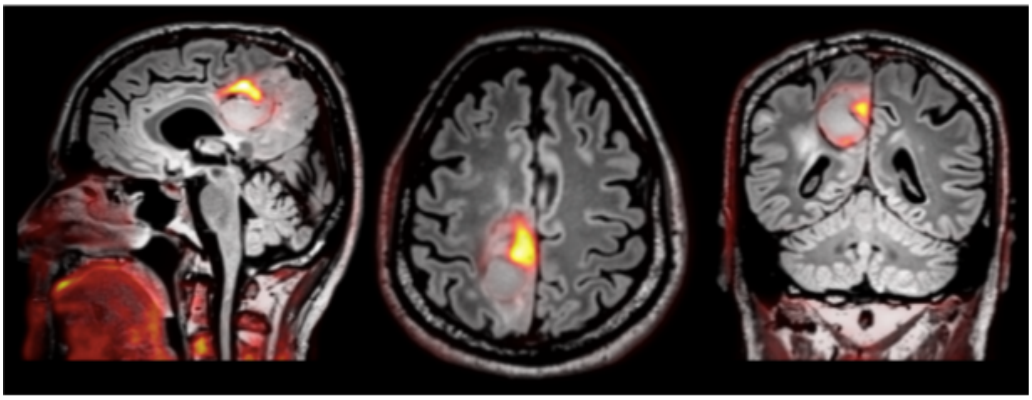

Figure 11. Fused MRI (greyscale image) and PET (red/yellow) images of a Grade IV glioma. The PET images demonstrated a high tumor-to-background ratio [54].

Some of the main application fields of combining SPECT or PET with MRI [50], are cardiology [51], neurology [52] and in particular, oncology [53]. PET/MRI systems are commonly used for the following-up of brain, neck, abdominal and prostate tumors due to the high image quality of soft tissues provided by the MRI. As an illustration, Figure 11 shows a fused PET/MRI image of a brain tumor (Grade IV glioma). Due to the improved diagnostic performance obtained when merging both imaging techniques, two European projects (MINDView [201] and TRIMAGE [55]) are dedicated to the development of two brain dedicated PET inserts.

There still some drawbacks of multimodal systems based on MRI, in comparison with hybrid PET or SPECT and CT. They require of larger acquisition times, it is almost impossible to be used in patients with metallic implants, and it is not straightforward the conversion of MRI images into an attenuation map, in addition to their high cost. It is also worth mentioning that, the combination of PET or SPECT with CT or MRI as a multimodal imaging modality is receiving great attention not only in emerging clinical applications but also in the preclinical field [56][57].

2. Positron Emission Tomography

2.1. PET History

PET imaging has undergone significant improvements over the past 60 years since it was first conceived as a medical imaging modality. Its history is full of milestones concerning both technological achievements and scientific advancements. This section summarizes the timeline of the most relevant events that have contributed to the development of PET as it is known today. For further information and details see for instance [58]-[62], and references therein.

As previously mentioned, the main physical principle upon which PET imaging is based on, is the positron-electron annihilation. Therefore, we can state that the two first milestones were the prediction of the positron by Dirac in 1929 [63] and its experimental discovery by Anderson in 1932 [64]. The next achievement took place only two years later, when Curie and Joliot discovered the radio-elements, motivating the use of the recently developed cyclotron at the University of California in Berkeley, to produce artificial radionuclides for biological experiments in plants [65]-[67]. In the following years many researchers, such as Ter-Pogossian and Wagner, tried to promote its use for medical applications [68]. And finally, in 1945 radiotracers were first used in humans [69]. Despite these achievements, the instrument used for the external detection of gamma rays was the Geiger-Müller counter, which was not suitable for the detection of high energetic 511 keV annihilation photons. Luckily, in 1948 Kallman reported the use of a new detector more suitable for the detection of 511 keV photons, the so-called photomultiplier tube, and in 1949 Cassen, Curtis and Reed reported the use of calcium tungstate as a detector for higher energy gamma photons [60].

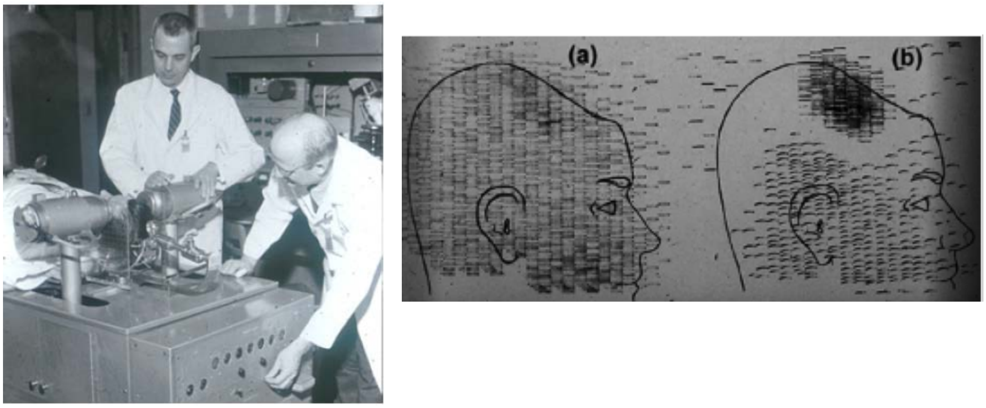

Figure 12. Left, first clinical positron imaging device. Drs. Brownell and Aronov are shown with the scanner and a patient. Right, coincidence scan (a) of a patient showing recurrence of a tumor under the previous operation site, and unbalance scan (b) showing asymmetry to the left (Image extracted from [61]).

Consequently, scientific interest concerning the advantages inherent to the detection of radiation as a result of the positron-electron annihilation, over single photon imaging showed up, and on 1951 Wren, Good and Handler from Duke University first reported on the possible use of coincidence detection [70]. In 1952 Brownell and Sweet from the Physics Research Laboratory of the Massachusetts General Hospital, suggested the use of nuclear disintegrations in the diagnosis and treatment of brain tumors, and in 1953 they built the first positron imaging device, designed for the localization of brain tumors [71], see Figure 12. During the following years, several attempts to improve this coincidence detection technique were performed, and in 1962 Rankowitz designed a positron scanner based on 32 NaI(Tl) detectors (see Section 3.1) in a ring geometry [72], and only one year later Anger and Gottschalk also reported on the design of a positron camera for brain tumor imaging [73][74].

Finally, between 1970 and 1973 the first fully systems appeared, Robertson and Thompson built the so-called Positome [75] but were unable to obtain true reconstructed cross-sectional images. In parallel, the Washington University group of Phelps, Hoffman, Mullani and Ter-Pogossian built the Positron Emission Transaxial Tomography system (PETT) [76]. This unit consisted of a hexagonal array of 24 NaI(Tl) detectors. By 1975 the system was upgraded to 48 Nal (Tl) detectors, and was expanded to the clinically applicable PET (III), a whole-body camera [77]. The group joined a collaboration with GE & ORTEC and built a commercial, single transaxial plane PET scanner known as the Emission Computerized Axial Tomograph (ECAT I), upgraded during the following years [78][81].

During the late 1970s and 1980s, advancements of PET cameras resulted on several designs such as a single ring of NaI(Tl) [82] and its expansion to multiple rings using Bismuth Germanate Oxid (BGO) crystals [83]. The major vendors of PET scanners accepted BGO as the scintillator of choice until LSO became available in the late 1990s. Nowadays, ring detectors based on fast scintillation crystals, such as LSO, for time-of-flight (TOF) detection schemes [84][85] are being studied.

It is worth mentioning that, in parallel to the advancements related to PET instrumentation, many efforts were dedicated to the improvement of radiotracers, such as the synthetization of ^{18}F-FDG in 1978 [86].

During the upcoming years, researchers have focused on the improvement of the detector block instrumentation [87], in particular on the system spatial and energy resolutions. In the early 1990s, the first brain dedicated PET was launched, the so-called High Resolution Research Tomograph (HRRT). The system is based on PMTs. Modern systems are based on APDs or SiPMs in order to optimize compactness, detector efficiency and its compatibility with magnetic fields. Many research studies also focused on the implementation of the photon Depth of Interaction (DOI) and Time of Flight (TOF) information and on the improvement of the system sensitivity as well as the image reconstruction techniques. In 1990, it was also recognized that PET could also play a decisive role in imaging small animals [87]-[90].

As mentioned in the prior section, in the last two decades, PET systems have been combined with anatomical imaging devices such as CT or MRI scanners. Many improvements have been achieved and PET scanners have also been designed to image other single organs such as the breast or the brain [62]. On the opposite to organ-dedicated molecular imaging system, currently the first total-body PET scanner, the EXPLORER, is being built, which is a 2 m system in axial length and contains as more as 560,000 individual detector elements [91].

2.2. PET basics

In PET imaging, the radiotracers injected to the patient are chemical compounds, similar to naturally occurring substances in the body, in which one or more atoms are substituted by positron-emitting radionuclides. The radiotracers decay produces positrons, which randomly travel inside the patient body until they collide with a cortical electron of the tissue. As a result of this collision, two 511 keV gamma-rays are emitted in almost opposite directions and detected in two detectors of the PET scanner. Finally, reconstruction algorithms are employed to generate an image showing the 3D distribution of the radiotracer in the subject. Figure 13 shows a scheme of the process. The physical principles underlying PET will be described in the following section.

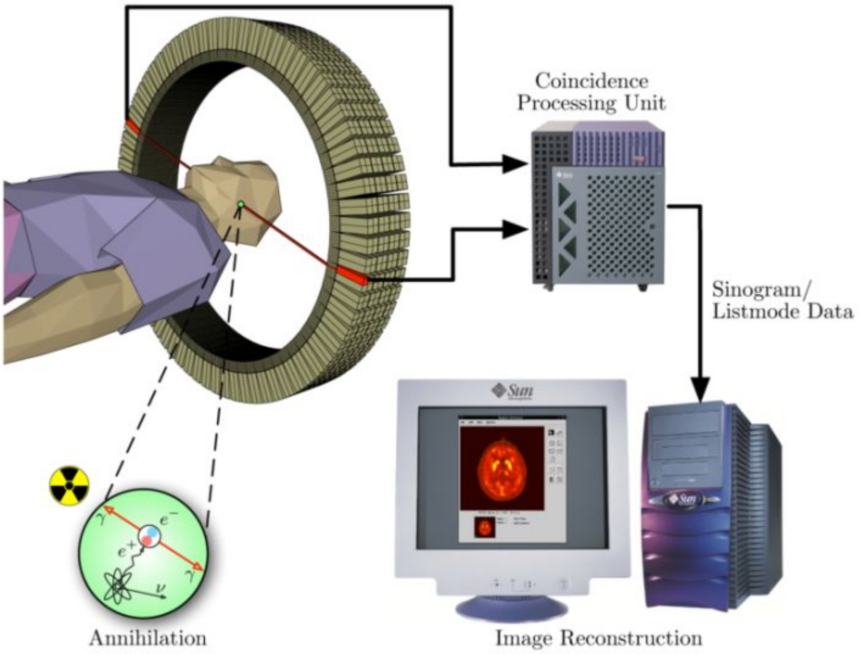

Figure 13. Sketch of the operation principle of a PET scanner.

Table I. Most commonly isotopes used for PET, showing information on its function and typical application.

Isotope	Tracer compound	Physiological process or function	Typical application
^{18}F	Fluoro-deoxy-glucose	Glucose metabolism	Oncology, neurology
^{18}F	Fluoro-mizonidazol	Hypoxia	Response to radiology
^{68}Ga	Prostate specific antigen	PSMA biomarker	Oncology
^{11}C	Methionine	Protein synthesis	Oncology
^{11}C	Flumazenil	Benzodiazepine receptor antagonist	Epilepsy
^{11}C	Raclopride	D2 receptor agonist	Movement disorders
^{13}N	Ammonia	Blood perfusion	Myocardial perfusion
^{11}C	Methionine	Protein synthesis	Oncology

Several types of radiotracers are used in PET, their selection depends on the study that is going to be performed [92][93]. Table I summarizes the most relevant radiotracers used and its typical application. Note that the most widely used radiotracer is ^{18}F-fluoro-deoxy-glucose (^{18}F-FDG). It is used as a glucose uptake tracer because it is relatively easy to synthesize and follows a similar metabolic pathway to glucose in vivo, with the only difference that remains trapped within the tissue because is not metabolized to CO_2 and water. This is of interest because proliferating cancer cells have above average rate of glucose metabolism [94][95].

2.3. Physical principles of PET

2.3.1. Positron emission and annihilation

The fundamental process that enables PET is the back-to-back emission of two 511 keV gamma photons coming from the annihilation of a positron (e^+) with its antiparticle, the electron (e^-). The positron results from a beta-plus decay (β^+ decay) process within a nucleus, in which a proton-rich isotope decays via positron emission. In this process, a proton in the nucleus decays to a neutron, a positron and an electron neutrino (ν_e), see Figure 14. As a result, the daughter isotope has an atomic number one less than the parent. Equation 1 describes this process:

$${}^{A}_{Z}X \rightarrow {}^{A}_{Z-1}X' + e^{+} + \nu_{e} \qquad (1)$$

The emitted positron travels through the patient body releasing its kinetic energy principally by Coulomb interactions with electrons following an erratic motion through the tissue. As a result of these interactions, the positrons may undergo large deviations in their trajectories. After many interactions, the positrons reach thermal energies and start to interact with electrons either by annihilation, which produces two 511 keV gamma-rays in opposite directions (see Figure 14) or by the formation of a hydrogen-like orbiting pair called positronium. Positronium has two states, ortho-positronium, where the spins of the electron and positron are parallel and self-annihilates by the emission, typically, of three photons [96], and para-positronium, where the spins are anti-parallel and decays by self-annihilation, generating two anti-parallel 511 keV photons. Both forms are susceptible to the pick-off process, where the positron annihilates with another electron. The result is an angular uncertainty in the direction of the 511 keV photons of around 4 mrad in the observer frame [97]. It is worth mentioning that the most probable annihilation processes are the ones producing two 511 keV gamma-rays.

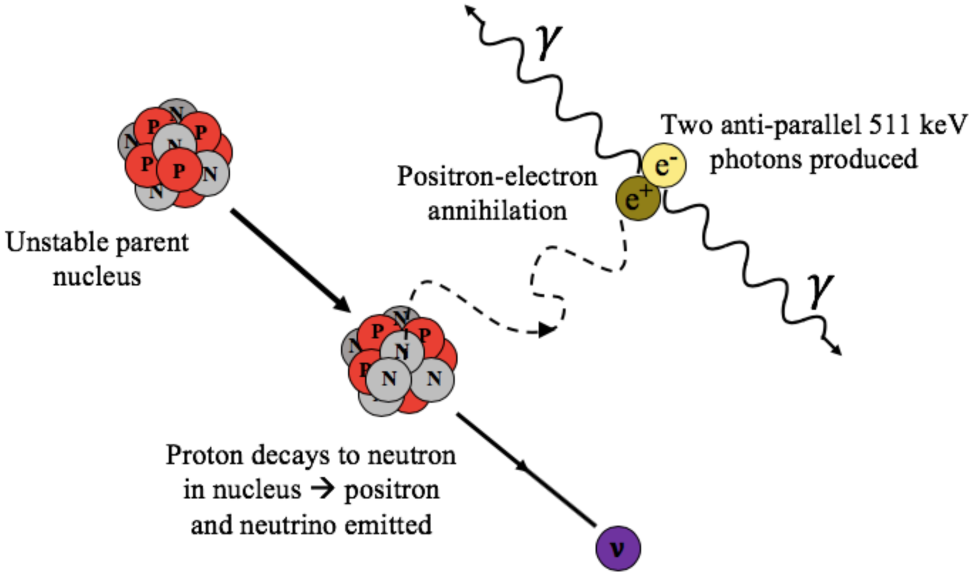

Figure 14. β+ decay scheme. A proton decays to a neutron in the nucleus emitting an electron neutrino and a positron. The positron is annihilated with an electron of the media emitting two opposite 511 keV gamma-rays.

The distance traveled by the positron before its annihilation is known as positron annihilation range and it is directly related to the initial kinetic energy of the positron and to the properties of the medium. The positron energy distribution can be calculated following an analytical expression valid for allowed or super allowed beta decays [96]-[98]. The theoretical energy distribution is of the form:

$$N(E)\, dE = g\, F(Z,E)\, p\, E\, (E_{max} - E)^2\, dE \qquad (2)$$

where $N(E)$ is the number of β+ particles with energy E, p is its momentum, E_{max} is the maximum energy allowed by the decay process, g is a coupling constant, $F(Z,E)$ is the Fermi function, and Z is the atomic number of the beta decay daughter nucleus. A non-relativistic approximation for the Fermi function, valid for allowed transitions of lighter elements is [99][100]:

$$F_{allowed}(Z,E) = 2\pi \frac{\eta}{(1 - e^{-2\pi\eta})} \qquad (3)$$

where $\eta = -Z\alpha E/p$ for positron decays, and $\alpha = 1/137$ is the fine structure constant. Figure 15 shows the expected positron energy distributions obtained using Equation 3 for some radionuclides of interest in clinical or preclinical PET such as ^{11}C, ^{68}Ga, ^{18}F, as well as ^{22}Na for its use in the characterization studies of detectors. Table II summarizes some important properties of these isotopes [98].

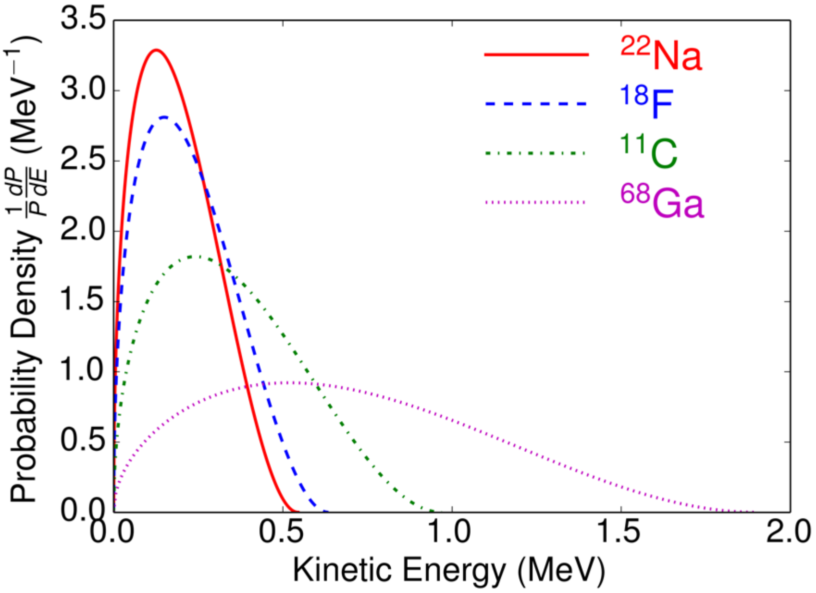

Figure 15. $\beta+$ decay energy spectra for different isotopes of interest for PET studies.

Table II. Most relevant characteristics of radionuclides of interest used in PET.

Isotope	Half-life	Maximum e$^+$ energy (MeV)	Mean e$^+$ energy (MeV)	Mean e$^+$ range in H_2O (mm)
^{11}C	1221.8 s	0.96	0.39	1.1
^{18}F	109.8 min	0.64	0.25	0.6
^{22}Na	2.6018 yr	0.55	0.22	0.5
^{68}Ga	67.8 min	1.89	0.89	2.9

2.3.2. Photon interaction with matter

The two 511 keV photons generated in the positron-electron annihilation are typically stopped using a high-density scintillation material. When the gamma-rays enter the scintillation material they can be either transmitted or attenuated. The attenuation may be due to absorption or dispersion processes. Equation 4 gives a good approximation to the number of gamma-rays that pass through matter. This equation is referred to as a Lambert's law, and is applicable for linear attenuation.

$$N(x) = N_0 e^{-\mu x} \quad (4)$$

$N(x)$ represents the number of photons that travel through the scintillator material without interacting, N_0 the initial number of photons, x the scintillator thickness and μ the linear attenuation coefficient which depends on the type of material and on the energy of the gamma radiation. In general, the photon matter interaction can be described in terms of particle collisions, where the energy of the incident gamma-ray is partially or completely transferred to the electrons or to the atom nuclei of the scintillation material that are explained in the following. There are three main dominant processes for the energy deposition in the scintillator material. Figure 16 schematically shows these processes.

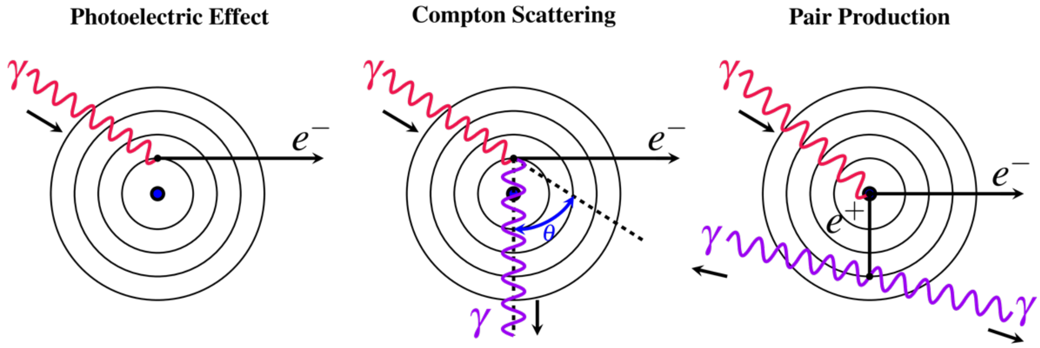

Figure 16. Interaction of a gamma-ray within an atom. Left, Photoelectric interaction. Center, Compton scattering. Right, pair production.

Photoelectric effect

The photoelectric effect was first observed in 1887 by Hertz. In this interaction, the incident gamma ray transfers all its energy to an electron located in one of the atomic shells and as a result, the electron is ejected from the atom with energy (E_e):

$$E_e = E_{hv} - E_b \quad (5)$$

where E_b is the binding energy of the atomic shell and E_{hv} is the energy of the incident gamma-ray. The ejected electron rapidly loses its energy and moves a relatively short distance from its original location. Therefore, part of the gamma-ray energy is used to overcome the electron binding energy and to remove it from the atom, and the remaining part is transferred to the electron as kinetic energy and is deposited in the surrounding matter.

As a result of the electron ejection, a vacancy is created in one of the atomic shells, and thus the atom is ionized. This vacancy is filled by a free electron or by an electron from a higher energetic level, where the energy difference is emitted (in most cases) as characteristic X-ray photons that travel a short distance before interacting or escaping. In some cases it produces the Auger effect. In the Auger effect, the energy is transferred to another electron from a higher level of the same atom ejecting the electron from the orbital (Auger electron), creating a new vacancy, so the atom remains ionized. Finally, another electron can fill the vacancy resulting in a fluorescence where an electron or an Auger photon is emitted, repeating the process. The electron and Auger photons are low energy (E <1 keV) so they have a very short mean free path. The probability of the photoelectric process is related to its cross section (σ_{pe}), that can be approximated as [101]:

$$\sigma_{pe} \propto \frac{Z^m}{{E_{h\nu}}^n} \quad (6)$$

where m can vary depending on the incident gamma-ray energy from 4 to 5 and n from 1 to 3.5 [102]. The probability of photoelectric absorption increases rapidly with increasing the atomic number of the absorber atom, and decreases rapidly with increasing the photon energy [96].

Compton scattering

The Compton interaction [103] describes the scattering of a photon with a charged particle, usually an electron. In this process, the incident gamma-ray interacts with an electron of the material transferring to this electron a portion of its energy, and thus the photon is deviated from its original trajectory with an angle θ. In this interaction, for a gamma-ray with incident energy $E_{\mathrm{h\nu}} = hc/\lambda$, the outgoing final state photon energy $E_{\mathrm{h\nu\prime}}$ can be expressed by:

$$E_{\mathrm{h\nu\prime}} = \frac{E_{\mathrm{h\nu}}}{1\ +\ (E_{\mathrm{h\nu}}/m_e c^2)\,(1 - cos\theta)} \quad (7)$$

Equation 8 can be particularized for the case in which the energy $E_{\mathrm{h\nu}}$ corresponds to the electron energy ($m_e c^2$):

$$E_{\mathrm{h\nu\prime}} = \frac{m_e c^2}{2 - cos\theta} \quad (8)$$

This is of relevance for PET scanners since the gamma-rays come from an annihilation process. The Compton cross section (σ_c), can be approximated using the Klein-Nishina differential formula [104], where it is assumed that the electrons are free and at rest:

$$\frac{d\sigma_c}{d\Omega} = \frac{x}{2}\frac{1}{[1 + \Delta(1 - cos\theta)]^2}\left(1 +\ cos^2\theta + \frac{\Delta^2(1 - cos\theta)^2}{1 + \Delta(1 - cos\theta)}\right) \quad (9)$$

Here, $r_e =\ e^2/E_e$ is the classic electron radius (r ≈ 2.83×10^{-13} cm). The probability of Compton scattering gets reduced with the incident gamma ray energy, depends on the material density, and is almost independent of the atomic number. This formula also shows the angular dependency of the energy transmission between the incident photon and the electron. The maximum energy deposition occurs when the incoming gamma-ray is dispersed in the opposite direction to its incidence.

Pair production

Pair production is a photon-matter interaction not encountered in nuclear medicine techniques since photons with energies larger than 1.02 MeV are required. In a pair-production interaction, the photon interacts with the nucleus in such a manner that its energy is converted into matter, producing a pair of particles, an electron and a positron. See reference [105] for the details about the pair production cross section.

As mentioned above, the probability for each one of these processes is related to its cross section. These cross sections are dependent upon the energy of the incoming gamma-ray and the material. The material total cross section is defined as the sum of the cross section of each of the individual processes, for the total number of processes n and the elements composing the scintillator material m:

$$\sigma_T(E) = \sum_{i=1}^{n} \sum_{j=1}^{m} \sigma_{ij}(E) \qquad (10)$$

Figure 17 shows the predominant regions for each one of these processes. The lines indicate where the cross section for two processes is equal. As an example, in a LYSO scintillator ($Z_{eff} \approx 63$) the most probable interaction is Compton scattering, although photoelectric is non-negligible.

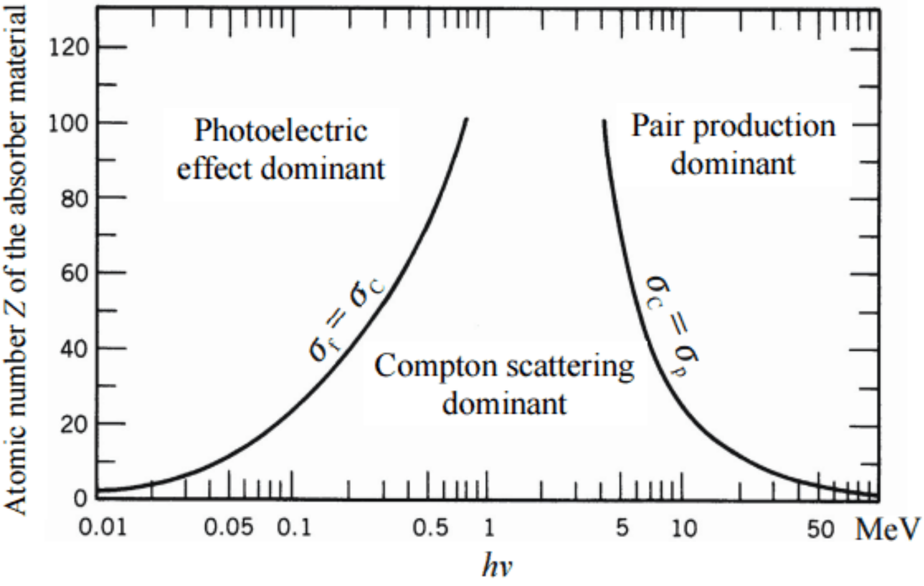

Figure 17. Dominant radiation-matter interactions as a function of the energy and the atomic number of the absorbent material.

2.3.3. Scintillation mechanism in inorganic scintillators

Scintillator materials can be organized in two main groups: organics and inorganics. Organic scintillators present a low effective atomic number (Z_{eff}) and are mainly used to track charged particles. On the contrary, inorganic scintillators, upon other properties, are more suitable to stop the 511 keV gamma-rays due to their higher Z_{eff} and therefore, are the most used in PET scanners.

The scintillation mechanism of inorganic crystals depends on the structure of the crystal lattice of the material. The crystals have a discrete structure of bands, called valence and conduction, being the energy between them the gap.

When a gamma-ray interacts within the crystal, via photoelectric effect or Compton scattering, it deposits its energy promoting electrons from the valence to the conduction band leaving a hole in the valence band and thus, creating an electron-hole (e-h) pair. The number of e-h created is proportional to the energy deposited. Such electrons return to the valence band emitting photons. However, the emission of a photon is an inefficient process and moreover, band gap widths in pure crystals are such that the resulting energy of the emitted photon is too high (ultra-violet (UV) range) to lie within the visible range (the energy of the emitted photons is the same than the energy needed to activate the e-h pair). For this reason, small amounts of impurities, called activators, are added to the crystal. These impurities create special sites in the lattice at which the band gap structure is modified. The energy structure of the overall crystal is not changed, just the energy structure at the activator sites, see sketch in Figure 18. As a result of this process, the electron can de-energize, emitting less energetic photons that lie in the visible range. Their energy is therefore, smaller than the energy needed to activate and e-h pair.

The conversion of the incident gamma-ray into optical photons can be therefore described as a three-step process: *i)* excitation, the e-h pairs are created, the holes rise to the valence band and the electrons drop to the bottom of the conduction band, this happens in a very short time of about 10^{-12} s; *ii)* thermal relaxation, the holes ionize the activation sites and an electron is captured; And *iii)* photoemission, the excited activator site decays through the emission of a photon. These three processes have a certain efficiency and therefore, only part of the energy deposited in the crystal by the incident gamma-ray is converted into low energy optical photons (the rest is converted into thermal energy through phonons).

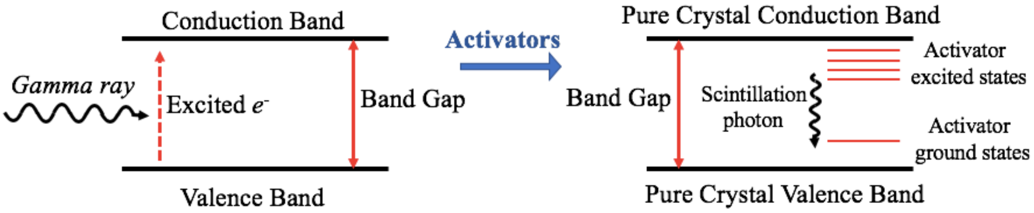

Figure 18. Energy band structure of an inorganic scintillator. Left, pure scintillator. Right, activated scintillator.

There are many types of inorganic scintillators used in PET. Table III summarizes the properties of the most commonly used, and its activators.

Taking into account the photoemission process, the ideal scintillator should present the following properties [106][107]:

i. *High light yield (LY).* The light yield is the number of scintillation photons (in the visible light spectra) generated per unit of deposited energy. The higher the *LY*, the better the determination of the gamma-ray impact position and also the better the energy resolution.
ii. *Linearity.* The produced amount of scintillation photons should be proportional to the energy deposited by the incident radiation.
iii. *Transparency.* The scintillator should be transparent to the wavelength of its own emission spectra. If not, the energy of the scintillation photon will be the same that the one needed to activate the e-h pair (UV emission). This is accomplished by adding impurities to the scintillator, as already described.
iv. *High Z_{eff} number.* For a fixed energy of the incident gamma-rays, its probability of interacting via photoelectric instead of via Compton scattering increases with Z_{eff}. As in the photoelectric interaction all the energy is deposited in a single interaction, and thus the line of response (LOR) connecting two opposite detectors, is determined more accurately.
v. *Fast decay time of the induced luminescence.* Should be as short as possible in order to avoid pile-up events, hence minimizing the dead time and improving the time resolution of the system.
vi. *Coupling.* The refraction index of the scintillator material should be as close as possible to that of the photodetector maximizing the light transmission.

Table III. Properties of common inorganic scintillator materials used in PET.

	NaI(Tl)	**BGO**	**GSO**	**$LaBr_3$**	**LSO**	**LYSO**
Z_{eff}	51	74	59	46.9	66	63
Refractive index	1.85	2.15	1.89	1.9	1.81	1.82
ρ (g/cm^3)	3.7	7.13	6.7	5.06	7.4	7.1
LY (ph/MeV)	41000	9000	9000	42500	29000	32000
Decay time (ns)	230	300	56	16	40	41
μ (cm^{-1}) @511 keV	0.35	0.95	0.698	0.476	0.866	0.83
Wavelength (nm)	410	480	440	380	420	420
Activator	Talium	-	Cerium	Cerium	Cerium	Cerium

2.4. Coincidence detection

The detection of the two back-to-back photons in two opposed PET detectors, within a time coincidence window, is called coincidence detection. A coincidence event is assigned to a LOR joining the two detectors involved. Note however, that due to both physical effects and the coincidence detection method, the assigned LOR may not coincide with the actual position of the emitted positron and therefore, the image quality may be degraded.

2.4.1. Main physical effects degrading the image quality

i. *Positron range.* Defined as the short distance travelled by the emitted positron before its annihilation with an electron. The quantity that directly degrades the spatial resolution is the effective positron range, defined as the average distance from the emitting nucleus to the end of the positron track, measured perpendicular to the LOR of the annihilation gamma-ray [98]-[106].

ii. *Acolinearity.* When the positron-electron annihilation occurs, the positron may still have some residual kinetic energy, which due to the energy-momentum conservation, may result in a small deviation from 180° in the angle at which the generated gamma-rays depart from each other. The acolinearity increases with the distance between detectors being the maximum deviation ± 0.25° [108]. This effect produces a mismatch in the LOR positioning, generating a Gaussian blurring profile at the center of the scanner proportional to the diameter of the detector ring. This deviation (R_{180°) can be expressed as a function of the acolinearity angle (θ) as:

$$R_{180^\circ} = R\, sin\left(\frac{\theta}{2}\right) \sim \frac{R \cdot \theta}{2} \quad (11)$$

The effect, in terms of FWHM, on the image spatial resolution is linearly dependent on the separation distance of the coincidence detectors and it can be expressed as $R_{180^\circ} = 0.0044 \times R\ (mm)$ [109]. For example, in the case of a small animal PET R = 58.5 mm [110] and in a whole-body PET scanner R = 400 mm, therefore the FWHM for blurring caused by acollinearity is approximately 0.25 mm and 1.76 mm, respectively.

iii. *Parallax error.* Gamma-rays travel some distance in the crystal before interacting, and therefore, when enter at an oblique angle, the position of the interaction point will not be the same as the point of entry into the crystal. If this distance is not considered, an incorrect LOR will be assigned to this interaction degrading the system spatial resolution [111]. Information regarding the photon depth of interaction can be included during the reconstruction process addressing the parallax error (see Section 2.4.1.1).

iv. *Detector size.* In PET scanners based on pixelated crystals, the spatial resolution is limited by the pixel size. However, when using monolithic blocks, the spatial resolution depends on other factors. A detailed explanation of both detector configuration and its impact on the spatial resolution is performed in the next chapter.

2.4.1.1. Role of DOI in PET

The depth at which the gamma-ray interacts within the crystal is known as Depth of Interaction (DOI), and is considered as the 3rd spatial coordinate of the LOR. The uncertainty in the DOI coordinate of the interaction point, when the photon enters at an oblique angle, produces an error in the determination of the true LOR degrading the spatial resolution and producing a blurring effect in the final reconstructed image. This error is known as the aforementioned parallax error and the development of DOI-encoding detectors is one of the major research topics in PET detector instrumentation. In PET scanners, the parallax error has an impact at the edges of the scanner FOV worsening its spatial resolution.

The parallax error increases for annihilations that take place closer to the edges of the FOV. For this reason, the effect is more pronounced for small ring diameters where, due to their small FOV, it is most likely to have those oblique LORs. Moreover, due to a worst characterization of the light distribution in thicker crystals and therefore a worst estimation of the photon impact coordinates closer to the edges, the effect is more accused in thicker crystals.

Figure 19, shows the real and virtual LORs assigned to two different events. In the case of events perpendicularly impinging to the detector surface, the true and virtual LOR match. However, in the case in which the photons are impinging with an oblique angle to the detector surface, the assigned virtual LOR does not match with the real one, producing the parallax error. Including DOI information during the LOR assignment allows one to address the parallax error and to improve the final image resolution specially for events at the edges of the scanner FOV.

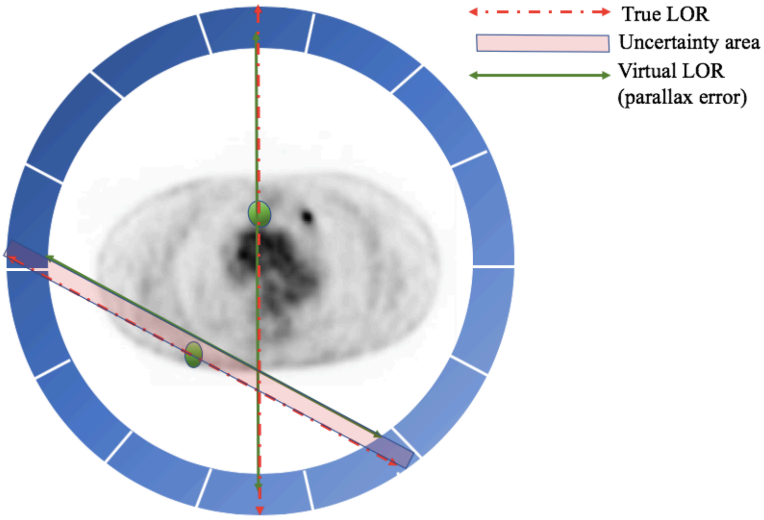

Figure 19. Parallax error. The dashed line represents the real LOR, while the continuous line shows the LOR that would be assigned in the absence of information about the impact depth of interaction.

2.4.2. Degradation caused by coincidence detection type

To accept only coincidence events, a coincidence time window (CTW) has to be selected. If two events are detected within the same CTW, those will be recorded as a coincidence. However, the coincidence resolving time of the system (CRT) is not perfect and sometimes, the system accepts false coincidence events. There are four main coincidence types [108]:

i. *True.* Neither detected gamma-ray experiences any form of interaction prior to detection, and no other event is detected within the CTW. See Figure 20a. Only true coincidences provide correct information about the radiotracer deposition in the subject.

ii. *Scattered.* One or both detected gamma-rays has suffered at least one Compton scattering and its direction is changed. The resulting coincidence event may be assigned to the wrong LOR, adding background to the true coincidence distribution and increasing the statistical noise to the signal. See Figure 20b.

iii. *Random.* Two gamma-rays from different annihilation events are detected within the CTW of the system, see Figure 20c. The distribution of random coincidences is almost uniform across the FOV and its rate increases with the square of the activity in the FOV. The rate of random coincidences can be estimated as:

$$R = 2\tau \cdot C_1 \cdot C_2 \quad (12)$$

where τ is the time width of the pulses in nanoseconds and C_1 and C_2 are the single count rates in counts/s on each of the two detectors. Both scattered and random coincidence events depend on the volume and attenuation characteristics of the imaged object, and on the geometry of the system. If not corrected the image contrast decreases and the isotope concentrations may be overestimated.

iv. *Multiple.* More than two gamma-rays are detected within the CTW in different detectors, making impossible to determine the correct LOR and causing event miss-positioning. See Figure 20d.

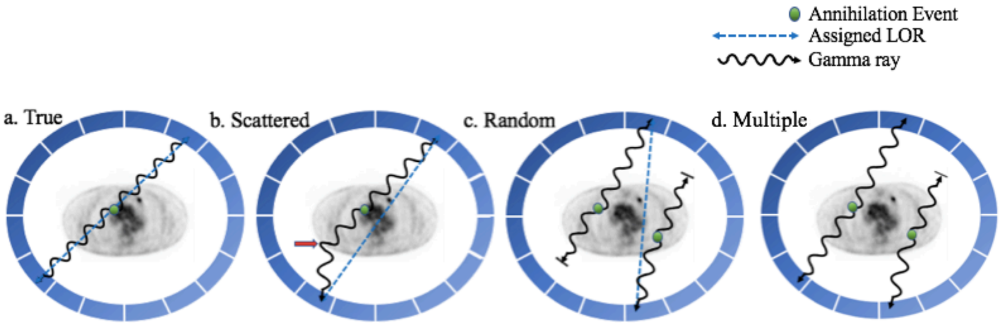

Figure 20. Types of coincidence events in PET. From left to right: True, scattered, random and multiple coincidences.

2.4.2.1. Role of TOF in PET

Current PET instrumentation is not able to provide the exact point in the LOR at which the positron-electron annihilation took place, and therefore, the same probability of occurrence is assigned to any position defining the LOR [112]. This assumption produces noise in the image during the reconstruction process. This problem can be addressed by knowing the temporal arrival information of the annihilation photons to each detector. If the CRT is good enough, it can be used to more precisely estimate the coordinates of the annihilation, ideally reducing the LOR to a point. Using this information, the position uncertainty in the LOR can be estimated as:

$$\Delta X = \frac{c \cdot \Delta T}{2} \qquad (13)$$

where ΔX is the annihilation coordinate uncertainty, c is the speed of the light and ΔT the time resolution between the detection of the annihilation photons at opposite detectors, i.e. the temporal resolution of the system. However, the measurement of ΔT is not perfect and there is an uncertainty associated to ΔX. Figure 22 shows a sketch of the conceptual principle of the TOF technique.

Implementing TOF information in PET systems will reduce the noise levels improving the signal to noise ratio (SNR). The gain factor of the SNR due to the TOF can be estimated as:

$$Gain\ in\ SNR = \left(\frac{D}{\Delta x}\right)^{1/2} = \left(\frac{2D}{c\Delta t}\right)^{1/2} \qquad (14)$$

Where D is the scanner diameter and Δt is the coincidence timing resolution. In terms of sensitivity, the gain can be estimated as:

$$Gain\ in\ Sensitivity = \frac{2D}{c\Delta t} \qquad (15)$$

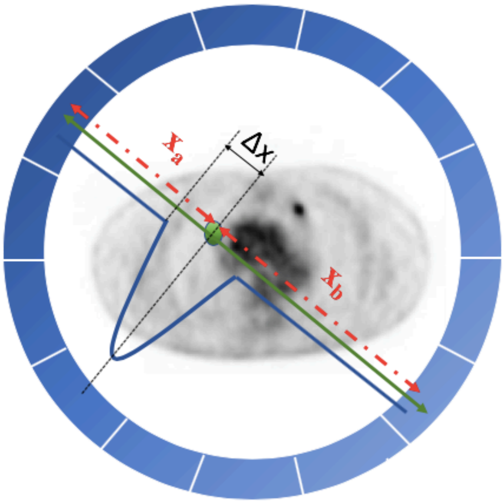

Figure 21. Scheme of the TOF. The green line represents the assigned LOR and the blue one the area considered after applying TOF techniques.

For example, if the TOF resolution improves from 600 ps to 100 ps, a gain of sensitivity increased by a factor of 6 is expected for the same organ under investigation. Since the SNR is improved the acquisition does not need as much statistics as before allowing to reduce the radiotracer dose to the patient. Moreover, TOF can be useful for systems with open geometries in which the number of detectors is reduced and therefore, a lack of angular information is present. Due to the incomplete sampling of the polar angles, limited angle coverages produce image artifacts. The number of angular views necessary for an artifact-free image reconstruction is reduced as TOF PET resolution improves [113][114].

Improving timing information is more feasible when using scintillators with high light yield and fast decay, combined with high-speed and sensitive photodetectors, and fast and stable electronics. With the improvement of the above mentioned elements, < 250 ps have been achieved for the very latest generation systems [115]-[117].

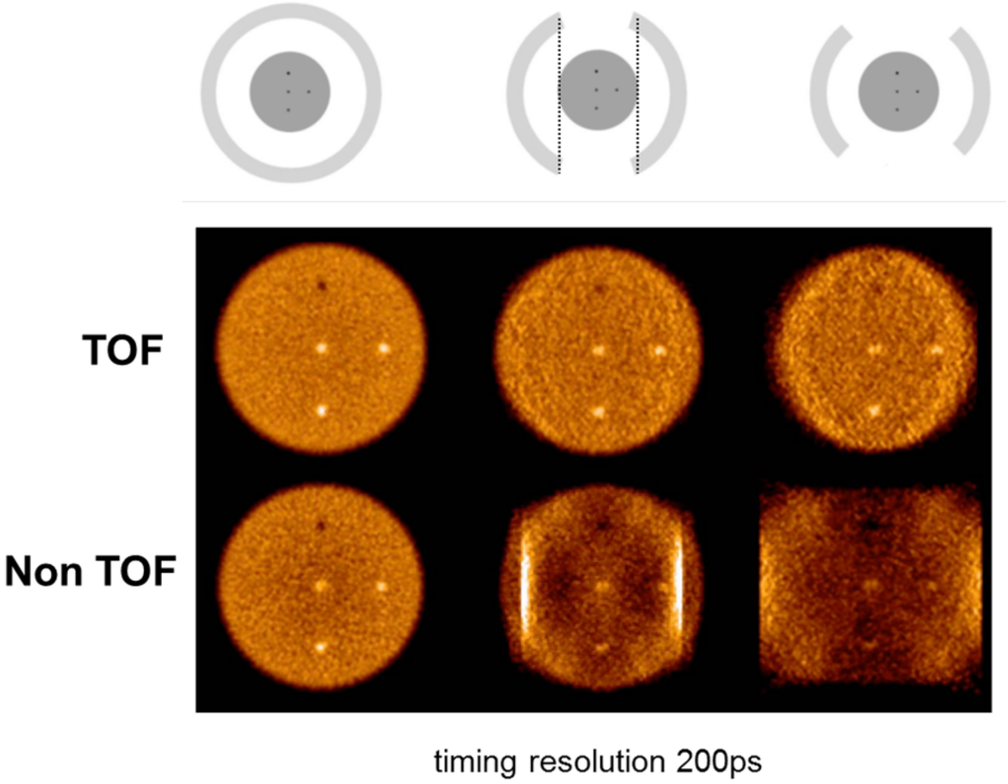

Figure 22. Effect of TOF for a limited angle coverage PET system reconstruction (Original image extracted from [118]).

2.5. Data acquisition: 2D and 3D PET mode

Nowadays, most PET scanners operate in 3D mode. A former 2D modality was however widely extended. Both acquisition modes produce 3D images since the nomenclature only specifies the type of acquired data.

In 2D mode, LORs through a specific imaging plane are considered and the 3D image is obtained by repeating 2D acquisitions and reconstruction for multiple axial slices. In this acquisition mode a thin septa, tungsten or lead, separates adjacent rings and coincidences are only accepted for detectors within the same ring or lying in close rings, see left panel of Figure 23. Coincidences between detectors in neighboring rings are merged to produce a dataset consisting of co-planar sets of LORs normal to the axis of the camera.

In the 3D mode, the septa are removed, and coincidences are allowed between detectors lying in any ring combination, see right panel of Figure 23. This acquisition mode significantly improves the scanner sensitivity [119], reducing therefore, the statistical noise. As a drawback, requires more powerful computational systems, storage capability and the 3D reconstruction methods are more complex and time consuming. Different methods have been developed in order to reconstruct 3D data with 2D algorithms [120]. Moreover, it has to also be mentioned that the geometry of the scanner has a significant effect on its performance, increasing the axial FOV acceptance angle the sensitivity to true coincidences is increased, but also to random and scattered events. These events come from the remaining activity outside of the FOV and are included in the data [121].

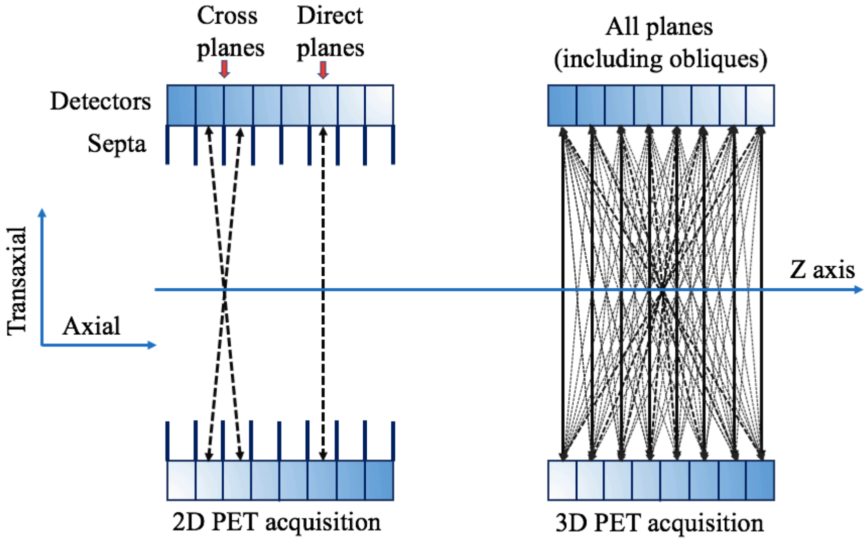

Figure 23. PET acquisition modes. Left, 2D acquisition mode showing a direct and a cross plane. Right, 3D acquisition mode showing all possible planes.

2.6. PET Image reconstruction

The final step of a PET scanner is thus, to provide certain image information of the unknown activity distribution in the subject of study (f) with a set of observations (p). This process is named image reconstruction. One way to represent such an image is using the linear equation:

$$p = Hf + n \quad (16)$$

where H is the known system model and n is the error in the observation. Depending on how the acquired data is considered, stochastic or deterministic, the reconstruction methods used in PET can be divided into two main groups namely analytic and iterative methods.

The more simplistic approach is to consider that the data is deterministic, therefore containing no statistical noise and thus n is a number with an exact value. Making this assumption, analytic reconstruction methods, that allow for a fast and direct mathematical solution, are used. The main drawback of these methods is that disregard the noise structure in the observation and are based on an idealized model of the system leading to reduced resolution images and typically poor noise properties.

A more accurate approach is considering that the acquired data values are stochastic. Real data is stochastic due to many physical aspects, such as the positron decay process, the gamma-rays undergoing attenuation, scattered and random effects, and the photon detection process. In contrast to analytic approaches, these methods are based on a more accurate description of the image process resulting however in a more complicated mathematical solution where it is impossible to find the exact value of n and therefore, iterative reconstruction methods have to be employed to solve this problem. In the following, there are brief descriptions of the analytic and iterative methods that are most used in PET reconstruction.

2.6.1. Analytic 2D reconstruction methods

2D central slice theorem

The 2D central slice theorem is also known as the central-slice or Fourier-slice theorem. The theorem postulates that the Fourier transform of a one-dimensional projection is equivalent to a section, at the same angle through the center of the two-dimensional Fourier transform of the object [122]. The theorem states that if we know $P(v_s, \phi)$ at all angles $0 \leq \phi \leq \pi$, then we can fill in values for $F(v_x, v_y)$. The inverse two-dimensional Fourier transform of $F(v_x, v_y)$ will give us $f(x,y)$, being $P(v_s, \phi)$ provided by the scanner, and $f(x,y)$ the

Back-Projection

The back-projection algorithm consists on placing a value of $P(v_s, \phi)$ back into the position of the appropriate LOR. However, in this projection step, the information regarding where the values came from is lost and therefore, a constant value is assigned to all elements along the LOR. The straight back-projection of all projections does not return the image because of an oversampling at the center of the Fourier transform. In order to have equal sampling the Fourier space is filtered. The two most used filtering approaches are:

i. *Back Projection-Filtering (BPF).* To filter the oversampling, a cone filter of the form $v = \sqrt{v_x^2 + v_y^2}$ is used. The process can be described as:

$$F(v_x, v_y) = vB(v_x, v_y) \qquad (17)$$

where $B(v_x, v_y)$ is the 2-D Fourier transform of the backprojected image, and $F(v_x, v_y)$ is the 2-D Fourier transform of the backprojection-filtered image. Finally, the inverse Fourier transform of $F(v_x, v_y)$ provides the image *f(x,y)*. The main disadvantage of the method is that the back-projection is computed first, requiring a larger matrix size than the size needed for the final result.

ii. *Filtered-Back Projection (FBP).* This is the most common analytically technique used to reconstruct the projections acquired in PET. This algorithm interchanges the order of the filtering and backprojection steps. The projections are first filtered for each angle in the Fourier space and then the inverse Fourier of the filtered projections is back-projected in the image space. The filtered projection includes a one-dimensional ramp filter, that is applied to each measured projection. With FBP the image can be efficiently calculated with a much smaller reconstruction matrix than can be used with BPF, for the same level of accuracy.

2.6.2. Analytic 3D reconstruction methods

In 3D PET acquisition mode are regions of missing data in oblique projection planes. The 3D reprojection algorithm (3DRP) solved the problem of the missing data in oblique measured projections [119]. The algorithm consists in three steps: *i)* A 3D image is formed with a 2D reconstruction of each transaxial slice; *ii)* The initial image is forward projected onto the regions of missing projection data; *iii)* The final image is obtained with 3D FBP using the complete set of data (the original and the new set). The method is slow and therefore, rebinning methods to reconstruct 3D data through 2D methods were developed, such as the Single-Slice Rebinning (SSRB) [123][124], the Multi-slice Rebinning (MSRB) [125] or the Fourier Rebinning (FORE) [126][127].

2.6.3. Iterative reconstruction methods

Iterative processes use more realistic models of the system but at the cost of more complex mathematical and computational procedures. These algorithms are based on reducing the uncertainty of an estimate of the unknown image through consecutive iterations. All iterative methods contain five basic components:

i. *Model for the image*. It is a discretization of the image in N distinct pixels (2D image) or voxels (3D image).
ii. *System model.* Relates the image to the data considering the probability of detecting the positron emission produced in one voxel and in one LOR.
iii. *Model for the data.* Relates how the projection measurements vary around their expected mean value. Poisson models are commonly used, however once the corrections for randoms, scatter or attenuation are applied, the data does not longer follow a Poisson distribution and other models are applied [119][128].
iv. *Governing principle.* Can be expressed as a cost or objective function, the most common principle for iterative reconstruction is the Maximum Likelihood approach.
v. *Algorithm*. Optimizes the cost function. The most typical algorithms are the Maximum Likelihood – Expectation Maximization and the Ordered Subsebts Expectation Maximization.

Maximum Likelihood–Expectation Maximization (MLEM)

The MLEM algorithm is based on the maximization of the logarithm of the Poisson likelihood cost function using expectation maximization [129]. Provides a realistic statistical model of the data and its convergence is guaranteed. However, since each interaction requires one forward and one back-projection, the process is slow and the image noise increases with each interaction.

Ordered subsets Expectation Maximization (OSEM)

The OSEM algorithm was introduced to speed-up the reconstruction MLEM process [130]. This algorithm divides the entire data into N subsets and in each iteration the image is updated N times (as the number of subsets indicates) speeding up the process *N* times compared to the MLEM. However, the convergence to the ML solution is not guaranteed and an optimization of the number of subsets and iteration is required.

2.7. PET image corrections

There are several corrections to the image which must be addressed in order to obtain a proper measurement of the radio-tracer concentration and distribution within the organ or patient. Attenuation, random coincidences, scatter coincidences, normalization and dead-time corrections are the most relevant applied during the image reconstruction process.

2.7.1. Attenuation correction

Attenuation is the loss of detection of true coincidence events because of their absorption in the body. CT or MRI scanners are used to generate attenuation maps as a function of the energy transmission differences throughout the body. It is interesting to mention that PET attenuation correction using MRI data is still a very active field of research since these scanners do not provide directly these maps and need to be extracted from certain specific MRI sequences. These maps are used to correct the absorption of the emitted photons [131]. Attenuation correction of data is necessary for accurate qualitative and quantitative measurements of the radio-tracer activity, if not corrected the image will present loss of uptake in the central region.

2.7.2. Random coincidences correction

There are several methods to estimate the number of random events. The most common correction for randoms is the so-called delayed coincidence technique [106], which is based on using two different coincidence windows. In this method the signal of one detector is delayed and coincidences are determined between this delayed detector and a non-delayed one. All coincidences detected within the delayed time window are randoms. An alternative method estimates the rate of random events (R) using equation 12, measuring the single count rate on each detector for a given time window [132]. Note that measured random events are affected by systematic errors associated with the PET scanner electronics.

2.7.3. Scatter correction

Scatter correction is essential because of the loss of contrast and resolution in the image [133] and therefore, several methods have been developed. Some methods use point sources to estimate the scatter function, such as the ones fitting an analytical function to the measured activity of the source and then interpolating the function to the real activity [134]-[137]. Alternatively to this, others convolve the measured scatter function with the source distribution to give an estimation of scatter data. The dual energy method for instance, is based on acquiring coincidences in two separated energy windows in order to discriminate the scatter fraction. In addition to the previous experimental methods, simulations based on Monte Carlo calculations are also employed to separate the scattered and un-scattered events from the measured events [138].

2.7.4. Normalization

Normalization correction accounts for physical variations in the detectors, such as gain differences between individual components. The detection efficiency of a detector pair varies from pair to pair, resulting in non-uniformities of the acquired data. Normalization of the acquired data is accomplished by uniformly exposing all detector pairs to a 511 keV photon source. Normalization factors are ideally calculated for each pair by dividing the average of counts of all detector pairs (LORs) by the individual detector pair count.

2.7.5. Dead-time correction

In general, the detector dead time becomes higher as the count rate increases. For high radio-tracer concentrations, the detector electronics are typically unable to generate an electrical pulse for each detected event. As a result, the detector saturates by stacking pulses, resulting in a considerable loss of counts. If not corrected, high intensity uptake will present a radio-tracer concentration lower than the real one, leading to significant errors in terms of quantification, and also image distortion. Dead time correction is made by measurement of observed count rates as a function of increasing concentrations of activity.

3. Design and methods for PET detectors

This chapter is dedicated to the description of the PET detector block elements namely the scintillator material, the photosensor types, and the read-out electronics. Moreover, this chapter includes a brief overview of the main positioning algorithm and calibration techniques used in PET systems based on monolithic blocks.

The chapter makes special emphasis in the characterization of the main materials and methods that have been used for the development of the articles presented in the thesis. In particular, the present work focuses on the studies of monolithic scintillators (see Section 3.1.1.2) coupled to SiPMs (including different geometries and configurations) and of the methods described in Section 3.3.1. Finally, a short description of the PET systems designed and built, as a result of the findings described below, is also included.

3.1. PET detector block

Detector blocks constituting PET systems have to be designed and optimized for the efficient stopping and detection of the incoming high energy radiation (511 keV). In addition, they have to be capable of providing enough information for an accurate estimation of the photon impact coordinates within the scintillation crystal. Three elements can be specifically distinguished in PET detector blocks, see Figure 24:

i. *Scintillation material.* The scintillation material stops the 511 keV annihilation photons generating as a consequence, many optical photons of lower energy (in the eV range). As described in Section 2.3.3, inorganic scintillation materials are more suitable to stop these gamma-rays and therefore, are the ones typically used in PET scanners.

ii. *Photosensor (or photodetector).* The photosensor has to efficiently convert the low signal from scintillation photons (visible range) into electrical signals in the emission wavelength of the scintillator. This property is called Photon Detection Efficiency (PDE).

iii. *Readout and front-end electronics.* The front-end electronics are responsible for conditioning and processing the output signals from the photodetectors. Output signals are typically analog and they are fed into a Data Acquisition System (DAQ) in order to be shorted by coincidences and later digitized. Alternative methods using digital information are the ASICs. Electronics have to improve the signal to noise ratio.

The combination of the above mentioned elements should maximize the detector block performance, providing high photon absorption efficiency of the 511 keV photons and exhibit good spatial, energy and time resolutions. The photon absorption mainly relies on the scintillator block type, higher photoabsorption is accomplished using high Z_{eff} scintillator materials that leads to a higher fraction of photoelectric interactions (smaller fraction of scattered events) and thus, to a higher SNR in the images.

The spatial resolution can be defined as the minimum distance between two sources of radiation (approximately point-like) at which are discernible. It depends however, not only on the scintillator but also on the photosensor and front-end ability to accurately determine the photon interaction position within the crystal.

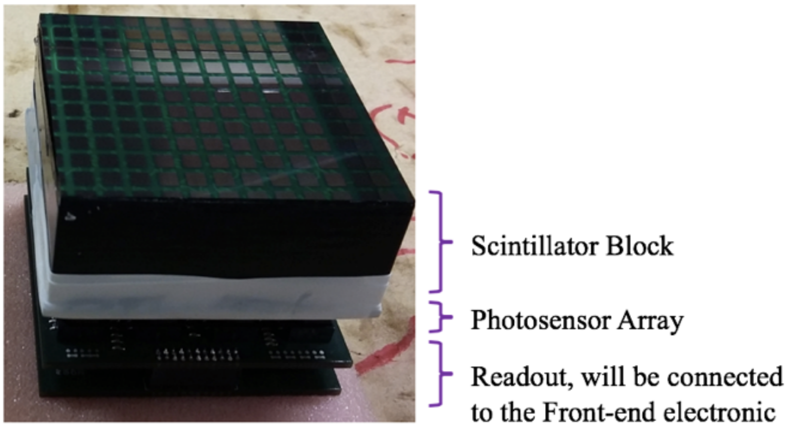

Figure 24. Photograph of a detector block composed by a monolithic LYSO scintillator block ($50 \times 50 \times 20$ mm^3) with the lateral walls black painted. The crystal has been coupled by means of optical grease to a photosensor matrix of 12 × 12 SiPMs array (can be seen through the crystal) and connected to an analog front-end readout electronics.

The energy resolution can be defined as the detector ability to distinguish the deposition of the incident energy (allowing to discard scattered events) and depends not only on the scintillator block but also on its coupling with the photosensor and on the electronics performance. The energy resolution improves with the number of collected scintillation photons, and therefore, it is convenient using high LY scintillators, coupling methods reducing optical losses and photosensors with high PDE.

The time resolution mainly depends on the scintillator and its associated electronics, but also on the photosensor. It allows one to determine true coincidence events based on their detection time. Timing capabilities are improved with scintillators exhibiting short decay times and short transit periods of the photons within the scintillator.

In addition to the reconstruction method, the final image in PET depends therefore of a combination of all the above mentioned elements. For this reason, the selection of the individual elements should guarantee the maximization of their performance. A more detailed description of these components is described below. Notice that, although the properties of a detector block can be characterized and studied separately, the system is working in coincidence mode, which implies the existence of a pair of two opposite detector blocks.

3.1.1. Scintillator crystal

As described in Section 2.3.3, incoming radiation from the positron-electron annihilation interacts with the scintillator block causing ionization or excitation of atoms and molecules. Ionized and excited atoms undergo recombination or deexcitation releasing energy. Part of the energy is dissipated as thermal energy and the rest is released as visible light (scintillation photons).

The main goal of the scintillation block is to efficiently stop and convert the 511 keV gamma-rays into low energy scintillation photons providing accurate 3D photon impact coordinates within the crystal. For this purpose, many crystal block types and configurations have been studied. There are two main block configurations namely crystal arrays (pixelated) and monolithic blocks. The first are made out of a single or multiple layers of scintillation matrices, see Figure 25 left, that are composed by an array of individual small scintillation pixels optically isolated. Monolithic blocks are made of a single piece of scintillation material as depicted on the right hand side of Figure 25. Within the context of this thesis, a hybrid configuration including monolithic and pixelated elements in a single detector has also been investigated. The advantages and disadvantages of each configuration have been widely described in the literature [139][140], and are summarized below.

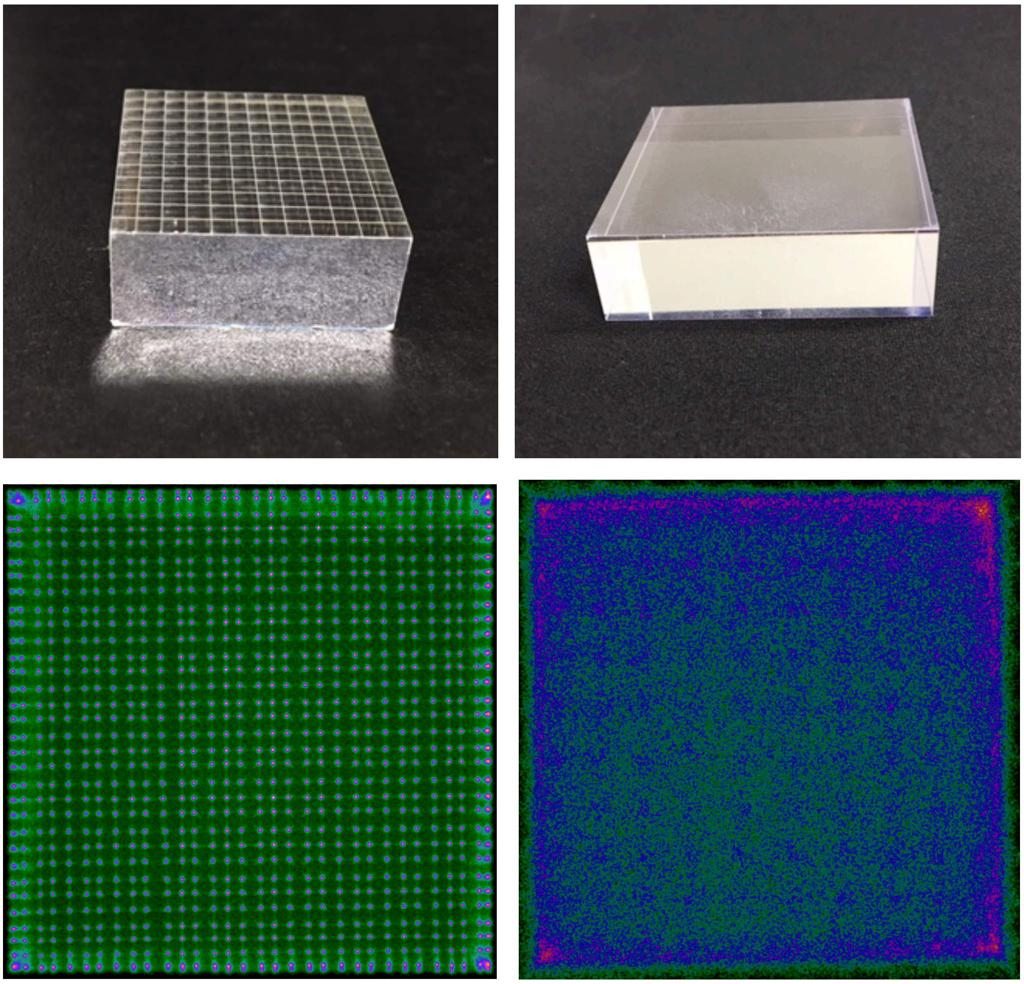

Figure 25. Top-Left, LYSO pixelated block, 2 mm pitch size. The lateral walls and the entrance face are coated with an ESR layer. Top-Right, LYSO rectangular monolithic block, 15 mm thickness. The bottom panels show flood maps of a LYSO pixelated (1.5 mm pitch) and a monolithic block (both with dimensions of 50 × 50 mm^2), respectively.

3.1.1.1. Pixelated crystals

Pixelated scintillator blocks are the result of coupling a discrete number of individual scintillator elements in a matrix. The pixilation process has to be done ensuring a high light output as well as an excellent pixel-to-pixel uniformity with minimal crosstalk.

The most traditional way of obtaining these pixelated blocks is mechanically cutting a big block of scintillation material from an ingot into smaller pieces (pixels), that are lately assembled in a matrix, see Figure 25 left. In the assembling process different treatments to the individual pixel surfaces can be applied, such as painting the walls with white paint or including a reflective layer to increase the amount of light that reaches the photosensor. They can be polished or left rough after cutting.

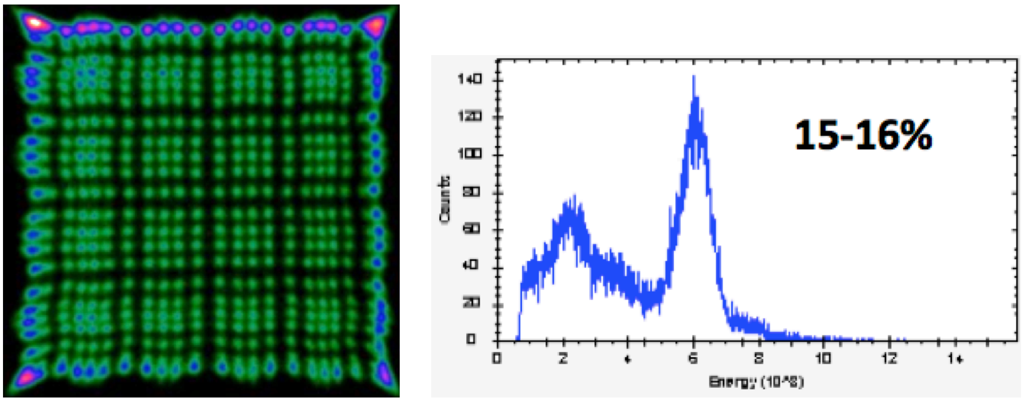

Figure 26. Left, flood map measured for an LFS pixelated block (1 mm pixel size). Right, energy spectra for a region of interest including 9 crystal pixels.

It should be noticed that current pixelated technology is capable of manufacture crystal arrays with gaps in between elements as narrow as 50 microns. An alternative procedure using lasers, the so-called Laser Induced Optical Barriers (LIOB), has been explored. This method consists on using a pulsed laser beam tightly focused in a small focal volume causing the material optical breakdown. As a result, an optical barrier with a refractive index different from that of the crystal bulk is created [141][142]. However, whereas the mechanical cutting is able to provide pixel sizes as small as 0.5 mm, LIOB is not. Moreover, there exist some crosstalk when the LIOB process is applied that might not be desired. Figure 26 shows a measurement that have been carried out at the i3M with an LFS crystal array, with pixel sizes of 1 mm generated using the LIOB technique. Pixel identification was good, but edge effects are larger than when using standard pixelated crystals.

Pixelated scintillator blocks provide discrete information on the 2D photon impact coordinates (*x*,*y*), without the need of complex mathematical methods. The final image resolution substantially relies on the intrinsic spatial resolution of these blocks which is mainly determined by the size of the individual detector elements. However, other factors such as the detector resolution (R_{det}), the acolinearity ($R_{180°}$) and the positron range (R_{range}) also contribute.

The detector intrinsic spatial resolution can be approximated as a Gaussian function with $FWHM = R_{det} = Pixel\ size$. Therefore, the spatial resolution of an uncollimated detector pair can be approximated as a Gaussian which $FWHM = R_{det}/\sqrt{2}$ at midplane. Derived from the system geometry, the system resolution becomes wider as the source moves towards either detector being $FWHM = R_{int}$ at the face of the detectors [109].The system resolution of a pair of pixelated PET detectors can be estimated as [109]:

$$R_{Total} = \sqrt{R_{det}^2 + R_{range}^2 + R_{180°}^2} \quad (18)$$

R_{range} and $R_{180°}$ have a relatively small effect on the spatial resolution when compared with R_{det} ($\propto$ pixel size) and therefore, one can state that the best spatial resolution that can be achieved is dominated by the pixel size.

Information regarding the depth of interaction (*z coordinate*), when using conventional pixelated crystals is not straightforward. Retrieving this coordinate is possible but requires the use of extra components (scintillation materials, photosensor or electronics) increasing manufacturing costs and technical challenges. There are various DOI-encoding designs suitable for pixelated blocks [143]:

i. *Discrete DOI measurement using a multi-layer detector*. Consists on multiple layers of stacked crystal arrays, optically-coupled to a common photosensor. The centroid of each pixel should be displaced, in x- and/or y-directions, with respect to the centroids of the pixels of the next layer [144], see first panel of Figure 27. As a result, the interaction positions in the flood images corresponding to each layer are separated. Due to light dispersion by the other layers, these approaches present disadvantages regarding light collection efficiency and timing performance. Moreover, the DOI information is discrete (limited to the number of layers) which resolution is determined by the crystal length [145].

ii. *Discrete DOI measurement, phoswich approach*. This method employs a combination of several scintillation crystals with different time constants or doping concentrations [146][147]. Crystal layers are stacked without any shifting in the centroid position, the contributions are distinguished by different pulse-shape characteristics. In addition to the drawbacks described in the previous case, due to different decay times the timing performance is also deteriorated. The second panel of Figure 27 shows a scheme of this configuration, the blue and green colors depict two different scintillator types.

iii. *Direct DOI measurement*. Consists on several layers of scintillation blocks individually coupled to a photosensor each and therefore, the DOI information is identified by the photosensors [148][149], see third panel of Figure 27. As a drawback, too many output signals are provided and the manufacturing cost rapidly increases with the high amount of materials needed.

iv. *Continuous DOI measurement using dual-ended readouts*. Two photosensors are coupled to both ends of a single crystal array as can be seen in the fourth panel of Figure 27. Their differences in light collection are used to estimate the DOI coordinate [150][151]. Despite the fact that this method provides continuous DOI information, it requires additional photosensors and compact front-end electronics to reduce the gamma-ray attenuation and scattering at the front of the scintillation block.

v. *Continuous DOI measurements using single-ended readout*. Consists on coupling two-pixel crystals partially covered by reflector materials. Reflectors can be triangular [152] or with different shapes allowing to use the light dispersion for increasing the DOI dependency [153]. Other approaches use phosphor-coated crystal detector to re-emit phosphor-converted light with a longer decay time that can be used (applying Pulse Shape Discrimination (PSD) techniques) to obtain the DOI information [154]. The main drawback of these methods is that the light collection efficiency typically worsens the detector time resolution. Another method, also providing continuous DOI has been accomplished using light sharing techniques including an acrylic window at the entrance face of the scintillator array [155].

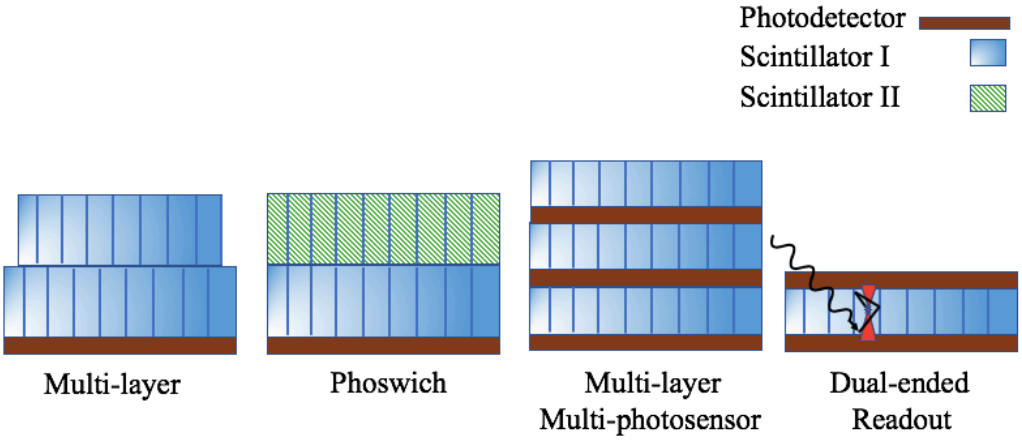

Figure 27. From left to right, sketch of the multi-layer, phoswich, multi-layer + multi-detector and dual-ended readout. The dual-ended case shows a Compton interaction of the gamma-ray and its multiple reflections before being absorbed.

Regarding energy resolution, the majority of the scintillation photons generated in pixelated based detectors reach the photosensor and therefore, its energy resolution is close, in general, to the intrinsic energy resolution of the scintillation material. For example, the intrinsic energy resolution at 662 keV for BGO, LSO and LYSO blocks is 12.0%, 10.0% and 8.0%, respectively [156].

Concerning TOF capabilities, pixelated blocks are good candidates, it is expected to obtain sub-100 ps time resolutions within the next years [116][157]. One of the difficulties relies on the use of long (≥ 20 mm) and narrow (4-5 mm) pixel crystals, required to improve the systems sensitivity, and therefore, its aspect ratio and attenuation properties yield significant variances in scintillation light collection and transit time to the photosensor (due to the different depth of interactions within the scintillator). Several approaches have been proposed to address this problem such as coupling the pixel to the photosensor by its long side [158]. Moreover, the majority of the 511 keV photons interact via Compton scattering and in some cases, the scattered photon is absorbed in a neighboring crystal element and the impact positioning becomes difficult.

3.1.1.2. Monolithic crystals

In recent years an increased interest has shown up for monolithic based PET detectors. These detectors employ continuous crystal slabs and therefore, there are no gaps allowing for higher packing fractions. Using one homogeneous piece of scintillator material it is possible facing several problems present in the pixelated approach, such as the inter-crystal scattering, light collection difficulties or manufacturing problems for smaller pixel sizes, although manufacturing big monolithic blocks is not strait forward given the size of the ingots. In continuous crystals the scintillation light spreads until reaching the photosensor (the spreading depends on the photon impact DOI and surfaces treatment) allowing to characterize the light distribution (LD) within the crystal. LD profiles can be measured in the photosensor and used to estimate the 3D photon impact coordinates providing information of the planar coordinates *(x,y)* but also on the depth of interaction *(z)* without the use of additional materials.

Differently from pixelated detectors in which the spatial resolution is limited by the pixel size, in the monolithic based detectors this is not longer the case. Nevertheless, there are other factors that contribute to the spatial resolution of the block such as those related to the photosensor. For instance, the spatial resolution depends on the photosensor element size, type and distribution of the elements composing the matrix. Photon DOI and scatter events, also play a role. These factors cannot easily be isolated and studied experimentally. For this reason, several works have focused on exploring the resolution limits through Monte Carlo simulations or other models [159][160]. All the above mentioned factors can be addressed and the final detector spatial resolution achieved using monolithic blocks is comparable to the one provided by pixelated detectors reaching a submillimeter range.

One of the disadvantages of continuous scintillators is that the spatial resolution degrades at the edges of the block due to the light truncation [161]. Within this thesis, in order to improve the impact determination at the edges, different crystal surfaces treatments and photosensor arrangements have been tested. In [3] for instance, it has been demonstrated the ability to characterize events as close as 0.25 mm from the crystal edge in a 15 mm thick monolithic LYSO block. Other works have studied the possibility of adding photosensors at the laterals [161] or reading the back side of the crystal [163] (double side reading). Monolithic based PET detectors have shown good energy and timing capabilities. However, the calibration of these systems requires complex processes.

Since the focus of the thesis is the performance study of thick monolithic blocks and their implementation in PET scanners, a description of the light distribution model is provided below. The positioning techniques applied to obtain the 3D impact coordinates are also detailed in the following.

Light distribution model

Since the scintillation light produced as a result of the conversion of the gamma-ray into low energy photons is emitted isotropically covering an area of 4π, the number of photons that reach any point ***r*** of the scintillation volume can be estimated by using the inverse square law:

$$dJ(\boldsymbol{r},\boldsymbol{r}_c) = \frac{J_c}{4\pi\,|\boldsymbol{r}-\boldsymbol{r}_c|^2}\,d\boldsymbol{S} \qquad (19)$$

where $\boldsymbol{r}_c$ are the coordinates of the gamma-ray interaction point within the scintillator block, J_c the number of scintillation photons produced as a consequence of the gamma-ray interaction whitin the crystal and $d\boldsymbol{S}$ the portion of the sphere surface covered by the photon flux. This law applies to conservative quantities isotropically radiated outward from a point source in three-dimensional space as it occurs with the scintillation photons under the assumption that self-absorption of the scintillation light is negligible. For example, in LYSO based scintillators the absorption length is 20 cm [162] and, since the thicknesses of PET detector blocks is typically below 20 mm, self-absorption can be considered negligible. As the emitted radiation gets further from the emission source, it is spread out over an area that is increasing in proportion to the square of the distance from the source. Hence, the intensity of radiation (number of photons) is inversely proportional to the square of the distance from the emission point.

Due to physical constrains such as internal reflection or photon absorption in the scintillator walls, not all the scintillation photons are collected by the photosensor. Moreover, the photosensor matrix for the scintillation light collection is coupled to, generally, only one side of the crystal covering a flat area. Therefore, only the scintillation photons projected over the *XY* plane defined by the photosensor matrix, will be detected. To make equation 19 valid in that case, a correction based on the law of cosines is applied. Thus, the photon flux corresponding to the surface $\boldsymbol{dS}$ will be covered by the surface of the sensitive area of the photosensor matrix $\boldsymbol{dS'}$, see Figure 28. The relation can be mathematically expressed as:

$$\boldsymbol{dS} = \boldsymbol{dS}' \cos\theta = \boldsymbol{dS}' \frac{z_c}{|\boldsymbol{r}-\boldsymbol{r}_c|} \qquad (20)$$

Therefore, the projected light distribution over the detector plane can be expressed as:

$$dJ(\boldsymbol{r},\boldsymbol{r}_c) = \frac{J_c\, z_c - z}{4\pi\, |\boldsymbol{r}-\boldsymbol{r}_c|^3}\, \boldsymbol{dS} \qquad (21)$$

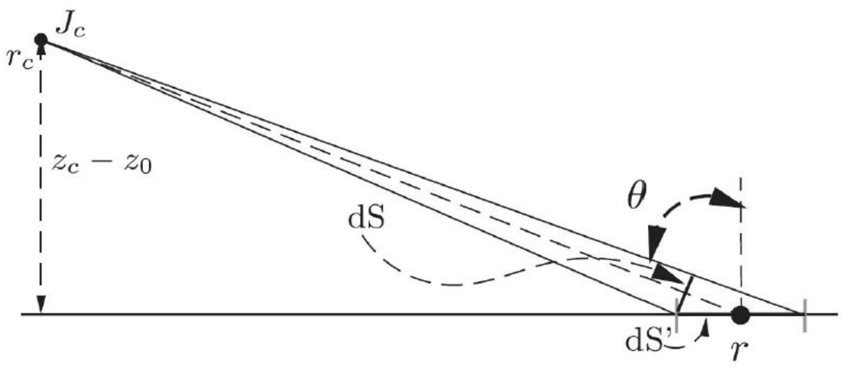

Figure 28. Correction of the inverse square law by the plane geometry of the photodetection area.

Some photon impact positioning algorithms work over one dimension and therefore it is convenient to express equation 21 as a one-dimensional model of the light distribution. Considering the scintillator with a finite dimension, the projection of the light distribution over one axis can be expressed as:

$$J_x = \int_A^B J(\boldsymbol{r},\boldsymbol{r}_c)\, dy = \int_A^B \frac{J_c\,(z_c - z)}{4\pi\, |\boldsymbol{r}-\boldsymbol{r}_c|^3}\, dy \qquad (22)$$

where $|\boldsymbol{r}-\boldsymbol{r}_c| = \sqrt{(x-x_c)^2 + (y-y_c)^2 + (z-z_c)^2}$, $z = 0$ if considering the photosensor plane as the origin of z, and A and B parameters are the photosensor dimensions in the Y axis. Computing the integral, the final expression for the light distribution model is:

$$J_x = \frac{J_c\, z_c}{4\pi\,(z_c^2 + (x-x_c)^2)}\left(-\frac{A}{\alpha_x} + \frac{B}{\beta_x} + y_c\left(\frac{1}{\alpha_x} - \frac{1}{\beta_x}\right)\right) \qquad (23)$$

where

$$\alpha_x(A, x, x_c, y_c, z_{c)} = \sqrt{(A - y_c)^2 + (x - x_c)^2 + z_c^2} \quad (24)$$

$$\beta_x(B, x, x_c, y_c, z_{c)} = \sqrt{(B - y_c)^2 + (x - x_c)^2 + z_c^2} \quad (25)$$

Concerning A and B parameters, it is worth mentioning that they do not have to exactly match with the dimension of the photosensor. This happens because in addition to the finite size of the scintillation crystal and the edge effect, the scintillator photosensor coupling reduces the acceptation angle of the light exiting the crystal. Therefore, the light distribution symmetry is truncated closer to the edge regions producing a compression effect in the obtained flood maps. Positioning algorithms should compensate this compression in order to provide accurate coordinates of the gamma-ray impact position.

Other groups have developed different theoretical models based on other mathematical approaches such as the Scrimger and Baker equation [164]-[166]. It is worth mentioning that equation 23, is not including any reflection on the walls of the scintillator block. For a more accurate description of the light distribution within the crystal such reflections have to be considered. The probability of reflections depends on the crystal roughness (ground, mechanically polished or chemically etched), the coating (Retroreflector layers (RR), Enhanced Specular Reflectors (ESR), Teflon, black paint…) and how the crystal is coupled to the photosensor (optical grease, optical cement, air…). Many codes have been developed to simulate reflections in the scintillation blocks, these codes are based on Lambertian distributions of the reflections [167], or on the crystal surfaces properties [168]. Different crystal surface treatments and coupling methods have been experimentally tested in this thesis in order to evaluate their influence on the accurate determination of the gamma-ray impact position, see Section 3.2.

Depth of interaction coordinate

A mathematical expression for the DOI as a function of z_c can be estimated using equation 23. Considering the origin of coordinates at the center of the detector plane and since the detector surface is symmetric, it can be stated that $B = -A$. For simplicity, in what follows we are going to also consider that the emission point was centered in Y thus, $y_c = 0$.

Along this thesis, an approximation for the DOI determination has been used. In particular, it is estimated using the *E/I* expression which is only valid for one dimensional projections such as the ones provided by our Row and Column readout (see Section 3.1.3.1 below). In the *E/I* expression, *I* represents the maximum value of the scintillation photons distribution and E the energy of the event that can be estimated as:

$$E = \int_{-A}^{A} J_x dx = \frac{J_c}{2\pi}\left[tan^{-1}\left(\frac{A(A+x_c)}{z_c\sqrt{2A^2+2Ax_c+x_c^2+z_c^2}}\right) + tan^{-1}\left(\frac{A(A-x_c)}{z_c\sqrt{2A^2-2Ax_c+x_c^2+z_c^2}}\right)\right] \quad (26)$$

the maximum value of the distribution (I), is obtained for $x - x_c = 0$:

$$I = \left.\frac{dJ_x}{dx}\right|_{max} = \frac{J_c A}{2\pi z_c\sqrt{A^2+z_c^2}} \quad (27)$$

The dependency of the *E/I* estimator with the dimension of the scintillator, versus z_c (for the ideal case in which $x_c = 0$) is depicted in Figure 29. As it can be seen for the ideal case of an infinite detector surface (A→ ∞), the dependency of the *E/I* estimator with z_c is linear.

$$lim_{A\to\infty}\frac{E}{I} = z_c\pi \quad (28)$$

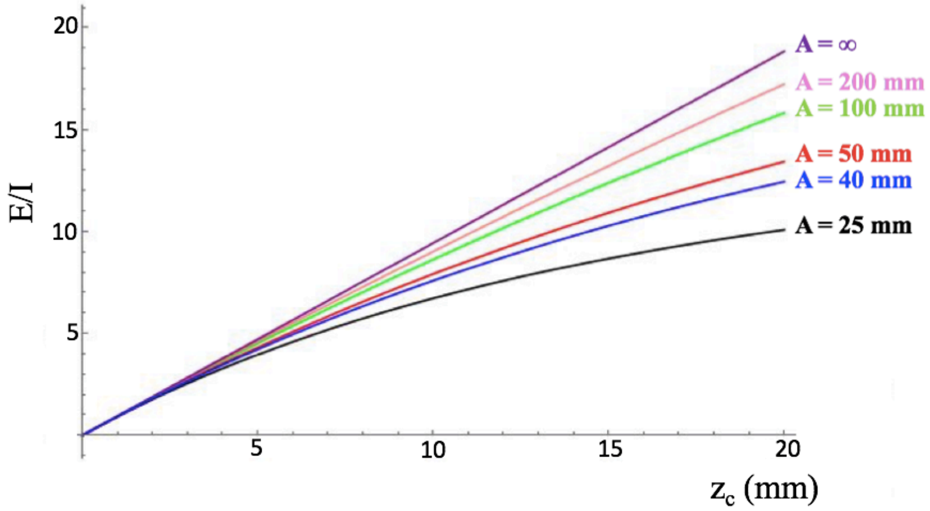

Figure 29. *E/I* estimator versus z_c as a function of the dimension of the scintillator surface. The curves have been plotted for the ideal case in which $x_c = 0$.

TOF in monolithic blocks

The light transport in monolithic scintillators is generally faster and more efficient that in long pixelated based detectors where the photon transport is limited by the large number of reflections the scintillation photons need to undergo before reaching the photosensor. Consequently, monolithic based detectors combined with fast photosensors offer excellent properties for the development of PET detectors with high TOF resolution. Many groups have shown the capabilities of using monolithic blocks for TOF applications. For instance, the group at TU Delft has reported a CRT of 214 ps FWHM using a 32 × 32 × 22 mm^3 LYSO:Ce block coupled to dSiPM [169]. The paper presented in this thesis [6], shows the capabilities to also provide good CRT using analog SiPMs. In a more recent work, we have reported 585 ps FWHM using the TOFPET ASIC II, analog SiPM and a 50 × 50 × 15 mm^3 LYSO [170][171].

The main drawback that monolithic blocks present for their use as a TOF detector is that they require precise calibration procedures. In a photosensor array coupled to a monolithic crystal, several photosensor elements are fired for each gamma ray impinging the block. Thus, walk and skew time corrections are needed to provide an accurate global timestamp [116].

3.1.1.3. Hybrid block

The hybrid blocks idea is to take advantage of both monolithic and pixelated crystals geometries. These designs are related to coupling in one PET detector module the two crystal configurations.

The monolithic block provides higher detection sensitivity, better DOI detection uniformity, continuous positioning (no pixelation artifacts), and lower cost. In contrast to this, the crystal array exhibits a uniform spatial resolution across the detector, defined primarily by the crystal size and better SNR ratio. For an initial solution, one might use the information of the crystal arrays during the reconstruction process to create a high resolution image, maybe high timing performance too. Then, this information could be used in a refined reconstruction as a prior, using the events at the monolithic block to increase the sensitivity and SNR. The article presented in this thesis [5], describes different combinations of monolithic and pixelated crystals, as well as their performance. The configurations showed in this work are specially designed for high performance small aperture PET systems, but applicable to larger PET systems.

Instead of coupling two blocks, another option is partially slotted isolated crystals [172]. In that approach the crystals-pixels are not completely optically isolated and some controlled light sharing across the photodetector plane occurs.

3.1.2. Photodetector

The role of photodetectors in PET is to convert the scintillation photons into detectable electrical signals that are proportional to the number of that incident optical photons. Photodetectors are optically coupled to the scintillator blocks by means of optically clear compounds (grease, silicone, cement). To reduce the electronic noise and therefore, to improve the detection efficiency, photosensors (especially regarding SiPMs) have to optimize the following factors:

i. *Photon Detection Efficiency (PDE).* The photosensor has to efficiently convert the low energy scintillation photons into an electrical signal that is in the emission wavelength of the scintillator. This property is the so-called $PDE(\lambda, V)$ and is defined as the number of photon-discharged microcells in the photosensor divided by the number of incident photons. The Quantum Efficiency ($QE(\lambda)$) strongly depends on the wavelength of the photons and represents the probability that an absorbed photon in the photosensor will produce a signal. Photosensor should present high $PDE(\lambda, V)$ and $QE(\lambda)$.
ii. *Gain.* This is a multiplicative factor related to the ratio of the photodetector current output and the current directly produced by the incident photons. Gain should be high and stable, its fluctuations is given by the Excess Noise Factor (ENF) magnitude.
iii. *Temperature coefficient.* This coefficient is directly affecting the applied overvoltage and also the gain. The gain dependency on the temperature decreases with increasing overvoltage.
iv. *Linearity.* The response of the photodetector should be linear to the incident radiation of a wide energy range.
v. *Time jitter.* This is the elapsed time between the arrival of the scintillation photon and the generation of the output signal. The timing capabilities of the system depends on the time jitter. Low time jitter allows for better time resolutions.
vi. *Compactness.* It is important to use compact photosensors in PET in order to develop compact systems.

In conclusion, a photosensor suitable for PET systems should present high $PDE(\lambda, V)$, high $QE(\lambda)$, high gain with low fluctuations, short response time (time jitter) and should be compact and insensitive to temperature fluctuations. Two main groups of photodetectors can be described: PMTs and SiPMs (including dSiPMs).

3.1.2.1. Photomultiplier tubes

PMTs are in charged of the conversion of the scintillation photons into an electrical signal that is subsequently amplified to useful levels by emission of secondary electrons. The light conversion process in a PMT starts when scintillation photons strike the photocathode, which is at a negative potential around [500-2000] V, as a consequence of photoelectric interactions primary electrons are ejected. These electrons are focused toward the electron multiplier which consists of a chain of several dynodes at an increasing bias (100 to 1000 V). The electrons are accelerated by the electric field and strike the first dynode emitting secondary low energy electrons that are in turn accelerated toward the second dynode, the process continues until reaching the anode which is at ground potential. The geometry of the dynode chain is such that a cascade occurs with an exponential increasing number of electrons being produced at each stage. Figure 30 shows the schematic of the process. All the PMT elements are placed inside a vacuum glass housing [173].

PMTs have high gain, low ENF and are extremely sensitive for light in the ultraviolet, visible, and near-infrared ranges of the electromagnetic spectra. The PMT electron collection efficiency is supposed to be 1 and therefore, $PDE(\lambda, V) \cong QE(\lambda)$. They are affected by magnetic fields, making them almost impossible to be used simultaneously with MRI. All initial designs of PET detector blocks started with PMTs. In order to specially develop detector blocks with magnetic field compatibilities, and other characteristics such as compactness, new designs included Avalanche Photodiodes (APDs) as photosensors, and nowadadys the most common type of photosensor is SiPM [174].

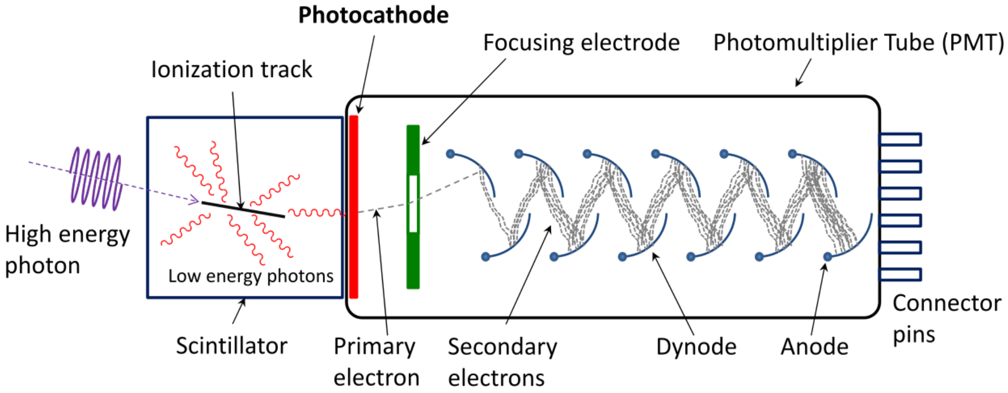

Figure 30. Schematic of a photomultiplier tube coupled to a scintillator for the detection of gamma rays. It can be seen the amplification process in the dynodes.

3.1.2.2. Silicon photodetectors

Silicon photodetectors are semiconductor (solid-state) based detectors. The main advantage of solid-state detectors is their compatibility with magnetic fields, allowing for their simultaneous use with MRI scanners.

The simplest level of silicon detectors is the PN junction, which are boundaries between two types of semiconductor materials (p-type with excess of holes and n-type with excess of electrons) inside a single semiconductor. PN junctions are photodiodes with reversed bias, creating an electric field in the region that keeps the electrons confined in the n-regions and the holes in the p-region. When a photon strikes with enough energy, it is absorbed in the electric field region generating an electron-hole pair. Within the electric field presence, the electron moves towards the n-region and the hole towards the p-region one, generating a flux of electrons and pairs. This process can spontaneously occur at non-zero temperatures generating a false signal called dark counts.

In the presence of higher electric fields, PN junctions are not feasible and APDs are used. Their operation way is similar to the one in PN junctions, the main difference occurs during the acceleration process [175]. Under high electric fields, the electron (or hole) is accelerated acquiring enough energy to strike the crystalline lattice losing part of its energy and generating a new electron-hole pair [176]. The primary electron and the secondary electrons and holes can accelerate again, producing an avalanche of electrons and holes. The holes should be collected before multiplication in order to have a signal proportional to the number of impinging photons. A relevant parameter in APDs is the breakdown voltage, which is the voltage that equals the rate at which new pairs are created with the rate at which they escape from the electric field. When an APD works in the Geiger mode (over the breakdown voltage) is called Single-Photon Avalanche Diode (SPAD) and can trigger a short-duration but relatively large avalanche current. As a drawback, APD and SPAD gains strongly depend on the applied voltage and temperature.

The most complex level of silicon detectors are SiPMs, which are based on the connection in parallel of multiple SPADs. Depending on their output signal can be grouped in analog SiPMs or digital SiPMs (dSiPMs).

Analog SiPMs

The development of SiPMs has been a key contribution to recent improvements in PET. SiPMs are novel solid-state silicon detectors with single photon counting capability. The number of SPADs constituting a SiPM is related to the number of photons that are expected to be measured. The number and configuration of the SPADs is variable depending on the manufacturer and application.

The current output of SiPMs, which is linearly dependent with the number of detected photons, is converted to a voltage pulse by a shunt resistor (R_s), and is amplified using generally a voltage preamplifier.

In SiPMs, the $PDE(\lambda, V)$ is affected by the applied overvoltage, the Geiger efficiency, the Geometrical efficiency and the $QE(\lambda)$. The $QE(\lambda)$ is related to a geometric factor relating the active and dead photodetections areas and also with the probability of an avalanche. These parameters are strongly influenced by the photon wavelength and the temperature. To obtain a high $PDE(\lambda, V)$, these parameters should be optimized and, in most cases, SiPMs have to be cooled down. There are 4 main elements contributing to the SiPM noise, they have to be addressed in order to provide accurate information on the gamma-ray impact position [177]:

i. *Dark Count Rate (DCR).* DCR are avalanches not being produced by incoming photons and depend on the carrier density in silicon, the overvoltage, the photodetection area and exponentially with the temperature. Other causes of DCR are, tunneling between bands, diffusion from neutral regions or release of a trapped electron.
ii. *Optical Crosstalk.* Secondary photons can travel to SPADs closer to the one receiving the primary photon, firing them. Generation of an electron-hole pair close to a neighboring cell can also produce their discharge.
iii. *Afterpulsing.* Due to the existence of impurities and defects in the crystalline lattice of silicon, some charges can be trapped, being released some time later and generating a second avalanche. The time that elapses until the release of these charges depends on the energy band in which they have been trapped. This time is longer for the loads that are between the valence band and the conduction band, and are called deep traps.
iv. *Dead Time.* This is the time elapsed until the SPADs are able to detect new photons after a primary detection. It depends on the active area of the SPADs.

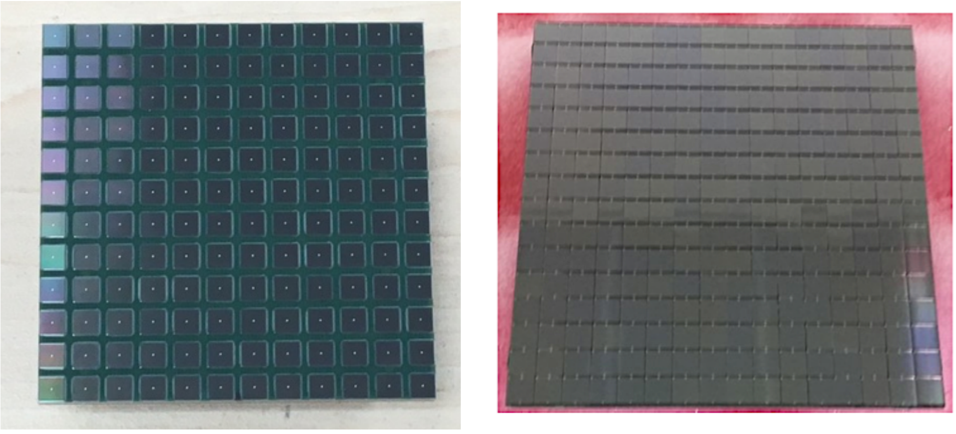

Figure 31. Photograph of two SiPM matrixes. On the left side a 12 × 12 SiPMs arrangement with TSV (Through Silicon Via) technology [178], and on the right one a 16 × 16 SiPMs arrangement also with TSV.

Table IV. Main characteristics of the SiPM array used for the evaluation tests.

	SensL	**KETEK**	**Hamamatsu**
	(35 μm MicroCell)	(25 μm MicroCell)	(50 μm MicroCell)
Breakdown Voltage (V_{BD})	24.2-24.7	25.7	53 ± 5
T. dependency of VBD (mV/°C)	21.5	18.0	54.0
T. dependency of gain (%/°C)	0.8%	0.3% @ 5V_{ov}	2%
Photodetection efficiency % @ 430 mm	31% @ 2.5V_{ov} 41% @ 5V_{ov}	31% @ 2.5V_{ov} 43% @ 5V_{ov}	40% @ 3V_{ov}
DCR KHz/mm^2	100-287 @ 2.5V_{ov}	400 @ 5V_{ov}	500-100 @ 3V_{ov}
Crosstalk probability %	7%	35 %	3%
Gain	3×10^6 @ 2.5V_{ov}	0.9×10^6@ 2.5V_{ov}	1.7×10^6 @ 3V_{ov}

SiPMs present some advantages, such as high gain with very low temperature drift, high granularity, low operating voltage and good timing performance. In addition, they are much more compact allowing for complex and mechanically robust systems reducing dead spaces. Nevertheless, the main feature is their compatibility with magnetic fields allowing to locate photosensors inside magnetic fields. Moreover, there is a larger availability of market suppliers providing larger number of configuration options. As an example, Figure 31 shows two photographs of different configurations of analog SiPM matrixes.

Table V. Spatial, energy and DOI resolution measured for the three 12 × 12 SiPMs photodetectors.

	Spatial Resolution (mm)	**Energy Resolution (%)**	**DOI Resolution (mm)**
SensL	1.6 ± 0.1	11.9 ± 0.4	3.2 ± 0.3
Hamamatsu	1.6 ± 0.1	11.9 ± 0.4	3.2 ± 0.7
KETEK	1.7 ± 0.1	12.0 ± 0.5	3.1 ± 0.6

For the development of the articles included in this thesis, different configurations of SiPMs have been used (always covering an area of roughly 50 × 50 mm^2) and also from different providers. In the course of this thesis, a comparison study using arrays of different providers have been carried out (12 × 12 SiPMs and a pitch of 4.2 mm). For these tests a 50 × 50 × 15 mm^3 monolithic LYSO bock (laterals black painted and entrance face including a retroreflector film) was coupled by means of optical grease to three different SiPM arrays provided by SensL (Cork, Ireland), Hamamatsu Photonics (Hamamatsu, Japan) and KETEK (Munich, Germany). For the characterization of the spatial and energy resolutions, normal incidence experiments using an 11 × 11 ^{22}Na source array attached to the scintillator was used. In order to explore the DOI resolution, side illumination experiments have been performed with a ^{22}Na source, 0.25 mm in diameter. Table IV summarizes the most relevant characteristics of the three SiPM arrays used, and Table V summarize the measured spatial, energy and DOI resolutions, using three different SiPM arrays. On average all three configurations show similar performance.

Digital SiPMs (dSiPMs)

One disadvantage of analog SiPMs lies in the fact that SPADs, are connected in parallel through long interconnections producing electronic noise. The resulting output signal is the sum of the individual currents of all cells and is deteriorated by those mentioned large interconnections as well as by the external load. An alternative to analog SiPMs, is the use of dSiPMs in which the interconnected SPADs are integrated with a CMOS circuit on the same substrate. Hence, the output signal is purely digital [178]. In dSiPMs, each single SPAD has its own readout circuit allowing to deactivate each one individually, and are independently integrated in a CMOS process, produced by an active quenching circuit.

The standard structure of dSiPMs is based in the aggrupation of a high number of SPADs (≈ 800). The SPADs aggrupation is called subpixel, which are in turn arranged in pixels (2 × 2 SPADs matrixes). Furthermore, each pixel is arranged in 2 × 2 matrixes (16 subpixels) completing a die. Pixels of the same die share a time digital converter (TDC), allowing to obtain a timestamp for each detected event. The digital sum of all the output signals provide the number of detected counts and the digitalization of the pulses allows one to minimize the electronic noise of the front-end panel.

Using dSiPMs offer high $PDE(\lambda, V)$, high uniformity, low operation voltage, high stability of operation, low gain drift, magnetic field compatibility and a high degree of scalability [179]. Furthermore, dSIPMs partially preserves the discrete spatio-temporal structure of the photon impact, providing high single photon time resolution and being therefore, good candidates for TOF-PET detectors [180].

3.1.3. Readout, front-end electronics

The last element composing the PET detector block is the readout system, whose role is the processing of the photodetector output signals and their posterior digitation in the data acquisition system. When working with digital photodetectors, front-end electronics are already integrated in the photosensor.

The acquisition should be fast in order to reduce dead times produced by the high amount of data transferred. However, in analog photodetectors, since the information is transferred to a DAQ, it is typically observed the use of reduction readout systems or multiplexing schemes, to diminish the number of signals to be digitized and thus, to reduce the system complexity and its costs.

For the articles presented here [1]-[5], only analog SiPMs have been used. Their electronics can be understood as a two-step process, namely: i) reduction of the number of signals; and ii) signal conditioning for their posterior digitation.

3.1.3.1. Projection readout, Row & Columns

The best approach, in terms of information, is to read-out every single element of the photosensor array, but this implies digitizing a huge number of signals, which is typically challenging. For example, in a PET system based on 48 modules with 12 × 12 SiPMs, such as the stand-alone brain PET system used for the measurements described in [1][3], the total number of signals to be digitized is 6912 (12 × 12 × 48), requiring complex DAQ systems. To diminish the problem, many techniques might be used to reduce the number of signals to be digitized. The so-called Anger logic is an implementation where all photosensor signals are combined using a resistor network and reduced to only 4. An improved approach to the Anger logic, is to use a projection readout that digitizes every row and column of the photosensor matrix. Here, a resistor network connects the photosensors (SiPMs in our case) of a row (or column) [181]. The number of output signals is therefore, the sum of the number of columns and rows. For example, with a projection readout the number of output signals for the case mentioned above is 24 for each detector and therefore, the total number of signals to digitize is reduced from 6912 to 1152.

The projection readout allows one to characterize the light distribution profiles of an event for both the *x*- and *y*-projections, and it has shown good results when working with monolithic blocks, as it will be described below. For these reasons, this readout is the one used in the articles presented in this thesis. Figure 32 left, shows an example of this projection readout scheme.

In a further step, to reduce even more the number of signals without compromising the characterization of the scintillation light, a reduction readout for these SiPM arrays has been implemented. The reduction scheme is based on keeping the 2 lateral row and columns, but merging the central ones from 2 to 1. Figure 32 right, shows an example of the reduction readout scheme. In the previous example, after this additional reduction the number of signals for each module is 16 for the 12 × 12 SiPMs and the total number of output signals for the complete system is 768, which implies a reduction of about 89% (768/6912). An exhaustive characterization of the read-out performance is presented in [3].

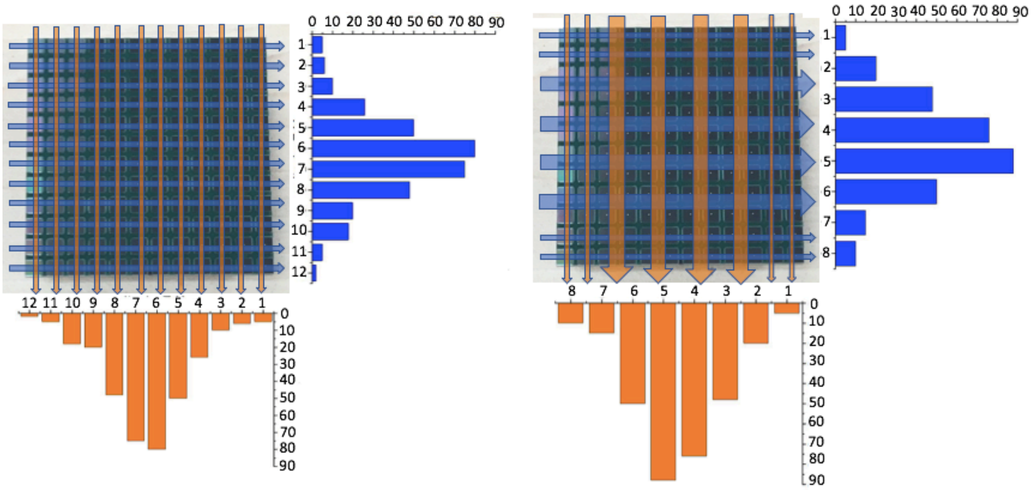

Figure 32. Left, projection readout scheme from 12×12 SiPMs to 12+12 signals. Right, reduction readout scheme from 12×12 SiPMs to 8+8 signals. In blue the resulting projections onto the *Y* axis, and in orange onto the *X* axis.

3.1.3.2. Application Specific Integrated Circuit

An Application Specific Integrated Circuit (ASIC) is an integrated circuit customized for a particular use such as reading out each SiPM for PET applications. The circuit typically incorporates preamplifiers, timing, shaping, and sample-and-hold capabilities. As mentioned, dealing with a huge number of signals is challenging with conventional readout electronics. Moreover, conventional projection readout schemes are not designed to provide precise timing information. In that sense, since ASIC readouts independently read out each SiPM photosensor pixel, allows achieving the best in terms of timing resolution. Recent studies have shown the capabilities of using ASICs for TOF-PET applications, with both pixelated [182] and monolithic blocks [170][171].

3.1.4. Data Acquisition system

The role of the DAQ is to digitize and send to a workstation (PC) the signals coming from the front-end electronics. In this thesis, the main DAQ system used with the projections readout is based on a modular architecture with a clock centralized in one trigger board. The trigger board generates synchronization signals for all the elements and controls the analog to digital conversion process (ADC) of each individual acquisition board connected to the trigger. The ADC sends the data via Ethernet connected to a switch with multiple inputs and one output for the data transmission to the PC. The digital control and processing of the ADC boards are centralized in a Field-programmable gate array (FPGA) that maximizes the performance and speed of the system. The channels at the ADC boards have 12-bit precision. The ADC board sends the information of the analog channels using an UDP data frame.

In the case of dSIPMs, the information provided by the photosensor is already digital. The trigger signal is generated in the pixels when a programmed threshold is reached, and therefore the information is sent directly to the PC.

3.2. Crystal surface treatment

The treatments to the scintillator crystal surfaces have an impact on the light transport within the crystal and on the collected LD profiles. The crystal roughness and the coupling of reflector devices influence the light reflection on the surfaces of the crystal. These treatments have to be optimized and carefully tested to improve the detector block performance. There are many different crystal treatments described in the literature, the most representative ones are listed below.

i. *Absorbent black paint.* This allows one to preserve the LD profiles of the event. Typically, the lateral walls and the entrance face of the crystal are black painted and therefore, all the scintillator photons that are not emitted in the direction to the face in contact with the photosensor are absorbed. The advantage of the treatment is the preservation of the LD. However, a high amount of scintillation photons is not collected negatively impacting the energy and time capabilities. This treatment has been used in data related to a small animal PET [183]. The performance of the spatial resolution is typically very good given the small crystal thickness (10 mm).
ii. *Teflon or white paint.* The laterals and entrance face of the scintillator are coated with Teflon or white paint. In this case, all the scintillation photons that are emitted to the walls are arbitrary reflected until reaching the photosensor. The amount of collected light is higher than in the previous case improving therefore, energetic and timing resolutions. However, the LD is not preserved and the spatial resolution is worsened when using analytic methods for the gamma-ray impact coordinates estimation (*E/I* estimator cannot be applied).
iii. *Enhanced Specular Reflectors (ESR).* This case is similar to the previous one, the faces are coated with specular reflective layers that increases the light collection.
iv. *Retroreflector layers.* When using retroreflector (RR) layers, it has been concluded that the best approach is to keep the lateral walls of the crystal black painted. The RR film is composed by several corner-cubes structures that are made of three-sided prisms (mutually perpendicular) reflecting light back directly towards the source, but displaced a little distance (0.1 mm - 6 mm). The incoming ray is reflected three times, once by each surface, which results in a reversal of the ray direction. Most of these structures are aluminized in order to achieve specular reflection. Following this principle, since the distribution of light is produced isotropically, adding an RR layer at the entrance detector face increases the scintillation light transferred to the photosensor, with respect to using a black absorbent. The main advantage of RR layers is that preserves the LD profiles (*E/I* estimator can be used). It has been proved that the spatial and energy resolution improve when including the RR layer [1].

To illustrate the main differences between each treatment surface, normal incidence measurements have been performed using an 11 ×11 ^{22}Na source array. For these tests a 50 × 50 × 15 mm^3 monolithic LYSO block coupled to a 12 × 12 SiPMs array (SensL, C-Series) by means of optical grease, and the projection readout system, have been used. Figure 33 shows on the top panels the flood maps obtained for each of the treatment cases described above. It can be appreciated how the compression of the sources at the edges toward the image center increases with the number of reflections of the scintillation light (black paint no reflections, white Teflon diffuse reflections). The lower panels show the *E/I* histograms for three different regions of interest (ROI) around central, lateral and corner sources. As depicted in Figure 33, the ESR and Teflon treatments break the expected LD profiles and therefore, the *E/I* estimator is not linear with *z*. The spatial and energy resolutions were characterized for one row of sources, Table VI shows the mean values.

Regarding the coupling between the scintillator block and the photodetector, silicone or optical grease are most commonly used. It is better to use coupling media with refractive indexes in between the index of the photosensor and the scintillator block, in order to reduce light transmission losses. The collection of scintillation light is crucial in order to provide accurate positioning. During this thesis additional tests using BGO monolithic blocks have been carried out. A variety of crystal treatments that made it possible to extract as more light as possible have been applied to those BGO blocks.

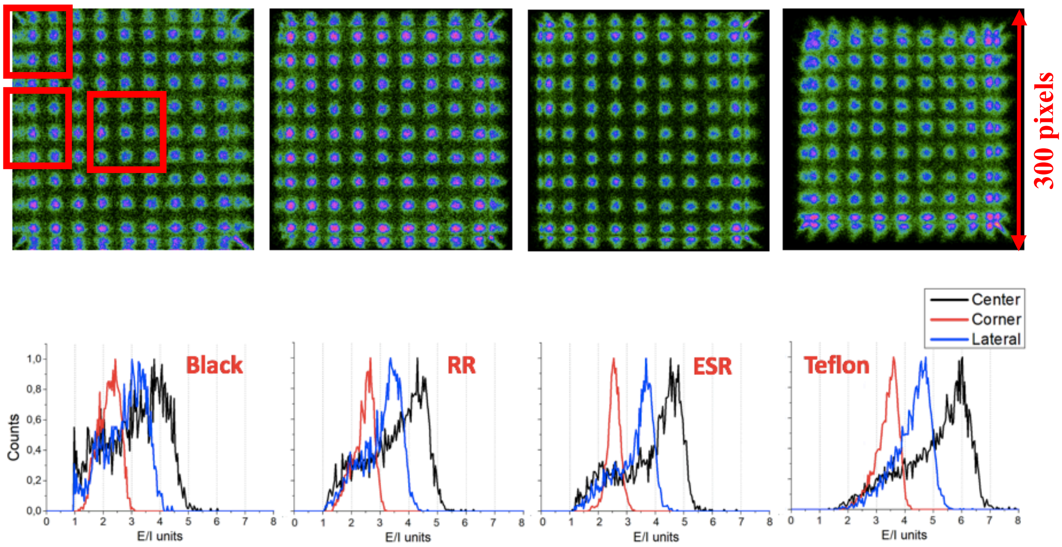

Figure 33. Top. Flood maps measured using a 11 × 11 ^{22}Na source array. From left to right: black, RR, ESR and Teflon treatments applied. Bottom, DOI histograms for ROIs at the central, lateral and corner sources for each case (the left flood map shows the selected regions in red).

Table VI. Mean spatial and energy resolution values obtained for each described crystal surface treatment.

Treatment	Spatial Resolution (mm)	Energy Resolution (%)
Black Paint	1.8 ± 0.4	19.5 ± 4.0
Retroreflector	1.6 ± 0.3	12.7 ± 1.8
ESR	1.7 ± 0.4	12.9 ± 1.3
Teflon	2.2 ± 0.7	10.2 ± 1.4

BGO based studies

BGO blocks offer high sensitivity and their cost is reduced (compared with LYSO blocks or other fast scintillator blocks). They present several drawbacks, given their slow decay time and relatively low light yield. However, their high stopping power for 511 keV energy photons [184], together with their reduced cost, make BGO blocks especially suitable for low-dose large-size PET scanners.

In this thesis it has been studied the possibility of re-introducing BGO blocks in PET developments. First tests were carried out using pixelated BGO blocks. Two different approaches were tested namely, i) an array of 10 × 10 elements with 2.5 mm pitch and 10 mm thickness; and ii) an array of 30 × 30 elements with 1.67 mm pitch and 3 mm thickness. A staggered DOI configuration was studied using two layers of 2.5 mm pitch BGO pixels, with 10 × 10 (top) and 11 × 11 (bottom) elements with a total thickness of 20 mm. Moreover, it is worth highlighting that an energy resolution as good as 12% FWHM was obtained. The results pointed out that both crystal configurations could be well suited for PET applications [184].

In a second set of measurements BGO monolithic blocks have been used as described in [4]. The blocks have dimensions of 50 × 50 × 15 mm^3, with black painted laterals and again the RR layer coupled to the entrance face of the crystal. To improve the light output, a special treatment to the scintillator exit face was also studied, the so-called nanopattern which is a thin layer of a specific high refractive index material shaped with a periodic structure allowing to increase the scintillation light output of the crystal. Figure 34 shows a sketch of the detector block configuration. The block was coupled to both 12 × 12 and 16 × 16 SiPMs photosensor arrays, to also study the impact of different photosensor active area coverage. Better overall performance of the detector block was achieved when using 16 × 16 SiPMs photosensor arrays. Despite the fact that the nanopattern structure improves the energy resolution, it also worsens the spatial and DOI resolutions and therefore, since the best detector performance is achieved as a compromise between all the relevant parameters in the detector, using only a RR layer coupled to the entrance face of the scintillator block is the preferred choice.

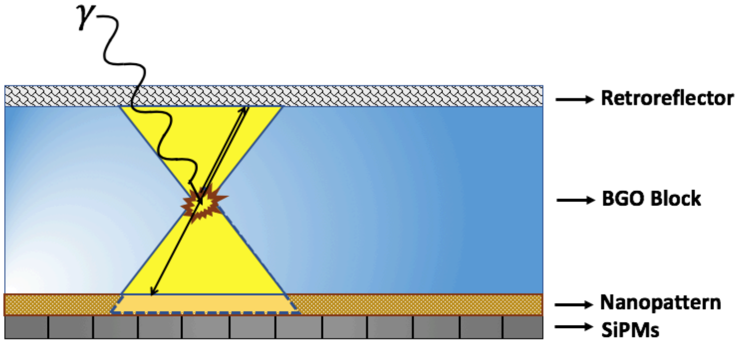

Figure 34. Schematic of the detector block configuration for the BGO studies. It can be distinguished the 120 μm RR layer, the 0.6 μm nanopattern and the 15 mm thick BGO monolithic used. Notice that the elements in the sketch are not scaled to the real dimensions.

3.3. Positioning algorithms in monolithic crystals

Once the data is acquired and digitized, the next step in PET acquisitions is providing accurate information on the 3D photon impact coordinates *x, y* and *z* (DOI). In Section 3.1.1.2 it has been described a theoretical model for the light distribution in monolithic blocks and in 3.1.3.1 the type of readout used in the current thesis, providing the light distribution projections through the SiPM row and columns. This is the information to be digitized and sent to the PC, where many algorithms can be used to provide the impact coordinates. There are several positioning algorithms such as the simplest ones based on studying the LD symmetries (Center of Gravity…) or more complex statistical methods that require, in monolithic blocks, previous calibration or input data (least squares, neuronal networks…).

The complexity of positioning algorithms in continuous crystals lies in the accurate location of the impact position coordinates when the interaction takes place close to the crystal edges. To improve the estimation of the coordinates, as previously described in 3.2, different crystal surface treatments might be applied. However, if energy or timing capabilities have to be improved reflective materials are used. Figure 35, shows a diagram with the most representative positioning algorithms for monolithic blocks, filled boxes represent the algorithms used in the present collection of articles.

Algorithms based on studying the LD symmetries are the ones selected for the data analysis of the experiments carried out within the thesis studies because they are easier to be implemented and are the ones providing the best performance when using the projection read-out system described in 3.1.3.1. In the following a brief description of the most relevant analytic and statistical methods is performed.

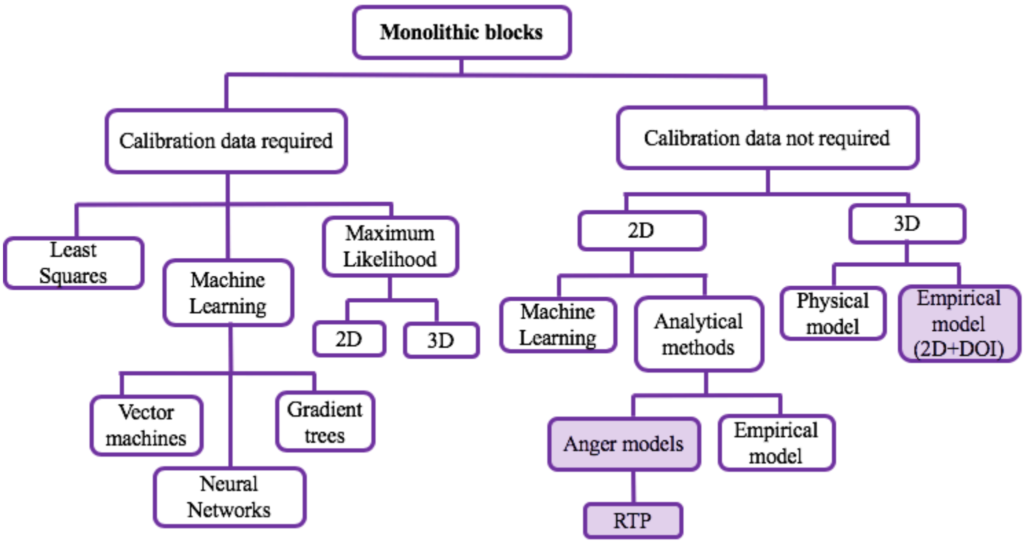

Figure 35. Blocks diagram summarizing the most representative positioning algorithm employed for monolithic blocks. Filled boxes show the algorithms used in the presented articles.

3.3.1. Center of gravity

The mean value of LD profiles provides good information on the geometrical centroid of the distribution, i.e., on the 2D photon impact coordinates (*x, y*) within the scintillator. The simplest method for the position determination of an event is its Center of Gravity (CoG), in which the coordinates are estimated as the weighted sum of the positions of the photodetector pixels. The weights correspond to the measured signal on each pixel [185]. The CoG algorithm works well when the LD profile is fully measured, as it happens for events interacting in the central area of the scintillator. However, close to the edges the estimation of the centroid position is affected by the truncation of the LD profile, and the estimation of the impact coordinates are less accurate. As a result, compression effects are observed in the flood maps, see Figure 33. These effects are also dependent with the crystal treatment as already described in 3.2, and photosensor geometry. The left panel of Figure 36 shows a flood map for an acquisition performed using the 11 × 11 ^{22}Na source array impinging normally to a 50 × 50 × 15 mm^3 monolithic LYSO block (the laterals were black painted and a RR layer was coupled to the entrance face by means of optical grease) coupled to a 12 × 12 SiPMs (SensL, C-Series). As it can be appreciated the two lines of sources closer to the edge are compressed.

Since this is the positioning method used in the included articles [1]-[5], this section includes a description of the *E/I* estimator used with the experimental data and the software collimation technique applied to improve the measured spatial resolution.

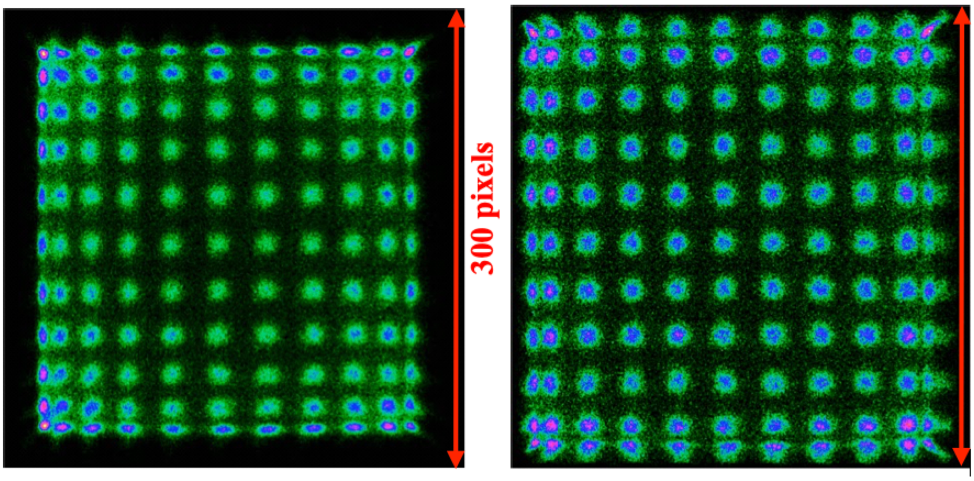

Figure 36. Acquisition performed using the 11 × 11 ^{22}Na source array impinging normally to a 50 × 50 × 15 mm^3 monolithic LYSO block coupled to a 12 × 12 SiPMs. Left, acquisition flood map processed using CoG. Right, Flood map of the same acquisition but processed using RTP = 2.

3.3.1.1. Raise to a power method

To improve positioning of the impact coordinates at the edges, a modified version of the CoG algorithm can be applied, the so-called RTP method (Raising to a Power) [186][187]. This method consists on rising to a power the digitized values, and it is mathematically expressed as:

$$X_c = \frac{\sum_i^n r_i^p x_i}{\sum_i^n r_i^p}, \qquad Y_c = \frac{\sum_i^n c_i^p y_i}{\sum_i^n c_i^p} \qquad (30)$$

where x_i and y_i are the SiPM physical positions on the detection surface, n is the number of elements in the row and column, and r_i and c_i are the digitized signals projected on x and y directions, respectively. The selection of the power (p) should be a compromise between the position dependence linearity and attraction effect to the center. The right panel in Figure 36, shows the flood map obtained for the same acquisition on the left panel but applying a power of 2 (*p=2, RTP2*). It can be appreciated how the events at the edges are better distinguished than in the CoG case. The left panel of Figure 37 shows a plot of the mechanical source position versus the measured position in the image, it can be seen how in the RTP2 case the relationship is more lineal for events near the edges. The dashed line represents the ideal case without edge effects.

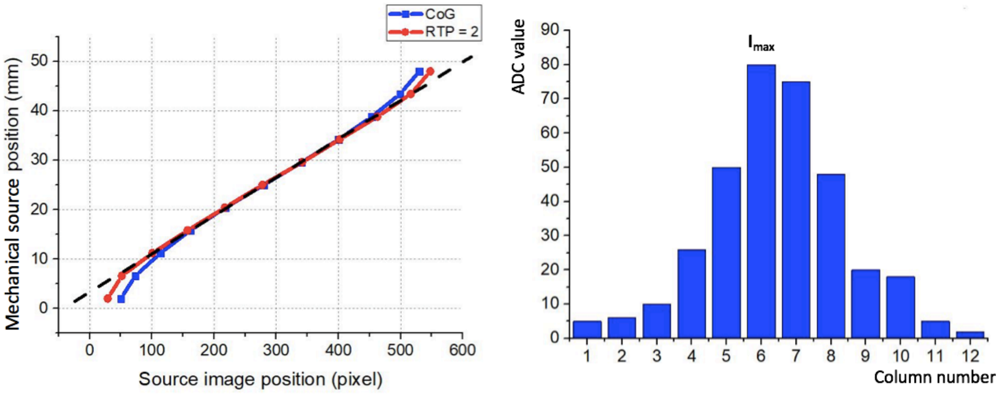

Figure 37. Left, mechanical source position as a function of the measured position in the detector image. The dashed line represents the ideal case without compression. As can be appreciated, the RTP2 case shows better linearity. Right, LD projection onto the Y axis showing the column numbers and the I_{max} value of the distribution.

3.3.1.2. *E/I* method

To measure the depth of interaction coordinate using the LD profiles the *E/I* estimator has been applied in this thesis, which is a relationship through the ratio of the energy (sum of rows or columns) and the maximum value (of the row or column respectively) of the distribution as it can be seen in the right panel of Figure 37. Experimentally, the measured DOIs histogram for a gamma source impinging perpendicular to the detector can be approximated as the convolution of Gaussian distributions and the exponential decay of the gamma-rays attenuation. Assuming that the intrinsic DOI resolution is constant along the crystal thickness, we can define an analytical expression for the DOI distribution [188]:

$$DOI(z) = A \cdot e^{-\mu z}\left[erf\left(\frac{b-z}{\sqrt{2}\sigma_{int}}\right) - erf\left(\frac{a-z}{\sqrt{2}\sigma_{int}}\right)\right] \quad (31)$$

where μ is the attenuation coefficient of the material, A is the amplitude, σ_{int} is related to the FWHM of the distribution as $2.35 \cdot \sigma_{int}$, *erf* is the Gaussian error function, and a and b are the lower and upper limits of the distribution. These two last parameters are used to calibrate the measured E/I_{max}.

To show the accuracy of the *E/I* estimator and its linear dependency with z, several lateral side experiments have been performed across the course of this thesis. A ^{22}Na source impinging laterally to the crystal at different depths was used. The top and bottom-left panels of Figure 38 depict the measured value for *E/I* as a function of known mechanical position. It can be observed a good linearity of such an estimator for the depth of interaction determination, when using a variety of different crystal thicknesses (10, 15 and 20 mm blocks) and surface treatments (black painted and black + RR), but also scintillation materials (LYSO and BGO), and two SiPMs photosensor arrangements (12 ×12 and 16 × 16). The bottom-right panel shows the DOI histograms obtained at each different depth in the case of an LYSO block with 15 mm thickness, the shadow pink histogram is the DOI histogram measured through normal incidence that overlaps with the lateral ones.

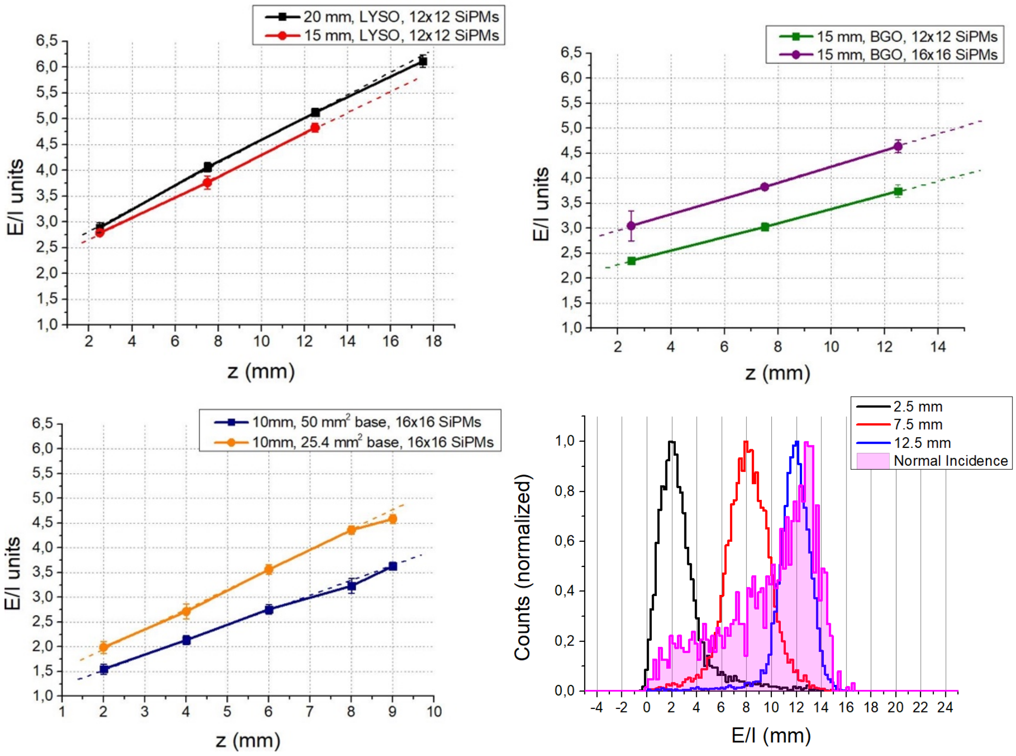

Figure 38. Top-left shows the linear dependency of the *E/I* estimator with *z* for 20 and15 mm thick LYSO blocks. Top-right shows the results when using BGO crystals and two photosensor types namely 12 ×12 and 16 × 16 SiPMs. It is observed how *E/I* values are higher for the 16 × 16 case, since the scintillation light collection increases (higher energy). The bottom-left panel shows the result for different aspect-ratio LYSO blocks. Bottom-right panel shows the DOI histograms measured at three different depths in the case of the LYSO 15 mm thick block.

3.3.1.3. Software collimation

As already described in 2.4.2, the detected events are not always due to true coincidence events. To reduce the number of false coincidences, such as random events during calibration procedures, tungsten or lead collimators are typically used. Moreover, this approach ensures that the detected pairs enter perpendicular to the crystal surface. However, using large collimators is not always possible when a PET scanner is already assembled, and moreover, its manipulation is not easy. For these reasons, instead of using mechanical collimators, it is possible to apply software collimation to the data allowing us to artificially collimate the beam without the need of physical collimation elements. In this thesis, it is refered to software collimation when a post-processing is carried out as a function of the LOR angle, and consists on allowing only events whose LOR has a slope smaller than a predefined one. For each coincidence the angle between its LOR and the normal ($\theta_{software}$) is calculated. If $\theta_{software}$ is smaller than the selected collimation angle, the event is accepted. The system accepts events from squared regions under this angular restriction. The selection of $\theta_{software}$ is a compromise between the acquired statistics and the spatial resolution. This collimation procedure has been applied to most of the data sets shown in the collection of articles.

Figure 39 shows the flood maps of an acquisition performed using an uncollimated ^{22}Na source (0.25 mm in diameter) attached to the front surface of one monolithic block. The left panel shows data obtained without any software collimation filtering, whereas on the central flood map a software collimation of 2.1° (from the normal) has been applied. The plot on the right-hand side depicts the measured spatial resolution (FWHM) values for different positions across the crystal surface and for different collimation angles. The spatial resolution improves when reducing the collimation angle.

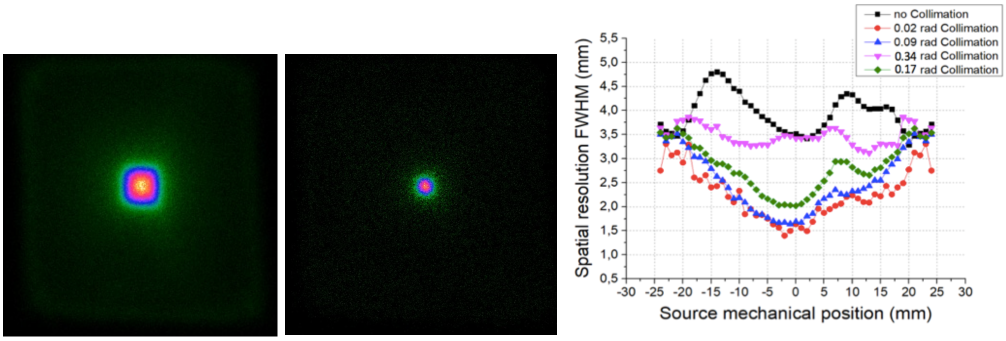

Figure 39. Left. Flood map obtained without any software collimation filtering. Center. Flood map after applying a software collimation of 2.1° (from the normal). Right. Measured spatial resolution (FWHM) values for different positions across the crystal surface and different collimation angles.

3.3.1.4. Voronoi diagrams

We are currently implementing a method that allows one to calibrate the energy and the photon impact coordinates, including the DOI, in monolithic based detectors using arrays of radioactive sources and Voronoi diagrams. The main feature of this method is that, in contrast to other methods, allows to calibrate the whole volume of the monolithic crystal.

The Voronoi diagram, or Dirichlet tessellation, is defined as the partitioning of the plane with *n* points into various convex polygons (Voronoi cells) as depicted in the central panel of Figure 40. Each polygon corresponds to each coordinate of the calibration set, with the property that an arbitrary point lies within a specified polygon, if and only if, the distance from this point to the belonging sample of associated polygon is closer than all other distances between this point and the remaining points [189]. The Voronoi diagrams have been used on the energy calibration of PET systems based on pixelated detectors, and other purposes, such as crystal elements identification in the detectors [190][191].

In the present method, we acquire flood maps of well known positioned sources, providing impact position and energy information, and later make use of Voronoi diagrams to retrieve a calibrated impact *XY*, DOI and energy. The new acquired data can be calibrated by interpolation. The interpolation is done using the square inverse interpolation (of the calibration factors) to the distance between the original data and its 3 closest Voronoi cells. Figure 40 shows, from left to right, the flood map of an acquired 11 × 11 ^{22}Na source array impinging normally to a 50 × 50 × 15 mm^3 monolithic LYSO block coupled to a 12 × 12 SiPMs, the Voronoi diagrams of the calibration measurements, and the flood map after the calibration in metric units, respectively.

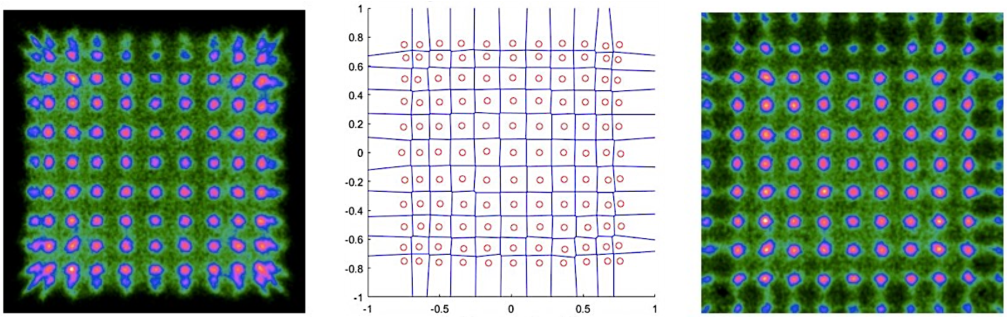

Figure 40. From left to right, calibration data set, Voronoi diagram showing the 121 cells, and calibrated flood map.

3.3.2. Statistical methods

Statistical methods are based on comparisons of the measured LD profiles with a pre-calibration data set, that can be both measured or theoretically estimated, in which the interaction positions are already known. The main drawback of this method is the need of a pre-calibration data set. To obtain calibration sets, the LDs are measured at many positions as possible with a beam impinging normally to the surface of the monolithic detector. The main drawbacks are the long time needed to obtain an accurate calibration set.

Moreover, scanning the detector when is already assembled in a PET scanner is impracticable thus, re-calibrations require of alternative approaches.

To avoid the acquisition of calibration data sets, methods based on simulations [192], and theoretical models [193][194] for the LD pattern over the crystal, have also been developed. In the following, some of the existing statistical methods are being described.

3.3.2.1. Least square

Least squares (LS) algorithms focus on finding a solution to the parameters needed for the fitting, event by event, to theoretical light distribution profiles, in such a way that the sum of the squares of the residual values is minimal [195][196].

In a first step an average reference data set is obtained for a reference number of positions of the calibration beam, for each unknown event. The calibration beam is typically generated using a collimated point source impinging perpendicularly to the detector under calibration. Distance values are computed for each event with respect to reference positions. The best estimate for the impact coordinate is taken as the reference measured position of the calibration beam associated with the smallest computed distance.

3.3.2.2. Chi square (χ^2)

In the χ^2algorithm, the root mean square fluctuations on the response of each single element are considered for each position of the reference data set. The main objective of the algorithm is to estimate the coordinates of the incident gamma-ray by minimizing the function distance of the row/column amplitude and the average value, over all the data set, of the same row/columns at the reference position. An improvement of this algorithm is the so-called Generalized Chi-Square (Gen χ^2) method, in which the root mean square vector of fluctuations is replaced by a matrix, that includes the correlations between row and columns pairs [195].

3.3.2.3. Nearest Neighbors

Nearest Neighbors algorithms calculate a complete set of events for each calibration beam position [197], on the contrary to the LS algorithm where only the average reference is computed. In the case of first Nearest Neighbor algorithm, the impinging beam position is estimated by considering the beam positions with the smallest LS value of all the calculated distances.

Variations of the method have been studied to improve the coordinate estimation, such as the 5 Nearest Neighbor algorithm in which the position is estimated with the mean of the 5 smallest LS lengths.

3.3.2.4. Maximum Likelihood

Maximum Likelihood (ML) methods estimate the parameters of a statistical model, given the calibration data set. It attempts to find the parameter values that maximize the likelihood function, given the observations. Positioning methods based on ML allow to include prior information achieving high spatial resolution [198]. However, the main drawback is that requires complex computing calculations preventing their use for real time events acquisitions and processing.

3.3.3. Neural Networks

Neural Networks (NN) are computational architectures based on the biological neural networks that constitute animal brains [199]. The goal of NN algorithms is to fit a function that, given as input the photodetector pixel response to an event, provides as output the sought after estimated positions. Knowledge is implicitly represented in the patterns of interactions between network components. The NN is trained making use of error minimization algorithms using reference data sets. The training process has to be significative (enough data has to be used to obtain accurate weights for the nodes) and representative (the training data has to cover all possible variables). Once the algorithm is trained it provides a straightforward position estimation without the need of comparisons with all the reference measurements.

NN are not limited to the selected positions for the reference data, providing continuous positions over the whole crystal. Moreover, it has been proved to provide a high spatial resolution with the data acquired using PET detectors based on monolithic blocks [200].

3.4. Contribution to PET systems

Molecular imaging studies involve systemic injection of radiotracers into the patient, the issue of radiation exposure became recently one of the critical aspects associated to nuclear medicine. In order to reduce the dose to the patient and the clinical personnel, efforts have been undertaken in order to increase the scanners sensitivity as much as possible. One option to achieve this goal are dedicated specific systems with an optimized geometry attaining the highest possible angular coverage of the dedicated organ.

Table VII. Main characteristics of some of the current commercial whole body PET systems.

System	Material (mm^3)	Operation	Detector	TOF	DOI	SR (mm)
Siemens Biograph mMR	10,383,360	Simultaneous	LSO APDs	No	No	4.6
Philips Ingenuity TF	9,974,272	Sequential	LYSO PMTs	Yes	No	4.9-5.5
GE Signa PET/MR	10,684,800	Simultaneous	LYSO SiPMS	Yes	No	4.1-5.3

Organ-dedicated molecular imaging systems present some advantages and disadvantages when compared to large size whole body PET scanners. Table VII summarizes the characteristics of some commercially available whole body PET/MR systems.

Organ-dedicated systems present as an advantage their improved performance when compared to standard whole body systems. This performance improvement is observed in the image quality and in both the clinical and physical sensitivity. Moreover, their manufacturing cost is reduced, allow for higher patient throughput and require from small footprint. However, these systems are mainly focusing on the examination of typically a single organ reducing their usage by different areas. Table VIII summarizes the main characteristics of some brain-dedicated PET scanners. As it can be appreciated the volume of required material is smaller than in whole body scanners. Other organ-dedicated systems focus on the study of the breast, the prostate or the heart. For further information and details see for instance [62] and references therein.

The advantages present in those organ-dedicated PET systems have encouraged our investigations. The motivation for the studies presented in the articles of the current work, is the performance improvements of PET detectors based on monolithic blocks and their system implementation. Three main systems, two of brain-dedicated scanners and a small animal preclinical scanner, have marked the time-line of these studies, namely: *i)* the MINDView human brain PET insert [2][201]; *ii)* the stand-alone CareMiBrain PET scanner [3]; and *iii)* the Albira small animal PET scanner [183].

The contribution to these systems including the challenges presented during their development and their main characteristics are briefly described in the following.

Table VIII. Main characteristics of some of the current brain-dedicated PET systems.

System	Material (mm^3)	Operation	Detector	TOF	DOI	SR (mm)
HRRT	884,740	Stand-alone	LSO PMTs	No	Yes	2.3-3.4
PET-Hat	610,579	Stand-alone	GSO PMTs	No	Yes	3.5-4.0
AMPET	3,564,000	Stand-alone	LSO SiPM	Yes	Yes	2.7
jPET-D4 PET	7,750,656	Stand-alone	GSO PMT	No	Yes	2.0-3.0
CareMiBrain	1,200,000	Stand-alone	LYSO SiPM	No	Yes	1.8-3.0
Brain PET Jülich	3,456,000	MRI	LSO APDs	No	No	2.5-5.0
TRIMAGE	1,951,418	MRI/EEG	LYSO SiPM	No	Yes	2.3-3.7
MINDView	3,000,000	MRI	LYSO SiPM	No	Yes	1.6-4

3.4.1. MINDView

MINDView (Multimodal Imaging of Neurological Disorders) is a European Union (EU) project leaded by i3M and founded through the FP7 program with the aim of developing effective imaging tools for diagnosis, monitoring and study mental disorders. One of the main technical objectives within the project is the development of a human brain PET insert compatible with MRI and therefore, allowing for simultaneous PET and MRI imaging modalities. The system is focus on the diagnosis and monitoring of schizophrenia. Another technical objective of the project is the study of new radiopharmaceuticals for specific imaging of neurotransmitters pathways relevant for schizophrenia and depression disorders [2][201]. Figure 41 left shows the PET insert (black ring) and RF-coil (white inner ring) inside the Siemens mMR system (a simultaneous whole body PET/MRI).

The MINDView PET insert is based on 3 rings with 20 detector modules each. It has a geometrical aperture of approximately 33 cm in diameter. Figure 41 right, shows a more detailed photograph of the scanner. The system covers an axial FOV of 154 mm, coincidence gamma-rays are allowed between one module and any of the 9 opposite modules (of all rings) producing a transaxial FOV of about 240 mm. Each detector module is based on a monolithic LYSO crystal with dimensions of 50 × 50 × 20 mm^3, coupled to a custom 12 ×12 SiPMs photosensor array from SensL (MINDView-Series type, similar to the J-series technology), and the related front-end electronics. See Table VIII for more details. A head dedicated transmitter/receiver (TR) RF coil system has been developed [2] by Noras, a partner in the consortium. In order to minimize distortions in the MRI performance, the distance between the PET shielding and the RF rungs conductor is about 3 cm. Carbon fiber composites have been chosen as main RF screens and different single pulses sequences were successfully carried out. The field map sequences showed no change in the B_0 field. Moreover, no effect on the PET reconstructed image resolution was observed independently of all tested MRI sequences including EPI, UTE, MPrage, T2-flair or ASL.

Different crystal surface treatments were proposed to optimize the detector block performance. The final block treatment design uses black painted lateral surfaces combined with a retroreflector layer [1] attached to the 50 × 50 mm^2 entrance surface. The article [1] of this thesis shows a detailed description of the experimental studies carried out with this crystal dimensions and photosensor array. Different RR layers were tested. Overall an improvement of the detector block performance of 25% was observed for the energy and measured spatial resolution, when compared to the case of all surfaces black painted. Best performance was found when using small pitch of the corner-cube structures in the RR films. The MINDView prototype is installed at the Klinikum Recht der Isaar in Munich, since early 2018. Performance studies inside the 3T Siemens mMR have been successfully carried out. Further details can be found in references [1][2] and [201].

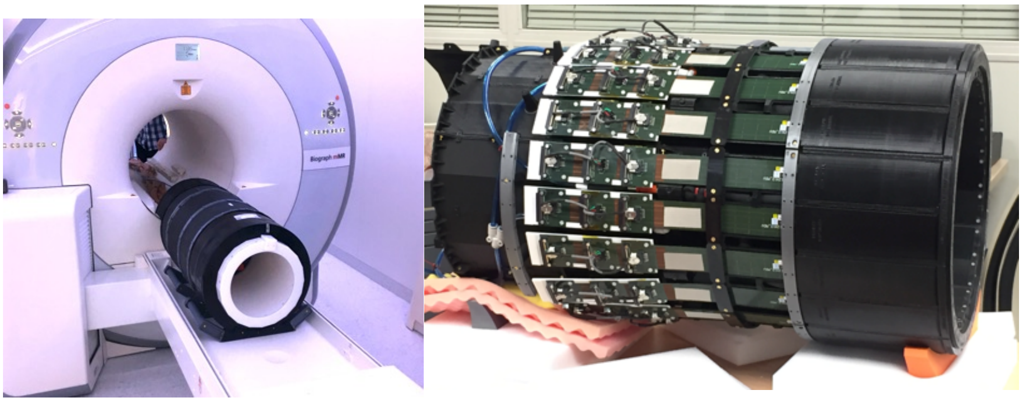

Figure 41. Left, photograph of the PET insert (black ring) and RF-coil (white ring) inside the 3T Siemens MRI scanner. Right, photograph of the PET insert electronics without the RF shielding.

3.4.2. CareMiBrain

The CareMiBrain is a EU project in which the i3M has actively participated under the Horizon 2020 research and innovation programme. Its technical objective is the development of a stand-alone brain-dedicated PET system, targeted to mental disorders and nuclear medicine units of hospitals. The system will be dedicated to the early detection of Alzheimer’s disease and other causes of cognitive decline. In the system the patient is in upright position (see Figure 42) to improve the diagnose quality. As mentioned in the introduction of this section, dedicated systems offer several advantages compared to whole-body PET systems in brain imaging such as an improve performance, smaller footprints in hospital facilities and lower radiotracer dose to the patient that leads to a lesser cost to the healthcare system.

The CareMiBrain system is composed by 48 LYSO monolithic detector blocks of 50 × 50 × 15 mm^3 dimensions coupled to arrays of 12 × 12 SiPMs. The blocks are arranged in 3 rings. The scintillators also have the lateral black paint and a RR layer coupled to the entrance face (same type as in the MINDView detectors). The system defines an axial and transaxial FOV of roughly 150 mm and 240 mm, respectively. See Table VIII for more details. The front-end electronics of the detector block includes a reduction readout system that instead of providing all row and columns of the SiPM array (24 output signals), it only provides 16 as described in Section 3.1.3.1. This number of signals is enough to provide accurate 3D photon impact positions, and allows one to resolve events as close as 0.25 mm to the crystal edges. The article [3] provides detailed information on the reduction readout [202] system performance and the validation of the detector block.

Figure 42. 3D rendering of the CareMiBrain system and photograph of the real system showing the patient in upright position.

3.4.3. Albira pre-clinical system

The Albira is a PET system for small animals composed by 24 detector blocks (50 mm size) arranged in 3 rings, with an axial and transaxial FOV of 148 mm and 80 mm, respectively. To reduce the gap between adjacent detectors, which is only 0.5 mm, monolithic LYSO blocks with trapezoidal geometry are used. The dimensions of the blocks are roughly 48 × 48 mm^2 entrance, 50 × 50 mm^2 bottom and 10 mm thick with the laterals and entrance faces black painted [183]. The system accurately determines the three spatial coordinates of the gamma impacts within the detector crystal, achieving an average homogeneous spatial image resolution below 1 mm, across the entire FOV when including the DOI information. Reference [183] shows a result example obtained with the first prototype built using this technology. The scintillator blocks are coupled to 12 × 12 SiPMs photodetector arrays and a read-out providing row and columns projections.

4. Scientific research

This chapter includes the most relevant scientific contributions, published in peer-reviewed journals, that have been considered for the collection of articles composing this thesis. They include most of the results achieved during the development of the PhD work.

The main objectives of the thesis have been studying and improving the use of large volume monolithic scintillators in PET detectors. It has been also aimed to build the detectors compatible with MRI systems. For these reason different SiPM providers and configurations have been studied. To accurately determine the 3D photon impact coordinates within the crystal, the SiPM matrixes were connected to a readout electronics system providing information of the projected *X* and *Y* profiles of the scintillation light distribution. In order to provide information on the photon time arrival, an ASIC circuit has also been tested.

In the collection of articles, an extensive study of the light distribution in monolithic blocks is performed, including a theoretical model and an experimental validation of the photon DOI determination within the scintillator. Many crystal types and geometries have been tested, in particular, the studies have focused on LYSO but also some on BGO blocks. Moreover, to improve the detector performance, different crystal treatments have been explored, including the use of retroreflector layers or nanopattern structures. Spatial and DOI resolution values (FWHM) below 2 mm and 5 mm have been achieved, respectively. The implemented detector blocks allowed to determine gamma-ray impacts as close as 0.25 mm to the crystal edges with a reduced number of signals.

As a consequence of those studies, two different detector blocks have been designed and are included in two brain dedicated PET systems. One design is implemented in the MINDView PET insert prototype and the second one is used in the stand-alone CareMiBrain PET system.

In the following an authorized copy of the research papers as published in the different journals, together with a summary and contextualization of each one is presented. As it was aforementioned in the preface, they represent the most important peer-reviewed papers published as first and second-author, during the course of this thesis. For those that I am the second author, I have equally contributed as the first author.

4.1. Performance Study of a Large Monolithic LYSO PET Detector With Accurate Photon DOI Using Retroreflector Layers

Authors: Andrea González-Montoro, Albert Aguilar, Gabriel Cañizares, Pablo Conde, Liczandro Hernández, Luis F. Vidal, Matteo Galasso, Andrea Fabbri, Filomeno Sánchez, José M. Benlloch, and Antonio J. González.

Published: IEEE Transactions on Radiation Plasma Medical Sciences, Vol. 1, No. 3, p. 229-237 (2017). https://doi.org/10.1109/TRPMS.2017.2692819

Impact Factor: 1.44 (estimated)

Summary:

The main objective of this work was to build and test a PET detector block based on large and thick monolithic crystals providing high sensitivity, accurate impact position including DOI-encoding and compatibility with MRI fields. The proposed detector block is based on a 50 × 50 × 20 mm^3 monolithic LYSO block coupled to a 12 × 12 SiPMs array by means of optical grease. The centroids of the light distribution projections are calculated through the modified version of the center of gravity method, the so-called RTP algorithm, and the photon impact DOI is calculated as the ratio of the sum of all 12 signals (photon energy, E) to the maximum signal value $(E/I_{max})_{r,c}$ for rows and columns (r, c).

To improve the detector performance all crystal faces are polished and the lateral walls of the scintillator were black painted. An RR structure composed by corner-cubes has been added to the crystal entrance surface reflecting light back directly towards the source. The original shape of the scintillation light distribution is preserved allowing for DOI-encoding. Four RR layers with different corner-cube structures were tested.

Best results are obtained when using optical grease as coupling between the crystal and the RR (in contrast to air-coupling), while keeping a good DOI linearity with an average DOI resolution of 4 mm. Approaches using RR layers return constant and good energy resolutions nearing 12%, compared to a range of 15% – 16% in the case of totally black painted blocks. Regarding the spatial resolution, about a 25% of improvement, in comparison with the black case, was observed when one of the smallest RR structures was used (120 μm corner cube size), being 1.7 mm at the entrance crystal layer and 0.7 mm in the layer closest to the photosensor.

Overall, the detector performance based on a 20 mm thick LYSO crystal coupled to an RR layer at the entrance surface shows a high performance at almost any position within the crystal volume. Due to such an excellent performance of this detector block, the design was included in the modules composing the MINDView brain PET insert, which is a European Union (EU) project leaded by i3M and founded through the FP7 program.

Performance Study of a Large Monolithic LYSO PET Detector With Accurate Photon DOI Using Retroreflector Layers

Andrea González-Montoro, Albert Aguilar, Gabriel Cañizares, Pablo Conde, Liczandro Hernández, Luis F. Vidal, Matteo Galasso, Andrea Fabbri, Filomeno Sánchez, José M. Benlloch, and Antonio J. González

***Abstract*—Clinical and organ-dedicated PET systems typically require a high efficiency imposing the use of thick scintillators, normally through crystal arrays. To provide depth of interaction (DOI) information, two or more layers are sometimes mounted in the staggered or phoswich approach. In this paper, we are proposing an alternative using thick and large monolithic crystals. We have tested two surface treatments for a 50 mm × 50 mm × 20 mm LYSO block. We provide data in this paper as close as 5 mm to the lateral walls. We left those walls black painted and the exit face coupled to the photosensor (12 × 12 SiPM array) polished. The entrance face was: 1) black painted or 2) coupled to a retroreflector (RR) layer. These configurations keep a good DOI linearity and, on average, reached 4 mm DOI resolution, measured as the full width at half of the maximum. Approaches using RR layers return constant and good energy resolutions nearing 12%, compared to a range of 15%–16% in the case of totally black painted blocks. The best result concerning the detector spatial resolution was obtained when one of the smallest RR was used (120 um corner cube size), being 1.7 mm at the entrance crystal layer and 0.7 mm in the layer closest to the photosensor. These values worsen at least 30% for the black treatment case.**

***Index Terms*—Monolithic scintillators, photodetector technology, photon depth of interaction (DOI), positron emission tomography, scintillators.**

I. INTRODUCTION

WHOLE body PET scanners typically result in a PET image resolution in the 4–5 mm full width at half of the maximum (FWHM) range [1], [2]. Scanners based on new technology have shown the possibility to improve the spatial resolution to 2–3 mm FWHM using iterative algorithms [3], as well as to increase the effective sensitivity when the photons time of flight information is used [4]. However, an improved spatial resolution nearing 1–2 mm is required to answer specific questions related to brain functions in small regions. This level of accuracy could be reached using detector blocks based on scintillation crystal arrays. An alternative to this type of crystal selection is the one based on monolithic scintillators. There are advantages and disadvantages to both types of crystal designs that have been described in [5]. Accurate depth of interaction (DOI) information is used to properly calculate the true line of response, correcting for the parallax error. DOI capability is of primary interest to achieve high spatial image resolution, especially toward the borders of the scanner field of view. For monolithic crystal designs, several DOI schemes have been proposed based on the correlation between the DOI and the measured light distribution (LD) [6]–[9]. An alternative approach, based on the linearly interpolated measured

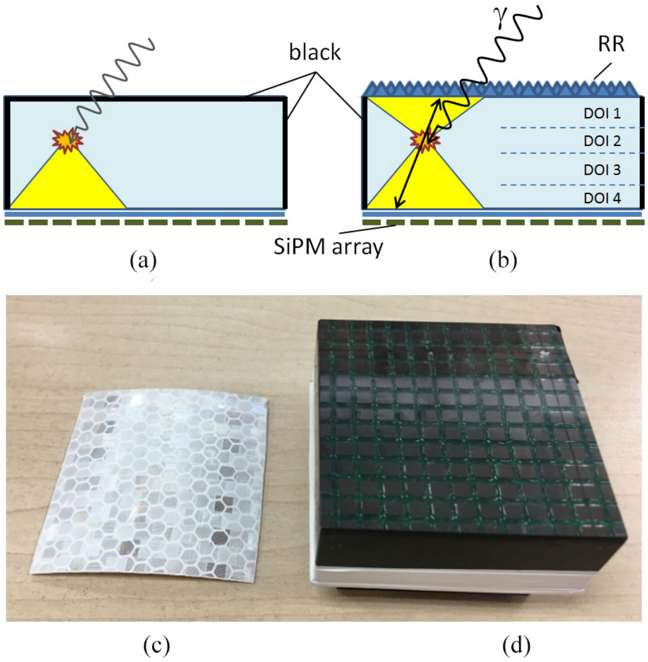

Fig. 1. (a) and (b) Sketch of the black painted crystal and the one with the entrance layer coupled to the RR. The yellow cones represent the scintillation LDs. DOI1–DOI4 represent the DOI regions of interest within the scintillation volume. (c) Photograph of the SiPM array through the 20 mm thick LYSO crystal. (d) Photograph of the 20 mm thick LYSO block with an RR layer at the entrance surface.

Manuscript received December 23, 2016; revised March 3, 2017; accepted April 5, 2017. Date of publication April 12, 2017; date of current version May 12, 2017. This work was supported in part by the EU FP7 program under Grant 603002, in part by the Spanish Plan Nacional de Investigación Científica, Desarrollo e Innovación Tecnológica under Grant TEC 2013-48036-C3-1-R, and in part by the Valencian Local Government under Grant PROMETEOII/2013/010 and Grant ISIC 2011/013. The work of A. J. González was supported by the CSIC through the Ramon y Cajal modality. *(Corresponding author: Andrea González-Montoro.)*

A. González-Montoro, A. Aguilar, G. Cañizares, P. Conde, L. Hernández, L. F. Vidal, F. Sánchez, J. M. Benlloch, and A. J. González are with the Institute for Instrumentation in Molecular Imaging, 46022 Valencia, Spain (e-mail: agonzalez@i3m.upv.es).

M. Galasso and A. Fabbri are with INFN Sezione Roma III, 00146 Rome, Italy.

Color versions of one or more of the figures in this paper are available online at http://ieeexplore.ieee.org.

Digital Object Identifier 10.1109/TRPMS.2017.2692819

intensities on the photosensor pixels surrounding the estimated impact coordinates, has shown to provide an average DOI resolution of 3.4 mm for 12 mm thickness scintillators [10]. Moreover, there have been works toward improving the performance of detectors based on these thick monolithic blocks by using different treatments to their walls, namely specular reflectors, black absorbent paint or white Teflon, among others [11].

In this paper, two treatments have been tested for the lateral and entrance walls of the scintillation block, namely absorbent black paint for all surfaces preserving the scintillation LD, see Fig. 1(a), and black painted lateral walls combined with a retroreflector (RR) layer on the 50 mm × 50 mm entrance surface, see Fig. 1(b)–(d). RR surfaces are optical devices that return visible light in the same direction as it enters into the device, but displaced by a small distance that depends on its microstructure, see Fig. 1(b). Previous works have already been done to improve the detector performance in monolithic crystals using RR structures, such as in the determination of the photon impact coordinates. Some works confirmed through both simulation and experimental results such an improvement on the spatial and energy resolutions [12]–[14]. They were limited to their current photosensor and readout technologies [12]. In another work [15] with small crystal sizes of roughly 6 mm × 6 mm and heights ranging from 5 to 20 mm, it was also shown an energy resolution improvement of about 28%. However, a worst spatial resolution was found using the RR with the thickest crystals. Other crystal treatments, such as white Teflon wrapping or specular enhanced reflectors are not considered in this paper. These optical elements hardly preserve the scintillation LD, which is currently a requirement for the methodology applied here, as it will be described below. In this paper, we are able to quantitatively show the improved detector performance when using the RR layers, especially on the photon DOI performance, using large and thick crystals combined with high granularity photosensors.

Our research focus is on the development of thick and large continuous detectors for PET imagers, with MR compatible components, as for brain imaging [16], [17]. This paper shows the studies carried out with a monolithic LYSO block (50 mm × 50 mm × 20 mm) combined with an RR optical device increasing the scintillation light transferred to the photosensor and, therefore, the detector block performance. We have focused on returning high spatial and energy resolutions, homogeneous across the whole crystal volume, but also accurate DOI. We are not aiming in this paper to provide detector timing capabilities.

II. MATERIALS

A. Crystal and Optical Elements

The current study uses LYSO scintillation blocks from Proteus (OH, USA) with dimensions of 50 mm × 50 mm × 20 mm. All crystal faces are polished and one of the large 50 mm × 50 mm faces coupled to the photosensor using optical grease (BC630, Saint Gobain, refractive index of 1.47).

TABLE I
CHARACTERISTICS OF USED RRs

Provider	Label	Corner cube size (µm)
3M	3M15	150
IMOS	IM6	6000
IMOS	IM1	1000
IMOS	IM12	120

Characteristics of the four different RR layers under study.

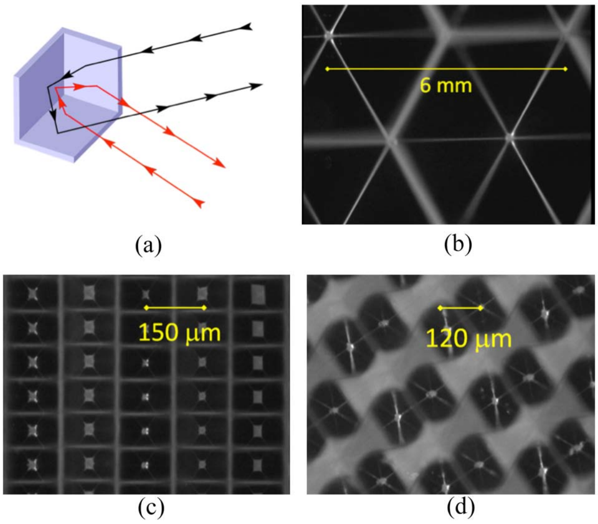

Fig. 2. (a) Sketch of the light paths in the RR corner cube. (b)–(d) Photographs of some of the tested RR layers using a microscope and ten augments (model 6121, Cambridge, U.K.) corresponding to IM6, 3M15, and IM12, respectively.

In the crystal configuration including the RR, one can almost preserve the original shape of the scintillation LD. RR are similar to that seen in bicycle reflectors and traffic signs. The RR structure is composed by several corner-cubes, these corner-cubes are made of three-sided prisms (mutually perpendicular) and reflects waves back directly toward the source, but displaced a little distance. The incoming ray is reflected three times, once by each surface, which results in a reversal of ray direction, see Fig. 2(a). Most of these structures are aluminized in order to achieve specular reflection.

We have tested four RR surfaces with different corner-cube structures, one manufactured by 3M (MN, USA) [18] and three provided by IMOS Gubela GmbH (Renchen, Germany) [19], see Table I. We have tested two different ways for coupling the RR to the entrance face, using optical grease or mechanical coupling through air. Fig. 2 shows the photographs through an optical microscope of some of the RR devices used in this paper. The pictures show the so-called corner cube structures in RR.

B. Photosensor

Two detector blocks have been used in this paper, one only as reference. To provide projections of the scintillation LD and, thus, 3-D photon impact information, each detector block is based on high-density custom designed arrays of SiPMs from SensL (MindView-Series type, similar to J-series) [20]. The photosensor matrix is composed of 144 SiPMs (35 um cell size), arranged in 12 by 12 columns and rows, covering an active area of approximately 51 mm × 51 mm, see Fig. 1. The SiPM package is through silicon vias and was already

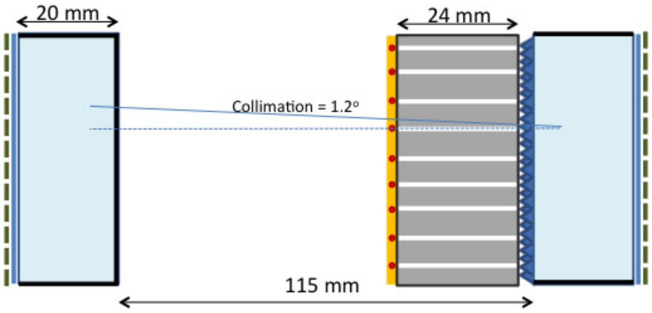

Fig. 3. Sketch of the experimental setup showing the array of ^{22}Na sources in front of the collimator (thickness of 24 mm and 1.2 mm drilled holes. Both detectors included a 20 mm thick LYSO crystal with black painted lateral walls and were read out using an array of 12 × 12 SiPMs. The detector under investigation includes an RR at the entrance face, whereas the reference one keeps here the black painted.

successfully tested in magnetic field environments [21]. Their individual active area is 3 mm × 3 mm and the pitch is 4.36 mm. Each array is typically operated at a bias voltage of about 31 V, 6.5 V over breakdown voltage [22]. Since SiPM photosensors are sensitive to temperature variations, the detectors are air cooled and kept at stable temperatures of approximately 15 °C–18°C, reducing the dark noise contribution and gain drifts.

C. Readout

Each SiPM array has been directly connected to a readout circuit that provides outputs for each row and column of the photosensor array [23]. This readout allows one to characterize the scintillation LD produced when a gamma photon interacts in the monolithic crystal. These 24 signals, in addition to the summed trigger signal and the temperature sensor information, are transferred to the data acquisition system by means of coaxial cables. The 24 row and column signals are digitized with custom ADC boards (12-bit precision). Such photosensor granularity allows one for the accurate sampling of the LD and, thus, better characterizing the effect produced by the truncation of the scintillation light at the crystal edges.

III. METHODS

In order to evaluate the spatial, energy and DOI resolutions we performed measurements in coincidence mode. The reference detector was placed at a distance of 11.5 cm using an LYSO crystal of also 50 mm × 50 mm × 20 mm dimensions and totally black painted, see sketch in Fig. 3. We have irradiated the crystal block under study with an array of 9 × 9 Tungsten collimated (24 mm thick, 1.2 mm holes) ^{22}Na sources (total activity about 1.8 μCi), 1 mm × 1 mm × 1 mm each (5 mm pitch).

Each detector module provides information for both X and Y projections of the scintillation LD. The centroids of these distributions are calculated through a modified version of the center of gravity method, consisting on raising the 12 digitized signals for each projection to a given power. The following equations describe the process [24]:

$$X_C = \frac{\sum_i^{12} r_i^p x_i}{\sum_i^{12} r_i^p}, \quad Y_C = \frac{\sum_i^{12} c_i^p y_i}{\sum_i^{12} c_i^p}. \tag{1}$$

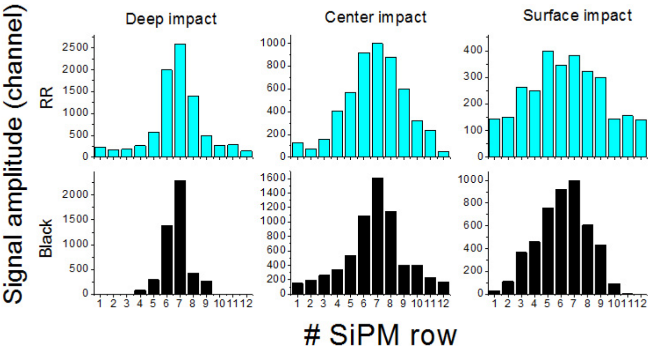

Fig. 4. Profiles of measured LD for a 511 keV photon impact at the crystal center (reducing light truncation at its edges), as a function of the deepness and crystal treatment. These distributions are given as the measured signal height amplitude in ADC channels for each of the 12 rows characterizing the LD in one axis direction.

In (1), x_i and y_i are the SiPM positions on the detection surface, while r_i and c_i are the digitized signals projected on x and y directions, respectively. In these studies, we have applied a second power ($p = 2$). The photon impact DOI is estimated by the ratio of the sum of all 12 signals (photon energy, E) to the maximum signal value $(E/I_{\max})_{r,c}$ for rows and columns (r, c) [25].

During the data processing, each detector area is subdivided in 600 × 600 pixels, and an electronic collimation of about 1.2° from the normal was applied to both detectors. In the current setup, this means to allow coincidence of the smallest "virtual" pixel unit (0.08 mm quadrant side length) with 60 pixels (*ca.* 5 mm) in the reference detector. An energy window of 15% at the 511 keV peak (434–588 keV) was also applied to the acquired data.

The shape and width of the measured LDs slightly vary depending on the crystal treatment. Fig. 4 shows the LD profiles, for the case of having RR or black paint at the entrance, for impacts at different depths of interaction. The bar plot shows the digitized values of the 12 rows of SiPMs for the different cases

A. Detector Spatial and Energy Resolutions

We have explored the measured detector spatial resolution by using the 9 × 9 ^{22}Na sources array. The spatial resolution was measured as the FWHM through multi-Gaussian fits of the sources point spread function, that is, FWHM of the estimated coordinate histogram for each source of the array. For every row of measured sources, we have first calculated the centroid of each source in channels. By plotting the real position versus the measured values, we can determine the degree of compression as well as to calibrate the axis in millimeters. Thus, after calibration, it is possible to obtain the detector spatial resolution (FWHM), as described above, but as a function of the DOI layer. The described procedure was applied for both black and RR crystal treatments.

The energy resolution is calculated as $\Delta E(\text{FWHM})/E_{\text{centroid}}$ and it was not corrected for possible SiPM nonlinear responses, but we can state that the ratio of the 1274/511 keV peaks observed with the ^{22}Na source showed a measured average constant ratio of 2.51 ± 0.3 (standard deviation) for all

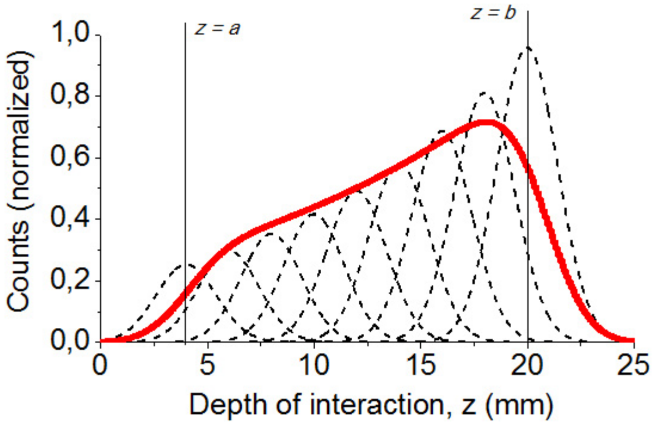

Fig. 5. Example of a theoretical distribution of DOIs for a gamma-ray beam impinging perpendicular to the photodetector array. Parameters a and b represent the crystal limits. The dashed lines are the theoretical DOI distributions at different depths and the solid red line represents the analytical DOI distribution.

studied cases. The energy resolutions for the black and RR treatment cases were evaluated for each selected DOI range.

B. DOI Resolution

For each detected photon impact, a single $E/I_{\max}$ value is obtained as the average of $E/I_{\max}$ obtained for X and Y LD profiles. The histogram of DOIs for a collimated gamma ray beam impinging normal to the detector can be understood as a profile distribution that appears as the convolution of Gaussian distributions and the exponential decay of the photon attenuation, see Fig. 5. Assuming that the intrinsic DOI resolution is constant along the crystal depth, we can define an analytical expression for the DOI distributions [26]

$$\mathrm{DOI}(z) = A \cdot e^{-\alpha z}\left[\operatorname{erf}\left(\frac{b-z}{\sqrt{2}\sigma_{\text{int}}}\right) - \operatorname{erf}\left(\frac{a-z}{\sqrt{2}\sigma_{\text{int}}}\right)\right] \qquad (2)$$

where α is the attenuation coefficient of the material, A is the amplitude, σ_{int} is the sigma of the distribution related to the FWHM as $2.35 \times \sigma_{\text{int}}$, erf is the Gaussian error function, and a and b are the lower and upper limits of the distribution. These two last parameters are used to calibrate the measured $E/I_{\max}$ values into millimeters for all crystal treatments in this paper. It is possible to deduce this equation assuming that z is linearly dependent on σ. The lower limit of the observed $E/I_{\max}$ histograms typically remains constant, independent of the impact position, but the upper limit of the distribution has a position dependence due to the truncation of the LD. In the case of black treatment, the DOI resolution (FWHM) can be obtained through the free parameter (σ_{int}) as

$$\mathrm{FWHM}_{\mathrm{DOI}} = 2.35 \times \frac{\text{crystal thickness}}{|b-a|} \times \sigma_{\text{int}}. \qquad (3)$$

We have done this only for the black crystal treatment for which (3) better suits. Although the RR treatment should also preserve the scintillation distribution, there might be slight changes that could lead to a misinterpretation of the $\mathrm{FWHM}_{\mathrm{DOI}}$ results and, therefore, (3) has been only used for the DOI layer calibration.

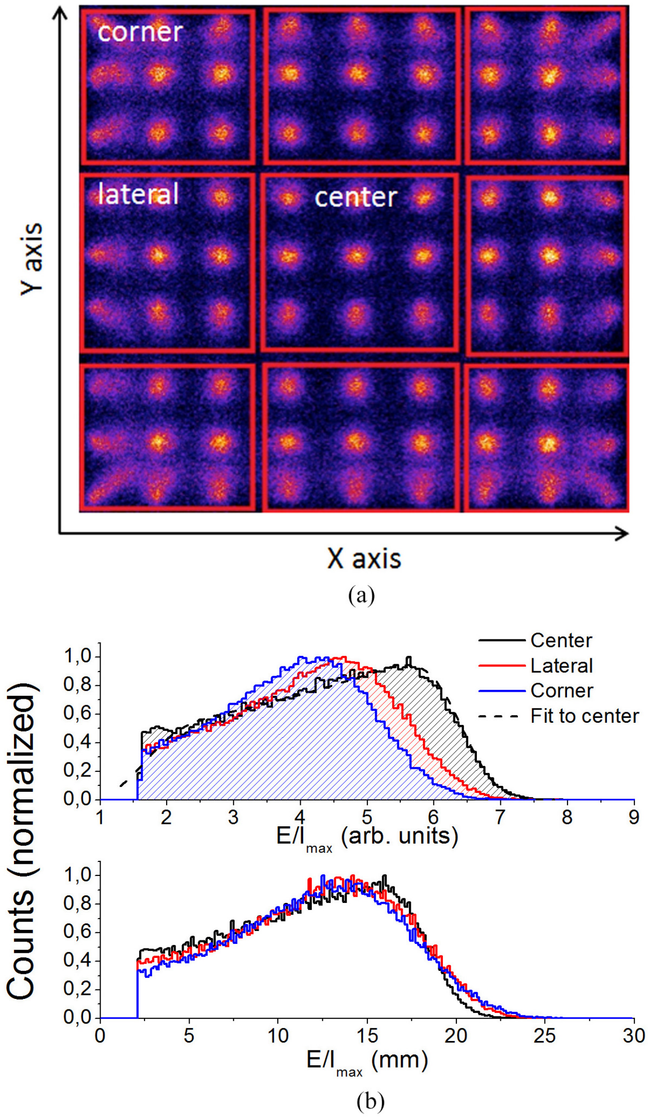

(a)

(b)

Fig. 6. (a) Flood map of the ^{22}Na source array with all data, but applying an energy filter (15% at 511 keV). (b) $E/I_{\max}$ distributions for three regions as marked in (a). Top panel in arbitrary units and bottom panel after fitting to the distribution the function shown in (2) in millimeters. As an example, the dashed black line is the fitted curve for the distribution in the center region.

In addition to provide DOI resolution results through the characterization of the $E/I_{\max}$ profiles, measurements with lateral incidence to the crystal were also carried out in steps of 5 mm, also using a Tungsten collimator, but with 30 mm thickness and with a drilled hole of 1.2 mm diameter. ROI of 4 mm × 4 mm were considered at each of those steps and for distances also in 5 mm steps from the crystal edge, reaching the crystal center. These tests were done for the black crystal treatment and for one of the RR cases.

IV. RESULTS

A. Detector Spatial Resolution

All the acquired data for ^{22}Na source array experiments in normal incidence resulted in flood maps as the one shown in Fig. 6(a), corresponding to the black paint treatment case. The analysis of the DOI distributions ($E/I_{\max}$) showed different

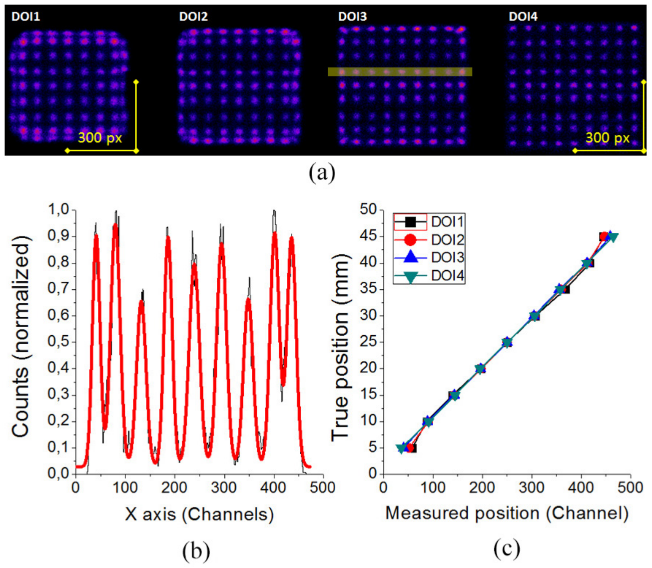

Fig. 7. (a) Flood maps using the 20 mm thick black crystal for four different DOI regions, see labeled regions in Fig. 1. (b) Profile for one row of sources (black rear curve) and a multi-Gaussian fit (red curve), corresponding to DOI3, see yellow shadow in panel (a). (c) True positions versus measured coordinates, showing the compression curves at the crystal edges.

profiles depending on the detector block area. Fig. 6(b) shows the $E/I_{\max}$ profiles for three detector regions, namely center, lateral, and corner. These changes in the shape of the profiles are produced because of different LD truncations. Fig. 6(b) (bottom panel) shows the calibrated DOI profiles. See as an example the fitted line (black dashed line), overlapping with the data corresponding to the center crystal region. The fit returns a and b as defined in (2). The cut-off in these plots at 2.1 mm is used to avoid impacts whose light is typically only detected by one SiPM. This value corresponds to half the SiPM pitch for a light scintillation profile characterized in 1-D by the truncated Cauchy distribution [27].

The detector resolution has been studied as a function of the photon DOI across the crystal. Therefore, we calibrated all nine detector regions to the proper DOI in metric units. We fitted each DOI distribution using (3). We split the data in four DOI regions, namely DOI1 (entrance), DOI2, DOI3, and DOI4. They correspond to crystal depths of 20–15.6 mm, 15.5–11.1 mm, 11–6.6 mm, and 6.5–2.1 mm, respectively, see Fig. 1(b). Applying this method to the data, we obtain four different flood maps for each treatment case. Fig. 7(a) shows those for the whole black-painted case. We can observe the compression effect affecting more the upper layers, where there is a stronger LD truncation. Fig. 7(b) shows a profile for one row of sources, corresponding to the DOI3 layer. On the right side in panel (c), we show the compression curves for this row of sources for the four DOI layers. Here, we observe a good linearity for the 30 mm central region, ranging from 10 mm to 40 mm, but the upper layers (DOI1 and DOI2) show a certain compression for data at 5 mm photon impact from the crystal border (position 5 and 45 mm).

Four types of RR layers are shown in this paper, as well as two types of coupling methods for those RR layers to the scintillator, namely using optical grease or direct mechanical contact (air). In Fig. 8, we can see the average detector spatial resolution for each DOI layer. In general, the detector FWHM spatial resolution improves with the photon DOI, obtaining better results closer to the photosensor. When the crystal is black painted, we obtained FWHM values of 2.6, 2.4, 2.0, and 1.8 mm for DOI1, DOI2, DOI3, and DOI4, respectively. An average error bar of about 0.2 mm was found (standard deviation). When the RR films are coupled to the crystal, there is always an improvement of the determined FWHM. In general, better results are obtained, when these layers are coupled to the scintillator using optical grease, as shown in Fig. 8(b). The worst RR performance is observed for the one with largest corner cubes sizes of 6 mm (IM6). When optical grease is used, smaller differences are observed for all RR films, except the aforementioned IM6. The values for the IM12og experiments show the best FWHM results of 2.1, 1.9, 1.7, and 1.4 mm (*ca.* 0.2 standard deviation) for DOI1, DOI2, DOI3, and DOI4, respectively.

To estimate the intrinsic detector spatial resolution, the contributions of the collimator and the finite source size have

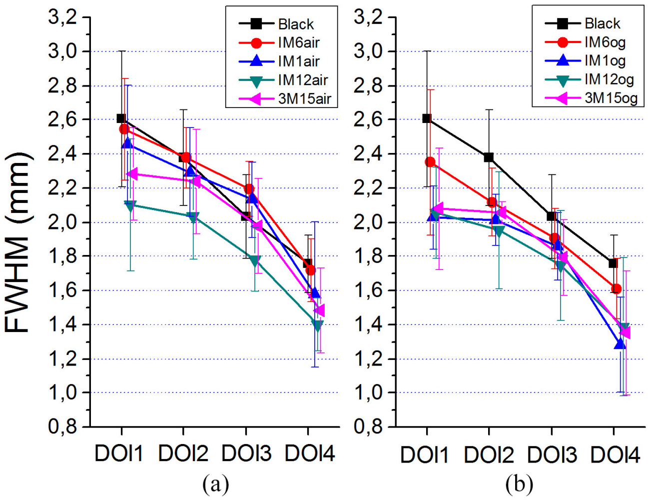

Fig. 8. Experimental spatial resolution results (without deconvolution). (a) We can see a plot of the detector spatial resolution as a function of the chosen DOI range, when using air coupling between the RR and the photosensor. (b) When using optical grease coupling.

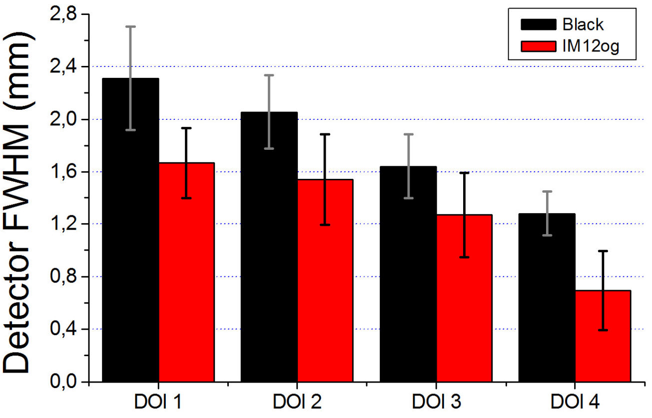

Fig. 9. Average detector intrinsic spatial resolution for each DOI layer for the black and IM12og cases.

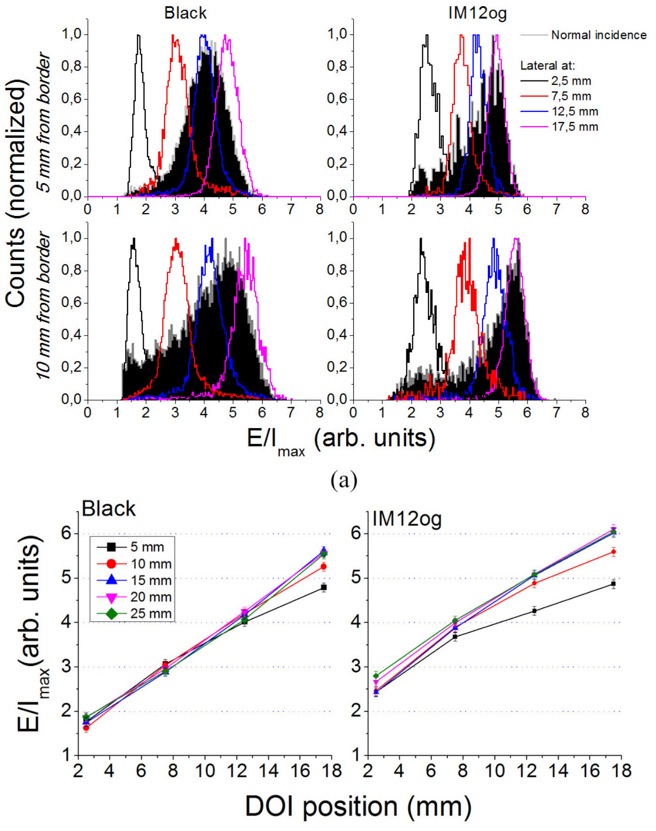

(a)

(b) (c)

Fig. 10. (a) $E/I_{\max}$ histograms for the black (left) and IM12og RR layer (right), and for a source at 5 mm (top row) and at 10 mm (bottom row) from the crystal edge, respectively. The normal incidence results are shown superimposed to the lateral incidence experiments. (b) and (c) Measured $E/I_{\max}$ as a function of the geometrical (true) DOI position for five regions of interest from the crystal edge (5–25 mm).

been taken into account for the black and IM12og cases. Fig. 9 shows the results for these two cases. Average FWHM values of 2.3±0.4 mm, 2.1±0.3 mm, 1.6±0.2 mm, and 1.3±0.2 mm are obtained for the black case for DOI1, DOI2, DOI3, and DOI4 regions, respectively. Those results improve for the IM12og treatment to 1.7±0.3 mm, 1.5±0.3 mm, 1.3±0.3 mm, and 0.7±0.3 mm, respectively. On average at least a 30% improvement is reached when using the RR devices.

B. DOI Resolution

In the case of the black treatment and normal incidence, we have fitted the histograms of measured $E/I_{\max}$ values using (2) and provided information on the DOI resolution (FWHM). Fig. 10(a) depicts the $E/I_{\max}$ distributions for two ROIs (*ca.* 4 mm × 4 mm), centered at 5 (top row) and 10 mm (bottom row) from the crystal edge. We observe a Gaussian-like distribution for the source at 5 mm offset, due to the truncation of the LD near the crystal edge, worsening the DOI FWHM. The expected shape of the DOI distributions is recovered beyond this point, where the scintillation light truncation is reduced, as shown in Fig.10(a) bottom-left. The black filled histograms observed for the RR cases and normal incidence, independently of the impact position, are slightly wider (higher $E/I_{\max}$ values).

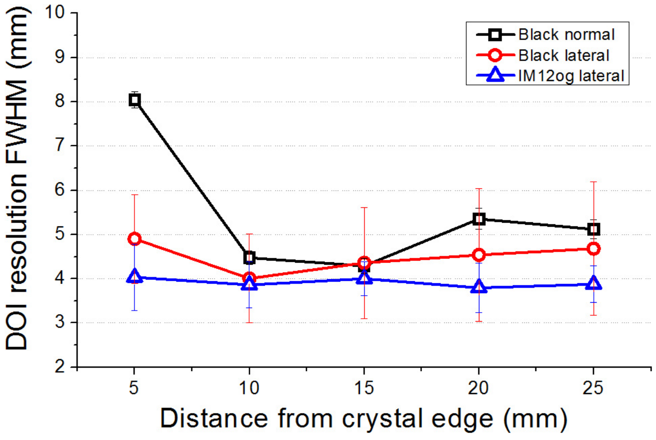

Fig. 11. DOI resolution (FWHM) for different crystal treatments and beam incidences as a function of the distance from the crystal edge.

Measurements with lateral incidence to the detector block were carried out for two treatment cases, black (panel *b*) and IM12og (panel *c*). 4 mm × 4 mm ROI for each depth and each distance from the edge was considered. Each plot in Fig. 10(a) depicts the histogram obtained through normal incidence and overlapping with this the $E/I_{\max}$ distributions found for four lateral impinging beams at 2.5, 7.5, 12.5, and 17.5 mm distance from the photosensor. The calibration curves with the known geometrical DOI position and the measured $E/I_{\max}$ value exhibited a good linearity (regression coefficient = 0.99) for impacts beyond 10 mm from the crystal edge, except the curve for the IM12og treatment at 10 mm, see Fig. 10(b) and (c). For that curve and those at 5 mm, both for black and IM12og, a second order polynomial was used (regression coefficient = 0.99), to correct for the light truncation effect at the crystal edges. The four profiles obtained through the lateral incidence experiments are fitted with Gaussian distributions, whose FWHMs provide direct information on the DOI resolution. At 10 mm from the crystal edge we obtained FWHM values for the IM12og case of 3.1 mm, 3.7 mm, 4.1 mm, and 3.9 mm, for known photon DOI of 17.5 mm, 12.5 mm, 7.5 mm, and 2.5 mm, respectively. For the black treated crystal, we found 4.1 mm, 4.1 mm, 3.9 mm, and 2.1 mm, respectively.

We have calculated the average DOI resolution up to the crystal center. In the case of black treatment, we depict the results both through normal and lateral incidence experiments, whereas for the IM12og treatment only laterally since (3) is not deduced for the case with internal light reflections. In the case of the lateral incidence data, the FWHM for the four beams corresponding to different interaction depths has been calculated by weighting the data for the theoretical contribution given by the exponential photon attenuation law. Fig. 11 shows the FWHM results as a function of the distance from the crystal edge. The best DOI results (FWHM) have been observed for the IM12og treatment case with an average (from 5 to 25 mm from the crystal edge) FWHM

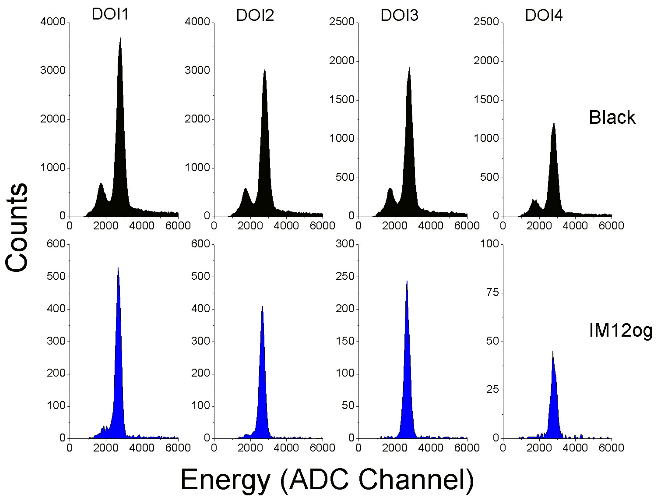

Fig. 12. Energy spectra for the black and IM12og cases as a function of the DOI layer.

of 3.7±0.2 mm. The lateral data obtained for the black case exhibited a value of 4.8±0.4 mm. This is slightly worse than in the IM12og case. The FWHM results found for normal incidence in the case of the black treatment are higher than those observed for the lateral experiments, on average 5.5±1.5 mm. Nevertheless, there is a good agreement between the results for the black treatment both through lateral and normal incidence, except at the crystal edge region, due to the stronger light truncation and, thus, worst characterization using (3).

C. Energy Resolution

The energy resolution has also been evaluated as a function of the different DOI layers and for the various crystal treatment cases. As an example, Fig. 12 shows the energy spectra for the black and RR IM12og cases on the top and bottom panels, respectively. These profiles are obtained for the central crystal area, see Fig. 6. Note that the energy peaks for both cases are roughly centered in the ADC channel 3000. This occurred, because the energy gain observed for the RR cases was equalized to the black paint treatment by reducing the bias voltage to about 29 V and, therefore, avoiding saturation problems in the readout chain. As earlier reported [17], [22], reducing the bias of these SiPMs from 31 to 29 V should almost not impact the SiPM performance.

Similarly to the spatial resolution results, the energy resolution improves when the RR layers are used compared to the black paint case, due to the increase of transferred scintillation light to the photosensor, as it was expected. Consequently, an improvement is also observed for layers closer to the photosensor array.

In general, we observe small differences for all RR results, when the RR is coupled to the scintillator through either optical grease or air. In the case of IM12og, we have measured the best and most uniform values across the four layers, see the violet triangles in Fig. 13(b). The energy resolution ranges from 12.6% at the entrance layer (DOI1) to 11.1% at the deepest layer (DOI4). The average energy resolution for the whole scintillation volume shows indeed the best results for the IM12 RR treatment, reaching 13.9±1.3% and 12.2±0.4%, when being coupled using air or optical grease, respectively. Values of 16% and 15% are determined for the black case for layers DOI1 and DOI4, respectively. The average for all impact positions increases here to 15.8±0.7%.

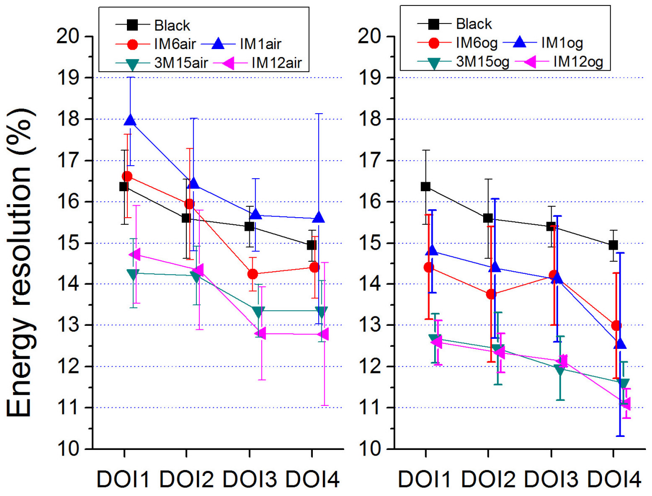

(a) (b)

Fig. 13. Energy resolution values obtained for the studied cases. (a) Plot of the energy resolution as a function of the DOI layer when using air coupling and (b) when using optical grease between the RR and the photosensor.

Additional studies showing the energy resolution as a function of the impact position have been carried out. Fig. 14(a)–(c) shows the energy resolution for three cases, namely black, 3M15og, and IM12og. The plots depict a very small energy resolution spread across the impact positions for a particular layer. However, a slightly larger variation is found for the black paint case at the entrance DOI layer (standard deviation equals 0.9%), due to the stronger light truncation. The spread for the 3M15og and IM12og cases for this layer reduces to only 0.5%. In deeper layers, these values remain again small, being 0.5%, 0.1%, and 0.4%, for layers DOI2, DOI3, and DOI4 (IM12og), respectively.

V. CONCLUSION

In this paper, we have described the detailed performance of a detector block suitable for the design of high sensitivity and spatial resolution PET systems. The main components of this detector block are a monolithic 20 mm thick LYSO scintillator, 50 mm × 50 mm base, and an array of 12 × 12 SiPMs with a pitch of 4.36 mm and 3 mm × 3 mm active area each.

Two crystal treatments have been tested, namely a black paint that preserves the scintillation LD, but also an additional and better performing case as described, where the lateral walls keep the black paint and the entrance surface of the scintillation block is coupled to an RR layer tends also to preserve the LD. This layer tends to also preserve the LD as it reflects the scintillation photons in the same incident direction. Thus, an increase of the scintillation light transferred to the photosensor was observed, almost without disturbing its distribution. Several of these RR layers have been tested with

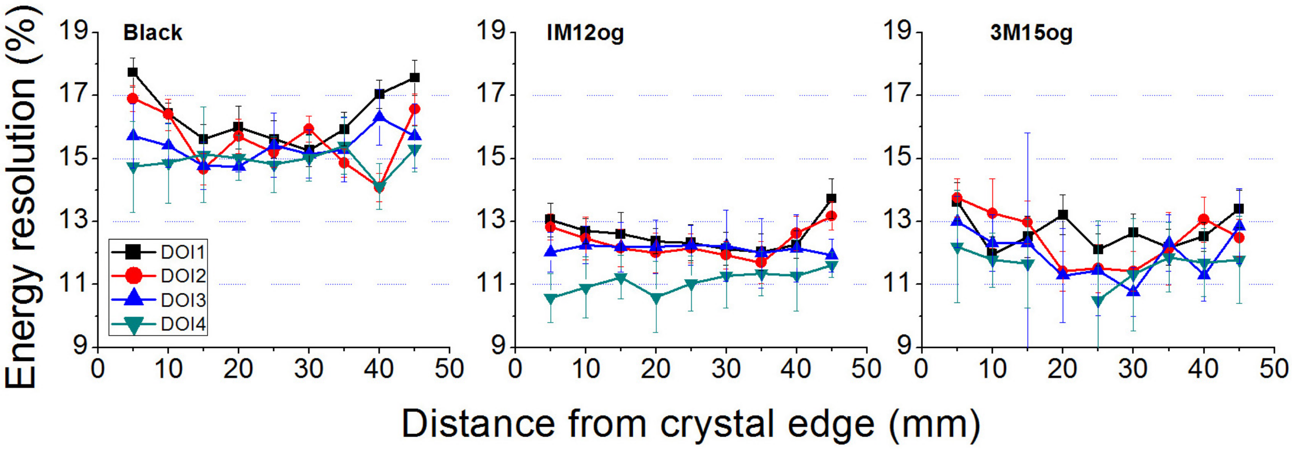

(a) (b) (c)

Fig. 14. Energy resolution values as a function of the impact position for the crystal surface treatment cases (a) black, (b) IM12og, and (c) 3M15og, respectively.

corner cube sizes ranging from 6 mm to 120 μm. The best performance was obtained for the smallest of these sizes, as it would be expected since this corresponds to a smaller *XY* shift of the back-bouncing scintillation light. In addition, we tried two ways of coupling the RR to the crystal, either using optical grease or direct contact (air coupling). The best results concerning spatial and energy resolution were observed for the case using optical grease.

We found detector resolutions (FWHM) values ranging from 1.7 mm on average at the entrance DOI layer, to 0.7 mm at the layer nearest to the photosensor. These results show an improvement when compared to former experimental data with monolithic scintillators using different crystal treatments [11]–[15]. When the crystal was black painted, a deterioration of at least 30% was observed. The RR layers tend to return an energy resolution that slightly depends on the interaction depth. In the case of the IM12og RR, a roughly flat energy resolution was found as a function of the DOI layer, better than 13%. However, the black treatment worsens these results varying from 16% (entrance layer) to 15% (photosensor) see Fig. 14.

We observed different DOI histograms as a function of the impact position, that have been possible to be locally corrected, see Figs. 6 and 10. Here, narrower $E/I_{\max}$ histograms were determined for impacts occurring at the crystal corners, due to the stronger truncation of those light scintillation distributions. In this paper, we split the crystal height into four DOI regions, although it is expected to provide a continuous DOI correction when using these detectors. Here, the determined average DOI resolution approaching 4 mm with the RR makes it possible to efficiently correct for the parallax error using such thick monolithic blocks.

Overall, the detector performance based on a 20 mm thick LYSO crystal coupled to an RR layer at the entrance surface shows a high performance at almost any position within the crystal volume. The presented study finally results in values for the three characteristic detector properties of spatial, energy, and DOI resolutions of 1.5 mm, 12%, and 4 mm, respectively.

REFERENCES

[1] G. Delso *et al.*, "Performance measurements of the Siemens mMR integrated whole-body PET/MR scanner," *J. Nucl. Med.*, vol. 12, pp. 1914–1922, Dec. 2011.

[2] S. Surti *et al.*, "Performance of philips gemini TF PET/CT scanner with special consideration for its time-of-flight imaging capabilities," *J. Nucl. Med.*, vol. 48, no. 3, pp. 471–480, 2007.

[3] A. M. Grant *et al.*, "NEMA NU 2-2012 performance studies for the SiPM-based ToF-PET component of the GE SIGNA PET/MR system," *Med. Phys.*, vol. 43, no. 5, pp. 2334–2343, 2016.

[4] S. Vandenberghe, E. Mikhaylova, E. D'Hoe, P. Mollet, and J. S. Karp, "Recent developments in time-of-flight PET," *Eur. J. Nucl. Med. Mol. Imag.*, vol. 3, pp. 1–30, Dec. 2016.

[5] C. S. Levin, "Detector design issues for compact nuclear emission cameras dedicated to breast imaging," *Nucl. Instrum. Methods. Phys. Res. A*, vol. 497, no. 1, pp. 60–74, 2003.

[6] T. Ling, T. K. Lewellen, and R. S. Miyaoka, "Depth of interaction decoding of a continuous crystal detector module," *Phys. Med. Biol.*, vol. 52, no. 8, pp. 2213–2228, 2007.

[7] P. Antich, N. Malakhov, R. Parkey, N. Slavin, and E. Tsyganov, "3D position readout from thick scintillators," *Nucl. Instrum. Methods Phys. Res. A*, vol. 480, nos. 2–3, pp. 782–787, 2002.

[8] S. Tavernier, P. Bruyndonckx, S. Leonard, and O. Devroede, "A high-resolution PET detector based on continuous scintillators," *Nucl. Instrum. Methods Phys. Res. A*, vol. 537, nos. 1–2, pp. 321–325, 2005.

[9] S. Stoll *et al.*, "Exploring the limits of PET resolution with a monolithic scintillator detector," in *Proc. IEEE NSS-MIC*, 2010, pp. 3210–3213.

[10] H. T. Van Dam *et al.*, "A practical method for depth of interaction determination in monolithic scintillator PET detectors," *Phys. Med. Biol.*, vol. 56, no. 13, pp. 4135–4145, 2011.

[11] M. Kaul, S. Surti, and J. S. Karp, "Combining surface treatments with shallow slots to improve the spatial resolution performance of continuous, thick LYSO detectors for PET," *IEEE Trans. Nucl. Sci.*, vol. 60, no. 1, pp. 44–52, Feb. 2013.

[12] A. Ros, Ch. W. Lerche, A. Sebastia, F. Sanchez, and J. M. Benlloch, "Retroreflector arrays for better light collection efficiency of gamma-ray imaging detectors with continuous scintillations crystals without DOI misestimation," *J. Instrum.*, vol. 9, no. 4, 2014, Art. no. P04009.

[13] B. Játékos, A. O. Kettinger, E. Lorincz, F. Ujhelyi, and G. Erdei, "Evaluation of light extraction from PET detector modules using gamma equivalent UV excitation," in *Proc. IEEE NSS-MIC*, Anaheim, CA, USA, 2012, pp. 3746–3750.

[14] J. W. Heemskerk *et al.*, "A micro-machined retro-reflector for improving light yield in ultra-high-resolution gamma cameras," *Phys. Med. Biol.*, vol. 54, no. 10, pp. 3003–3014, 2009.

[15] D. P. McElroy, S.-C. Huang, and E. J. Hoffman, "The use of retro-reflective tape for improving spatial resolution of scintillation detectors," *IEEE Trans. Nucl. Sci.*, vol. 49, no. 1, pp. 165–171, Feb. 2002.

[16] N. J. Shah *et al.*, “Advances in multimodal neuroimaging: Hybrid MR–PET and MR–PET–EEG at 3 T and 9.4 T,” *J. Mag. Reson.*, vol. 229, pp. 101–115, Apr. 2013.

[17] A. J. González *et al.*, “The MINDView brain PET detector, feasibility study based on SiPM arrays,” *Nucl. Instrum. Methods Phys. Res. A*, vol. 818, pp. 82–90, May 2016.

[18] [Online]. Available: www.3m.com

[19] [Online]. Available: http//www.imos-gubela.com

[20] C. Jackson, K. O’Neill, N. Wall, and B. McGarvey, “High-volume silicon photomultiplier production, performance, and reliability,” *Opt. Eng.*, vol. 53, no. 8, 2014, Art. no. 081909.

[21] A. J. González *et al.*, “A novel brain PET insert for the MINDView project,” in *Proc. IEEE NSS-MIC*, 2014, pp. 1–4.

[22] A. J. González *et al.*, “Performance study of a wide-area SiPM array, ASICs controlled,” *IEEE Trans. Nucl. Sci.*, vol. 62, no. 1, pp. 19–26, Feb. 2015.

[23] A. V. Stolin, S. Majewski, G. Jaliparthi, R. R. Raylman, and J. Proffitt, “Evaluation of imaging modules based on SensL array SB-8 for nuclear medicine applications,” *IEEE Trans. Nucl. Sci.*, vol. 61, no. 5, pp. 2433–2438, Oct. 2014.

[24] R. Pani *et al.*, “Preliminary evaluation of a monolithic detector module for integrated PET/MRI scanner with high spatial resolution,” *J. Instrum.*, vol. 10, no. 6, 2015, Art. no. C06006.

[25] R. Pani *et al.*, “Continuous DOI determination by Gaussian modelling of linear and non-linear scintillation light distributions,” in *Proc. IEEE NSS-MIC*, Valencia, Spain, 2011, pp. 3386–3389.

[26] C. W. Lerche *et al.*, “Dependency of energy-, position- and depth of interaction resolution on scintillation crystal coating and geometry,” *IEEE Trans. Nucl. Sci.*, vol. 55, no. 3, pp. 1344–1351, Jun. 2008.

[27] P. Conde *et al.*, “Analysis of the statistical moments of the scintillation light distribution with dSiPMs,” *IEEE Trans. Nucl. Sci.*, vol. 62, no. 5, pp. 1981–1988, Oct. 2015.

4.2. Initial Results of the MINDView PET Insert Inside the 3T mMR

Authors: Antonio J. Gonzalez, Andrea Gonzalez-Montoro, Luis F. Vidal, Julio Barbera, Sebastian Aussenhofer, Liczandro Hernandez, Laura Moliner, Filomeno Sanchez, Carlos Correcher, Edwin J. Pincay, Gabriel Cañizares, Efthymios Lamprou, Sebastian Sanchez, Juan V. Catret, Santiago Jiménez-Serrano, Jorge Cabello, Markus Schwaiger, Amadeo Iborra, Thibaut Merlin, Dimitris Visvikis and Jose M. Benlloch.

Published: IEEE Transactions on Radiation Plasma Medical Sciences, Early access (2018). https://doi.org/10.1109/TRPMS.2018.2866899

Impact Factor: 1.44 (estimated)

Summary:

This work summarizes the preliminary results obtained with the MINDView brain PET insert. This is a PET insert compatible with all clinical MRI installed worldwide. The main challenge of the project is to achieve good PET performance when working simultaneously with MRI scanners. In order to achieve these objectives, it is required using high readout granularity, high detector performance and high sensitivity, to mention but a few. To achieve these goals the detector blocks composing the systems are the ones described in the articled presented in the thesis: “Performance Study of a Large Monolithic LYSO PET Detector With Accurate Photon DOI Using Retroreflector Layers”. The system consists of 60 scintillator blocks of 50 × 50 × 20 mm^3 arranged in 3 rings of 20 detector modules each, being the largest PET system based on monolithic LYSO blocks. The system defines a FOV of 240 mm in diameter and 154 mm axially.

This article presents the working performance of the MINDView prototype, within a 3T MRI system. The preliminary results reported a spatial resolution of 1.7 mm (FWHM), degrading at 100 mm off- radial center to only 3 mm for the radial and axial components, and 2.5 mm for the transversal using iterative reconstruction algorithms. Moreover, an average energy resolution measured for all detectors and crystal volume was very similar (sigma = 1.5%) with an average value of 17.5%. The measured sensitivity using a small size ^{22}Na source at the center of the field of view (CFOV) is almost 7% for an energy window of 350-650 keV. Regarding phantom acquisitions, rods of a small Derenzo phantom of 2.5 mm were clearly resolved, independently of all

tested MRI sequences including EPI, UTE, MPrage, T2-flair or ASL. The PET insert did not show any count rate degradation also under those sequences.

The prototype design and construction have been successfully accomplished, and the PET insert is already installed at the Klinikum Recht der Isaar in Munich where patient selection is undergoing.

This article has been accepted for publication in a future issue of this journal, but has not been fully edited. Content may change prior to final publication. Citation information: DOI 10.1109/TRPMS.2018.2866899, IEEE Transactions on Radiation and Plasma Medical Sciences

Initial Results of the MINDView PET Insert Inside the 3T mMR

Antonio J. Gonzalez, Andrea Gonzalez-Montoro, Luis F. Vidal, Julio Barbera, Sebastian Aussenhofer, Liczandro Hernandez, Laura Moliner, Filomeno Sanchez, Carlos Correcher, Edwin J. Pincay, Gabriel Cañizares, Efthymios Lamprou, Sebastian Sanchez, Juan V. Catret, Santiago Jiménez-Serrano, Jorge Cabello, Markus Schwaiger, Amadeo Iborra, Thibaut Merlin, Dimitris Visvikis and Jose M. Benlloch

Abstract**—Hybrid molecular and anatomical imaging devices, especially when simultaneously working, have shown to provide advantages over sequential acquisitions. In particular, we present in this preliminary study, the working performance of a brain PET insert, within a 3T MRI system. To our knowledge, this is the largest PET system based on monolithic LYSO blocks. It consists of 60 scintillator blocks of 50 mm × 50 mm × 20 mm arranged in 3 rings of 20 detector modules each. An effective FOV of 240 mm in diameter and 154 mm axially is defined. The crystals included a retroreflector layer at the entrance face, and are coupled to custom arrays of 12 × 12 silicon photomultipliers (SiPM), 3 mm × 3 mm each. Frontend electronics provide X and Y projections of the scintillation light by sampling each row and column of the SiPM arrays. The insert is thermally stabilized by using temperature-controlled air to about 27ºC.**

The PET insert has been installed at the Klinikum rechts der Isar (Munich) and tested within the whole-body Siemens Biograph mMR, a 3T MRI combined with a PET scanner. A system sensitivity of almost 7% for an energy window of 350-650 keV was measured using a small size source at the center of the field of view (CFOV). Current system evaluation showed a spatial resolution at the CFOV of 1.7 mm using iterative algorithms, being below 2 mm within a centered diameter of 120 mm. Rods of a small Derenzo phantom of 2.5 mm were clearly resolved, independently of all tested MRI sequences including EPI, UTE, MPrage, T2-flair or ASL. The PET insert did not show any count rate degradation also under those sequences for a variety of MR imaging acquisitions.

Index Terms**—Molecular imaging, brain PET, monolithic crystals, SiPM, hybrid PET/MR insert.**

I. INTRODUCTION

BRAIN positron emission tomography (PET) instrumentation has greatly evolved from its infancy, when it was used in regional localization, to currently providing excellent resolution with imaging characteristics that can notably impact clinical management [1]. Notice that the first PET scanner was already a dedicated brain PET system [2]. In brain imaging, as in most of other imaging modalities, combining functional and anatomical information becomes very important, but also technologically challenging. This complementary information helps clinicians to for instance better localize the lesion under study. The predominant type of anatomical and functional imaging combination in brain has been PET and computed tomography (CT). However, in the last decade there has been a significant push forward to develop simultaneous PET and magnetic resonance imaging (MRI) brain imaging. Whole-body PET-MRI systems have been used for brain studies [3][4], among other applications.

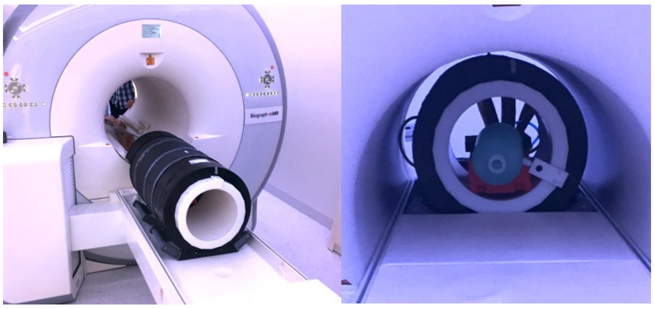

Fig. 1. Photographs of the MINDView PET insert. Left, it is shown when outside the MR ready to allocate patient head. Right, inserted in the MR while imaging a bottle.

With the aim of improving the image performance for brain studies, dedicated PET inserts have been developed in the past, as the one combined with the Siemens MAGNETOM Trio MRI [5][6]. Another system was developed at the Sogang University in Seoul, using silicon photomultipliers (SiPMs) [7]. The system contains 72 detectors on a ring structure of 330 mm aperture using LYSO crystals of $3 \times 3 \times 20$ mm^3. The SiPM signals are transmitted to preamplifiers using a 300 cm flexible flat cable. Also using SiPMs, a brain PET insert was developed at the National Institute of Radiological Sciences in Japan. A particular characteristic of this design is the use of

This work was supported in part by the EU Grant 603002 under the FP7 program. It has also been supported by the European Research Council (ERC) under the European Union's Horizon 2020 research and innovation program (grant agreement No 695536). It has also been supported by the Spanish Ministerio de Economía, Industria y Competitividad under Grant TEC2016-79884-C2-1-R and through PROSPET (DTS15/00152) funded by the Ministerio de Economía y Competitividad.

A.J. Gonzalez, A. Gonzalez-Montoro, L.F. Vidal, L. Hernandez, L. Moliner, F. Sanchez, E.J. Pincay, G. Cañizares, E. Lamprou, S. Sanchez, J.M. Benlloch are with Instituto de Instrumentación para Imagen Molecular (I3M), Centro Mixto CSIC — Universitat Politècnica de València, Valencia, SPAIN (e-mail: agonzalez@i3m.up.ves).

C. Correcher is with Bruker NMI, Valencia, SPAIN.

J. Barbera, J.V. Catret, S. Jiménez-Serrano are with Oncovision, Valencia, SPAIN.

S. Aussenhofer, is with NORAS MRI products GmbH, Hoechberg, GERMANY.

J. Cabello and M. Schwaiger are with Nuklearmedizin, Klinikum rechts de Isar, Technische Universität München, Munich, GERMANY.

A, Iborra, T. Merlin and D. Visvikis are with LaTIM, INSERM, UMR 1101, Brest, FRANCE.

four-layer DOI detectors integrated with the head coil of the MRI [8]. LGSO scintillators are arranged in 12 × 4 × 4 layers. The size of each crystal element was 2.9 mm × 2.9 mm × 5.0 mm. It makes use of DOI information based on multilayer crystal arrays [9]. The detector and some electric components are packaged in a copper shielding box.

More recently, two projects were EU granted to build brain PET dedicated inserts. Both projects aim at developing instrumentation tools to clinically diagnose schizophrenia or depression, two major mental disorders. MRI and fMRI have showed to differentiate diagnosed schizophrenia from healthy controls only on a statistical basis. The utility of PET imaging here is practically limited by: the significant high cost, and the limited sensitivity and resolution of current scanners. The TRIMAGE research project develops an integrated brain PET-MRI-electroencephalogram (EEG) scanner. The MRI has a compact 1.5-T cryogen-free magnet and the PET scanner is based on SiPM technology [10]. Two LYSO crystal arrays layers with 8 and 12 mm height and 3.3 mm pixel size will be mounted. The inner PET diameter is 312 mm with an axial length of 167 mm. The second project refers to the MINDView project [11]. We report in this work the current status performance of the brain PET insert developed under the MINDView project, see photographs in Fig. 1.

This work does not intend to exhaustively follow the NEMA standard but to demonstrate the working performance of the designed and constructed brain PET insert. It has been recently installed at the nuclear medicine department in Klinikum rechts der Isar (Munich) and also exhaustively tested inside the Siemens mMR, a whole body PET-MR with a 3T main magnetic field. A variety of MR sequences routinely used for brain imaging (including those for PET attenuation correction) have been run, and the PET response measured.

II. MATERIALS AND METHODS

A. *Detector blocks*

The MINDView PET insert is composed by three rings of 20 detector blocks each [11][12]. The detector blocks include a thick monolithic LYSO crystal with dimensions of 50 mm × 50 mm × 20 mm. The crystals have all faces polished, with their laterals black painted and the entrance one coupled to a retroreflector layer. Accurate studies have shown the advantage of using a retroreflector layer at the entrance face of the monolithic crystal [13].

Each crystal is coupled to a custom array of 12×12 SensL SiPM (3 mm × 3 mm) with 4.36 mm pitch. SiPMs are of the MINDView-series type (similar to J-series) and were biased to about 30 V. The photosensor array is connected to an analog read-out electronics providing information for each row and column of such array. This read-out allows one to characterize the projected (X and Y) scintillation light distribution. Photon DOI is estimated from these projections as the average (X and Y) of the ratios of the energy to the maximum read-out signal (E/I_{max}) [13]. Therefore, it is possible to determine the 3D interaction position.

A trigger signal for each detector is conformed by summing all row signals. Typical rise and decay times for this signal are 25-50 ns and 200-300 ns, respectively. Each detector block includes a temperature sensor. All analog signals, as well as the temperature reading, are brought outside the MR field of view (FOV) using thin printed circuit boards (PCB) that minimize nickel components and, thus, avoid MR distortions. They are fed into a data acquisition (DAQ) system using multi-coaxial cabling.

The DAQ is formed by three sets of 10 ADC boards with 12 bits precision. Every ADC manages 2 detector blocks and are programmed with 250 ns charge integration windows. Each set of 10 ADCs includes a trigger card, to which all 60 trigger signals from the detectors are fed. In this design, each trigger card controls the ADCs belonging to one PET ring (see sketch in Fig. 2). In practice the modular system behaves like 3 independent interconnected acquisition systems assembled in separated racks but all 60 detectors work independently. Time alignment between all ADCs (60 detectors) has been achieved taken special care in the design of the acquisition system in order to achieve a maximum intrinsic error of about 200 ps. Current coincidence window is 5 ns. Every detector has allowed coincidences with its 9 opposite blocks in all rings.

B. *System architecture*

The distance from opposite crystal-to-crystal is about 330 mm. This, together with the allowed map of coincidences, defines a system FOV of 240 mm in diameter (transaxial) and 154 mm in the axial direction. The total volume of LYSO material is 3000 cm^3, and the number of digitized signals as high as 1440 (total insert PET weight about 45 kg). These compare to about 9175 cm^3 of LYSO and 4032 channels, for the PET within the Siemens mMR. The total scanner diameter including radio-frequency shielding is 42 cm, with an axial length of roughly 80 cm.

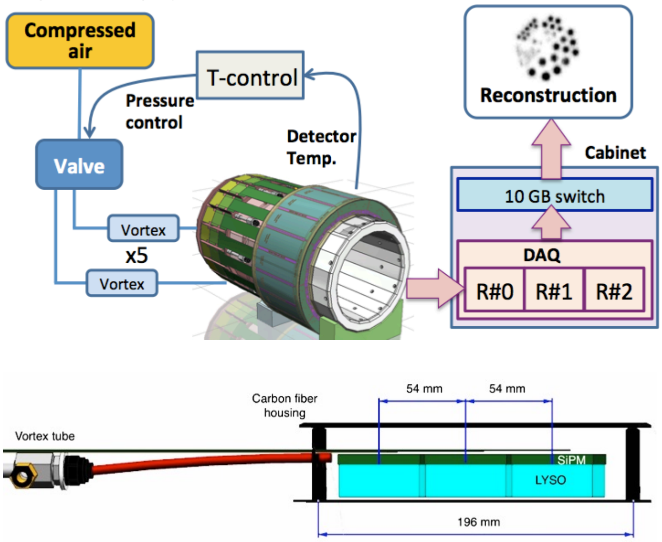

Fig. 2. Top, skecth of the system architecture: left blocks show the temperature control and right panels show the data acquisition scheme. Bottom, lateral view example of the crystals position, SiPMs, carbon fiber housing and vortex tube.

The whole DAQ electronics, together with detector blocks power supplies, and temperature regulation, are located in a cabinet that is non-ferromagnetic and radio-frequency (RF) shielded.

The detector blocks are temperature stabilized using temperature controlled air flow, resulting after controlling the input pressure to five vortex tubes. The temperature sensors at the read-out electronics (near the SiPM arrays) are read and a PID controller manages the output air temperature, see Fig. 2. All PET measurements inside the MR were carried out at a stable average temperature (60 blocks) of 27.5 ºC. As it can be seen in Fig. 3, the temperature spread during 7 hours while continuously running MR sequences, was below 0.05 ºC (sigma). A detail of one set of various sequences is also shown in Fig. 3. The temperature regulation is visible, however even when running aggressive-pulsing sequences such as ultra-short time echo (UTE) or echo-planar imaging (EPI), no effect on the average temperature was observed. This target temperature is a compromise between PET system performance and demanding air flow.

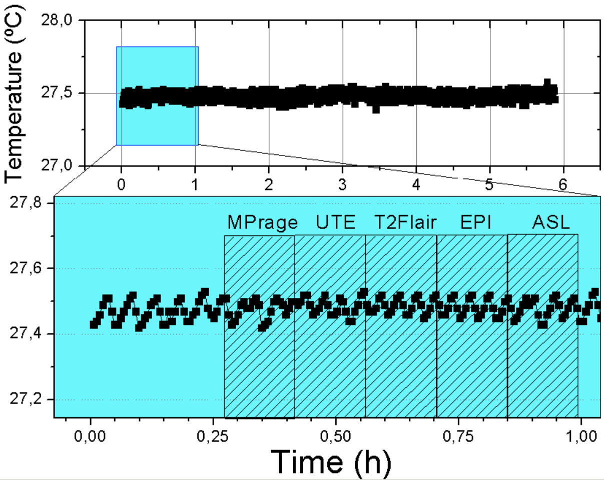

Fig. 3. Average system temperature for 7 hours (non-stop) with different brain MR imaging sequences (top) and detail of the temperature when runing specific MR sequences (bottom).

C. *RF coil and B0-B1 fields shielding*

A dedicated RF coil with a birdcage configuration, transmit-receive, has been developed and simultaneously tested with the PET insert. It is made out of 16 rungs providing a geometric aperture of 25 cm, suitable for an ample and comfortable head allocation. The Siemens mMR has a 60 cm bore and an actively shielded whole-body gradient coil system (amplitude of 45 mT/m and slew rate of 200 T/m/s) [14]. The main MR sequences programmed to test the insert PET/MR compatibility have been EPI, arterial spin labeling (ASL), T1w (Magnetization-Prepared Rapid Gradient Echo - MPrage), T2w (Fluid-Attenuated Inversion Recovery - Flair) and UTE, which are regularly used in clinical routine for a variety of neuro-applications with the mMR scanner. Preventing electronic noise from the B1 field and possible eddy currents arising from the switching gradient field, have been achieved by implementing a Faraday-cage made out of 200 µm overlaying carbon fiber sheets [15], see sketch in Fig. 2.

D. *Sources and phantoms*

PET performance tests have been carried out using several encapsulated ^{22}Na sources as well as a variety of fillable phantoms namely a custom phantom with inserts in a warm background, NEMA imaging quality for small animals and a mini-Derenzo. The sources (1 inch × 6 mm PMMA encapsulation) were 1 mm and 0.25 mm in diameter ^{22}Na sources with currently about 740 kBq and 37 kBq activity, respectively.

A custom phantom was used to study the recovery coefficients in a large phantom. It has dimensions of 113 mm height and 139 mm in diameter in a warm background, and it includes 6 rods inserts with diameter ranging from 4.5 mm to 20 mm (height 55 mm), see Fig. 4. Several concentration ratios were tested, as it will be described bellow.

The small animal NEMA phantom is composed of a main fillable uniform region chamber, a lid that attaches to the main fillable region, containing 2 smaller cold region chambers, one that was filled with water and the other with air, and a solid acrylic glass region with 5 fillable rods drilled through with diameters of 1, 2, 3, 4, and 5 mm, respectively. The image-quality phantom was filled with ^{18}F-FDG solution (32 MBq) and acquired applying a 350 to 650 keV energy window. Each acquisition lasted 180 seconds.

In the mini-Derenzo the rods diameters range from 1.5 mm to 6.5 mm in steps of 1 mm, with a pitch distance equals this diameter.

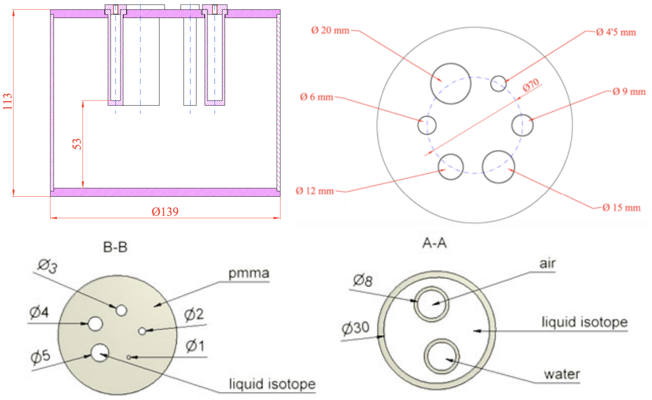

Fig. 4. Drawings of the phantoms used during the PET insert evaluation. Top row shows the recovery coefficients phantom filled with warm uniform background and 6 inserts. Next row shows the NEMA quality imaging phantom for small animals.

E. *Reconstruction methods*

Regarding image reconstruction, we have used iterative algorithms such as list mode ordered subsets (LMOS) [16], maximum likelihood expectation maximization (MLEM), as well as its accelerated variant ordered subsets MLEM (OSEM). The so-called IRIS projector is currently under investigation [17]. The purpose of using such variety of algorithms is to show there is not a bias of the scanner regarding the reconstruction method, and to also study if there is one that optimizes the results.

LMOS implements the tube of response (TOR) projector and multiple CPU processing, and only scatter corrections are programmed during the reconstruction process. MLEM makes use of multiple graphical processing units (GPUs) capabilities and both scatter and random corrections considered. Virtual detector pixels between 1.4-2 mm have been tested, combined with voxel sizes of 0.7-1 mm. The open-source CASToR platform [18] has been used to perform OSEM reconstructions, considering both virtual detector pixels and voxel sizes of 1 mm. The Siddon projector and OpenMP parallelism have been used for OSEM reconstructions. No scatter or random corrections are considered when using this method. Table I shows the algorithm method used for the different experiments, including number of iterations and/or subsets.

TABLE I. TESTS AND ALGORITHMS

Test	Algorithm	Voxel/Pixel	It./subs.
Spatial resolution	LMOS	0.7/1.4 mm	1 it/15 subs.
Spatial resolution	FBP	0.25-1 mm	
Recovery coeff.	MLEM	1/1 mm	10-24 it
IQ NEMA spatial res.	LMOS	1/2 mm	1 it/15 subs.
IQ NEMA MRI seq.	CASTOR	1/1 mm	2 it/10 subs.
Brain phantom	MLEM	1/1 mm	60 it

F. *Detector calibration*

Every PET detector was position and energy calibrated using an already described procedure based on position-known sources [13][19]. Notice that the 60 detectors were calibrated using an ^{18}F filled phantom with hot spots following an array distribution matching the holes of the Tungsten mask described in [13], covering an area of 46 mm × 46 mm. We collected around 10^7 coincidences for each detector block.

III. RESULTS

A. *Detector blocks performance*

The performance of the detector blocks used in this work has been extensively reviewed in a prior publication [13]. Since there exist slight differences from that experimental first set-up to the finally constructed system, we show in Fig. 5 left flood maps of FDG sources (11×11, 4.6 mm pitch) for three example detectors namely M19, M24 and M56 (corresponding each one to a different ring of detectors), as a function of the 4 DOI layers (5 mm thickness each). The first column shows the maps for the entrance layer where stronger image compression is observed, as expected. The panel on the right hand side shows the measured FWHM for three detectors, also as a function of the DOI layer. By using a method based on software collimation [20], we have estimated the average intrinsic detector resolution for each detector block to be about 1.3±0.1 mm.

We have determined the energy resolution of all detectors using one of the FDG fillable phantoms at the CFOV. Fig. 6 shows the energy spectra of detectors with odd module numbering. The spectra show all events happening in the crystal volume covered by the area of 46 mm × 46 mm. We measured an average energy resolution of 17.5±1.5 % (standard deviation) for the entire system. The results shown in this work do not include events in the last 2 mm region near the crystal edge.

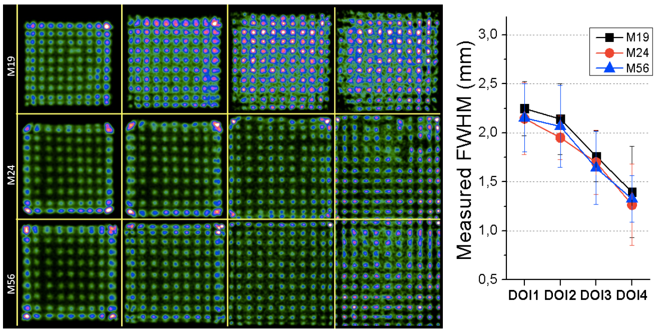

Fig. 5. Left: Flood maps for three detectors, one for each ring (top row M19, center row M26, bottom row M56), of 11×11 collimated FDG sources, as a function of the DOI layer. From left to right, entrance crystal layer 20 – 15 mm (DOI1) to exit layer (closer to photosensor, DOI4) 5 – 0 mm. Right: measured spatial resolution (FWHM) versus DOI layer for these detectors.

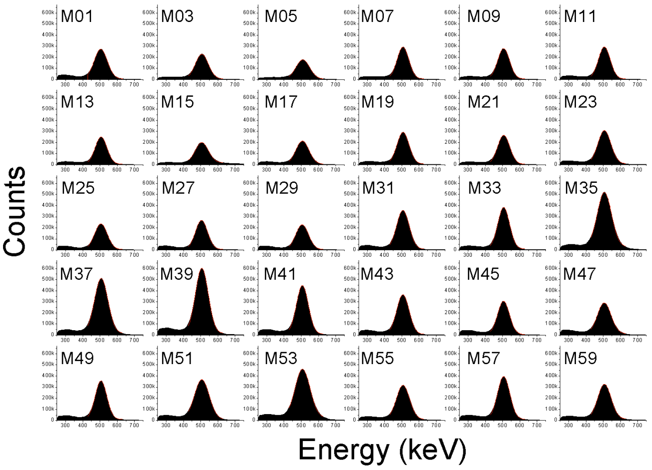

Fig. 6. Energy spectra for detectors with odd numbering.

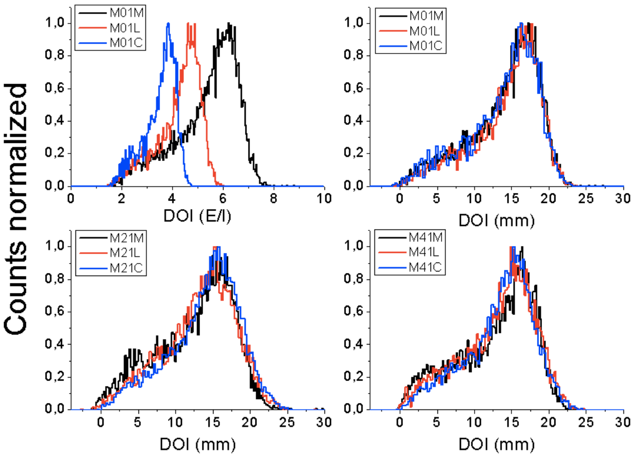

Fig. 7. Top-left shows the distributions before calibration for M01. Calibratied DOI distributions at the center (M), lateral (L) and corner (C), for modules M01, M21 and M41, are shown on top-right and bottom panels.

The DOI was only analyzed using normal incidence collimated gamma ray beams [13]. We plot in Fig. 7 top-right and bottom panels, the DOI distributions, after calibration to millimeters, interactions contained in regions of interest defined at the center (M), lateral (L) and corners (C) of detector modules M01, M21 and M41. As an illustration, Fig. 7 top-left also shows the DOI distribution of detector M01 before calibration where the different light scintillation truncations are observed as a reduction of the upper limit of E/I. We expect DOI resolutions in the range of 4±1 mm for all detectors.

B. *PET performance*

The 1 mm ^{22}Na source was moved across the axial FOV, in steps of 0.5 mm, in order to measure the system sensitivity. Fig. 8 shows the measured sensitivity curve for an energy range of 350-650 keV. We observed almost 7% sensitivity at the CFOV, agreeing well with previous measurements with one ring [15] and also with expected values [12]. Noise Equivalent Count curves have not yet been analyzed but initial results show system capabilities to manage above 150 MBq within the FOV, without apparent image deterioration.

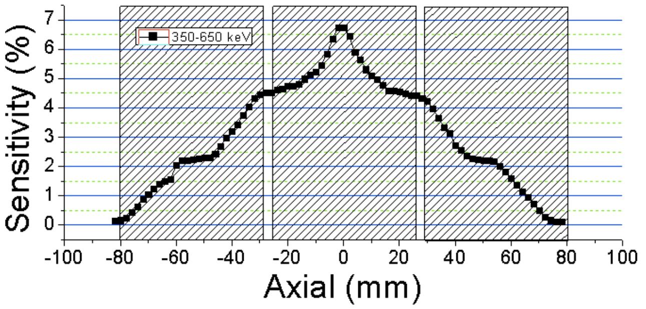

Fig. 8. Sensitivity plot measured with a small size ^{22}Na source across the axial FOV.

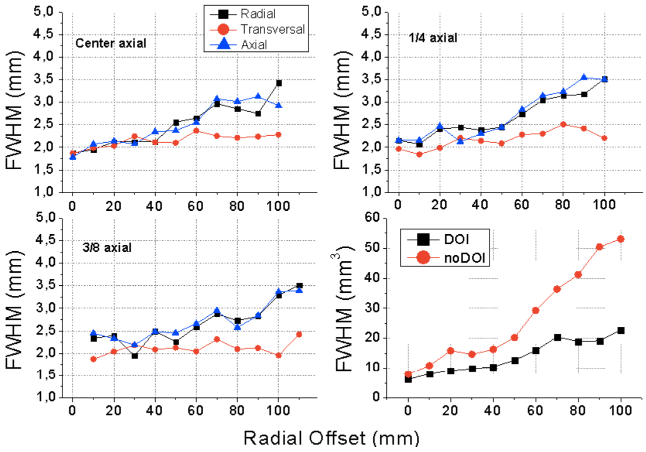

Fig. 9. Measured spatial resolution results (FWHM) of a point source (1 mm diameter) as a function of the radial offset and for three axial positions using the LMOS algorithm. The bottom-right panel shows the volumetric FWHM comparison for data with and without photon DOI correction.

The 0.25 mm in diameter ^{22}Na source was moved along the radial axis, at three axial positions namely the center of the FOV, 1/4 and 3/8 of this axis. The data were reconstructed using LMOS with 0.7 mm voxels (cubic dimensions) and 1.4 mm virtual size pixels. One iteration and 15 subsets were selected [21]. As depicted in Fig. 9, the FWHM of the radial, transversal and axial components at the CFOV are about 1.7 mm, degrading to 3 mm in the case of the radial and axial components, and to 2.2 mm in the case of the transversal at 100 mm off-radial distance. No significant deterioration is observed at other axial positions. The results show good uniformity across the FOV, especially for the 120 mm in diameter center, as it was expected, due to the accurate DOI correction. We have calculated the volumetric FWHM for the case of sources placed at the axial center and compared with data obtained without DOI correction. We observed a high degradation towards the FOV edges.

In addition to iterative algorithms, and according to the NEMA protocol, sources at center of the axial system center, and at two radial offsets, have also been reconstructed using single slice rebining and filtered backprojection with a butterworth filter. The image matrix was 240 mm × 240 mm × 154 mm, and different cubic voxel sizes tested. Table II summarizes the results at 10 mm and 100 mm off-radial center.

TABLE II. SPATIAL RESOLUTION FBP, FWHM (MM)

Position	Voxel 1 mm	Voxel 0.5 mm	Voxel 0.25 mm
10 mm off-radial			
Transverse radial	3.4	2.5	2.1
Transverse tangent.	3.0	1.8	1.5
Axial	2.5	2.1	2.2
100 mm off-radial			
Transverse radial	3.5	3.0	2.3
Transverse tangent.	4.9	3.9	2.7
Axial	4.0	3.9	3.1

C. *Recovery coefficients in a warm background*

The recovery coefficients for these tests, named RCi, are calculated in a similar way as the NU-2008 [22]. To obtain these coefficients, Volume Of Interest (VOI) for each rod with dimensions of twice its diameter and 25 mm height are considered. The intensity of the voxels inside of each VOI is summed axially. The voxel corresponding to the highest value is selected as the x-y profile coordinate. The z-profile average is calculated and divided by the background VOI (35 mm diameter and 25 mm height). The resulting ratio is divided by the known concentration ratio [21]. We have determined the RCi for 2 concentration ratios namely 11 and 5 (±20%), respectively. We calculated the RCi for inserts with diameters of 4.5, 9, 12 and 20 mm. The other two inserts were contaminated with higher activities while filling. The images were reconstructed using MLEM including attenuation corrected, but no filter was applied to those. Fig. 10 shows the determined RCi as a function of the number iterations.

D. *PET performance vs. MR sequences*

The effect of different MR sequences was evaluated with different FDG filled phantoms. We have measured the count rates for all phantoms as a function of the different MR sequences (and time). Fig. 11 top shows the number of acquired counts (prompt) as a function of time and for different MR sequences, for three phantoms. The data points (black squares) have been fitted to an exponential decay curve fixing the ^{18}F half-life (red line in the top panels). Initial activities were 12 MBq, 40 MBq, and 32 MBq, for the named mini-Derenzo, Uniform and NEMA phantoms, respectively. We have estimated the percentage of randoms events, and they are in the range of 2-4%. The panels below depict the residue (open circles) in absolute counts (left axis) and in percentage (right axis). No significant count losses are observed, all differences are below 1%.

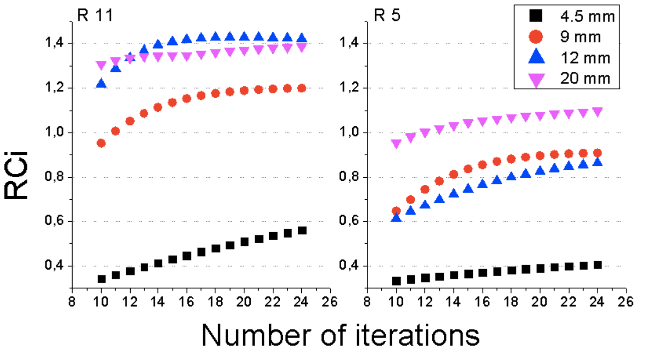

Fig. 10. RCi as a function of the number of iterations using the MLEM algorithm, for different rod diameters and for two rod/background concentrations namely 11 (left) and 5 (right).

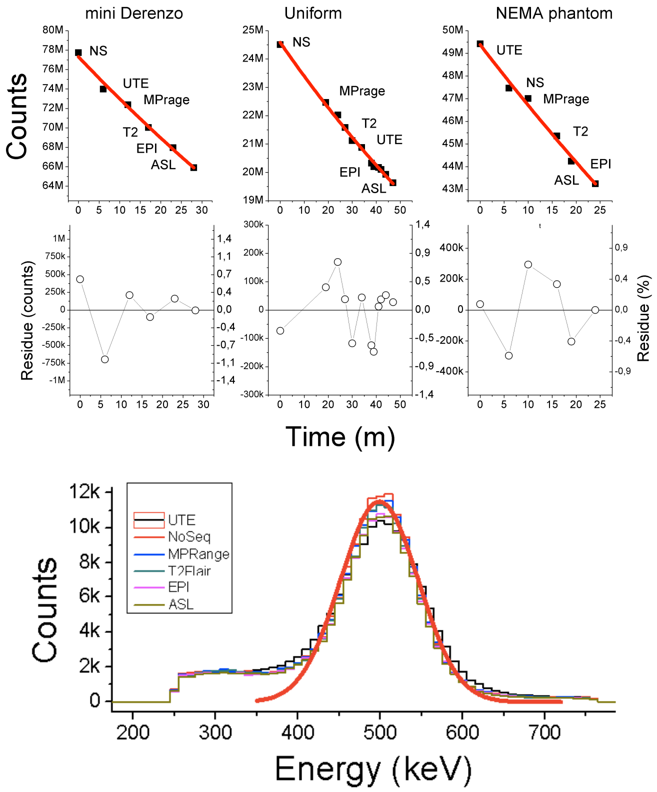

Fig. 11. System performance as a function of the MR sequence. Top panels show the number of counts as a function of time (MR sequence type) for three phantoms. Center panels depict the residue of a fit carried out with the exponential decay curve of ^{18}F. Bottom plots exhibits the energy profiles for one detector module and for the different sequences.

In addition to count rate studies, we have also studied the energy profiles for some detectors for all sequences. We did not observe significant differences among all the measurements. As an example, Fig. 11 bottom shows the energy profile for one detector when running experiments with the NEMA phantom. A slightly 2-3% worsening energy resolution, but not count rate losses, was observed during UTE.

We reconstructed acquisitions of the small animal NEMA phantom using LMOS with 1 mm voxel size and 2 mm virtual pixel, see top row in Fig. 12. We analyzed a profile across the smallest rods for all cases, as plotted in the bottom-left panel. We have determined the Gaussian widths and plotted them against the sequence type without observing any significant deterioration for any particular sequence. In a further step, LMOS reconstructions of acquisitions with the PET insert but using cubic voxels of 0.7 mm and virtual pixels of 1.4 mm were also possible, showing an improved image quality (FWHM) of about 10%.

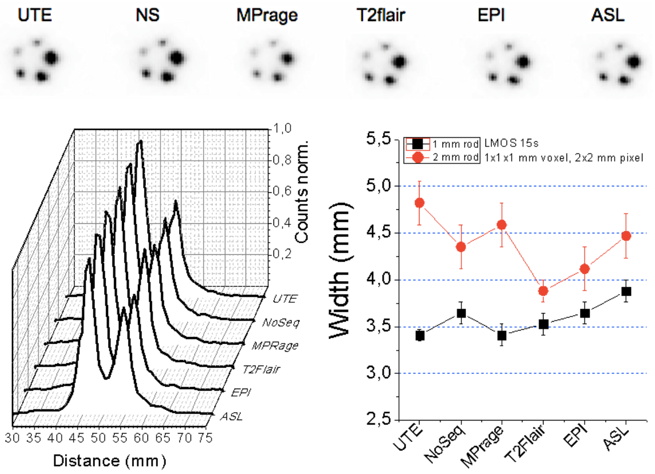

Fig. 12. Top, images acquired of the small animal NEMA phantom as a function of the MRI sequence (NS stands for non-sequence). Bottom-left, profile across the 1 and 2 mm in diameter rods. Bottom-right, measured Gaussian widths vs MRI sequence.

The image quality phantom for small animals was also used to provide information on the SNR and recovery coefficients, as a function of the MR sequence. The data were reconstructed using OSEM (CASTOR) since it allowed varying the number of iterations and subsets finding the optimum for these tests. Indeed, best performance has been achieved for 1 or 2 iterations and 10 subsets. Moreover, the 2 mm rod was unfortunately in the exact CFOV and, using CASTOR it was possible to minimize and underestimate the mean values by computing the sensitivity matrix directly from the normalization data. The SNR was calculated as the ratio of the difference of the mean values obtained for the rods and background, to the standard deviation of the background. The VOI of the rods had diameters matching the true rod diameters and a height of 12 mm. The background was taken from a cylindrical VOI of 4 mm in diameter and 12 mm height in the center volume of the 5 rods. The RC were calculated as the maximum of the VOI over the mean value of the uniform area (25 mm diameter times 10 mm height). The standard deviation of the RC was also calculated using the methodology described in [23]. In general, both the SNR and the RC show no dependencies with the MR sequence. SNR improves with the rod diameter, as expected. Also the recovery coefficients exhibit this behavior.

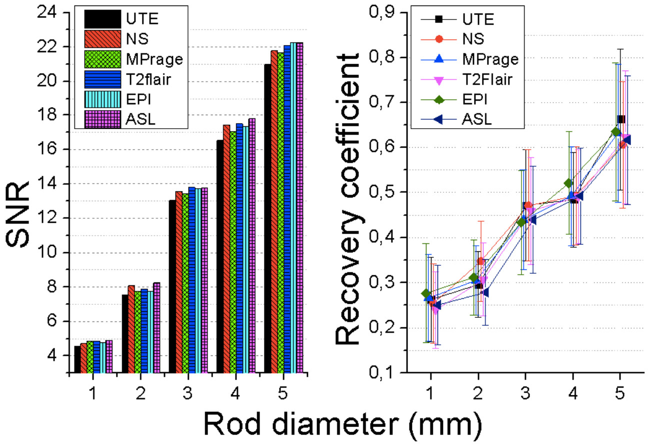

Fig. 13. SNR (left) and recovery coefficients (right) as a fucntion of the rod diameter, and for different MR sequences, using the CASTOR algorithm.

Additional tests to explore the effect of the MRI sequences on the PET insert performance were carried out using the mini-Derenzo phantom. The phantom was placed parallel to the patient bed. The images in Fig. 14 top, that are in absence of an MR sequence, show the reconstructed images for data sequentially obtained with mMR PET and PET insert, left and right, respectively. The mMR PET makes use of an OSEM algorithm with voxel sizes of 1 mm × 1 mm × 2 mm (axial). A few rods of 2.5 mm were not well filled. The images are displayed without applying any filter. The PET insert image is obtained using MLEM with 63 iterations, whereas the mMR image is again an OSEM with 3 iterations and 21 subsets and, therefore, equivalent effective iterations. The PET insert, in contrast to the mMR image, shows the capability to resolve the 2.5 mm rods. We have plotted in Fig. 14 bottom profiles of a row of 2.5 mm capillaries for different MR sequences, without observing any degradation.

E. B1 performance

We studied the B0 and performance of the MRI when the PET insert was placed inside and normally working. A standard Siemens SNR sequence was run to retrieve information about the B1 uniformity. An SNR map was obtained for each pixel as the ratio of the mean value over the sigma of the background measurement. We did this for an acquisition without the PET (left panel in Fig. 15) and with the PET in place and powered ON (right panel). The SNR for the first case was 232, whereas this only varied to 215 with the PET inserted and powered ON (a reduction in SNR of about 7%).

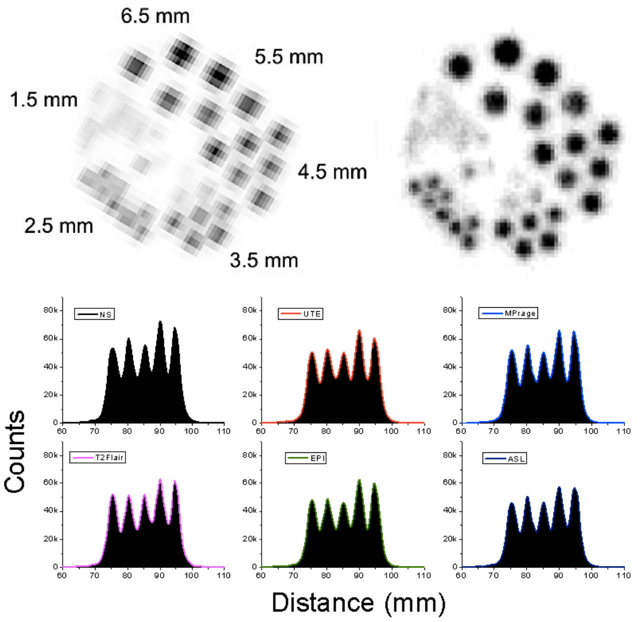

Fig. 14. Top, Derenzo phantom images acquired with the mMR PET (left) and MINDView PET insert (right), no MR sequence applied. Bottom, profiles of a row of 2.5 mm capillaries as a function of the MR sequence, obtained with the PET insert.

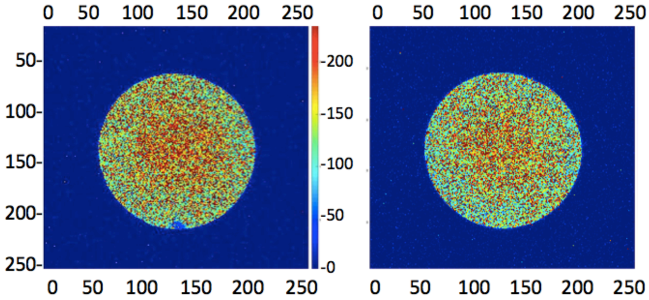

Fig. 15. SNR maps for the B1 field, without the PET insert (left) and with the PET powered ON (right). Transversal slice through the standard Siemens phantom bottle (3.75g $NiSO_4 \times 6H_20$ + 5g NaCl in 1000 ml H_20). X and Y axis are in millimeter. The SNR scale varies from 0 to 250 for both images.

F. Brain phantom images

Initial tests with a human brain phantom, so-called Hoffman, have been carried out in order to show the system performance with large and detail volumes. The phantom was filled with about 15 MBq of a solution of FDG and Gadolinium, and scanned for 20 minutes inside the mMR. The images shown in Fig. 16 are transversal views with 5 mm thickness. They were reconstructed using MLEM with 60 iterations. Attenuation correction on these images was based on a pilot PET image segmentation approach. A median-3d filter with kernel size equals to 3 was used.

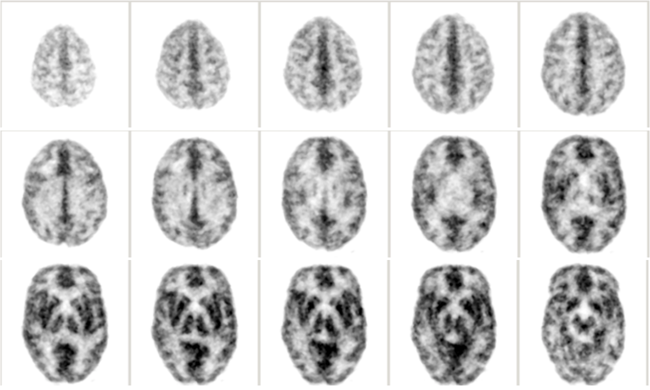

Fig. 16. Transverse views (5 mm thick) of a human brain phantom. The phantom was filled with about 15 MBq of FDG and a Gadolinium solution.

IV. DISCUSSION AND CONCLUSION

In this work we show pilot results of the brain PET insert developed under the MINDView project in terms of system performance when combined with a 3T MR. Although the PET insert has not been tested with different MR systems regarding vendors or main field strengths, we envisage a good system performance (including 7T MR) due to the followed design constrains.

The prototype design and construction have been accomplished. The system showed a physical sensitivity at the CFOV with a small size ^{22}Na source of nearing 7% for an energy range of 350-650 keV. The average energy resolution measured for all detectors and crystal volume was very similar (sigma = 1.5%) with an average value of 17.5%. This value slightly differs from expected values as shown in [13]. This might be explained because the current prototype uses photosensor arrays coupled to specially designed PCBs to avoid MR distortions and induced currents, and also the software collimation applied here is wider than in [13]. The detector blocks, including part of these PCBs, were inserted in temperature controlled housing keeping an average system temperature of 27.5ºC. Significant lower temperatures (10-15ºC lower) might show some PET image performance improvements, however, this would cause a large and constant compressed air input flow.

Photon DOI is corrected for each LOR prior to reconstruction. This made it possible to reach spatial resolutions of 1.7 mm (FWHM), degrading at 100 mm off-radial center to only 3 mm for the radial and axial components, and 2.5 mm for the transversal. A strong image deterioration is observed when DOI is not used. Some improvements in the gamma-ray impact calibration as a function of the DOI are being currently undergoing which could improve the spatial resolution worsening dependence with the radial position.

We have shown the benefits of three iterative reconstruction algorithms. We did use LMOS for the point sources reconstruction because 0.7 mm voxels were possible with this method. Some phantoms were also successfully reconstructed using these parameters. MLEM and OSEM (CASTOR) are well-established algorithms for PET imaging. They present benefits and drawbacks, and this is why both have been arbitrarily used. MLEM, although slow in some implementations, in the current tested, made use of 4 GPU and, therefore, reconstruction times of few minutes were feasible for the range of 20-30 iterations. On the other hand, OSEM exhibited a good image analysis of the small quality NEMA phantom.

Both RCi obtained with the custom phantom having inserts in a warm background, and the RC obtained from the small animal NEMA image quality phantom agree well with expected values. In the case of the RCi, it was complex to provide the exact true concentration ratio and, therefore, slightly values higher than 1 are obtained for the largest inserts.

The system works well under any of the tested MR sequences that are suitable for brain imaging. Several FDG fillable phantoms were scanned using the PET insert inside the 3T MR of the Siemens mMR. Count rate degradations were not observed of the insert PET data for any of these sequences, including strong EPI or UTE. Regarding the detectors performance, they did not also show any deterioration.

Concerning performance comparison with a state-of-the-art whole body PET system, the PET insert shows an improved spatial resolution as for instance observed through the mini-Derenzo. Currently, the system is in Klinikum rechts der Isar (Munich) and patients selection is undergoing.

ACKNOWLEDGMENTS

The authors would like to thank all members of the MINDView consortium for their support on this project. We would like to also acknowledge the help from Bruker team. Experimental data at the UPV Bunker could not have been achieved without the help of M. Hassan from U. Valencia.

REFERENCES

[1] A.T. Abraham and J. Feng, "Evolution of brain imaging instrumentation," Seminars in Nuclear Medicine 41, 202-219, 2011.

[2] G.L. Brownell and W.H. Sweet, "Localization of brain tumors with positron emitters," Nucleonics 11, 50, 1953.

[3] I. Rausch, et al., "PET/MRI for Oncologic Brain Imaging: A Comparison of Standard MR-Based Attenuation Corrections with a Model-Based Approach for the Siemens mMR PET/MR System," J. Nucl. Med. 58, 1519-1525, 2017.

[4] G. Schramm, et al., "Validation of ZTE head attenuation correction in the GE SIGNA PET/MR - initial results," J. Nucl. Med. 58, 644, 2017.

[5] H. Herzog et al., "High resolution BrainPET combined with simultaneous MRI," Nuklearmedizin 50, 74-82, 2011.

[6] N.J. Shah et al., "Advances in multimodal neuroimaging: Hybrid MR–PET and MR–PET–EEG at 3 T and 9.4 T," J. Mag. Res. 229, 101-115, 2013.

[7] K.J. Hong, et al., "A prototype MR insertable brain PET using tileable GAPD arrays," Med. Phys. 40, 042503, 2013.

[8] F. Nishikido, et al., "Feasibility of a brain-dedicated PET-MRI system using four-layer DOI detectors integrated with an RF head coil," Nucl. Instrum. Methods A 756, 6-13, 2014.

[9] F. Nishikido, et al., "Development of 1.45-mm resolution four-layer DOI–PET detector for simultaneous measurement in 3T MRI," Radiol. Phys. Technol. 8, 111–119, 2015.

[10] A. Del Guerra, et al., "TRIMAGE: A dedicated trimodality (PET/MR/EEG) imaging tool for schizophrenia," Eur. Psy. 50, 7, 2018.

[11] J.M. Benlloch, et al., “The MINDVIEW project: First results,” Eur. Psy. 50, 21, 2018.

[12] A.J. Gonzalez, et al., “The MINDView brain PET detector, feasibility study based on SiPM arrays,” Nucl. Instum. Meth. A 818, 81, 2016.

[13] A. Gonzalez-Montoro, et al., “Performance Study of a Large Monolithic LYSO PET Detector With Accurate Photon DOI Using Retroreflector Layers,” Trans Rad Plasma Med Sci 1, 229, 2017.

[14] G. Delso, et al., “Performance Measurements of the Siemens mMR Integrated Whole-Body PET/MR Scanner,” J. Nucl. Med. 52, 2011.

[15] A.J. Gonzalez, et al., “A Brain PET Insert MR Compatible: Final Design and First Results,” IEEE Conf. Proceeding, 2016.

[16] L. Moliner, et al., “Implementation and analysis of listmode algorithm using tubes of response on a dedicated brain and breast PET,” Nucl. Instum. Meth. A 702, 129-132, 2013.

[17] A. Iborra, et al., “A. Iborra, et al., “IRIS projector adaptation for pet scanners based on monolithic crystals,” *IEEE Medical Imaging Conference*, 2017..

[18] T. Merlin, et al.,, “CASToR: A generic data organization and processing code framework for multi-modal and multi-dimensional tomographic reconstruction,” IEEE Medical Imaging Conference, 2016.

[19] A.J. Gonzalez, et al., “A PET Design Based on SiPM and Monolithic LYSO Crystals: Performance Evaluation,” Trans. Nucl. Sci. 63, 2471-2477, 2016.

[20] A. Gonzalez-Montoro, et al., “A Method to Measure the Intrinsic Detector Resolution on Monolithic Crystals,” IEEE Medical Imaging Conference, 2017.

[21] L. Moliner, et al., “Performance characteristics of the MAMMOCARE PET system based on NEMA standard,” J. Instrum. 12, C01014, 2017.

[22] NEMA, NEMA Standards Publication NU 4-2008. Performance Measurements of Small Animal Positron Emission Tomographs , National Electrical Manufacturers Association, Rosslyn Virginia USA (2008).

[23] Q. Bao, et al. “Performance evaluation of the inveon dedicated PET preclinical tomograph based on the NEMA NU-4 standards,” J. Nucl. Med. 50, 401-408, 2009.

4.3. Detector block performance based on a monolithic LYSO crystal using a novel signal multiplexing method

Authors: Andrea González-Montoro, Filomeno Sánchez, Rosana Martí, Liczandro Hernández, Albert Aguilar, Julio Barberá, Juan V. Catret, Gabriel Cañizares, Pablo Conde, Efthymios Lamprou, Francisco Martos, Sebatián Sánchez, Luis F. Vidal, Jose M. Benlloch, Antonio J. González.

Published: Nuclear Instruments and Methods in Physics Research A, Available Online (2018). https://doi.org/10.1016/j.nima.2017.10.098

Impact Factor: 1.34

Summary:

Due to its key contribution in both the diagnose and study of some diseases, PET is one of the most used Nuclear Medicine techniques. For this reason, many efforts have been carried out in order to improve the quality of the images provided by such scanners. A fundamental element determining the performance of PET detector blocks is the scintillator crystal. The interest of using monolithic based scintillator has increased. They allow for continuous encoding of the DOI information. However, the truncation of the light distribution worsens its performance towards the crystal edges.

The best approach to improve the characterization of the light distribution is to read out every single element in the photosensor matrix. However, this typically implies digitizing a huge number of signals which is technically challenging and requires complex data acquisition schemes. With the objective of reducing the number of signals to be digitized, many approaches have been suggested. This article proposes a reduction readout suitable for photosensors arrays. The electronic scheme reduces the signals to X and Y projections with fewer number of signals than those defining the SiPM size.

To evaluate the performance of the proposed reduction scheme a monolithic LYSO block with dimensions of 50 × 50 × 15 mm^3 was coupled to a 12 × 12 SiPMs matrix with 3 × 3 mm^2 elements and a pitch of 4.2 mm. To improve its performance the scintillator laterals walls were black painted and a retroreflector layer was coupled to its entrance face. The reduction readout only provides 16 (8+8) signals. In particular, the 8 central ones (row and columns) are merged from 2 to 1. This number of signals is enough to provide accurate 3D photon impact positions.

For the characterization of the detector block parameters, 1 mm size ^{22}Na sources impinging normally to the scintillator have been used. An average measured spatial resolution of 1.8 mm FWHM (without corrections for source size), and an average energy resolution of 13% FWHM have been achieved. Impacts as close as 0.25 mm from the crystal edge were well resolved. The DOI resolution was evaluated through side beam illumination experiments achieving values of 3.7 mm FWHM.

The work was presented in July 2017 on the 8th international conference on New Developments in Photodetection (NDIP) that was hold in Tours, France. The document was accepted as a poster presentation and awarded with the “Young Scientist Best Poster Award” for the session “Le Rosé”.

Nuclear Inst. and Methods in Physics Research, A ▮ (▮▮▮▮) ▮▮▮–▮▮▮

Contents lists available at ScienceDirect

Nuclear Inst. and Methods in Physics Research, A

journal homepage: www.elsevier.com/locate/nima

Detector block performance based on a monolithic LYSO crystal using a novel signal multiplexing method

Andrea González-Montoro [a,*], Filomeno Sánchez [a], Rosana Martí [a], Liczandro Hernández [a], Albert Aguilar [a], Julio Barberá [b], Juan V. Catret [b], Gabriel Cañizares [a], Pablo Conde [a], Efthymios Lamprou [a], Francisco Martos [a], Sebatián Sánchez [a], Luis F. Vidal [a], Jose M. Benlloch [a], Antonio J. González [a]

[a] *Instituto de Instrumentación para Imagen Molecular (I3M), Centro Mixto CSIC — Universitat Politècnica de València, Camino de Vera s/n, 46022 Valencia, Spain*
[b] *Oncovision, 46022 Valencia, Spain*

ARTICLE INFO

Keywords:
Monolithic scintillators
Silicon photomultipliers
Reduction readout system
Photon depth of interaction (DOI)
Positron emission tomography
Dedicated systems

ABSTRACT

Organ dedicated PET devices provide improved imaging performance when compared to whole body systems. The present study summarizes the test carried out to study a new detector block designed for an organ dedicated PET system. This block includes three novel components namely the scintillator geometry and a retroreflector layer coupled to the entrance face, the photosensor and the readout electronics. We used arrays of 12 × 12 SiPM photosensors with 3×3 mm^2 active area each and a pitch of 4.2 mm. We are proposing a new readout electronics that permits to reduce the 12 row and columns signals to only 8 without significant detector performance degradation. This approach also allows for resolving radioactive sources in the whole volume of the proposed crystal, significantly reducing the edge effect that typically rejects these events.

An overall spatial resolution of about 1.8 mm FWHM is obtained for the whole scintillation volume, with an average energy resolution of 13% FWHM and a photon depth of interaction resolution (FWHM) of 3.7 mm.

1. Introduction

Positron Emission Tomography (PET) systems allow detecting gamma rays emitted indirectly by a positron-emitting source, providing functional images to observe metabolic processes of the patient body. Nowadays, PET systems are increasingly being used in the clinical and preclinical practice due to its value in the diagnosing and study of cancer [1,2]. For some applications, organ dedicated PET systems have shown an improved performance when compared to conventional whole-body PET. Current PET detectors technologies can be improved, namely their spatial, energy, time and depth of interaction (DOI) resolution performance [3,4]. There is currently a significant effort to combine PET and Magnetic Resonance (PET/MRI) in order to supplement the functional images with the anatomical one provided by the MRI [5]. Merging PET and MRI has lead to the use of solid state photosensors such as Silicon Photomultipliers (SiPMs).

A fundamental element composing the detector block is the scintillator crystal that is typically of the type of crystal arrays or continuous blocks [6]. The performance of monolithic scintillators tends to be compromised at the crystal edges [7]. This occurs due to the truncation of the light distribution here. However, when using high granularity photosensors and readout electronics, it is possible to improve the detector block performance, including its edges. The best approach is to read out every single element of the photosensor array, but this typically implies digitizing a huge number of signals. Novel techniques have been lately used to reduce the number of channels to be digitized. One of the oldest approaches is the so-called Anger logic where all photosensor signals are combined using a resistor network and reduced to only 4. An improved method to the Anger logic is to digitize every row and column of the photosensor array, among others [8–11]. This approach has shown good results both using crystal arrays and especially with monolithic blocks since it allows characterization of the light distribution.

Our research is focused on further reducing the number of signals to be digitized, without compromising the detector performance especially at the crystal edges, when using monolithic crystals. For this work, an array of 12 × 12 SiPMs with 3×3 mm^2 active area each and a continuous

---

[*] Corresponding author.
E-mail address: andrea.gm@i3m.upv.es (A. González-Montoro).

https://doi.org/10.1016/j.nima.2017.10.098
Received 18 September 2017; Received in revised form 19 October 2017; Accepted 23 October 2017

Please cite this article in press as: A. González-Montoro, et al., Detector block performance based on a monolithic LYSO crystal using a novel signal multiplexing method, Nuclear Inst. and Methods in Physics Research, A (2018), https://doi.org/10.1016/j.nima.2017.10.098.

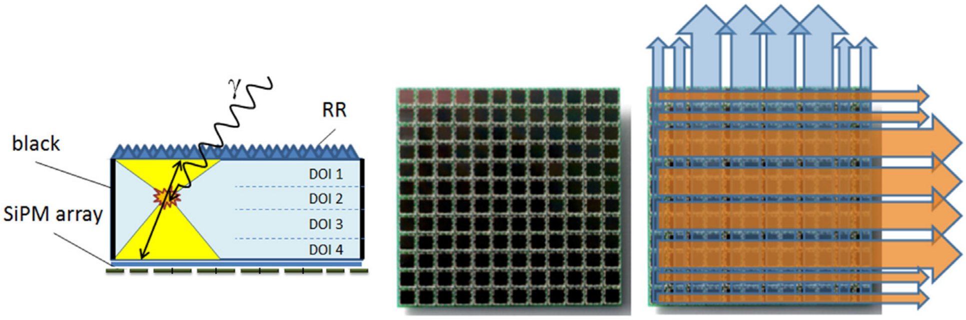

Fig. 1. Left, sketch of the crystal treatment and scintillation light distributions. Center. Photographs of the 12 × 12 SiPM array photosensor. Right. Reduction readout scheme from 12 rows and columns to 8 + 8 signals.

LYSO scintillator with $50 \times 50 \times 15$ mm^3 dimensions were used. We will show the detector block capabilities to resolve events at the crystal edge, using the proposed readout scheme with high performance.

2. Methods and materials

2.1. Scintillator block and optical devices

Two identical detector blocks, working in coincidence, have been used in this study. We have used LYSO scintillation blocks (Proteus, Ohio, US) with all crystal faces polished. The four lateral walls (50×15 mm^2) are black painted and the entrance face (50×50 mm^2) is optically coupled to a retroreflector layer (IMOS Gubela GmbH, Renchen, Germany). This layer is composed by corner cube structures, which are three-side prisms, that allow to bounce back the scintillation light to the photosensor, increasing the collected amount of light and, moreover, preserving its light distribution [12]. Fig. 1 left shows a scheme of the retroreflector behavior. The other large 50×50 mm^2 face (exit face) is coupled to the photosensor using optical grease (BC630, Saint Gobain).

2.2. Photosensor and readout

Each detector block is based on a high-density array of SiPMs from SensL (C-Series, 35 μm cell size) as the one shown in Fig. 1 center. The photosensor matrix is composed of 12 × 12 SiPMs photosensors with 3×3 mm^2 active area each, and a pitch of 4.2 mm. The arrays are operated at a bias voltage of 30 V, 5.5 V over breakdown voltage [13].

In contrast to reading all photosensors individually (144 signals), each SiPM has been connected to a readout circuitry that provides outputs for each row and columns of the photosensor matrix [14].

This approach results on 12 + 12 signals to digitize. Here, the X and Y projection of the light distributions (LD) produced when a gamma photon interacts in the monolithic crystal can be characterized. This means determining the centroid and the depth of interaction (in monolithic crystals) of the impinging photons. We have investigated in this work to further reduce the number of output signals, without significantly degrading the detector block performance. For this, the proposed readout electronics reduces the 12 signals for each projection to only 8, resulting on a total of 8 + 8 outputs per photon impact. This reduction is based on keeping the 2 lateral row and columns, but merging the 8 central ones from 2 to 1. This still preserves the good sampling of the light at the crystal edges and, thus, a good characterization of the effect produced by the truncation of the scintillation light therein. Fig. 1 right schematically shows the concept. The proposed readout scheme makes it possible to reduce the total number of signals of a detector of 12 × 12 photosensors to only 16. The signals are digitized with custom ADC boards (12-bit), see for instance Ref. [12] for more details.

The performance of the proposed detector block module including the reduction readout system, has been compared to a standard 8 × 8 SiPMs photosensors from SenSL (J-Series, 35 μm cell size) with 6×6 mm^2 active area each, and a pitch of 6.33 mm.

3. Methods

The performance of the proposed detector block was evaluated by means of the spatial, energy and DOI resolutions. Both perpendicular to entrance face and lateral incidence measurements to the crystal were carried out. In the case of normal incidence measurements, the reference detector was placed at a distance of 25.8 cm. The module under study was irradiated with an array of 11 × 11 ^{22}Na sources, 1 mm in diameter and 1 mm height each (4.6 mm pitch), placed in front of a Tungsten collimator (24 mm thick, 1.2 mm diameter holes), which was in contact with the crystal.

The LD projections for both X and Y axes are obtained for each impinging 511 keV photon. The centroids of these distributions are calculated using the center of gravity method [15]. The photon impact DOI is estimated by the ratio of the sum of all 8 signals (photon energy, E) to the maximum signal value (E/I_{max}) [16].

During the data processing, each detector area is subdivided in 600 × 600 virtual pixels, and a software collimation of about 2.1° (total aperture) was applied, this means allowing coincidence of the smallest pixel unit with an area of 120 × 120 pixels in the reference detector. An energy window of 15% at the 511 keV peak (434–588 keV) was also applied in the data analysis. Smaller software collimation apertures can be applied, but we have chosen this particular one because it guarantees the best compromise between the detector spatial resolution and the measurement statistics of the analyzed measurement.

3.1. Detector spatial and energy resolution

The measured detector spatial resolution has been evaluated using the imaged 11 × 11 ^{22}Na collimated sources, as shown in Fig. 2 left. We calculated the centroid of each source in channels, as shown in the profile of the top panel in Fig. 2 right, using multi-Gaussian distributions. Calibration from channels to millimeters is done after plotting the real position versus the measured values, followed by a fit to a third order polynomial. After the calibration, it is possible to obtain the detector spatial resolution for each source as the FWHM of the multi-Gaussian fits. The spatial resolution for each source was calculated as the average of the X and Y projections, and as explained below, as a function of the DOI layer.

The energy resolution is determined as FWHM/E$_{\text{centroid}}$ and it was not corrected for possible SiPM nonlinear responses. We can state that the ratio of the 1274/511 keV observed with the ^{22}Na source was about 2.5, for all studied cases. The energy resolution was evaluated for only one quadrant of the detector block (6 × 6 sources) due to the expected symmetry behavior, see Fig. 3 bottom. We have also carried out this for each selected DOI range.

3.2. Edge effect reduction

Traditionally, in PET systems based on monolithic scintillators, events close to the crystal edge [17] are hardly considered for the

Please cite this article in press as: A. González-Montoro, et al., Detector block performance based on a monolithic LYSO crystal using a novel signal multiplexing method, Nuclear Inst. and Methods in Physics Research, A (2018), https://doi.org/10.1016/j.nima.2017.10.098.

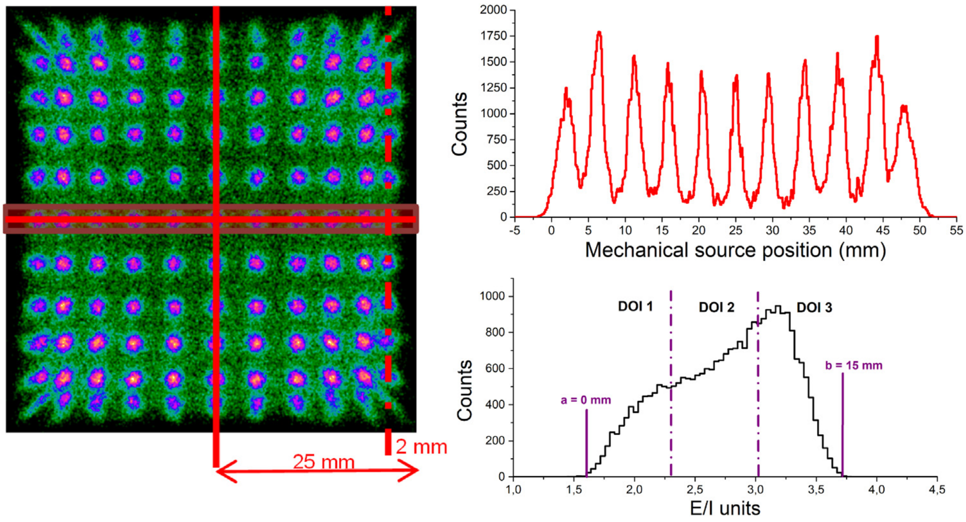

Fig. 2. Left, flood map of the measured 11 × 11 ^{22}Na collimated array source, the pitch between sources is 4.6 mm. Right-top, profile of the central row of sources calibrated into mm, the 11 sources can be well distinguished. Right-bottom, DOI distribution of a source placed at 15 mm from the edge.

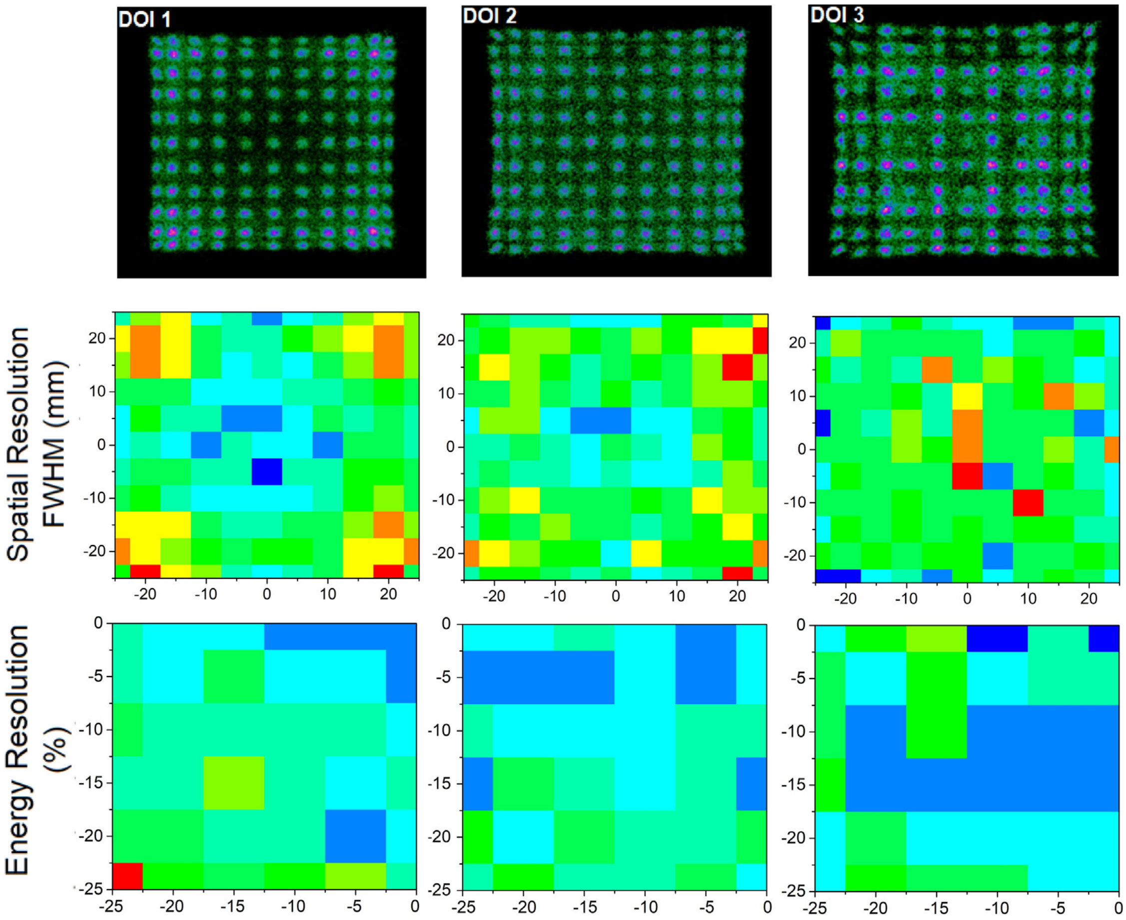

Fig. 3. Top, flood maps using the 15 mm thick LYSO block for three different DOI regions. Center, spatial resolution maps for the mentioned layers. Bottom, energy resolution maps for the mentioned layers. Left, entrance (15–10 mm). Center (10–5 mm). Right, exit (5–0 mm).

image reconstruction due to its poorer characterization. In this work, in order to study how close to the crystal edge can events be properly characterized, a second set of experiments was carried out using normal incidence by means of a pinhole Tungsten collimator with 30 mm thickness and with a drilled hole of 2 mm diameter together with a small size ^{22}Na source (1 mm in diameter, encapsulated in a 1 inch in diameter PMMA disk, current activity about 1 μCi). In these experiments the source was displaced in small steps of 0.5 mm across the entire X axis of the crystal.

3.3. Layer identification and DOI resolution

For each detected photon impact, a single E/I_{max} value is calculated as the average of E/I_{max} obtained for X and Y LD profiles. The

Please cite this article in press as: A. González-Montoro, et al., Detector block performance based on a monolithic LYSO crystal using a novel signal multiplexing method, Nuclear Inst. and Methods in Physics Research, A (2018), https://doi.org/10.1016/j.nima.2017.10.098.

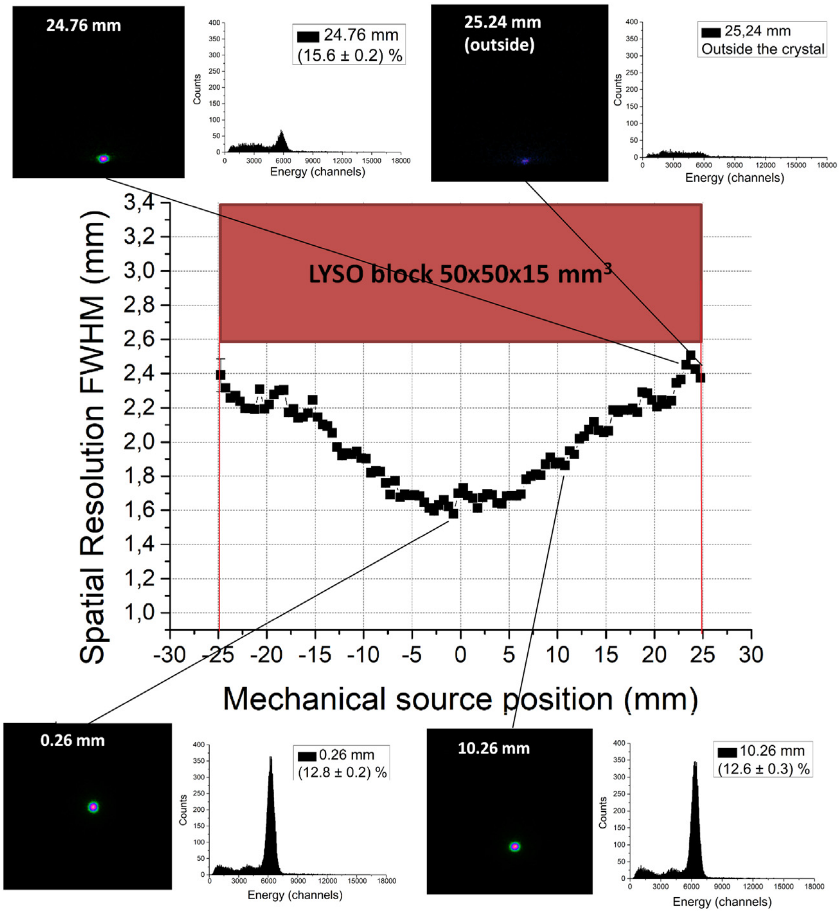

Fig. 4. Examples of the measurements and energy spectra at 0.26 mm, 10.26 mm, 24.76 mm and 25.24 mm (outside the crystal) and measured FWHM values as a function of the known beam position across the crystal surface.

histogram of DOIs for a collimated gamma ray beam impinging normal to the detector can be understood as a profile distribution that appears as the convolution of a Gaussian functions and the exponential decay of the photon attenuation [18]. Assuming that the intrinsic DOI resolution is constant along the crystal depth, an analytical expression can be defined for the DOI distribution [12]. The DOI histograms have been used for the DOI calibration and DOI region identification, see Fig. 2 bottom right. Following this, each source (121 ROIs) is properly DOI calibrated into metric units. When required, we have split the data into three DOI regions, namely DOI1 (entrance), DOI2 and DOI3 (exit), which correspond to crystal depths of 15–10 mm, 10–5 mm and 5–0 mm (near the photosensor), respectively. This allows obtaining three different flood maps, as shown in Fig. 3 top.

To provide accurate DOI resolution values, lateral incidence measurements were carried out in steps of 1 mm, also using the pinhole collimator. ROIs of 4 × 4 mm^2 were carried out at step distances of 5 mm from the crystal edge, reaching the crystal center. This allows one characterization of the DOI in the whole volume of the scintillator.

4. Results

4.1. Detector spatial and energy resolution

Fig. 3 top shows the flood maps for the 11 × 11 collimated sources as a function of the DOI layer, as explained above. We can observe a stronger compression effect for impacts occurring in the upper layer (DOI1), where there is a stronger LD truncation. In the DOI3 (exit) layer we observe a pattern of the collimated sources. This is produced by the reduction readout system, for which the central area has a pitch that is twice the one at the edge regions. Thus, for events really close to the photosensor, in which the LDs are narrower, an irregularity can be observed due the mentioned change in pitch

We obtained average (X and Y projections) FWHM measured values of 1.8 ± 0.2 mm, 1.9 ± 0.2 mm and 1.9 ± 0.3 mm for the DOI1, DOI2 and DOI3 regions, respectively. As it can be observed in the central row of panels in Fig. 3, the region closer to the entrance face of the scintillator (DOI1) depicts a worsening of the spatial resolution nearing the detector block corners due to the accused LD truncation. This behavior is opposite in the layer closer to the photosensor (DOI3), where poorer results are observed at the center block due to the larger pitch size. Yet an almost homogeneous spatial resolution is obtained for the whole scintillator volume.

The energy resolution has also been evaluated as a function of the different DOI layers. The panels of Fig. 3 show these results. We determined average values of 13.1 ± 0.7%, 12.7 ± 0.7% and 12.6 ± 0.4%, for the DOI1, DOI2 and DOI3 regions, respectively. This shows that the energy resolution, as well as the spatial resolution, is almost constant for the whole scintillator volume.

4.2. Edge effect reduction

The panels in Fig. 4, show four examples of flood maps and corresponding energy spectra for source impacts at about 0.26, 10.26, 24.76 and 25.24 mm (outside the crystal area) from the crystal center across the X axes. The energy spectra allow ensuring that the source was indeed impinging or not in the scintillation volume. Events as close as 0.24 mm to the crystal edge (24.76 mm from the center) are well resolved, with an energy resolution of 15.6 ± 0.2%. The energy resolution improves up to 12.8 ± 0.2% at the center region, as expected. The plot in Fig. 4 shows the measured FWHM values as a function of the

Please cite this article in press as: A. González-Montoro, et al., Detector block performance based on a monolithic LYSO crystal using a novel signal multiplexing method, Nuclear Inst. and Methods in Physics Research, A (2018), https://doi.org/10.1016/j.nima.2017.10.098.

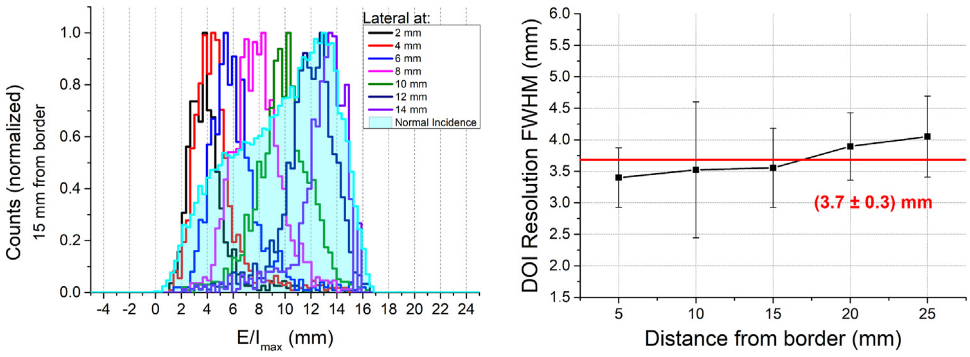

Fig. 5. Left, dependency of E/I versus DOI position. Right, DOI resolution (FWHM) as a function of the impact position in the crystal. (For interpretation of the references to color in this figure legend, the reader is referred to the web version of this article.)

known beam position across the crystal surface. On average, a spatial resolution (FWHM) of 1.9 ± 0.2 mm is obtained without correcting for the source size and without filtering for DOI impacts, for the [−23, 23] mm range. We also used here an electronic collimation of 2.1°. The spatial resolution improves towards the center (1.6 mm) due to better sampling of the scintillator light distribution.

4.3. DOI resolution

The left panel in Fig. 5 shows the plot of some of the histograms obtained at 15 mm from the crystal edge through normal incidence (blue area) and overlapping with this the DOI distributions found for the lateral impinging beams. The calibration curves with the known beam positions and the measured E/I_{max} value exhibited in general a good linearity.

Once the calibration into metric (mm) units is performed, the profiles obtained through lateral incidence, for each distance from the edge, are fitted to Gaussians distributions, whose FWHMs provide direct information on the DOI resolution. The true average FWHM$_{\mathrm{DOI}}$ has been calculated by weighting the data corresponding to different interaction depths with the theoretical contribution given by the exponential photon attenuation law. The right plot in Fig. 5 shows the FWHM$_{\mathrm{DOI}}$ results as a function of the distance from the crystal edge. Best FWHM$_{\mathrm{DOI}}$ are observed near the crystal edge, namely 3.4 mm at 5 mm from the edge. This value degrades to only 4 mm at the crystal center. This degradation might be explained by three reasons. First, there is a stronger truncation effect at the edge that typically tends to underestimate the results. Second, towards the crystal center there is a significant loss of statistics due to the exponential attenuation of gamma rays in the LYSO block. Third, in the central region the sampling is wider, which can also lead to a slightly worse sampling in this area. Nevertheless, considering all the positions, an average DOI resolution of 3.7 ± 0.3 mm was estimated.

4.4. Comparison with standard SiPM arrays

The detector performance has been compared to two additional photosensors and readout electronics schemes, namely (i) a standard 12 × 12 SiPM array (pitch 4.2 mm) and 12 + 12 row and column readout SiPM signals and (ii) a standard 8 × 8 SiPM array (pitch 6.33 mm) and 8 + 8 readout signals. For this test, a 9 × 9 ^{22}Na array sources (1 mm size) was used, the pitch between sources was 5 mm. Fig. 6, shows the flood maps for the acquired data on the top. Below these maps we have done an idealization of the SiPM rows/columns size. The ^{22}Na array was 2.5 mm off-center.

The profiles in Fig. 6 bottom show that when using our current approach and case (i), all 81 sources were clearly resolved, including those located at the edges, as expected. However, for case (ii) where the SiPMs pitch at the edge is 6.33 mm, the last line of sources is almost indistinguishable. Following the procedure describe in the methods section, we have determined the average spatial resolution for the three cases, obtaining values of 1.8 ± 0.2 mm, 1.9 ± 0.1 mm and 2.0 ± 0.3 mm for cases (i), current approach, and (ii), respectively. Concerning the energy we measured values of 14.2 ± 0.8%, 14.1 ± 0.7% and 11.2 ± 0.4%, respectively. The improvement in case (ii) for the energy resolution is due to the fact that the active area coverage of this photosensor is significantly larger of about 92% compared to the 12 × 12 SiPM arrays that result an active area of only 52%.

5. Conclusions

We have tested a detector block using a LYSO crystal with 50 × 50 mm^2 size and 15 mm thickness, using a retroreflector layer at the entrance scintillator face. A SiPM array made by 12 × 12 elements is merged to a novel readout electronics only providing 8 + 8 row and column signals without limiting the detector performance. Average performance parameters are a measured spatial resolution FWHM of 1.8 mm (without corrections for source size), a DOI resolution FWHM of 3.7 mm and an energy resolution of 13% FWHM. This overall detector bock performance would allow one building PET scanners, for instance organ dedicated systems, such as brain or breast imaging. These systems suggest resolutions in the whole FOV in the 1–2 mm range with ring diameters typically not exceeding 25 cm, which can only be accomplished by having a DOI resolution better than 5 mm.

Moreover, the proposed readout allows one to resolve impact near the crystal edge as in the case when digitizing all 12 + 12 SiPM row and column signals but it improves the performance when compared with the direct 8 × 8 SiPM readout. Using the proposed readout electronics but determining the planar and DOI photon coordinates using more elaborated methods such as least squares, neuronal networks or maximum likelihood approached, to name but a few, could improve the impact determination accuracy at the crystal edges.

In contrast with previous works where events close to the crystal edge were not considered, the proposed detector block including the readout, makes it possible to use the whole volume of the monolithic block with high spatial and energy resolution values. This in turn translates into a significant increase in the PET system sensitivity.

Acknowledgments

This work was supported by the Spanish Ministerio de Economía, Industria y Competitividad under Grant Nos. FIS2014-62341-EXP and TEC2016-79884-C2-1-R. This project has also received funding from the European Union's Horizon 2020 research and innovation programme under grant agreement No. 711323. This project has received funding from the European Research Council (ERC) under the European Union's Horizon 2020 research and innovation programme (grant agreement No. 695536).

Please cite this article in press as: A. González-Montoro, et al., Detector block performance based on a monolithic LYSO crystal using a novel signal multiplexing method, Nuclear Inst. and Methods in Physics Research, A (2018), https://doi.org/10.1016/j.nima.2017.10.098.

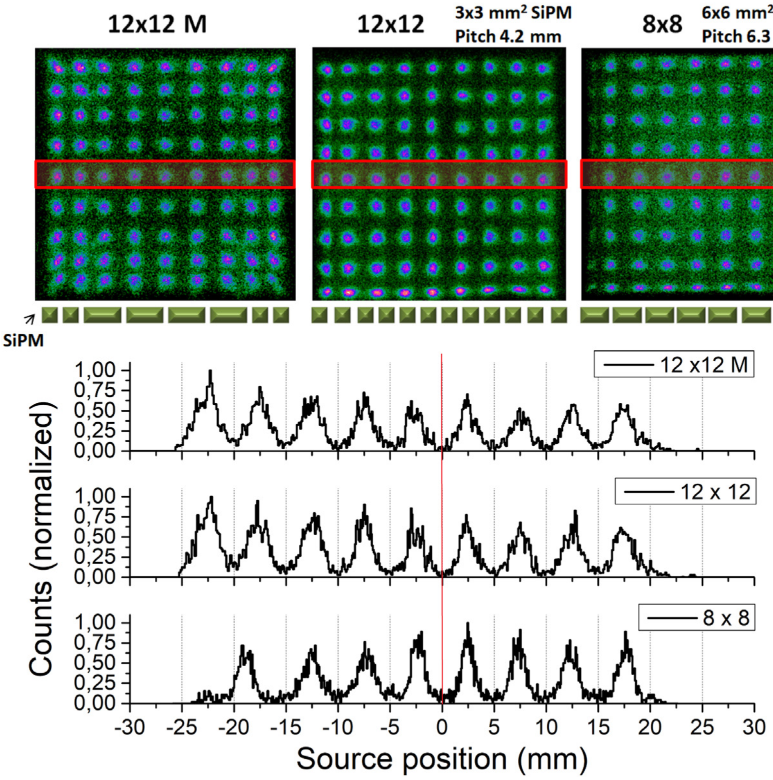

Fig. 6. Top, flood maps obtained when using (left) the described 12 × 12 photosensor and the reduction readout electronics, (center) the standard 12 × 12 photosensor and (right) the standard 8 × 8 photosensor. Bottom, profiles for one row of sources using the mentioned approaches, notice that the array was shifted 2.5 mm to the edge.

References

[1] U. Nestle, W. Weber, M. Hentschel, A.L. Grosu, Phys. Med. Biol. 54 (2009) R1–R25.
[2] J.B. Bomanji, D.C. Costa, P.J. Eii, Lancet Oncol. 2 (2001) 157–164.
[3] Tom K. Lewellen, Phys. Med. Biol. 53 (2008) R287–R317.
[4] S. St. James, Y. Yang, S.L. Bowen, J. Qi, S.R. Cherry, Phys. Med. Biol. 55 (2010) N63–N74.
[5] H.F. Wehrl, M.S. Judenhofer, S. Wiehr, B.J. Pichler, Eur. J. Nucl. Med. Mol. Imaging 36 (2009) 55–68.
[6] C.S. Levin, Nucl. Instrum. Methods Phys. Res. A 497 (2003) 60–74.
[7] M.C. Maas, D.R. Schaart, D.J. Van der Laan, P. Bruyndonckx, C. Lemaître, F.J. Beekman, C.W.E. Ejik, Phys. Med. Biol. 54 (7) (2009) 1893–1908.
[8] V. Popov, S. Majewski, A.G. Weisenberg, IEEE Nucl. Sci. Symp. Med. Imaging. Conf., Vol. 3, 2003, pp. 2156–2159.
[9] V. Popov, S. Majewski, B. Welch, Nucl. Instrum. Methods A. 567 (2006) 319–322.
[10] P. Olcott, J. Talcott, C. Levin, F. Habte, A. Fourdray, Compact readout electronics for position sensitive photomultiplier tubes, IEEE Trans. Nucl. Sci. 52 (2005).
[11] S. Majewski, J. Proffitt, A. Stolin, R. Raylman, IEEE Nucl. Sci. Symp. Conf. Record., 2011, pp. 3939–3944.
[12] A. Gonzalez-Montoro, A. Aguilar, G. Cañizares, P. Conde, L. Hernandez, L.F. Vidal, M. Galasso, A. Fabri, F. Sanchez, J.M. Benlloch, IEEE Trans. Rad. Plasm. Med. Sci. 1 (2017) 229–237.
[13] A.J. González, et al., Performance study of a wide-area SiPM array, ASICs controlled, IEEE Trans. Nucl. Sci. 62 (2015) 19–26.
[14] A.V. Stolin, S. Majewski, G. Jaliparthi, R.R. Raylman, J. Proffitt, IEEE Trans. Nucl. Sci. 61 (2014) 2433–2438.
[15] R. Pani, A.J. Gonzalez, M. Bettiol, A. Fabbri, M.N. Cinti, E. Preziosi, C. Borrazzo, P. Conde, R. Pellegrini, E. Di Castro, J. Instrum. 10 (2015) C06006.
[16] R. Pani, S. Nourbakhsh, P. Pani, P. Bennati, S. Lo Meo, M. Nerina Cinti, R. Pellegrini, B. Cassano, M. Bettiol, R. Scafe, Proc.IEEE NSS-MIC, 2011. pp. 3386–3389.
[17] L. Zhi, M. Wedrowski, P. Bruyndoncx, G. Vandersteen, Nonlinear least-squares modeling od 3D interaction position in a monolithic scintillator block, Phys. Med. Biol. 55 (2010) 6515.
[18] C.W. Lerche, A. Ros, V. Herrero, R. Esteve, J.M. Monzo, A. Sebastia, F. Sanchez, A. Munar, J.M. Benlloch, IEEE Trans. Nucl. Sci. 55 (2008) 1344–1351.

Please cite this article in press as: A. González-Montoro, et al., Detector block performance based on a monolithic LYSO crystal using a novel signal multiplexing method, Nuclear Inst. and Methods in Physics Research, A (2018), https://doi.org/10.1016/j.nima.2017.10.098.

4.4. Highly improved operation of monolithic BGO-PET blocks

Authors: Andrea Gonzalez-Montoro, Filomeno Sanchez, Stan Majewski, Silvia Zanettini, Jose M. Benlloch and Antonio J. Gonzalez.

Published: Journal of Instrumentation, Vol 12, C11027, 2017. https://doi.org/10.1088/1748-0221/12/11/C11027

Impact Factor: 1.30

Summary:

Some of the first PET scanners designs made use of BGO crystals. Advantages in BGO blocks are their high effective atomic number ($Z_{eff} = 74$), high density (ρ = 7.13 g/cm^3), they are easier to be grown in comparison with fast Lutetium-based scintillators. Moreover, they present a short attenuation length (1.1 cm for 511 keV gamma-rays). As a disadvantage, BGO scintillators have long decay times (300 ns) and low light yield (10 photons/keV$\cdot \gamma$). These factors have discouraged researchers to use BGO blocks in new PET designs.

BGO scintillators are cheaper than LYSO crystals and therefore might be good candidates for building scanners requiring high volume of scintillation material such as total body PET scanners. This article develops the idea of reintroducing BGO scintillators in the form of monolithic blocks. To improve the light yield and performance of those BGO blocks, a retroreflector layer bouncing back the scintillation light to the photosensor, and a nanopattern structure increasing the scintillation light extraction were added to the entrance and exit face of the crystal, respectively. The nanopattern structure consists of a thin layer of a specific high refractive index material shaped with a periodic pattern, that allows the extraction of some scintillation photons that are striking the scintillator exit face at an angle larger than the particular critical angle. Without the nanostructure, that photons would be internally reflected. Since the photon exiting angle is changed, the light distribution profile is modified

A 50 × 50 × 15 mm^3 BGO monolithic block with black-painted lateral walls was used. Four different configurations were tested, namely 12 × 12 and 16 × 16 SiPMs arrays (3 × 3 mm^2 each), with or without a nanopattern treatment to the crystal exit face. Better energy performance was achieved when using the 16 × 16 SiPMs due to the larger active area of the photosensor (92% compared to 52% for the 12 × 12). Energy resolution values of 20% were obtained with the approach using the nanopattern structure and the retroreflector layer. Apparently, the nanostructure slightly breaks the light distribution profile worsening the spatial and DOI resolution. Therefore, considering all three parameters, spatial energy and DOI resolution, the overall best detector performance is achieved for the 16 × 16 SiPMs array and the retroreflector layer but without including the nanopattern at the exit face.

Published by IOP Publishing for Sissa Medialab

Received: *September 6, 2017*
Revised: *October 20, 2017*
Accepted: *November 10, 2017*
Published: *November 24, 2017*

19th International Workshop on Radiation Imaging Detectors
2–6 July 2017
AGH University of Science and Technology, Kraków, Poland

2017 JINST 12 C11027

Highly improved operation of monolithic BGO-PET blocks

A. Gonzalez-Montoro,[a] F. Sanchez,[a] S. Majewski,[b] S. Zanettini,[c] J.M. Benlloch,[a] and A.J. Gonzalez[a,1]

[a] *Instituto de Instrumentación para Imagen Molecular (I3M),*
Centro Mixto CSIC — Universitat Politècnica de València,
Camino de Vera s/n, 46022 Valencia, Spain
[b] *Radiology and Biomedical Engineering, University of Virginia,*
480 Ray C Hunt Drive, 22903 Charlottesville, U.S.A.
[c] *NAPA Technologies,*
Boulevard Gambetta 12, 10000 Troyes, France

E-mail: agonzalez@i3m.upv.es

Abstract: In PET scanners both scintillation crystals and photosensors are key components defining the system's performance and cost. Original PET systems used BGO or NaI(Tl) scintillators but achieved limited performance due to its slow decay and relatively low light output. Moreover, NaI(Tl) has low stopping power for 511 keV annihilation photons. In this study we report the possibility to reintroduce BGO crystals, and in particular in the form of monolithic blocks, especially suitable for low-dose large-size PET scanners, offering significantly improved sensitivity at a highly reduced cost compared to LYSO type fast scintillators.

We have studied the performance of a monolithic BGO block as large as $50\times50\times15\,\mathrm{mm}^3$ with black-painted lateral walls to reduce lights spread, enabling accurate photon depth of interaction (DOI) measurements. A directional optical layer, called retro-reflector, was coupled to the entrance face bouncing back the scintillation light in the direction of the emission source and, therefore, adding to the light signal while preserving the narrow light cone distribution. Four configurations namely 12×12 and 16×16 SiPM arrays (3 mm × 3 mm each) as photosensors, with or without a nanopattern treatment at the crystal exit face, have been studied. This structure consisted of a thin layer of a specific high refractive index material shaped with a periodic nanopattern, increasing the scintillation light extraction. The readout returned information for each SiPM row and column, characterizing the X-Y light distribution projections. We have studied the detector spatial resolution

---

[1] Corresponding author.

https://doi.org/10.1088/1748-0221/12/11/C11027

using collimated ^{22}Na sources at normal incidence. The DOI resolution was evaluated using collimated gamma beams with lateral incidence.

The overall best detector performance was obtained for the 16×16 SiPM array offering higher readout granularity. We have determined the spatial resolution for 3 separated DOI layers, obtaining the best results for the DOI region near to the photosensor.

KEYWORDS: Gamma camera, SPECT, PET PET/CT, coronary CT angiography (CTA); Photon detectors for UV, visible and IR photons (solid-state) (PIN diodes, APDs, Si-PMTs, G-APDs, CCDs, EBCCDs, EMCCDs etc)

Contents

1 Introduction

Positron Emission Tomography (PET) scanners were initially developed using scintillation crystals such as Bismuth Germanate (BGO) or NaI. BGO is especially interesting for this purpose because of its short attenuation length (1.1 cm for 511 keV gamma rays), due to its high effective atomic number and high density. BGO crystals are rather easy to be grown, especially when compared to Lutetium-based fast scintillators (LYSO, LSO). However, BGO lacks high light yield and it has long decay time (10 photons/keV $\cdot\gamma$ and 300 ns, respectively) compared to these new fast scintillators that have high light yields (about 32 photons/keV $\cdot\gamma$) and much shorter decay times (~40 ns). These comparatively poor BGO parameters have discouraged investigation of new BGO based PET designs. However, BGO is significantly cheaper than LYSO (about a factor 3–4 concerning the cost of the row material) and therefore, when dealing with large numbers of crystals as in systems for large animals or following the concept of total body PET scanners [1], BGO might still become a practical alternative.

In PET scanners both scintillation crystals and photosensors are key components defining the system's performance, and also its cost. Nowadays, PET systems have improved quality images arising from higher detector intrinsic performance such as spatial, energy and time resolution. LYSO is the common scintillation material in current developments. Spatial resolution improved due to higher photosensor and readout granularity but also higher granularity of the typically used crystal arrays. Energy resolution has improved using better scintillators (higher light yield) but also due to better photosensors in terms of quantum efficiency.

BGO crystals have been recently shown to provide accurate spatial and energy resolutions using high photosensor and high readout granularity [2]. Initial studies carried out by our team have shown BGO based detector imaging capabilities high enough to resolve crystal arrays of 30×30 elements with 1.67 mm pitch (6 mm height) and energy resolutions as good as 12% [3]. In a prior study using larger pixels of 2 mm, it was also shown the system capability to provide photon depth of interaction (DOI) information using two staggered crystal arrays (10 mm + 10 mm total thickness) with an energy resolution in the 16% range [4].

In the current study we show the capability of monolithic BGO crystals, to be used in low-dose large-size scanners, with high overall performance, including photon depth of interaction (DOI) [5–7]. Figure 1 left shows a realization of a large aperture PET. Monolithic crystals have

2017 JINST 12 C11027

some advantages and disadvantages compared to the widely implemented crystal arrays. On one hand, using position sensitive photosensors and optimized readout electronics [8], it is possible to get a continuous good estimate of the 511 keV photon's DOI. However, in crystal arrays the DOI codification is typically limited to the scintillator layer thickness [9, 10]. Most important for the present application, the monolithic solution is significantly cheaper than high granularity crystal arrays (with pixels smaller than 1.5 mm). On the other hand, since the scintillation light is spread among many photosensor elements, energy resolution tends to degrade compared to crystal arrays, and the timing information of the impinging annihilation photon is rather more complex to extract.

New implementations of BGO crystals for large aperture scanners have also been suggested by other groups [11], but using BGO crystal arrays instead of a continuous monolithic block per detector as described in this report.

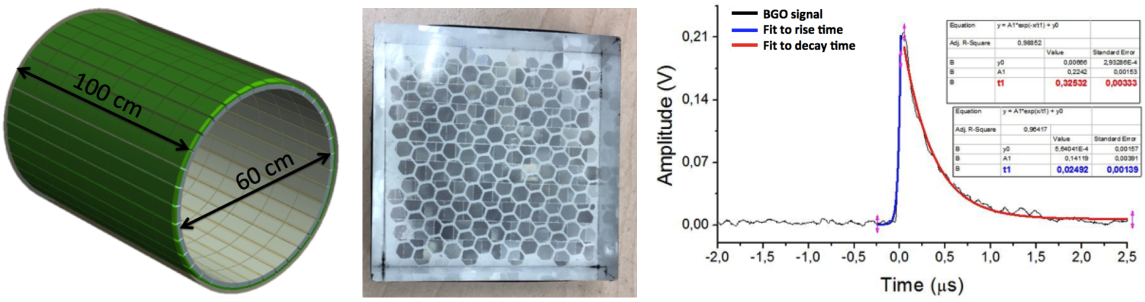

Figure 1. Left: example of realization of a 1 meter PET scanner suitable for imaging of a human torso or of large animals (the scintillation crystals are represented in white colour, the SiPM arrays and associated electronics in green). Centre: photograph of the 5 cm × 5 cm monolithic BGO, showing the RR structure at the entrance face. Right: pulse shape of the BGO block. The short blue and long red fitted curves represent the rise (25 ns) and decay times (325 ns) of trigger signal (energy proportional), respectively.

2 Materials and methods

2.1 Materials

The BGO monolithic block used in the present study has dimensions of 50 mm × 50 mm × 15 mm with black-painted lateral walls (50 mm × 15 mm), see photograph in figure 1 center. A novel directional optical barrier (RR) is coupled to the entrance face bouncing back the scintillation light in the direction of the emission source and, therefore, adding signal while preserving the narrow light distribution [8]. This RR structure is composed from several so-called corner-cubes. Those are made of three-sided prisms that reflect light back directly towards the source, but displaced by a little distance (120 µm range in our case). These structures are aluminized in order to achieve specular reflection.

Two arrays of SiPMs with 3 mm × 3 mm active area per SiPM have been used as photosensor (SensL, Cork, Ireland). One includes 12 × 12 SiPMs whereas the other is built from 16 × 16 SiPMs (see figure 2 right), with both arrays covering about 5 cm × 5 cm total active area. The SiPMs in the case of the 16 × 16 configuration are custom mounted with a pitch of 3.26 mm (total package size 3.16 mm × 3.16 mm) and are similar to the J-Series type [8]. This configuration results on an active area coverage of about 92%. In the case of the 12 × 12 SiPMs arrays, we tested standard arrays of their C-Series (4.2 mm pitch). Here, due to the larger pitch, compared to the previous configuration, the active area coverage reduces to about 52%. Both, SiPM series performed very similarly; as in terms of dark count rates, gain, voltage bias, etc. . . In all experiments carried out, the detector blocks were kept at a stable temperature of about 20° C using temperature controlled air-cooling. The SiPMs were biased at about 30V.

The readout returned digitized (12 bit precision) information for each SiPM row and column, and that translates to 12+12 and 16+16 signals, respectively. Each row and column signal was charge integrated with a time gate of 600 ns (see figure 1 right for a signal example). We have already shown that this value is optimal for our data acquisition system [3, 4]. This row-column readout approach makes it possible to characterize the scintillation X-Y light projections.

One of the tests for each SiPM array configuration included a nanopattern structure at the scintillator exit surface [12]. The nanopattern (NP) consists of a periodic pattern of high refractive index TiO_2 pillars. The thin layer TiO_2 diffraction grating has a 1 µm period (0.5 µm base diameter and 0.6 µm height) and has been fabricated by nano-imprint lithography on the whole 50 mm × 50 mm exit face of the BGO crystal. It allows a better extraction of photons from the scintillator towards the SiPM array, due to the optical principles of diffraction and refractive index matching. Alternative approaches for this nano-imprint have also been tried with BGO crystals. A three-layer graded-refractive-index antireflection coating was prepared by sol-gel technology. A light intensity enhancement as high as 15.9% was observed when compared with the reference sample without coating [13].

2.2 Methods

We have studied the detector spatial resolution both planar and DOI, as well as the energy resolution using two detector blocks operating in coincidence (with 9 ns coincidence window), as shown in figure 2 left. We have used mechanical (array of 1.2 mm drilled holes in a 24 mm thick Tungsten plate) and software collimated via coincidence requirement ^{22}Na sources (cylinders of 1 mm in diameter and 1 mm high) at normal incidence for the investigation of the planar coordinates. The software collimation was 2.1 degrees total aperture. The ^{22}Na sources were mounted with a pitch of 5 mm, in a 9 × 9 array (aligned with the drilled holes in the Tungsten collimator) and encapsulated in PMMA. The Tungsten collimator is attached to the detector under study, and the radioactive sources are placed in front of the collimator.

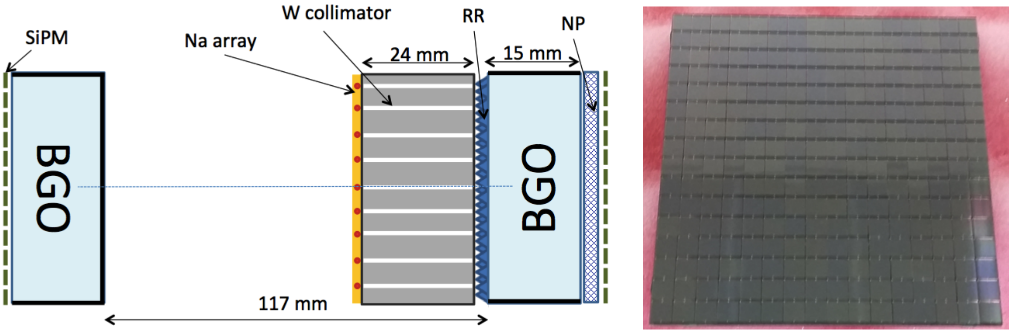

Figure 2. Left: 2D sketch of the set-up. Detectors are placed opposite to each other at a distance of about 117 mm. Air forced cooling is applied to keep a stable 20^{o}C temperature of the detector blocks. Right: photograph of the 16 × 16 SiPM array with 3.26 mm pitch and 3 mm × 3 mm active surface SiPMs.

The DOI performance was evaluated using focused 511 keV beams with lateral incidence to the crystal, see the sketch in figure 3 top-left. The lateral collimated beam, impinging the BGO block, was positioned at 2.5 mm, 7.5 mm and 12.5 mm distance from the photosensor. These measurements allowed us to determine the block DOI resolution through the FWHM of those distributions. The DOI position is estimated using the average ratio of the summed signal (proportional to the total event energy) to the maximum digitized SiPM row/column (E/I_{max}) [7]. The energy resolution (in percentage) was evaluated through the ratio of the FWHM of the 511 keV energy peak to its centroid. The energy linearity of the system was confirmed by measuring the ratio of the 1274 keV and 511 keV peaks appearing when using ^{22}Na sources (in single acquisition mode).

3 Results

We tested four configurations, namely 12 × 12 or 16 × 16 SiPM, with and without NP crystal treatment. They are labelled as 12 × 12 RR, 12 × 12 RR+NP, 16 × 16 RR and 16 × 16 RR+NP, respectively. Figure 3 top-right shows a flood map (reconstructed map of all recorded events) for the 16 × 16 RR+NP configuration when carrying out the lateral incidence experiment. The intensity of the 511 keV photons beam is exponentially attenuated from the crystal edge entrance point towards the scintillator depth as it is observed here. The map in this figure exhibits the so-called edge effect. The scintillation light is truncated inside the monolithic block, especially at the edges. Therefore, when using center of gravity approaches to determined the reconstructed map, there is a miss positioning of the photon impact coordinates towards the crystal center.

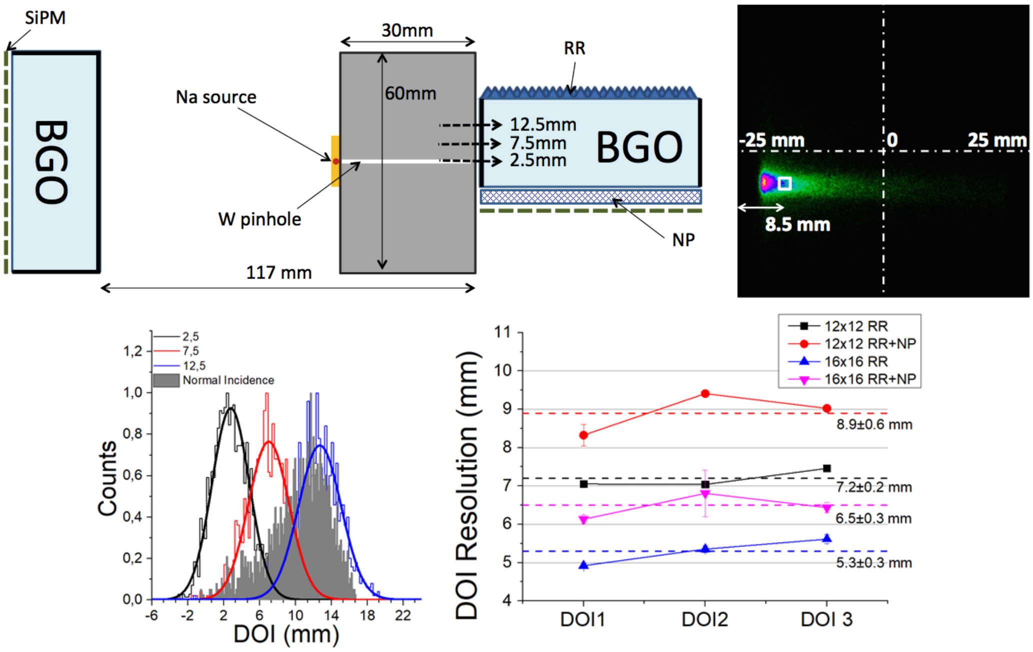

Figure 3. DOI results. Top-left: sketch of the set-up for DOI resolution measurements. Top-right: flood map for the measurement at 2.5 mm from the photosensor showing the exponential 511 keV beam attenuation behavior entering through the crystal edge at left, using the 16 × 16 RR+NP configuration. Bottom-left: normalized distributions for the lateral impinging beams, overlaid with a distribution for a photon beam normally incident on the crystal (grey filled pattern) and measured at the same ROI. Bottom-right: DOI resolution curves (FWHM) as a function of the DOI for the four experimented configurations.

2017 JINST 12 C11027

The DOI resolution is studied for regions of interest (ROI) of approximately 3 mm × 3 mm were selected, at a reference distance of about 8.5 mm from the crystal edge. ROIs deeper into the crystal, towards the centre, lacked of good measurement statistics. Nevertheless, we do not expect significant resolution improvements further towards the scintillator centre, as shown elsewhere for LYSO [8]. For the four configurations, the obtained centroids in arbitrary units (E/I_{max}) are linearly calibrated and converted into millimetres. Next, the DOI resolution (FWHM) is obtained as the average of the Gaussian FWHM found for the three positions (see figure 3 bottom-left).

Figure 3 bottom-right shows the calibrated DOI resolution (in mm) as a function of the lateral impinging position (DOI1 corresponds to the furthest crystal layer at 12.5 mm from the photosensor surface). Overall, we observe small dependence of the DOI FWHM as a function of the DOI. The dashed lines depict the average value for each configuration. As expected, better results are obtained for the large active coverage SiPM arrays (the 16 × 16 structure). The best DOI FWHM of 5.3 ± 0.3 mm was obtained for the 16 × 16 approach without NP, degrading to 8.9 ± 0.6 mm for the 12 × 12 array with NP. These results suggest that dividing our data into 3 DOI layers is a good compromise between statistics and performance.

Spatial resolution of the detector blocks was studied with the aforementioned collimated ^{22}Na sources. The DOI distribution depends on the XY impinging position due to the different light distribution truncations. Therefore, we had to convert the DOI values into millimeters for each of the 81 impinging beam positions. This allowed us to effectively separate the data into the 3 DOI layers. Figure 4 shows the three flood maps corresponding to the 81 sources. Based on these data we have studied the detector spatial resolution as a function of X-Y position and the DOI layer. DOI1 layer is the one closest to the crystal entrance, whereas DOI3 corresponds to the 5 mm region closest to the photosensor. The spatial resolution for each layer is calculated as the average of the FWHM obtained for the 9 measured Gaussian distributions for a central X and Y projections. Figure 4 bottom-left depicts the projection of the central row of sources for the three layers and for the 16 × 16 case without NP.

As before, better spatial resolution results are obtained for the larger photosensor coverage variants with 16×16 SiPMs, namely 2.1 ± 0.4 mm (without NP) and 2.3 ± 0.5 (with NP). Figure 4 at bottom-right shows the spatial resolution for the three DOI layers. The dashed lines show again the average value. When using the 12 × 12 array, the results slightly worsen to 2.4 ± 0.6 mm. It should be noted that the spatial resolution improves with the crystal depth due to the reduced scintillation light cone truncation. In the 16 × 16 case without NP, we found 2.5 ± 0.4 mm at the entrance layer (15–10 mm), 2.2 ± 0.4 mm in the middle layer (10–5 mm) and 1.6 ± 0.4 mm (5–0 mm, layer near the photosensor).

Concerning energy resolution, it improved when using the NP, most likely due to the increase of the amount of extracted scintillation light. Best results were also obtained for the 16 × 16 SiPM configurations. Here, for the 16×16 case with NP, average energy resolution results of 19.7 ± 0.7 % FWHM were obtained. For the same array but without NP, a value of 21.8 ± 0.5 % was found. Values above 25 % were always measured when the 12 × 12 array was used. Figure 5 shows, at the left, the energy spectra for the 16 × 16 case with NP for a centred ROI (15 mm × 15 mm) in the crystal and for the three DOI layers. On the right side of this figure, energy resolution for the 4 cases as a function of the DOI layer is plotted. The use of the RR at the entrance crystal face helps returning a rather uniform energy dependency with the crystal depth. The dashed lines are the calculated average values across the 3 layers.

2017 JINST 12 C11027

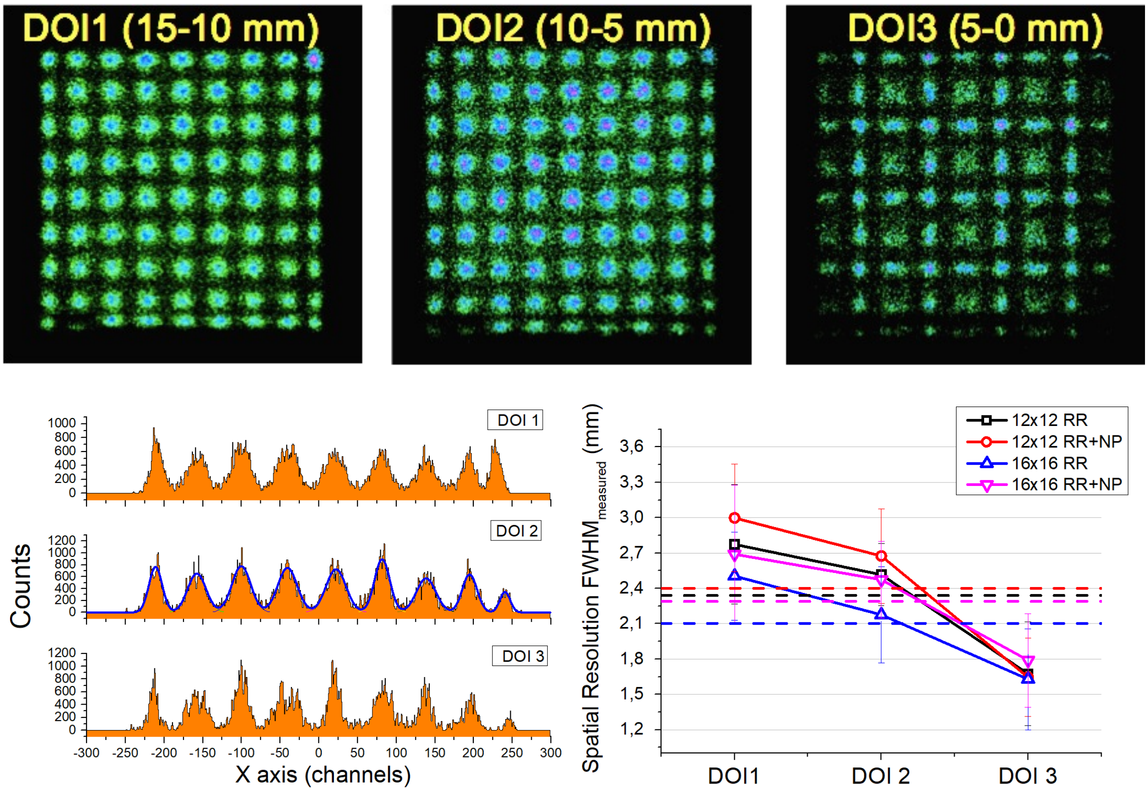

Figure 4. Top: flood maps for the 16 × 16 case without NP as a function of the DOI layer. Bottom-left: projection of the centre row of sources for each DOI layer. The blue curve shows the fit carried using a multi-Gaussian distribution to the profile for DOI2. Bottom-right: average spatial resolution FWHM as a function of the DOI layer for the four configurations.

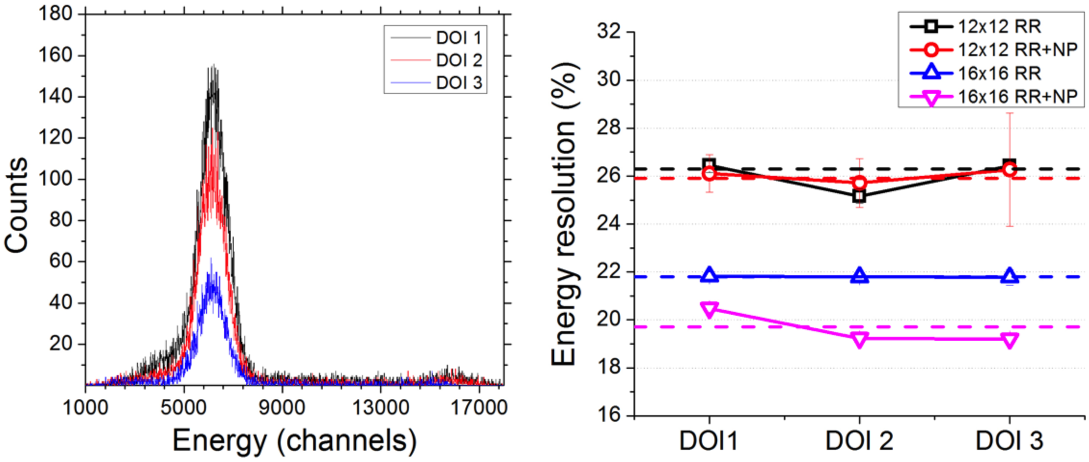

Figure 5. Left: energy spectra for the 16 × 16 case without NP for the three DOI layers. Right: energy resolution as a function of the DOI layer and for the four studied cases.

4 Conclusions

In this report we demonstrate the overall good performance of monolithic BGO blocks with large dimensions of $50 \times 50 \times 15\,\mathrm{mm}^3$. The main field of application would certainly be in the design of low-rate PET. However, other advantages as the increased stopping power and photofraction when compared to Lutetium-based scintillators make this option very attractive. The main motivation of this work is a new opportunity to build PET systems requiring large volume of scintillators at a moderate cost. We have recently showed the possibility of a dual-layer BGO block using crystal arrays [4]. Here, we have also demonstrated the possibility of using monolithic blocks achieving almost 5 mm FWHM in DOI resolution.

In the tested configurations, the crystal treatment included an optical retro-reflector layer that improves the detector block performance as shown in previous works [8]. This reflector certainly contributed to the achieved good performance. Without this reflector, an energy resolution nearing 30% was achieve for the 12×12 case without NP (this result was not shown in this report). Additional nano-pattern treatment to the output face has shown to improve the energy resolution since more scintillation light is extracted from the crystal towards the photosensor. However, other parameters such as spatial and DOI resolution did not improve, most likely, because this extraction does not follow the scintillation light distribution. Better detector block performance was definitely obtained with the larger coverage of the photosensor active area (16×16 SiPM), as it was expected.

Summarizing, with a $50{\times}50{\times}15\,\mathrm{mm}^3$ monolithic BGO crystal, we reached an energy resolution better than 20% FWHM, an average spatial resolution for all DOI layers of 2.1 mm FWHM, and a DOI resolution as good as 5.3 mm FWHM. This suggests that a monolithic BGO detector block solution coupled to SiPM arrays is a good candidate for low-dose high-volume PET scanners.

Acknowledgments

This work was also supported by the Spanish Ministerio de Economía, Industria y Competitividad under Grants No. FIS2014-62341-EXP and TEC2016-79884-C2-1-R. This project has received funding from the European Research Council (ERC) under the European Union's Horizon 2020 research and innovation programme (grant agreement No 695536).

References

[1] S.R. Cherry, R.D. Badawi, J.S. Karp, W.W. Moses, P. Price and T. Jones, *Total-body imaging: Transforming the role of positron emission tomography*, *Sci. Trans. Med.* **9** (2017) eaaf6169.

[2] Y. Zhang, H. Yan, H. Baghaeil and W.H. Wong, *Lower-cost Depth-of-Interaction PET Detector Designs Using Dichotomous-3D Decoding*, *IEEE Nucl. Sci. Symp. Med. Imag. Conf.*, San Diego, U.S.A. (2015).

[3] A.J. González et al., *Performance of Large BGO Arrays Coupled to SiPM Photosensors — Continued Study*, *IEEE Nucl. Sci. Symp. Med. Imag. Conf.*, San Diego, U.S.A. (2015).

[4] A.J. González, F. Sánchez, S. Majewski, P. Parkhurst, K. Vaigneur and J.M. Benlloch, *Pilot Studies With BGO Scintillators Coupled to Low-Noise, Large-Area, SiPM Arrays*, *Trans. Nucl. Sci.* **63** (2016) 2482.

[5] S. Tavernier, P. Bruyndonckx, S. Leonard and O. Devroede, *A highresolution PET detector based on continuous scintillators*, Nucl. Instrum. Meth. **A 537** (2005) 321.

[6] T. Ling, T.K. Lewellen and R.S. Miyaoka, *Depth of interaction decoding of a continuous crystal detector module*, Phys. Med. Biol. **52** (2007) 2213.

[7] R. Pani et al., *Preliminary evaluation of a monolithic detector module for integrated PET/MRI scanner with high spatial resolution*, 2015 *JINST* **10** C06006.

[8] A. González-Montoro et al., *Performance Study of a Large Monolithic LYSO PET Detector With Accurate Photon DOI Using Retroreflector Layers*, IEEE Trans. Radiat. Plasma Med. Phys. **1** (2017) 229.

[9] F. Nishikido, N. Inadama, E. Yoshida, H. Murayama, T. Yamaya, *Four-layer DOI PET detectors using a multi-pixel photon counter array and the light sharing method*, Nucl. Instrum. Meth. **A 729** (2013) 755.

[10] M. Ito, et al., *A Four-Layer DOI Detector With a Relative Offset for Use in an Animal PET System*, IEEE Trans. Nucl. Sci. **57** (2010) 976.

[11] W.H. Wong, Y. Zhang, S. Liu, H. Baghaei, R. Ramirez and J. Liu, *The Initial Design and Feasibility Study of an Affordable High-Resolution 100-cm Long PET*, IEEE Nucl. Sci. Symp. Conf. Rec., Honolulu, U.S.A. (2007).

[12] A. Knapitsch and P. Lecoq, *Review on photonic crystal coatings for scintillators*, Int. J. Mod. Phys. **A 29** (2014) 1430070.

[13] F. Tong, B. Liu, H. Chen, Z. Zhu and M. Gu, *Enhanced light extraction of Bi3Ge4O12 scintillator by graded-refractive-index antireflection coatings*, Appl. Phys. Lett. **103** (2013) 071907.

2017 JINST 12 C11027

4.5. A scintillator geometry suitable for very small PET gantries

Authors: Antonio J. Gonzalez, Andrea Gonzalez-Montoro, Albert Aguilar, Gabriel Cañizares, Rosana Martí, Sofía Iranzo, Efthymios Lamprou, Sebastian Sanchez, Filomeno Sanchez and Jose M. Benlloch.

Published: Journal of Instrumentation, 12, C12018, 2018. https://doi.org/10.1088/1748-0221/12/12/C12018

Impact Factor: 1.30

Summary:

It has already been described the advantages and disadvantaged of both pixelated and monolithic approaches. The main objective of this article is to merge both technologies, monolithic plus pixelated in the dubbed hybrid approach, and to test their combined performance. The particular proposed design is based on a dual-layer scintillator approach composed of a monolithic LYSO crystal (5–6 mm thickness) and a LYSO crystal array with 4–5 mm height (0.8 and 1 mm pixels). The main goal of the design is to achieve three-dimensional spatial resolution with DOI-encoding and to increase the detection efficiency at a reasonable cost. Block sizes of 25 × 25 mm^2 and 25 × 16 mm^2 have been used.

The performance of the hybrid approach has been compared with single monolithic blocks with dimensions matching the combined (pixelated plus monolithic) hybrid volumes. SiPM arrays of 16 × 16 elements that have an active area of 3 × 3 mm^2 and a pitch of 3.26 mm, have been used as photosensors.

In the experimental set-up the incoming radiation was impinging first on the pixelated scintillation array placed in the front of the module, and therefore, light from the pixelated component reaches the photodetector by traversing the second inner scintillator piece that operates in this case as the light guide. All crystal pixels elements were resolved independently of their size (0.8 and 1 mm). The monolithic block achieved measured FWHM spatial resolution as good as 1.5–1.7 mm including the 1 mm source size and a DOI resolution (FWHM) nearing 3 mm. Comparable performances were obtained when compared to a single monolithic block. The measured energy distributions indicate a differentiation that is good enough to separate both crystal contributions. In addition to the energy, DOI characterization also served to

distinguish between the two sets of events. The proposed design improves the spatial response uniformity across the whole detector module, and especially at the edge regions.

JINST

Published by IOP Publishing for Sissa Medialab

Received: *September 27, 2017*
Accepted: *November 15, 2017*
Published: *December 11, 2017*

19th International Workshop on Radiation Imaging Detectors
2–6 July 2017
AGH University of Science and Technology, Kraków, Poland

2017 JINST 12 C12018

A scintillator geometry suitable for very small PET gantries

A.J. Gonzalez,[1] A. Gonzalez-Montoro, A. Aguilar, G. Cañizares, R. Martí, S. Iranzo, E. Lamprou, S. Sanchez, F. Sanchez and J.M. Benlloch

Instituto de Instrumentación para Imagen Molecular (I3M),
Centro Mixto CSIC — Universitat Politècnica de València,
Camino de Vera s/n, 46022 Valencia, Spain

E-mail: `agonzalez@i3m.upv.es`

Abstract: In this work we are describing a novel approach to the scintillator crystal configuration as used in nuclear medicine imaging. Our design is related to the coupling in one PET module of the two separate crystal configurations used so far there: monolithic and crystal arrays. The particular design we have studied is based on a two-layer scintillator approach (hybrid) composed of a monolithic LYSO crystal (5–6 mm thickness) and a LYSO crystal array with 4–5 mm height (0.8 and 1 mm pixels). We show here the detector block performance, in terms of spatial, energy and DOI information, to be used as a module in the design of PET scanners. The design we propose allows one to achieve accurate three-dimensional spatial resolution (including DOI information) while assuring high detection efficiency at reasonable cost. Moreover, the proposed design improves the spatial response uniformity across the whole detector module, and especially at the edge region. The crystal arrays are mounted in the front and were well resolved. The monolithic crystal inserted between crystal array and the photosensor, provided measured FWHM resolution as good as 1.5–1.7 mm including the 1 mm source size. The monolithic block achieved a DOI resolution (FWHM) nearing 3 mm. We compared these results with an approach in which we use a single monolithic block with total volume equals to the hybrid approach. In general, comparable performances were obtained.

Keywords: Gamma camera, SPECT, PET PET/CT, coronary CT angiography (CTA); Photon detectors for UV, visible and IR photons (solid-state) (PIN diodes, APDs, Si-PMTs, G-APDs, CCDs, EBCCDs, EMCCDs etc)

---

[1] Corresponding author.

https://doi.org/10.1088/1748-0221/12/12/C12018

Contents

2017 JINST 12 C12018

1 Introduction

With the increasing number of animal models of human diseases, e.g., transgenic mice, Positron Emission Tomography (PET) represents an essential non-invasive tool to assess physiological functions in small animal studies [1–5]. It is necessary to visualize and accurately measure radiopharmaceutical accumulation in structures that have dimensions down to a millimeter or even less. This requires the detector to achieve both high spatial resolution and sensitivity. Recently, there is also very high interest in the development of PET/MRI systems capable of simultaneous acquisition of Magnetic Resonance Imaging (MRI) and PET images [6–9]. True PET/MRI integration requires PET detectors that are very compact, do not distort the operation of the MRI system and are insensitive to magnetic fields to provide simultaneously PET and MRI images. Silicon photomultipliers (SiPM) are being used in the development of current generations of PET/MRI systems due to their compactness, insensitivity to magnetic fields and high signal-to-noise ratio [10].

In this work we describe a novel approach to the scintillator crystal configuration for applications in nuclear medicine imaging. Our design is mainly focused on the implementation of high performance PET detector modules to be used in PET scanners dedicated to imaging human organs or small animals. Our research is specifically related to the coupling of the two crystal configurations that are extensively but separately used so far: monolithic blocks and crystal arrays. Moreover, the proposed detector module design is compatible with MRI scanners. There are advantages and disadvantages of the monolithic and pixelated crystal designs that have been described in the literature [11]. Some advantages of the continuous monolithic crystal design are higher detection sensitivity per unit area (no crystal dead areas), better spatial detection uniformity (no sharp discontinuities), continuous positioning (no pixelation artifacts), depth-of-interaction (DOI) reconstruction capability, and lower cost. Advantages of the pixelated crystal designs are that intrinsic spatial resolution is uniform across the modules, defined primarily by the crystal size, focused scintillation light cone (better signal-to-noise ratio), and in general improved spatial response linearity. Partially slotted crystals [12] have also been considered elsewhere. The partially-optically isolated crystals approach was extensively used in the past, when the pitch of the photodetectors (photomultipliers) was much coarser than that of the discrete scintillation crystals. In that approach, the crystals-pixels are not completely optically isolated and some controlled light sharing across the photodetector plane occurs. Although, this effect can also be produced by simply adding a separate light diffuser between the crystal array and photodetector plane, in this case there is no extra amount of scintillator material, and thus there is no additional increase of sensitivity for the same detector module thickness. This work shows the feasibility of combining monolithic and pixelated crystal arrays to provide enhanced performance of gamma-ray detectors, especially suited for PET scanner designs.

In the approach we have studied, improving upon our previous pilot research [13], we consider a two-layer scintillator design: a monolithic LYSO crystal layer optically coupled to a pixelated LYSO array. The main goal of the design we propose is to achieve high three-dimensional spatial resolution (including DOI information) while assuring high detection efficiency at a reasonable cost. We have studied main hybrid detector performances assuming two small size crystal designs, both with the incoming radiation impinging first on the pixelated scintillation array placed in the front of the module. The photosensor is placed at the bottom of the detector stack with respect to the impinging radiation and reads-out the scintillation light from both components of the hybrid scintillator module. Light from the first outer component of the module is reaching the photodetector by traversing the second inner scintillator piece that operates in this case as the light guide. At the same time the plate scintillator is also functioning as active material detecting additional incoming gamma radiation. The crystal array provides high resolution, whereas the monolithic block helps increasing the system sensitivity. The two blocks still provide high DOI performance.

2 Materials and methods

2.1 Materials

We have carried out tests with two volumes of scintillation material, 25 mm × 25 mm × 10 mm (case 1) and roughly 25 mm × 16 mm × 10 mm^3 (case 2). Small volumes improve the Noise Equivalent Count Rates (NECR) performance and allow one for more compact designs. All scintillation material is of the type LYSO (Proteus, Ohio, U.S.A.). Optical coupling between different elements of the detector package was achieved using optical grease (type BC630, Saint Gobain). The performance obtained with the hybrid approaches has been compared to data obtained with a single monolithic block with dimensions matching the combined (pixelated plus monolithic) hybrid volumes. Figure 1 shows the four studied cases. The monolithic blocks have lateral walls black painted. For cases 1.1 and 2.1, the entrance face was covered with an optical device called retroreflector that bounces back the light to the emission source [14]. In the hybrid approach, the monolithic crystal has a thickness of 5 mm for case 1.2 but 6 mm for case 2.2. The LYSO crystal array had 1 mm size and 5 mm height pixels (case 1.2) and 0.8 mm size and 4 mm height (case 2.2), respectively. All pixels were as-cut (not polished) and covered by reflective material (Enhanced

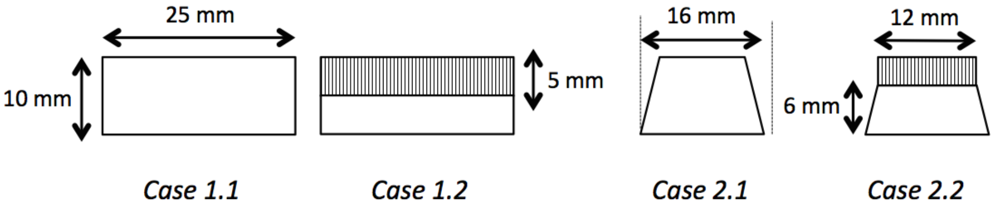

Figure 1. Sketch of the front size for the four crystal cases studied. All have about 25 mm size in the perpendicular direction to the drawing. The line pattern on the top blocks represents the crystal arrays.

Specular Reflector, ESR, $3M^{TM}$). The entrance face of the crystal arrays was also covered with ESR film.

We have used SiPM arrays of 16 × 16 elements (MicroFJ-30035 TSV, SensL, Ireland) that have an active area of $3 \times 3\,\mathrm{mm}^2$ and a pitch of 3.26 mm. The measurements were carried out at a temperature of about 18 ± 2 °C. The supplied bias voltage to the SiPM array was 28–29 V. In these experiments, when performed in coincidence, we used a reference detector based on an identical photodetector array (256 SiPMs) with a monolithic crystal with dimensions of $50{\times}50{\times}10\,\mathrm{mm}^3$. The readout makes use of a network providing information for each SiPM row and column output [5, 6].

2.2 Methods

The signals obtained from the readout electronics were fed to Analog to Digital Converter (ADC) boards with 12 bit precision and 250 ns integration window. A software collimation of 2.4° from the normal has been applied to all data and, selected as a compromise between performance and statistics. The XY planar impact positions are calculated using a center of gravity algorithm of the projected scintillation light distribution through the readout chain. All digitized row and column signals are raised to the power of two before the center of gravity calculation [15]. In the case of the monolithic blocks, the spatial resolution is studied using collimated positron-emitter sources. We have calculated the measured FWHM of the imaged distributions at the photosensor, after calibration into metric units. The measured FWHM depends on the size source, and this has not been subtracted in all presented data.

The readout allows one to also provide information on the photon DOI in the monolithic blocks since the scintillation light distribution is determined. Here, for each detection event, the ratio of the energy and the maximum value for each row and column (E/I) is calculated and the average value obtained [16]. The DOI performance was evaluated by using collimated 511 keV photons beams impinging on the lateral walls of the scintillation blocks. After calibration of the measured data (E/I units) into metric units (mm), we determined the average FWHM of the DOI distributions.

3 Results

3.1 Case 1.1

A ^{22}Na source (0.25 mm in diameter) was mounted in the front of a Tungsten collimator (2 mm drilled hole, 30 mm thick, 60 mm outer diameter) and scanned in steps of 0.5 mm across the surface (1D) of the monolithic block to study both the spatial and energy resolutions. In figure 2 left we

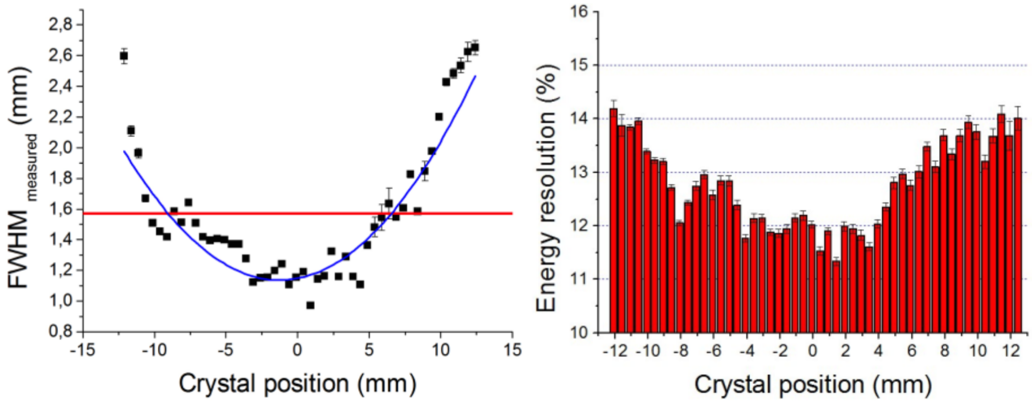

Figure 2. Measured FWHM (left) and energy (right) resolutions, as a function of the beam position in the crystal surface.

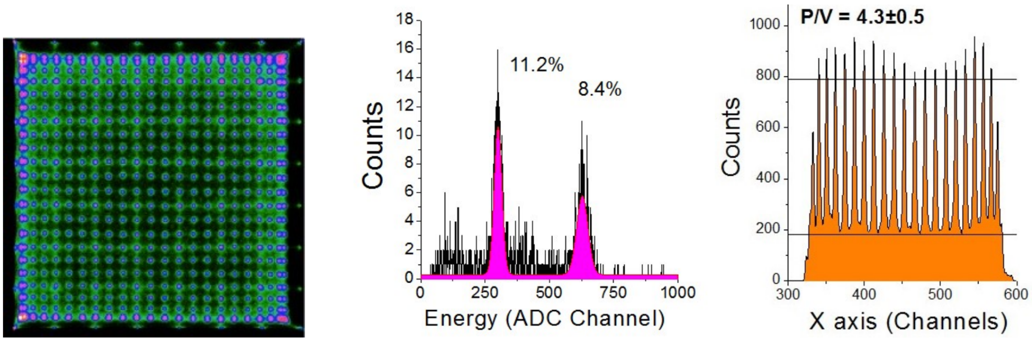

Figure 3. Left, flood map obtained for the hybrid case 1.2. Center, energy spectra for a small ROI. Right, one row of pixels after energy filtering at the photopeak of the pixelated contribution.

show the measured FWHM for all point impacts. As expected, best results are obtained for impacts in the crystal center due to a reduced light distribution truncation. Figure 2 right depicts the energy resolution as a function of the beam position. As for the spatial resolution, better energy resolution values are also obtained at the crystal center where it is possible to transfer the highest amount of scintillation photons to the photosensor. Average spatial and energy resolutions of 1.6 ± 0.4 mm and 13 ± 1% were found, respectively.

Concerning the performance of the photon depth of interaction, we carried out experiments with the source impinging laterally to the crystal block in steps of 1 mm. An average DOI resolution (FWHM) of 3.1 ± 0.5 mm was obtained for the whole crystal volume.

3.2 Case 1.2

Case 1.2 includes the hybrid approach of a monolithic and a pixelated block (1 mm pixels) of the same thickness (5 mm). The spatial resolution is differently studied for the two crystal types. For the evaluation of the spatial resolution performance of the crystal array, we used an extended ^{22}Na source at a distance of 1 cm to the crystal block working in singles mode. Figure 3 left shows the flood map of one acquisition. Both crystal contributions are included in this contour plot. In figure 3 center we depict the measured energy distribution for a small region of interest (ROI) of about 3× 3

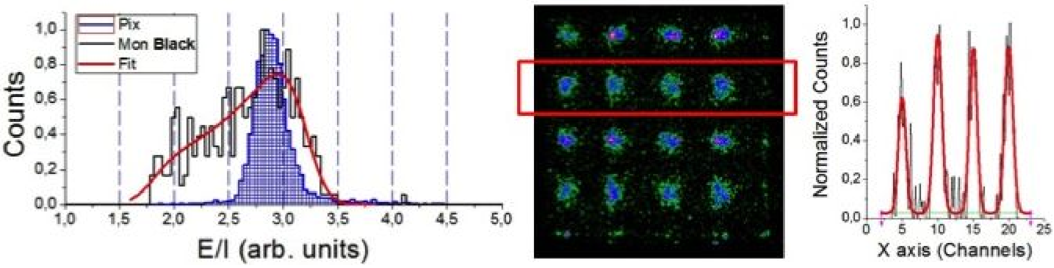

Figure 4. Left, DOI distributions for the pixelated and monolithic blocks (energy filtering). Center, flood map of collimated sources (monolithic contribution). Right, profile for the marked row of sources.

2017 JINST 12 C12018

LYSO pixels at the detector center. The contribution of the two crystals is very well differentiated, with the one for the crystal array at high ADC channels, whereas impacts in the monolithic block are identified at lower channels. This is understood as more scintillation photons are transferred to the photosensor in the first case. Notice that in the monolithic crystal there is more light spread and, thus, more light absorption in the black walls. The impacts corresponding to the crystal array are isolated by an energy filter of 15% at the photopeak (channels 530–720 in figure 3 center). We have studied the spatial resolution by measuring the peak-to-valley ratio (P/V). Notice that all pixels were resolved though. We determined a P/V of about 4.3 ± 0.5, see figure 3 right. The measured energy resolution for single crystal pixels is as good as 8.4%.

The contribution of the two crystal types regarding the DOI is also different. Figure 4 shows the DOI distributions for the two crystal types after energy filtering using normal incidence beams to the crystal. Different from the energy contributions case, the DOI data for the two crystals overlap. The crystal array contribution results in a single thin profile, whereas the DOI distribution for the monolithic follows the expected decay law [14]. Nevertheless, in this experiment it was sufficient to separate the two crystals contributions by means of the energy filters.

To evaluate the performance of the monolithic crystal, a 5×5 ^{22}Na sources array (1 mm diameter, 5 mm pitch) was placed in front of a collimator (1.2 mm drilled holes, 24 mm thick Tungsten) and a software collimation also applied to the data in order to provide spatial and energy resolution information on the monolithic block. A slightly worse energy resolution was determined for this block, on average 13 ± 1%. Figure 4 center depicts the flood map obtained for the monolithic crystal block, including energy filtering around its photopeak (15%, channels 255–345). The measured spatial resolution is calculated using multi Gaussian fits as depicted in figure 4 right. We found an average FWHM for all measured sources of 1.6 ± 0.2 mm.

3.3 Case 2.1

The ^{22}Na source and pinhole collimator described in case 1.1 have been used also for case 2.1. Due to the rectangular block shape, the source and collimator were moved across the short and long axial axes of the monolithic crystal. Figure 5 top-left shows the measured profiles for the long axis in pixel channels. The central panel in this figure depicts the measured FWHM. The energy resolution dependency is also shown on the right hand side. On the bottom panels, center and right, we depict the results for the short axis. Although degradation was observed towards the crystal edges, as expected, both axes resulted on an average measured spatial resolution of 1.8 ± 0.2 mm. The energy

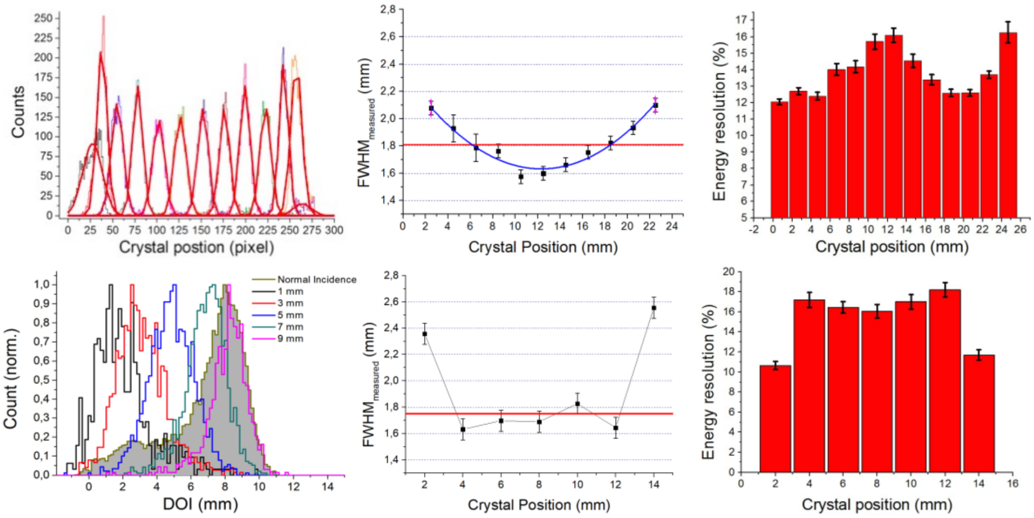

Figure 5. Results for the long (top) and short (bottom) axis. Top-left, profiles of the sources. Top-center, measured FWHM as a function of the impact position. Top-right, energy resolution vs. impact position. Bottom-left, DOI distribution for lateral and perpendicular beams. Bottom-center, measured FWHM as a function of impact position. Bottom-right, energy resolution vs. impact position.

resolution was also measured as a function of the impact position, see bar plots in this figure. Again, consistent average energy resolutions were observed for the two axes of about 15 ± 1 %.

The DOI performance is shown in figure 5 bottom-left. We depict 5 distributions in steps of 2 mm through lateral incidence to the crystal. The plot also shows the DOI profile obtained when radiation impinges normal to the entrance face (grey full curve). We obtained average FWHM values for the DOI of 2.5 ± 0.5 mm.

3.4 Case 2.2

For this case, two crystal pixel sizes were considered (0.8 and 1 mm pitch). As we described for the case 1.2, when the two crystal types are combined we differentiate well the two contributions by the energy spectra. Figure 6 shows on the top-left panel a flood map when uniform radiation is applied. By selecting events in the 15% energy window of the crystal array (see figure 6 bottom-left), we determined the P/V for both crystal arrays. Figure 6 top-center shows a projection along the long axis for the 1 mm size crystal array. The system showed the capability to resolve all pixels and exhibits a P/V of 3.6 ± 0.8 for the 1 mm pixels and 1.9 ± 0.7 for the 0.8 mm pixels. The spatial resolution for the monolithic contribution is again obtained using the coincidence detector. The collimated ^{22}Na source (0.25 mm) was scanned along the two axes of the hybrid crystal assemble. We obtained similar average results for the two axes (1.6–1.7) ±0.5 mm, see figure 6 top-right.

On the bottom of this figure, the energy spectra for a small ROI is shown, where both contributions can be separated, although in this realization the separation of the two photopeaks is slightly smaller than that observed in case 1.2. The energy resolution was studied after DOI filtering the data, in the ranges of 0–3 and 3.1–4.0 (E/I units) for the monolithic and pixelated cases, respectively (see bottom-right panel in this figure). This figure also shows the energy resolution results for the

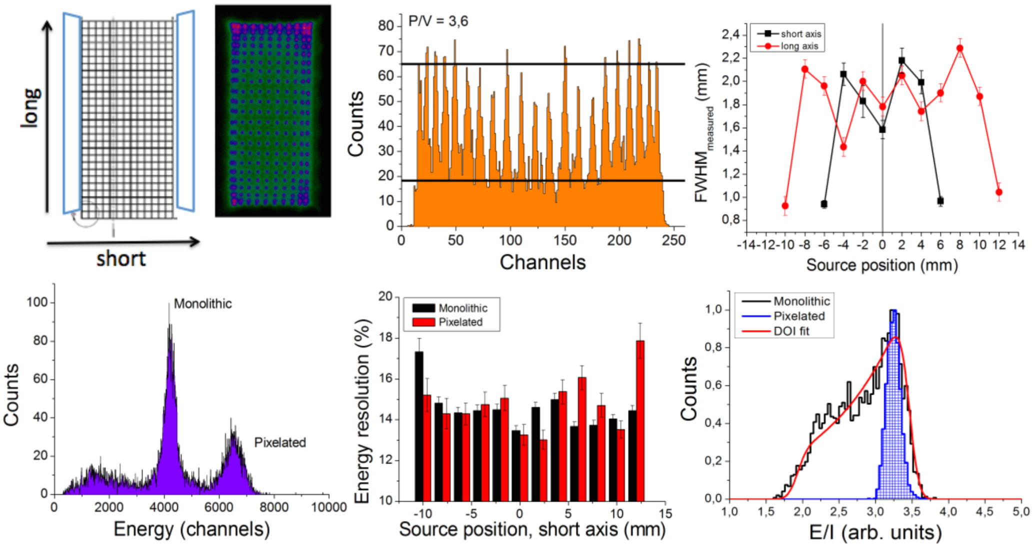

Figure 6. Top-left, sketch and flood map obtained for case 2.2 with 0.8 mm pixels. Center panel shows profile for one row of 1 mm crystal pixels. Top-right, measured FWHM as function of the impact position for the short and long for the monolithic block. Bottom-left, energy distribution for a centered ROI. Bottom-center, measured energy resolution for contributions on the two crystals. Bottom-right, DOI distributions for the two crystal types.

short axis for the two crystal contributions, finding an average of 15 ± 2 %. The data for the long axis also returned similar results of about 14 ± 1 %, not shown in the figures.

By using a beam with lateral incidence to the scintillators we observed the different DOI performance for the two crystals. Impacts in the monolithic crystal return DOI values dependent on the beam height, as expected. However, the impacts occurring on the crystal arrays always return the same DOI value. An average DOI resolution of 2.7±0.4 mm was determined for the monolithic block.

4 Discussion and conclusions

A proof of concept for a novel monolithic-pixelated hybrid crystal configuration has been studied. In particular, two crystal volumes have been tested, as described in case 1 and case 2. The current results can be extended to other detector sizes. The proposed design improves the spatial response uniformity across the whole detector module, and especially at the edge regions. It is expected to use the information of the crystal arrays (0.8 and 1 mm size) as a prior information in reconstruction algorithms. This array permits to accurately define a high intrinsic resolution front detector (0.8 mm) while its sensitivity is increased by means of adding the monolithic slab behind it. Since most of the scintillation light in the crystal array is transferred through the continuous scintillator without significant losses, its energy resolution and position resolving power are mostly preserved.

In this work, pixel sizes as small as 0.8 × 0.8 mm^2 were resolved for this type of scintillator configuration, whereas a detector FWHM spatial resolution of the monolithic block as good as 1.6 mm was obtained (case 2.2). Moreover, the hybrid approach provides different types of DOI information, discrete (4–5 mm) in the case of the crystal arrays but continuous for the monolithic slabs with a DOI FWHM in 2–3 mm range. This would translate into at least 3–4 DOI regions for a 5+5 mm (crystal array + monolithic) total thickness of the hybrid crystal.

The measured energy distributions indicate a differentiation that is good enough to separate both crystal contributions. There are means to further separate the two energy contributions, as for instance using higher light yield pixelated crystals (LFS, GAGG, . . .). In addition to the energy information, DOI characterization also served to distinguish between the two sets of events.

The hybrid concept can be extended to more than two components. For example the pixelated array can be split into two or more arrays. Using staggered configuration with the arrays shifted sideways against each other could potentially provide another means to get better DOI definition.

Acknowledgments

This work was supported by the Spanish Ministerio de Economía, Industria y Competitividad under Grants No. FIS2014-62341-EXP and TEC2016-79884-C2-1-R. This project has received funding from the European Research Council (ERC) under the European Union's Horizon 2020 research and innovation programme (grant agreement No 695536).

References

[1] R. Myers, *The biological application of small animal PET imaging*, *Nucl. Med. Biol.* **28** (2001) 585.

[2] A.F. Chatziioannou, *Molecular imaging of small animals with dedicated PET tomographs*, *Eur. J. Nucl. Med. Mol. Imaging* **29** (2002) 98.

[3] S.R. Cherry, *Fundamentals of positron emission tomography and applications in preclinical drug development*, *J. Clin. Pharmacol.* **41** (2001) 482.

[4] S.P. Hume and R. Myers, *Dedicated small animal scanners: a new tool for drug development?*, *Curr. Pharm. Des.* **8** (2002) 1497.

[5] A.J. Gonzalez et al., *A PET design based on SiPM and monolithic LYSO crystals: performance evaluation*, *IEEE Trans. Nucl. Sci.* **99** (2016) 1.

[6] A.J. González et al., *The MINDView brain PET detector, feasibility study based on SiPM arrays*, *Nucl. Instrum. Meth.* **A 818** (2016) 82.

[7] P. Cerello et al., *An innovative detector concept for hybrid 4D-PET/MRI imaging*, *Nucl. Instrum. Meth.* **A 702** (2013) 6.

[8] H.S. Yoon et al., *Initial results of simultaneous PET/MRI experiments with an MRI-compatible silicon photomultiplier PET scanner*, *J. Nucl. Med.* **53** (2012) 608.

[9] A. Kolb et al., *Technical performance evaluation of a human brain PET/MRI system*, *Eur. Radiol.* **22** (2012) 1776.

[10] Y. Lu et al., *Development of a SiPM-based PET imaging system for small animals*, *Nucl. Instrum. Meth.* **A 743** (2014) 30.

[11] E. Roncali and S.R. Cherry, *Application of silicon photomultipliers to positron emission tomography*, *Ann. Biomed. Engineer.* **39** (2011) 1358.

[12] N. Giokaris, G. Loudos, D. Maintas, et al., *Partially slotted crystals for a high-resolution γ-camera based on a position sensitive photomultiplier*, *Nucl. Instrum. Meth.* **A 550** (2005) 305.

[13] A.J. Gonzalez et al., *Continuous or pixelated scintillators?, not longer a discussion*, *IEEE Nucl. Sci. Symp. Med. Imag. Cond (NSS/MIC)* (2014) M19-114-1472.

[14] A. Gonzalez-Montoro et al., *Performance study of a large monolithic LYSO PET detector with accurate photon DOI using retroreflector layers*, *Trans. Rad. Plasma Med. Sci.* **1** (2017) 229.

[15] R. Pani, S. Nourbakhs, P. Pani, et al., *Continuous DOI determination by gaussian modelling of linear and non-linear scintillation light distributions*, *IEEE Nucl. Sci. Symp. Med. Imag. Cond (NSS/MIC)* (2011) 3386.

[16] R. Pani et al., *Preliminary evaluation of a monolithic detector module for integrated PET/MRI scanner with high spatial resolution*, 2015 *JINST* **10** C06006.

2017 JINST 12 C12018

4.6. Pilot tests of a PET detector using the TOF-PET ASIC based on monolithic crystals and SiPMs

Authors: Abert Aguilar, Andrea González-Montoro, Antonio J. González, Liczandro Hernández, Jose M. Monzó, Ricardo Bugalho, Luis Ferramacho and Jose M. Benlloch.

Published: Journal of Instrumentation, Vol 11, C11033, 2016. https://doi.org/10.1088/1748-0221/11/12/C12033

Impact Factor: 1.30

Summary:

Providing very precise time information requires strategies that preserve the temporal information related to the rise time of the signal pulse and needs to independently read out each photosensor element composing the photosensor matrix. One option for single channel reading is using Application Specific Integrated Circuits (ASICs). They present some advantages in comparison with traditional approaches based on multiplexing SiPM signals. Many works have shown the potential of using ASICs for timing application in PET but most of them focused on using pixelated based detectors. In this article the main objective is to provide accurate time information of the photon interaction in a PET detector based on ASICs combined with monolithic scintillators.

This work made use of the commercial TOF-PET ASIC coupled to 8 × 8 SiPMs arrays from Hamamatsu Photonics with 3 × 3 mm^2 active area. Different crystal configurations have been tested, namely: *i)* two LYSO crystal arrays (12 × 12 elements and 2 × 2 mm^2 each) with a thickness of 5 mm and lateral walls covered with reflective material (ESR) and; *ii)* two monolithic LYSO blocks with 24.5 × 24.5 mm^2 size and 10 mm and 5 mm height surrounded with ESR. For each case, the energy, spatial and time resolutions have been studied. Moreover, a calibration of the main ASIC features required to obtain accurate results enabling a fast response has been performed, such as the TDC leakages adjusting the timestamps and the Time-over-threshold (ToT) values linearizing the energy.

Regarding the pixelated configuration, all crystals were well resolved with a signal to noise ratio of 6. Although the energy was not calibrated, using the ToT spectra an energy resolution better than 20% has been observed. Time resolution was evaluated through the CRT reaching 370 ps for a pair of photosensors (not time alignment calibration) at the optimum SiPMs bias. With

the monolithic approach, a single-pixel LYSO reference crystal helped to explore the CRT performance and many strategies have been explored to provide the best timestamp determination. Times around 1 ns FWHM have been achieved. In terms of spatial and energy resolution, values of about 3 mm and better than 30% were found, respectively. The capability of this system (monolithic and ASIC) to return accurate DOI information and, therefore, their usefulness in future developments to correct for parallax error has been demonstrated.

Since the publication of this work the performance of the experimental set-up has been improved using the next generation of the ASIC obtaining improved results as shown in [171].

JINST

Published by IOP Publishing for Sissa Medialab

Received: *September 30, 2016*
Accepted: *December 5, 2016*
Published: *December 15, 2016*

18th International Workshop on Radiation Imaging Detectors
3–7 July 2016,
Barcelona, Spain

Pilot tests of a PET detector using the TOF-PET ASIC based on monolithic crystals and SiPMs

2016 JINST 11 C12033

A. Aguilar,[a,1] **A. González-Montoro,**[a] **A.J. González,**[a] **L. Hernández,**[a] **J.M. Monzó,**[a]
R. Bugalho,[b] **L. Ferramacho**[b] **and J.M. Benlloch**[a]

[a] *Group of Detectors for Molecular Imaging, Institute for Instrumentation in Molecular Imaging—CSIC,*
Cami de Vera S/N, Valencia, Spain
[b] *PETsys Electronics SA, Taguspark,*
Science and Technology Park, Edificio Tecnologia I, Lisbon, Portugal

E-mail: `alagta1@i3m.upv.es`

Abstract: In this work we show pilot tests of PET detector blocks using the TOF-PET ASIC, coupled to SiPM detector arrays and different crystal configurations. We have characterized the main ASIC features running calibration processes to compensate the time dispersion among the different ASIC/SiPM paths as well as for the time walk on the arrival of optical photons. The aim of this work is to use of LYSO monolithic crystals and explore their photon Depth of Interaction (DOI) capabilities, keeping good energy and spatial resolutions. First tests have been carried out with crystal arrays. Here we made it possible to reach a coincidence resolving times (CRT) of 370 ps FWHM, with energy resolutions better than 20% and resolving well 2 mm sized crystal elements. When using monolithic crystals, a single-pixel LYSO reference crystal helped to explore the CRT performance. We studied different strategies to provide the best timestamp determination in the monolithic scintillator. Times around 1 ns FWHM have been achieved in these pilot studies. In terms of spatial and energy resolution, values of about 3 mm and better than 30% were found, respectively. We have also demonstrated the capability of this system (monolithic and ASIC) to return accurate DOI information.

Keywords: Gamma camera, SPECT, PET PET/CT, coronary CT angiography (CTA); Electronic detector readout concepts (solid-state)

---

[1] Corresponding author.

doi:10.1088/1748-0221/11/12/C12033

Contents

2016 JINST 11 C12033

1 Introduction

In a PET (Positron Emission Tomography) design with limited angle tomography, the absence of accurate impact timing information typically degrades the reconstructed image quality. A PET with such missing angular information produces non-uniformities and artefacts in the reconstructed image across the field of view [1]. This is the case, for instance, of some suggested PET approaches for cardiac or prostate imaging. In these systems, detector panels are placed close to the imaging source. However, using PET detectors with TOF (Time of Flight) capabilities, a significant improvement of the reconstructed image quality has been observed [2].

It has been demonstrated that obtaining very accurate time information requires to independently read each photosensor element (SiPM). This strategy implies preserving the time information related to the rise time of the signal pulse [3]. Application Specific Integrated Circuits (ASICs) are one of the most suitable solutions to carry out this work since several channels can simultaneously be read. ASICs require internal calibrations such as for the amplifiers or TDCs (Time to Digital Converters). There are several works showing the use of dedicated ASICs obtaining accurate PET detector performances when combined with scintillation crystal arrays [4, 5]. Alternatively to ASICs and pixelated crystals, there are studies using monolithic blocks read by dSiPMs [6] returning high performance timing results. Our goal is to study analog SiPMs read by the TOF-PET ASIC [7] and combined with continuous LYSO scintillators to explore the potential capabilities of building high performance PET detectors with limited angle information. In this work we present different pilot experiments where the described technology is evaluated, with greater focus on the results based on continuous LYSO crystals.

2 Materials and Methods

2.1 ASIC features

We have used the PETsys TOF-PET ASIC [7] in order to efficiently process multiple channels of a SiPM photosensor array. This ASIC has been designed for PET applications and its main features are: 64 analog input channels, input rate of 160 kHz/ch, an internal TDC with a time resolution of 50 ps FWHM and a small power consumption of 11 mW/ch at 1.5 V. Both the multiple channel capability and its good TDC resolution are the two most remarkable characteristics. One of its limiting factors is the maximum input rate, which for some PET applications based on continuous scintillators might be tight. This is becuase more SiPMs, when compared to crystal array detectors, may fire simultaneously.

Analog signals coming from the SiPM photosensors are injected into the ASIC. It has two thresholds namely one for the timing concerning triggering on the first photoelectrons, and another for rejecting events outside an energy threshold. The total amount of charge per channel is collected making use of the time-over-threshold (ToT) technique. In this approach, the charge is estimated through the time the signal is greater than a predefined threshold. In terms of logic integration, it is quite easy compared to a charge integration amplifier. Those amplifiers require high dynamic ranges to condition signals with very few photons than others with many more photons. The digital outputs of the ASIC are fed into an FPGA-based readout system containing information for each channel regarding the estimated charge, timestamp and SiPM number, with a maximum output rate of 640 Mbps.

2.1.1 Calibration

The ASIC has several parameters that need calibration. For instance, to avoid oscillations of the operational amplifiers (OAs) and enabling a fast response, it is recommended to inject a test pulse in the input nodes of the ASIC amplifiers using an internal calibration circuit. The TDCs also need calibration to compensate for leakage current variations. The more time between an input pulse and the following, the more leakages that the TDC suffers. Thus, each TDC is calibrated injecting different pulses at different arrival times and amplitudes so that the leakages can be compensated. For each channel, a correction table is generated and then applied as a function of the arrival time difference between each current pulse and the prior one.

In addition to the OA and TDC calibration, it is necessary to characterize the non-linearity of the ToT with the pulse charge. Therefore, we sequentially injected different amplitude pulses making it possible to generate a look-up-table (LUT) with the conversion of ToT to charge. Moreover, there is still the need to convert the measured charge to energy (keV). To establish such a relation, we measured with different radioactive sources, i.e., ^{22}Na, ^{137}Cs and ^{133}Ba, with energy peaks at 511 keV (and 1274 keV), 662 keV and 250 keV, respectively.

2.2 Set-up

The set-up is based on SiPM arrays, LYSO crystals (both continuous and pixelated depending on the test) and the TOF-PET ASIC (see figure 1). We used the 8×8 MPPC arrays (Mod. s12642-0808pb) from Hamamatsu Photonics with 3×3 mm^2 active area. These sensors have a breakdown voltage

2016 JINST 11 C12033

of 65 ± 5 V, 200 kcps/mm^2 dark count rate and a PDE of 35%. We have first made use of two LYSO crystal arrays (12 × 12 elements and 2 × 2 mm^2 each) with a thickness of 5 mm and lateral walls covered with reflective material (ESR). These blocks were used for ASIC characterization purposes. In addition to this set-up, two monolithic LYSO blocks with 24.5 × 24.5 mm^2 based and 10 mm and 5 mm height surrounded with ESR, except on the exit face, were also used. The coupling between the photosensors and the crystals has been made using optical grease (Saint Gobain BC-630, n = 1.47).

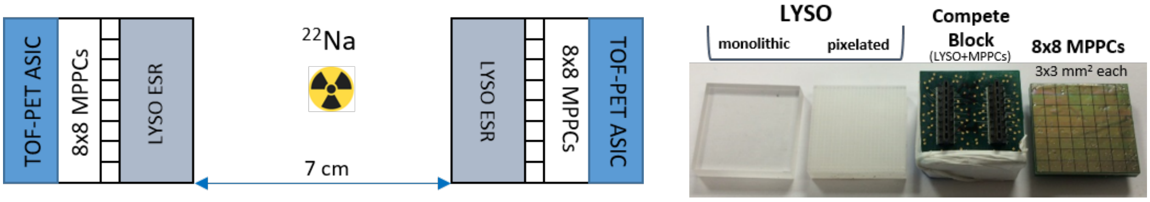

Figure 1. Left: sketch of the set-up. Right: different parts and components of the PET detectors used.

We have designed a dedicated housing for each detector ensuring a constant temperature to the blocks by means of cold dry air. A small size 1 × 1 × 1 mm^3 ^{22}Na source has been used in the experiments with an activity of about 0.8 μCi. The input baseline for the internal ASIC discriminators was set above 5 photoelectrons.

3 Results

The goal of these experiments has been to evaluate this ASIC for its potential use in readout design of gamma ray detectors, especially towards using continuous crystals. However, we have dedicated a subsection in the following to explore the provider ASIC specifications with crystal arrays.

3.1 Crystal arrays

When crystals and photosensors (SiPMs here) are coupled one to one, most of the scintillation light is directly transferred to a single SiPM photosensor. This typically gives the best performance in terms of energy and timing. However, when using monolithic blocks, the scintillation light is unavoidably shared among several SiPMs. Therefore, we have chosen a crystal array with smaller crystal pixels than the SiPM pitch. An acrylic layer (2 mm thick) was located in between the crystal and the photosensor to properly diffuse the light. The photon impact coordinates (crystal elements) are found by using center of gravity (CoG) approaches.

The two blocks in the set-up were separated by 7 cm. The ^{22}Na source was placed in the middle of the system. We acquired data for 30 minutes at a stable temperature of about 15° C. The SiPM bias voltage was set to 67.5 V after performing a small range scan. The flood map in figure 2 left shows all the crystal pixels (12 × 12). On the left of this figure we have depicted the profile for one row of pixels. This shows a very good signal to noise ratio (SNR) between the peaks and the baseline (P/V), resulting on average P/V = 6.

The energy profile corresponding to a small region of interest (two crystal pixels) was analyzed showing an energy resolution better than 20% (see figure 3 left). It should be noticed that here the

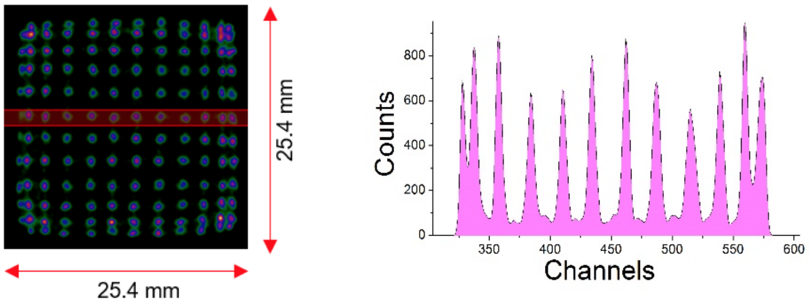

Figure 2. Left: flood map showing the 12 × 12 LYSO crystal elements with $2 \times 2\,\mathrm{mm}^2$ size. Right: projection for one row of pixels.

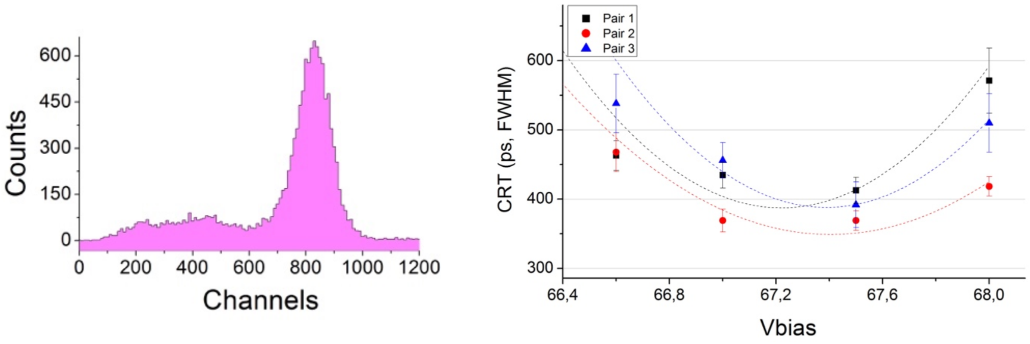

Figure 3. Left: energy profile for a region of interest considering two crystal pixels. Right: CRT as a function of the SiPM bias voltage for three pairs of SiPMs.

ToT was not calibrated to energy units. The time resolution was evaluated after removing the acrylic diffusor and, thus, providing more scintillation light to each photosensor. In addition to the light collection, we also decreased the temperature to around 10° C obtaining a higher gain on the Multi Pixel Photon Counters (MPPCs) and reducing the dark counts rates as well. The ^{22}Na source was placed on top of one detector improving the coincidences rate. We carried out a scan of the SiPM bias voltage but only plotting the results for the three pairs of MPPC with the highest number of events (see figure 3, right). Single MPPC pairs were only considered due to the time misalignment between paths. The best CRT (coincidence resolving time) was found at about 370 ps (FWHM) at a bias voltage of 67.5 V.

3.2 Monolithic blocks

The energy resolution for the monolithic block was studied using one LYSO monolithic block with 10 mm thickness, and a single LYSO pixel ($3 \times 3 \times 10\,\mathrm{mm}^3$) in the opposite detector and optically coupled to a single SiPM sensor. The ^{22}Na source was placed close to the reference detector to allow it to trigger as many events as possible. An acquisition of 2×10^5 events was recorded. The

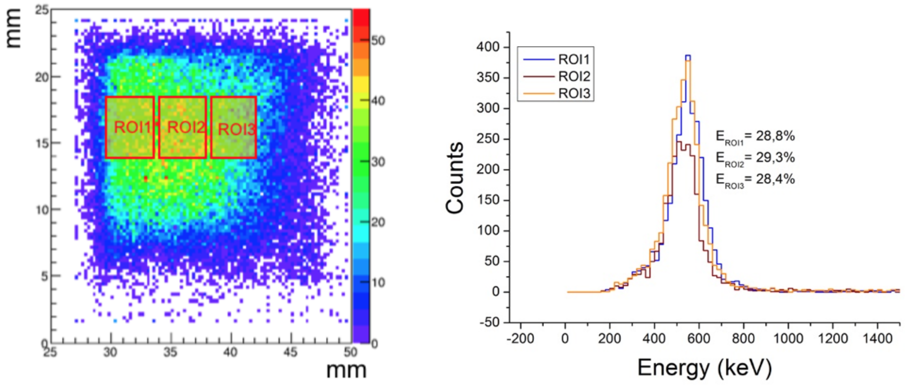

Figure 4. Left: flood map of the monolithic block (source not centered) showing the ROIs. Right: energy profiles for these ROIs depicting the energy resolution values.

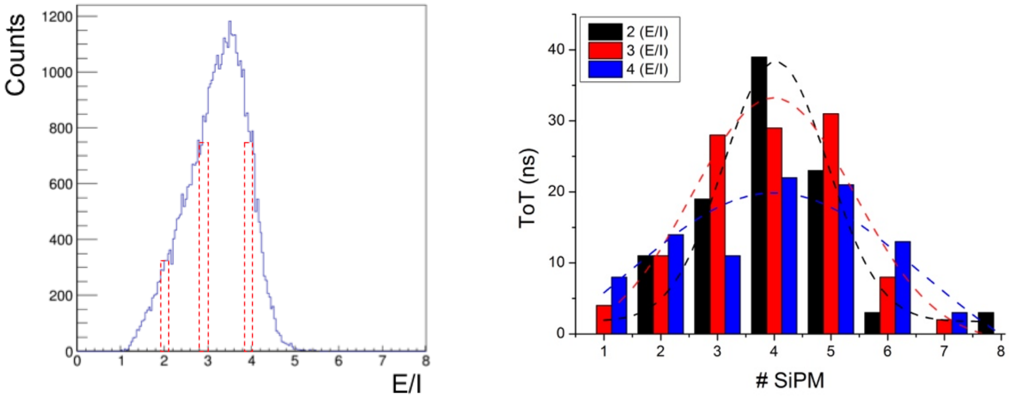

Figure 5. Left: DOI spectrum after filtering in energies both detectors and for ROI2 considered in figure 4, left. Right: three examples of light distributions for this ROI2 showing how their width decreases with the impact depth. The dashed lines correspond to the light distribution fitted on each projection.

energy was evaluated at different regions of interest on the detector. An energy filter around the 511 keV peak was also applied to the reference detector reducing signal contributions of SiPMs different to the one coupled to the LYSO pixel. In the results shown in figure 3 we determined energy resolutions ranging from 28–29%.

DOI is only typically available with crystal arrays using the phoswich approach with two crystal type layers or staggered blocks. This information allows one to properly calculate the 3D photon impact position and, therefore, return a more precise line of response during the reconstruction process, reducing the parallax error [9]. Monolithic blocks help to provide DOI decoding in a simpler way than crystal arrays. We have worked on a DOI estimator based on the ratio of energy to the maximum intensity of one of the row or column projected signals, named here as E/I. It has been already demonstrated that E/I obtained through the scintillation light distributions, provides accurate photon DOI [8]. Figure 5 left shows the histogram of E/I for centered ROI and after filtering events around the 511 keV [490–520 keV] peak. To show the goodness of this DOI

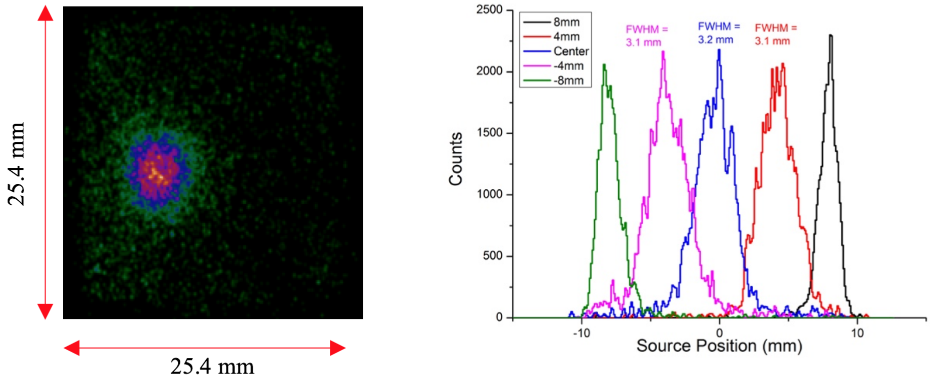

Figure 6. Left: flood map in the monolithic crystal after irradiation with the collimated 1 mm^3 size source. Right: profiles for the 5 collimated positions.

determination method, we have selected three events at different E/I values showing, therefore, different light distribution profiles. Figure 5 right shows with black bars an impact very close to the photosensor and, thus, a narrow light distribution. The red distribution represents an impact with a photon DOI around 5 mm. Finally, the blue bars depict a light distribution produced near the entrance layers of the crystal (8–10 mm).

We made use of a thin tungsten collimator with a 0.8 mm diameter aperture and 70 mm thick, having the ^{22}Na source at one side. The collimator was placed in contact with the detector mounted on 10 mm crystal thickness. We moved the assembly to 5 different positions along the X axis with steps of 4 mm and determined the impact positions using the CoG algorithm (see figure 6). The average FWHM through a Gaussian fit to the 5 distributions was 3 mm, without correcting for the source or collimator sizes.

During the timing measurements, we kept the configuration with the single LYSO pixel as reference detector. The goal was to characterize the monolithic block and extrapolate the obtained results afterwards. There is a different time path among all SiPM channels in the ASIC. Therefore, different channels have different timestamps for signals arriving at the same time with the same energy. Moreover, we have time walk errors for different energies. The SiPM signal amplitude changes with the number of collected optical photons. Thus, since the rise time of the signal is preserved [3] and the trigger threshold giving the timestamp is fixed, the SiPM-ASIC would return different timestamps when the received number of photons changes.

For each gamma impact on the monolithic block, several SiPMs are fired. In our experiments, we observed an average of 20 SiPMs receiving scintillation light over the threshold. Therefore, when calculating the CRT, we considered several of the fired SiPMs. This implies characterizing misalignments between these SiPMs (ASIC channels). For this reason, we came up with the calibration set-up which provides a light homogeneity to the SiPMs.

For each of the 128 channels we plot the CRT differences (between the monolithic and the reference pixel) as a function of the ToT. Thus, by projecting the CRT distribution at certain ToT values, we fitted those to a Gaussian distribution. With this information, we built a LUT with the following information: number of channel, ToT value, Gaussian Centroid, and Gaussian

2016 JINST 11 C12033

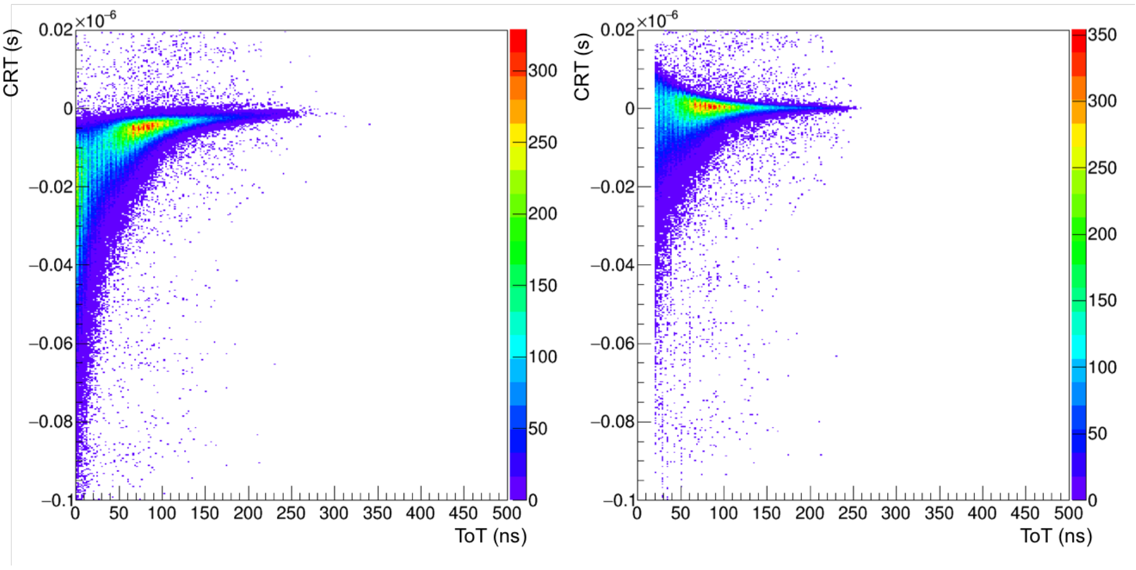

Figure 7. 2D histograms of the CRT measured as a function of the ToT collected for all channels. The left one corresponds to the one before time alignment. The right one is the result after compensating the events by the measured offset.

Sigma. With this information, it is possible to correct the timestamp for each channel as: $CRT = ts_{\mathrm{REF}} - ts_{\mathrm{mono}} \rightarrow CRT_{\mathrm{cor}} = ts_{\mathrm{REF}} - (ts_{\mathrm{mono}} - t_{\mathrm{off}})$, being ts_{REF} the timestamp for the reference detector, ts_{mono} the timestamp for the monolithic block, CRT_{cor} the corrected CRT value and ts_{off} the timestamp offset to add, consisting of the Gaussian centroid fitted to the Y projections. Figure 7 left shows distribution CRT versus ToT before calibrating. It can be observed how the uncertainly CRT increases for low ToT values. This plot is the collection of all channels that indeed shows very small differences among all of them for this figure. Figure 7 right shows the flood map (CRT versus ToT) after correcting the offset (t_{off}). The center of the new distributions is centered near CRT zero. When not enough data is considered for building the LUT (some Gaussian fits do not converge), artefacts begin to appear on the image. We can correct for each impact the timestamp and perform the correct time differences. Unlike the pixelated arrays where the timestamp is typically assigned to the first photosensor whose signal overcomes the trigger threshold, in monolithic scintillators, some other methods have been demonstrated to be more appropriate [6]. They consist of considering not only the first fired photosensor but others too and the average of their timestamps. We have implemented three methods for comparison with different timestamps namely simple average, average weighting with the sigma from the CRT vs. ToT calibration fits, and average by energy.

The plot in figure 8 depicts the CRT values (henceforth in FWHM) after calibration with the three described averaging methods, as a function of the number of timestamps (SiPMs) considered. The best results are obtained with the SiA (Sigma Average) reaching 1.15 ns CRT for 3 timestamps. The energy average (EA) method provides a slightly better CRT than the simple average, being around 1.3 ns CRT again for 3 timestamps. We could stay that the optimal number of timestamps to consider is 3. Notice that the obtained CRTs consider the contribution of the reference detector too, resulting on 1.15 ns when subtracting it (0.32 ns considered for the reference).

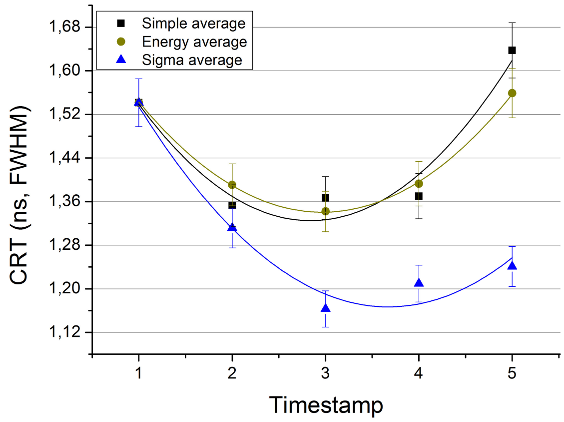

$$
\begin{aligned}
t_{\mathrm{SA}} &= \frac{\sum_{i=0}^{n} t_i}{n} \\
t_{\mathrm{EA}} &= \frac{\sum_{i=0}^{n} t_i \cdot C_i}{\sum_{i=0}^{n} C_i} \\
t_{\mathrm{SiA}} &= \frac{\sum_{i=0}^{n} t_i/\sigma_i}{\sum_{i=0}^{n} 1/\sigma_i}
\end{aligned}
$$

Figure 8. Plot for the determined CRT as a function of the number of fired SiPMs (number of timestamps) for the three described methods.

4 Summary and discussion

In this work, the performance of a commercially available ASIC has been evaluated, using SiPMs arrays and different scintillation crystal types. For each case, we have studied the energy, spatial and time resolution. We calibrated the key ASIC features required to obtain accurate results such as the OAs operation levels enabling a fast response, the TDC leakages adjusting the timestamps and the ToT values linearizing the energy.

First, crystal pixels of 2 mm were well resolved with a signal to noise ratio of 6. Although the energy was not calibrated, using the ToT spectra we can observe an energy resolution better than 20%. Time resolution was evaluated through the CRT reaching 370 ps for a pair of photosensors (not time alignment calibration) at the optimum SiPMs bias. This value is the result of adding the errors due to the ASIC, which is around 150 ps, the LYSO uncertainty and the variation on the transit time of the SiPMs electrons for a single photoelectron event.

In the set-up with continuous crystals, we obtained an energy resolution of about 28% for several detector regions of interest. This value will be reduced when using the next generation of the ASIC, where a dedicated charge integration circuit will be included instead of the ToT method. We have shown the system capabilities to return DOI information and, therefore, their usefulness in future developments to correct for parallax error. The spatial resolution was estimated to be about 3 mm, with CoG positioning algorithms and without applying electronic collimation. Both, energy and spatial resolutions results with monolithic blocks are still worse than what can be achieved with other ASICs or with analog readouts. Therefore, further investigation is required. Regarding time measurements, a complete calibration process has been carried out to reduce the influence of time walk and time alignment paths in the ASIC. After this calibration, several averaging methods when considering the timestamps of a given impact have been applied, obtaining the best value when we averaged weighting for the sigma average method (SiA) and resulting in a CRT of 1.2 ns.

Using an ASIC as a readout circuit for gamma ray detectors is an advantage when comparing with traditional approaches based on multiplexing SiPM signals. With this approach, one can have access to every single SiPM, enabling the possibility to apply complete 2D maps of the light distribution when combined with monolithic crystals. These pilot tests have confirmed the potential advantages of combining these two technologies. Other authors have shown significantly improved results in terms of timing also using monolithic blocks, some at very low temperatures (-20° C) to achieve very low noise rates and improving the SiPMs detection efficiency [6]. We are presenting here the first pilot results using the TOF-PET ASIC combined with monolithic blocks. There is a work in progress to improve the current results using SiPMs after significantly reducing dark count rates compared to the current results.

Acknowledgments

Work supported by Spanish Ministry of Economy and Competitiveness, TEC2013-48036-C3-2-R.

References

[1] S. Surti and J.S. Karp, *Design considerations for a limited-angle, dedicated breast, TOF PET scanner*, *Phys. Med. Biol.* **53** (2008) 2911.

[2] S. Surti and J.S. Karp, *Advances in time-of-flight PET*, *Phys. Med.* **32** (2016) 12.

[3] A. Aguilar et al., *Time of Flight measurements based on FPGA and SiPMs for PET-MR*, *Nucl. Instrum. Meth.* **A 734** (2014) 127.

[4] H. Matsuda, J. Kataoka, H. Ikeda, T. Kato, T. Anbe, S. Nakamura et al., *Development of ultra-fast ASIC for future PET scanners using TOF-capable MPPC detectors*, *Nucl. Instrum. Meth.* **A 699** (2013) 211.

[5] A. Aguilar et al., *Timing Results Using an FPGA-Based TDC with Large Arrays of 144 SiPMs*, *IEEE Trans. Nucl. Sci.* **62** (2015) 12.

[6] H. T. van Dam et al., *Sub-200 ps CRT in monolithic scintillator PET detectors using digital SiPM arrays and maximum likelihood interaction time estimation*, *Phys. Med. Biol.* **58** (2013) 3243.

[7] M. D. Rolo et al., *TOFPET ASIC for PET applications*, 2013 *JINST* **8** C02050.

[8] A. J. González et al., *The MINDView brain PET detector, feasibility study based on SiPM arrays*, *Nucl. Instrum. Meth.* **A 818** (2016) 82.

[9] A. J. González et al., *A PET Design Based on SiPM and Monolithic LYSO Crystals: Performance Evaluation*, *IEEE Trans. Nucl. Sci.* **63** (2016) 2471.

5. Summary and Conclusions

In recent years, the progress in the development of PET detector blocks based on monolithic scintillators, has made them suitable candidates to replace traditional detector blocks using pixelated scintillators. Monolithic based detectors allow one for an accurate estimation of the 3D photon interaction coordinates within the crystal reaching DOI resolutions as good as 2 mm [183]. Moreover, when crystals are coupled to SiPMs (or APDs), it is possible to simultaneously use them within MRI scanners. The main objectives of this thesis are to design, validate and system assemble high performance PET detector blocks.

The principal requirements for the detector design were to provide high spatial, energy and DOI resolutions when working in the presence of magnetic fields, as well as high physical sensitivity. To meet the aforementioned requirements, a design was based on a monolithic LYSO block with dimensions of 50 × 50 × 20 mm^3 coupled to a high-density custom designed photosensor array of 12 × 12 SiPMs (SensL, MINDView-Series type). A frontend electronics providing signals for the 12 rows and 12 columns was designed, allowing to characterize the scintillation light projections. The planar impact position is determined using a modified center of gravity algorithm [164], whereas the DOI is provided using the ratio of the energy to the maximum signal [1]. The SiPM package is of the through-silicon via type and was successfully tested in magnetic field environments. The present work provides extensive comparative results with two crystal treatments namely all faces black painted and, lateral walls black painted and a retroreflector (RR) layer coupled to the entrance face of the scintillator. Several types of RR layers have been tested. The best results concerning impact position determination and energy resolution were observed for the case using the smallest RR. The detector block achieved an average DOI resolution of 4 mm and a measured detector spatial resolution (FWHM) of 1.5 mm. Moreover, a uniform energy resolution, better than 13%, was found. Overall, the detector performance based on 20 mm thick LYSO crystals including an RR layer at the entrance surface exhibits high performance at almost any position within the crystal volume [1].

As a consequence of the excellent performance achieved with the detector block presented in [1], it was selected as the building block of the MINDView brain PET insert [201]. The MINDView scanner is based on 3 rings of 20 detector modules each. It has a geometrical aperture of 33 cm in diameter and covers an axial FOV of app. 15 cm. Another objective of this thesis has been the assembly and validation of this PET insert prototype. It has been already installed at the Klinikum Rechts der Isaar (Munich) [201]. Preliminary results within a 3T MRI scanner (whole-body Siemens Biograph mMR) are reported in [2]. In the system, the photon DOI is corrected for each LOR, allowing to achieve tomographic reconstructed spatial resolutions of 1.7 mm (FWHM) at the CFOV, only degrading to only 3 mm at 100 mm off-radial center. An average energy resolution for all the 60 modules of 17.5% was measured. The PET reaches a maximum physical sensitivity nearing 7% (energy range of 350-650 keV) at the CFOV. Moreover, several FDG fillable phantoms were scanned using the PET insert inside the 3T Siemens mMR, and the system performed well under any of the tested MR sequences, including EPI or UTE that account for high duty cycles of the gradient coil. Count rate degradations were not observed for any sequence. An improved image spatial resolution was observed through the mini-Derenzo phantom, when compared to the PET image provided by the Siemens mMR PET [2].

Making use of the experience obtained during the characterization of the MINDView detector block, another detector block was designed and validated. This new design keeps black painted the scintillator lateral walls and a RR layer coupled to the entrance face as in [1]. However, to provide a more homogeneous resolution across the detector volume and therefore, a reduced edge effect, instead of using 20 mm thick LYSO blocks, 15 mm thick crystals were selected. Regarding the photosensor, also a 12 × 12 SiPMs array was used (SensL, C-Series, 35 um cell size) but, instead of reading all photosensors individually (144 signals) or, the 12 rows and 12 columns, each SiPM has been connected to a readout circuitry that provides only 8 outputs signals for each X and Y light distribution profiles [3]. The readout is based on keeping the 2 lateral rows and columns, but merging the 8 central ones from 2 to 1, specially preserving a good sampling of the light at the crystal edges. Experiments have demonstrated the ability of the system to resolve events as close as 0.25 mm from the crystal edge. It should be noticed then that the 100% of the crystal volume can therefore be used during the reconstruction. In contrast to this achievement, the data currently obtained with the MINDView detector block (20 mm thick) rejects impacts in the 2 mm edge region. The detector performance resulted on an average measured spatial resolution (FWHM) of 1.8 mm, a DOI resolution (FWHM) of 3.7 mm, and an energy resolution of 13% (FWHM). Moreover, the proposed detector block has shown better performance resolving events at the edge when compared to a standard 8×8 SiPMs photosensors from SensL (J-Series, 35 um cell size) with 6×6 mm^2 active area each. This design is used in the stand-alone CareMiBrain PET system which is composed by 48 of these detector blocks arranged in 3 rings. The system is currently under evaluation

In the search for optimum, cost-effective, PET developments, the performance of detectors based on BGO scintillators has been explored. These results have increased the interested on the more challenging use of thick monolithic BGO blocks. The main drawback of BGO blocks is their lower light yield as compared with new fast scintillators. Initial tests were performed with pixelated BGO crystals showing an excellent performance [184]. To improve the light extraction performance, a retroreflector layer at the entrance face as well as a nanopattern structure at the exit were tested. However, lateral walls were kept black painted preserving the detection accuracy of the impinging gamma-rays. The best performance was achieved with a 16 × 16 SiPMs due to a larger active area coverage (92%) of the photosensor. Energy resolutions as good as 20% were achieved. It is interesting to mention that although the nanopattern improves the light extraction and, therefore, the energy resolution, it deteriorated the 3D impact determination. This occurred, most likely, due to an extraction of scintillation light breaking the expected distribution and, therefore, novel-positioning algorithms might be required. An average DOI resolution of 5.3 mm was achieved. The measured spatial resolution was determined for discrete DOI layers being 2.5 mm at the entrance layer (15-10 mm from the photosensor array), 2.2 mm (10-5 mm) and 1.6 mm (5-0 mm) [4]. These results suggest that monolithic BGO detector blocks are good candidates for low-dose high-volume PET scanners.

Another relevant study carried out in this thesis is a single detector that combines monolithic and pixelated crystal arrays. The aim is to provide enhanced performance of gamma-ray detectors. The design is a dual layer with the pixelated crystal in the front, and the monolithic in between this and the photosensor. The pixel array permits to accurately define a high intrinsic resolution while its sensitivity is increased by means of adding the monolithic slab behind it. Since most of the scintillation light in the crystal array is transferred through the continuous scintillator without significant losses, its energy resolution and position accuracy are mostly preserved. In this work, pixel sizes as small as 0.8 × 0.8 mm^2 were resolved for the crystal array, whereas the monolithic block returned an average measured spatial resolution as good as 1.6 mm. The hybrid approach provides different types of DOI information, discrete (4-5 mm) in the case of the crystal arrays but continuous for the monolithic slabs with a DOI resolution values in 2–3 mm range [5]. The measured energy and DOI distributions permit differentiating the two crystal contributions. This hybrid concept can be extended to more than two components, providing high three-dimensional spatial resolution (including DOI information) while assuring high detection efficiency at a reasonable cost.

Both the BGO and hybrid approaches show a proof-of-concept of less conventional detector block designs that yet keep an overall good performance. The hybrid design will be suitable for small animal scanners providing accurate resolution. In contrast to pre-clinical designs, the BGO approach, thanks to its lower cost, is suitable for whole or total body scanners, where large volumes of scintillation material are required, as for instance in long axial scanners such as the EXPLORER [91].

During the course of this thesis, PET instrumentation capable to provide accurate timing information of the detected gamma rays has also been investigated. Timing information improves the quality of reconstructed images (see Section 2.4.2.1). In this thesis the PETsys TOF-PET ASIC coupled to an 8 × 8 SiPMs arrays (Hamamatsu Photonics, 3 × 3 mm^2 active area) has been studied. For characterization purposes, the ASIC was first coupled to a LYSO crystal array and achieved a time resolution, evaluated through the CRT, of 370 ps FWHM. After the characterization, two monolithic LYSO blocks with 24.5 × 24.5 mm^2 size, and 10 mm and 5 mm height, respectively, both covered with ESR have been studied. In this case, a complete calibration process showed the system capabilities to return DOI information and good spatial resolution. In addition, several averaging methods considering the timestamps of a given impact have been studied. It was possible to achieve a CRT of 1.2 ns [6]. It should be noticed that the scintillation light sharing among different SiPMs when using monolithic crystals, significantly reduced the SNR and accurate timing determination is challenging. To improve this, the second generation of this ASIC was tested in addition to different crystal treatments, including the RR layer. An improvement in the detector performance was achieved reaching values of 585 ps with a 15 mm LYSO monolithic block [171]. This work also shows the electronics capabilities to reach 208 ps if one-to-one coupling of the crystal pixel to SiPM is carried out, at the cost of missing DOI information and a limited spatial resolution to the pixel size (3 mm). Further investigations are being carried out making use of accurate 3D positioning and timing information in systems with limited angle tomography designs. Examples of these systems are two panels PET for cardiac studies (maybe curved), or for prostate cancer biopsy guidance.

Along this thesis, a theoretical model for the LD profiles has been used assuming that the scintillation light produced as a result of the conversion of the gamma-ray into low energy photons is isotropically emitted and can be characterized by the inverse square law. This equation can be derived to obtain a valid three-dimensional model for the light distribution in monolithic crystals. Regarding the DOI coordinate, a mathematical expression has been deduced. This expression uses the *E/I* estimator which is only valid for one dimensional projections such as the ones provided by our row and column readout (see Section 3.1.3.1). Moreover, the linear dependency of the *E/I* estimator with *z* for different block geometries, thicknesses and crystal surface treatments has been experimentally validated using lateral side experiments.

In conclusion, in this thesis PET detector blocks based on thick monolithic blocks and SiPMs arrays have been explored. Overall, a good characterization of the light distribution profiles providing accurate estimation of the 3D photon impact coordinates has been demonstrated. When DOI information is used, a significant image improvement at the FOV edges has been observed. There is still some dependence of the impact position (edge effect) and its DOI for thick monolithic crystals. Current investigations deal with characterizing these findings, improving the spatial resolution dependence with the radial position at the image FOV.

Increasing the collection of scintillation photons improves the overall detector performance. Different crystal surface treatments have been proposed. The LD profiles need to be preserved when making use of the projection readout, to properly estimate the 3D impact coordinates through center of gravity and *E/I* methods. For this reason, better results were achieved when using the RR layers. However, other treatments such as ESR or white Teflon that avoid preserving the LD could also be implemented but require alternative algorithms as for instance neural networks or machine learning, with some room for improvement, especially at the crystal edges.

A translation of this thesis research to the clinical and preclinical environments has been successfully performed. Two brain PET systems have been implemented. Both the MINDView and the CareMiBrain scanners are PET systems dedicated to the study of the brain. As outlined in Section 3.4, dedicated systems present some advantages in comparison with current whole-body scanners such as, higher spatial resolution and increased sensitivity allowing to reduce the radiotracer dose to the patient and to the clinicians. In addition, dedicated systems require small footprint at hospitals and are more affordable. All these advantages help to generate accurate diagnoses and treatment monitoring of patients. The aim is that this thesis will contribute to further improve the performance of novel PET systems. The MINDView PET insert has been already validated with simultaneous MR acquisitions showing high performance. The successful merging of both PET and MRI techniques will help to provide accurate images of mental disorders and brain tumors, to name but a few. Therefore, the results obtained in this work have given a strong experimental support to the concepts and research lines followed by the group and will lead to further developments and improvements along these lines in the future.

6. Resumen y Conclusiones

La medicina nuclear es una especialidad médica que utiliza sustancias radiactivas con fines diagnósticos y terapéuticos. Dentro de esta rama de la medicina encontramos numerosas técnicas diagnósticas tales como la gamma cámara, la tomografía por emisión de un único fotón (SPECT, del inglés *Single Photon Emission Computed Tomography*) y la tomografía por emisión de positrones (PET, del inglés *Positron Emission Tomography*). Estas técnicas de imagen médica permiten visualizar procesos fisiológicos y bioquímicos del cuerpo humano *in vivo*, mediante la administración de un elemento radiotrazador. Los radiotrazadores son compuestos químicos, similares a las sustancias naturales del cuerpo, en las que uno o más átomos son sustituidos por radionúclidos emisores de fotones, para su uso en gamma cámaras y SPECT, o de positrones (la antipartícula del electrón) para PET.

La técnica PET ha experimentado mejoras significativas en los últimos 60 años, estableciéndose en la actualidad como una herramienta diagnóstica imprescindible en medicina. Por este motivo y con el fin de mejorar la calidad diagnóstica, el objetivo principal de esta tesis doctoral ha sido el desarrollo de nuevos detectores PET de gran rendimiento.

La obtención de la imagen PET comienza con la inyección del elemento radiotrazador en el sujeto de estudio, allí se desintegra emitiendo positrones que viajan en el interior del cuerpo del paciente al azar hasta que colisionan con un electrón cortical del tejido. Como resultado de esta colisión se emiten dos rayos gamma de 511 keV, en direcciones casi opuestas, que son detectados en coincidencia en el escáner PET registrando un evento. La información relativa a estos eventos es enviada a un ordenador, donde finalmente, algoritmos de reconstrucción son empleados para generar una imagen mostrando la distribución tridimensional del radiotrazador en el interior del cuerpo. La selección del radiotrazador depende del estudio que se va a realizar. Por ejemplo, la 18F-fluoro-desoxi-glucosa (^{18}F-FDG), que es el compuesto más utilizado en PET, se emplea como un trazador de captación de glucosa ya que sigue una ruta metabólica similar a la glucosa *in vivo*, la única diferencia es que permanece atrapada dentro del tejido sin metabolizarse en CO_2 y agua. Esto es de especial interés en oncología dado que las células cancerosas proliferantes tienen una tasa metabólica de glucosa superior a la media, y captan la ^{18}F-FDG.

La técnica de imagen PET se emplea fundamentalmente en el estudio de enfermedades oncológicas, cardiovasculares y neurológicas. Cabe mencionar, no obstante, su especial relevancia en el estudio del cerebro y de sus enfermedades asociadas, de hecho, el primer dispositivo de imagen basado en la detección en coincidencias de positrones fue construido en 1952 por Brownell y Sweet [69], y era un sistema dedicado al estudio del cerebro. No fue hasta 1970-1973 cuando Robertson y Thompson construyeron el primer escáner PET completo, llamado *Positome* [74].

La calidad diagnóstica derivada del PET, está ligada a la calidad de la imagen proporcionada, la cual depende a su vez de la eficiencia de los bloques detectores que constituyen el escáner. Estos bloques están constituidos por tres componentes principales: el cristal centelleador, el fotosensor y su electrónica asociada. El cristal centelleador es el encargado de frenar los rayos gamas de 511 keV emitidos desde el interior del paciente, generando fotones ópticos de menor energía que serán detectados en el fotosensor. La información recolectada se procesa con la electrónica asociada y se envía al ordenador para su posterior reconstrucción. Durante el proceso de reconstrucción numerosas correcciones tales como la corrección por atenuación, normalización o dispersión son aplicadas.

En la actualidad, la mayoría de sistemas PET comerciales están constituidos por bloques detectores basados en cristales centelleadores pixelados (matrices de pequeños cristales) y tubos fotomultiplicadores (PMT, del inglés *Photomultiplier Tubes*). Los cristales pixelados permiten estimar las coordenadas (x, y) del impacto del fotón de manera sencilla, sin embargo, la obtención de la coordenada de profundidad de interacción (z), imprescindible para corregir el error de paralaje y obtener una buena resolución espacial sobretodo en los bordes del campo de visión del escáner, resulta una tarea difícil requiriendo el uso de materiales extras y por tanto incrementando el precio del escáner. Además, la resolución espacial de estos bloques está limitada por el tamaño del pixel. En el caso de los PMT, su gran tamaño e incompatibilidad con campos magnéticos limita su uso.

Una alternativa a la configuración anterior, es el uso de cristales monolíticos y fotodetectores de silicio (SiPM, del inglés *Silicon Photomultiplier*). Estos bloques de cristal monolítico están constituidos por una única pieza de material centelleador que permite "observar" la distribución de fotones ópticos generada. Esta información es utilizada para obtener las coordenadas 3D de impacto del fotón (*x, y, z*) en el cristal con buena resolución sin necesidad de materiales extra. Además, son más fáciles de producir y por lo tanto más económicos especialmente cuando los comparamos con pixeles de cristales de tamaño < 1.5 mm. Los SiPM son detectores de estado sólido, su desarrollo ha sido una contribución clave a las recientes mejoras en PET ya que son más compactos que los PMT permitiendo la construcción de escáneres más robustos, tienen una mayor granularidad lo que mejora la recolección de la luz de centelleo, presentan una gran cantidad de configuraciones y, además, son compatibles con campos magnéticos. Los Capítulos 1y 2 de esta tesis doctoral describen en detalle las técnicas de Imagen Médica de mayor relevancia en la actualidad y los principios físicos que rigen la técnica PET.

Los objetivos de esta tesis doctoral pueden dividirse en dos etapas. Una primera etapa que ha consistido en el estudio, desarrollo y mejora de bloques PET basados en cristales monolíticos y SiPMs, y una segunda etapa dedicada a su implementación en equipos reales. Para cumplir los objetivos establecidos, se ha estudiado desde una perspectiva más teórica la distribución de la luz de centelleo en el bloque monolítico y las ecuaciones que caracterizan dicha distribución. Desde la perspectiva experimental, se ha investigado el efecto del tratamiento aplicado a las caras del cristal mejorando la determinación de las coordenadas 3D de interacción del fotón, su acoplamiento con el fotosensor reduciendo perdidas ópticas y también los algoritmos utilizados para comprender y utilizar la información medida. Numerosos tipos de cristales, tratamientos y fotosensores han sido estudiados y evaluados experimentalmente. Como resultado de los estudios realizados, destaca el diseño de dos bloques detectores de alta eficiencia que se han incorporado en dos escáneres PET dedicados al estudio del cerebro (ambos financiados por la Unión Europea) y la obtención de seis publicaciones en revistas de gran interés en la comunidad científica. A continuación, se resumen los resultados obtenidos más relevantes.

El primero de los diseños, esta basado en el uso de un cristal LYSO monolítico de dimensiones de 50 × 50 × 15 mm^3, acoplado a un photosensor de lectura de 12 × 12 SiPMs (SensL, C-Series, 35 um tamaño de celda). La electrónica de readout incluye un sistema innovador de reducción del número de señales que une las filas y columnas centrales del fotosensor manteniendo, por tanto, una buena caracterización de la distribución de luz en los bordes del bloque. Cabe mencionar que en cristales monolíticos la distribución de la luz se trunca en las zonas cercanas a los bordes dando lugar a un posicionamiento erróneo de las coordenadas de interacción, por este motivo es imprescindible caracterizar eficientemente la luz en estas zonas. La electrónica utilizada, dado que mantiene un buen sampleado en los bordes, permite detectar eventos con buena resolución en todo el volumen del cristal sin necesidad de un sistema electrónico complejo. El sistema reduce 12+12 señales a tan solo 8+8 por bloque detector. En el caso del CareMiBrain se han reducido 6912 señales a tan sólo 768. El rendimiento del bloque se ha evaluado usando fuentes radioactivas de ^{22}Na. Los resultados obtenidos muestran una resolución espacial media de 1.8 mm (FWHM), una resolución en DOI de 3.7 mm (FWHM) lo que permite diferenciar los eventos en función de su profundidad de interacción, y una resolución energética del 13% (FWHM). Además, el bloque ha mostrado un buen rendimiento caracterizando eventos cercanos al borde en comparación a un fotosensor estándar de 8 × 8 SiPMs de SensL (J-Series, 35 um cell size). Estos resultados se encuentran en la publicación *"Detector block performance based on a monolithic LYSO crystal using a novel signal multiplexing method"* [3] incluida en el compendio de artículos de esta tesis.

Destaca el hecho de que, debido al buen rendimiento obtenido, este diseño ha sido el seleccionado para la construcción de un equipo PET diseñado dentro de un proyecto nacional perteneciente al programa de investigación e innovación Horizonte 2020 de la Unión Europea. Su objetivo ha sido el desarrollo de un sistema PET, llamado CareMiBrain, dirigido a unidades de trastornos mentales y de medicina nuclear de hospitales en Europa, EE. UU. Y Japón. El sistema está dedicado a la detección temprana de la enfermedad de Alzheimer y a otras causas de deterioro cognitivo.

Cabe mencionar, no obstante, que a pesar de que la técnica PET es uno de los métodos de imagen más utilizados en el ámbito clínico ya que proporciona imágenes altamente específicas y cuantitativas, la ausencia de información anatómica dificulta, en algunos casos, la interpretación de la distribución del radiotrazador, conduciendo a interpretaciones erróneas de las imágenes. Para ayudar al personal médico a localizar y evaluar mejor las lesiones, muchos algoritmos fusionan las imágenes funcionales PET con las imágenes anatómicas proporcionadas por un escáner de tomografía computerizada (CT, del inglés *Computed Tomography*) o de resonancia magnética (MR, del inglés *Magnetic Resonance*).

En algunos casos del ámbito neurológico, como por ejemplo en el diagnóstico de la esquizofrenia y la depresión, está fusión cobra vital importancia. Por un lado, la MR proporciona información anatómica muy detallada pero que no puede ser usada de manera eficiente para diagnosticar clínicamente dichos trastornos mentales, si no que únicamente permite diferenciar la esquizofrenia ya diagnosticada de los controles sanos sobre una base estadística. Por otro lado, la obtención de imágenes PET es extremadamente útil para comprender el tratamiento farmacológico de estas enfermedades y ha ayudado a desarrollar la generación más reciente de medicamentos efectivos. Sin embargo, su utilidad para el diagnóstico clínico de estos trastornos mentales está limitada por: el alto coste, la complejidad de la infraestructura requerida para generar radiofármacos y la limitada sensibilidad y resolución de los escáneres actuales.

Con el objetivo de fusionar la información proporcionada por la MR con la del PET de manera eficiente y así mejorar el estudio de estas enfermedades, surgió el proyecto europeo MINDView. Es un proyecto de naturaleza multidisciplinar cuyo objetivo principal es el diseño y construcción de un innovador escáner PET de alta sensibilidad y resolución, compatible con todos los escáneres de resonancia magnética del mundo. El sistema está dedicado al examen cerebral y al estudio de trastornos psiquiátricos, concretamente al diagnóstico y control de la esquizofrenia. El escáner PET requiere un bloque detector eficiente, compatible con campos magnéticos y de bajo coste facilitando así su transferibilidad. Con este objetivo propusimos el diseño del segundo bloque detector desarrollado en esta tesis doctoral. Este detector está constituido por un cristal monolítico LYSO de dimensiones 50 × 50 × 20 mm^3, acoplado a una matriz de 12 × 12 fotosensores de SensL (MindView-Series). Para mejorar la eficiencia del bloque, se han estudiado dos tratamientos de la superficie del cristal: *i)* pintar todas las caras de negro (excepto la que está en contacto con el fotosensor) y, *ii)* pintar las caras laterales de negro y acoplar una lámina retroreflectora a la cara de entrada del cristal. Esta lámina retroreflectora refleja la luz en la misma dirección de incidencia, incrementando la cantidad de luz que llega al fotosensor pero sin romper la forma de la distribución de la luz, esto es de vital importancia para poder obtener de manera eficiente las coordenadas de interacción del fotón. Numerosas láminas retroreflectoras con diferentes configuraciones han sido evaluadas. Así mismo, se han investigado dos tratamientos para acoplar la lámina al cristal, el uso de aire y grasa óptica. Los mejores resultados se han obtenido usando grasa óptica y láminas pequeñas (rango micrométrico), observándose una mejora de hasta un 25% en la eficiencia global del bloque detector en términos de resolución espacial y energética. Los valores obtenidos son resoluciones espaciales del detector de 1.5 mm, resoluciones en DOI de 4 mm y una resolución energética homogénea a lo largo de todo el cristal del 13%. Una explicación detallada de los experimentos realizados y de la obtención de la coordenada de profundidad de interacción se encuentra en la publicación *"Performance Study of a Large Monolithic LYSO PET Detector With Accurate Photon DOI Using Retroreflector Layers"* [1].

Durante la tesis se ha ensamblado y validado el primer prototipo del escáner MINDView, que ya incluye el bloque detector descrito en [1] El equipo está instalado en el hospital Klinikum Recht der Isaar en Munich y se están realizando pruebas de validación y diagnósticas con pacientes. Los resultados preliminares obtenidos con el equipo se encuentran resumidos en el artículo científico *"Initial Results of the MINDView PET Insert Inside the 3T mMR"* [2]. El equipo está compuesto por 3 anillos con 20 bloques detectores cada uno. Tiene un diámetro de 33 cm y un campo de visión de 15.4 cm, lo que permite la visualización completa de las estructuras cerebrales. El escáner ha sido validado dentro de un campo magnético de 3T (Siemens Biograph mMR) mostrando una alta eficiencia y sin observarse deterioro en los resultados del PET en adquisiciones simultaneas PET y MR. En las imágenes reconstruidas se ha incluido la corrección por DOI, lo que ha dado lugar a resoluciones espaciales de 1.7 mm (FWHM) en el centro del escáner, degradando a tan solo 3 mm (FWHM) a 100 mm del centro. Cuando la DOI no se incluye este valor degrada hasta 7 mm. En la evaluación inicial se ha obtenido una sensibilidad del 7% para un rango energético de 350-650 keV, lo que representa casi un factor 2 de la obtenida con un PET estándar de cuerpo entero. En general, las imágenes obtenidas sugieren una resolución mayor que la provista por los escáneres actuales de cuerpo completo que se usan en los hospitales para estudios neurológicos, demostrando la relevancia del escáner.

Tanto el CareMiBrain como el MINDView son escáneres PET dedicados al estudio del cerebro. Como se ha descrito en la sección 3.4 de esta tesis, los equipos dedicados presentan ciertas ventajas en comparación a los sistemas de PET de cuerpo entero utilizados en estudios neurológicos, tales como una resolución más alta, sensibilidad mayor, un precio competitivo (hasta tres veces menor), necesidades de instalaciones hospitalarias más pequeñas y menor dosis de radiotrazador para el paciente lo que conduce a un menor coste para el sistema de salud. Con todos estos avances se espera una detección temprana de las enfermedades neurológicas, mejorando el pronóstico del paciente. Actualmente, ambos equipos han superado las pruebas de certificación y los primeros pacientes ya han sido escaneados. Estos equipos presentan como desventaja el hecho de que sólo pueden ser usados para estudiar un órgano.

Otro objetivo abordado en la tesis, ha sido la investigación de bloques detectores PET basados en cristales centelleadores BGO, con la finalidad de mejorar su rendimiento. Los cristales de BGO fueron introducidos durante los años 1970-1980, y fueron la opción favorita para construir escáneres PET. No obstante, fue finalmente sustituido por cristales más rápidos y eficientes tales como LSO y LYSO. El principal inconveniente que presentan los cristales centelleadores de BGO es su bajo *Light Yield*, es decir, la eficiencia de conversión de la energía depositada por el rayo gamma de 511 keV en fotones ópticos. Esto se traduce en un peor rendimiento del bloque en términos de resolución energética y temporal.

En una primera aproximación estudiamos el rendimiento de bloques BGO pixelados obteniendo buenos resultados en términos de resolución espacial y energética, así como una determinación discreta de la profundidad de interacción [184]. Tras esto, a fin de ahondar en todas las ventajas que presentan los bloques monolíticos, extendimos nuestro estudio a dichos bloques. En este caso, para mejorar la transferencia de luz al fotosensor, investigamos el uso de nano-estructuras. Estas estructuras se imprimen en la cara de salida del cristal (la que está en contacto con el fotosensor) y, debido a principios de difracción y de acoplamiento de los índices de reflexión permiten aumentar de manera aleatoria la extracción de fotones. Al igual que en los diseños anteriores, el bloque incluye una lámina retroreflectora acoplada a la cara de entrada y los laterales pintados de negro [1][3]. Además, se han estudiado dos configuraciones de la matriz de fotosensores, la primera es una agrupación de 12 × 12 SiPMs (SensL C-Series, 52% área activa) mientras que la segunda está basada en una agrupación de 16 × 16 SiPMs (SensL J-Series, 92% área activa). Dada su mayor área activa, mejores resultados han sido obtenidos con la configuración de 16 × 16 SiPMs. Respecto a los tratamientos evaluados, la mejor resolución energética (~ 20%) ha sido obtenida usando la estructura de nanopattern. Sin embargo, dicha estructura, dado que la extracción de fotones se produce de manera aleatoria cambiando su trayectoria, rompe ligeramente la forma de la distribución de la luz empeorando, por tanto, la resolución espacial y DOI. De esta manera, si tenemos en cuenta los tres parámetros más relevantes a la hora de caracterizar un bloque detector, resolución espacial energética y DOI, mejor rendimiento global ha sido obtenido para el fotosensor de 16 × 16 SiPMs y el tratamiento incluyendo la lámina retroreflectora pero sin la nano-estructura. Para este caso en concreto, se ha obtenido una resolución DOI de 5.3 mm, lo que nos ha permitido distinguir tres capas de interacción en el cristal, obteniendo resoluciones espaciales de 2.5 mm en la entrada del cristal (15-10 mm desde el fotosensor), 2.2 mm (10-5 mm) y 1.6 mm (5-0 mm). Ver el artículo *"Highly improved operation of monolithic BGO-PET blocks"* [4] incluido en la tesis. Estos resultados sugieren que los bloques monolíticos BGO acoplados a SiPMs son unos buenos candidatos para construir escáneres PET de alta sensibilidad que requieren grandes volúmenes de material centelleador. Un ejemplo es el actual equipo EXPLORER, que está siendo construido y en el cual el volumen de material requerido es muy grande [91].

El último bloque detector PET diseñado y validado en esta tesis es un bloque hibrido que además permite ser utilizado de manera simultanea con equipos de resonancia magnética. Este diseño combina en un solo bloque detector, cristales pixelados y monolíticos, beneficiándose de las ventajas presentes en cada uno de ellos. Por un lado, el cristal pixelado dota al bloque de una resolución espacial homogénea en todo el detector, determinada por el tamaño del pixel empleado. Por otro lado, el bloque monolítico aumenta la sensibilidad del detector y permite una caracterización continua de la DOI. En el diseño propuesto hemos ubicado el bloque monolítico en contacto con el fotosensor de manera que, el rayo gamma atraviesa primero el bloque pixelado. De esta manera, la mayor parte de la luz de centelleo se transfiere al fotosensor a través del cristal monolítico, que actúa como una guía de luz, sin perdidas significativas y por tanto la buena resolución energética y de posicionamiento del cristal pixelado son preservadas. En este estudio, hemos utilizado pixeles de tan solo 0.8 × 0.8 mm^2, que han podido resolverse completamente. En el cristal monolítico hemos obtenido una resolución espacial media de 1.6 mm (FWHM). Además, este bloque híbrido proporciona dos informaciones DOI distintas, una discreta de 4-5 mm y otra continua (gracias al bloque monolítico) en el rango de 2-3 mm (FWHM). Además, la buena resolución energética obtenida junto con la resolución DOI permite diferenciar los eventos en función de la capa de interacción. Este concepto híbrido puede extenderse a más de dos componentes y provee una buena resolución tridimensional de las coordenadas de interacción a la vez que una buena eficiencia de detección a un coste razonable. Para más detalles ver el artículo *"A scintillator geometry suitable for very small PET gantries"* [5].

Tanto la propuesta del bloque BGO como la híbrida, muestran una prueba de concepto de dos bloques detectores innovadores que presentan una buena eficiencia. El diseño híbrido podría emplearse en equipos de pequeños animales obteniendo imágenes de alta resolución. El diseño BGO, dado su reducido coste, sería un muy buen candidato para construir equipos PET de cuerpo entero donde el volumen de material centelleador requerido es elevado y la dosis administrada es baja.

El último objetivo abordado en la tesis ha sido el estudio de la resolución temporal de los bloques PET basados en cristales monolíticos. Este objetivo esta motivado por el hecho de que incluir información temporal de la interacción del fotón en el cristal durante la reconstrucción permite acotar la línea de respuesta y mejorar sustancialmente la imagen final. Dado que la electrónica que hemos empleado en el desarrollo de los bloques detectores presentados previamente no es óptima para obtener buenas resoluciones temporales, para este estudio hemos utilizado ASICs. En concreto, hemos estudiado e implementado el PETsys TOF-PET ASIC acoplado a un fotosensor de 8 × 8 SiPMs (Mod. s12642-0808pb) de Hamamatsu Photonics con 3 × 3 mm^2 de área activa. En un primer acercamiento al uso de estos ASICs y con la finalidad de caracterizar el bloque detector hicimos uso de cristales LYSO pixelados obteniendo una resolución temporal, evaluada a través del CRT (del inglés *Coincidence Resolving Time*), de 370 ps. Tras estos experimentos, comenzamos a validar el sistema con dos cristales LYSO monolíticos de 24.5 × 24.5 mm^2, y 10 mm and 5 mm de altura respectivamente. Dado que la resolución temporal está directamente relacionada con la cantidad de luz que llega al fotosensor, con el objetivo de incrementar dicha cantidad de luz las caras del cristal fueron cubiertas con material reflejante ESR. En este caso se demostró la habilidad para obtener una buena resolución DOI y espacial utilizando ASICs. Se investigaron numerosos métodos para obtener la marca temporal de cada impacto, obteniendo el mejor resultado con el método *averaged weighting for the sigma average*, se obtuvo un CRT de 1.2 ns. Los detalles del método están descritos en *"Pilot tests of a PET detector using the TOF-PET ASIC based on monolithic crystals and SiPMs"* [6].

Dicho valor no es óptimo, por este motivo a fin de mejorarlo, se implementó y estudió la segunda generación del ASIC, junto con el uso de láminas retroreflectoras. Una mejora en el rendimiento del bloque fue obtenida alcanzando valores de resolución temporal de 585 ps en un bloque LYSO monolítico de 15 mm [171]. Actualmente estamos investigando métodos para mejorar este valor y poder incluir dicha información en equipos de geometría abierta con limitaciones angulares.

En conclusión, en esta tesis doctoral hemos diseñado y evaluado el rendimiento de bloques detectores PET basados en cristales centelleadores monolíticos y fotodetectores de SiPMs. En general, se ha obtenido una buena caracterización de los perfiles de la distribución de la luz de centelleo generada en el cristal. Esta información ha sido utilizada para estimar las coordenadas de impacto del fotón, incluyendo la coordenada de profundidad de interacción, obteniendo una buena resolución espacial, energética y de DOI. Se ha observado un gran deterioro en la calidad de la imagen reconstruida cuando la información relativa a la profundidad de interacción no se ha incluido demostrando, por tanto, la relevancia de dicha coordenada. Actualmente estamos investigando métodos para calibrar la posición de interacción en función de la profundidad de interacción, lo que podría mejorar la resolución espacial a lo largo del eje axial del escáner.

Así mismo, se ha demostrado que aumentando el numero de fotones de centelleo recolectados aumenta el rendimiento del bloque detector. A lo largo de la tesis se han evaluado numerosos tratamientos de las superficies de los cristales, siempre aumentando dicha recolección. Cabe mencionar, que siempre se ha intentado preservar todo lo posible la forma de la distribución de la luz ya que los algoritmos de posicionamiento empleados, *CoG, RTP y E/I* requieren su conservación. Por este motivo el tratamiento que mejor resultado general ha proporcionado es el uso de láminas retroreflectoras acopladas a la cara de entrada del cristal centelleador. No obstante, si utilizásemos otros métodos de posicionamiento que no requieran preservar la forma de la distribución de la luz, tales como redes neurales o algoritmos basados en el *machine learning* permitirían la aplicación de otros tratamientos tales como láminas reflectoras, ESR en todas las caras. El siguiente paso en nuestra investigación es mejorar la resolución temporal obtenida con los cristales monolíticos acoplados al ASIC para mejorar la imagen final obtenida y aplicar este conocimiento a sistemas en los cuales la geometría es abierta.

Como resultado de las investigaciones llevadas a cabo, dos de los bloques detectores diseñados han sido utilizados en la construcción de dos sistemas PET dedicados al estudio del cerebro, por tanto, se ha conseguido la traslación de nuestra investigación al ámbito clínico. Además, uno de los sistemas ha sido exitosamente testeado bajo la influencia de campos magnéticos demostrando el potencial de los fotosensores SiPMs. Muy buenos resultados han sido obtenidos para estos equipos PET, incluso trabajando simultáneamente con secuencias de resonancia muy intentas tales como la EPI o UTE. La fusión de PET y resonancia magnética proporcionarán imágenes funcionales del cerebro muy precisas mejorando por tanto el diagnóstico clínico.

Los avances en instrumentación son clave para el continuo desarrollo y mejora de los escáneres PET y por tanto de la calidad diagnóstica de determinadas enfermedades. Con este objetivo, esta tesis doctoral aborda el estudio, diseño e implementación de nuevos bloques detectores de alta eficiencia. Los resultados obtenidos durante la tesis dan soporte experimental a los conceptos y a las líneas de investigación seguidas por el grupo y, además, motivan el continuo desarrollo y mejora de estos bloques, impulsando también el continuo avance en la investigación para mejorar el diagnóstico clínico y por tanto la calidad de vida de los pacientes.

7. Resum i Conclusions

La medicina nuclear constitueix una especialitat mèdica que utilitza substàncies radioactives amb fins de diagnòstics i terapèutics. Dins d'aquesta branca de la medicina trobem nombroses tècniques de diagnòstic com ara la Càmera Gamma, la tomografia per emissió d'un únic fotó (SPECT, de l'anglès *Single Photon Emission Tomography*) i la tomografia per emissió de positrons (PET, de l'anglès *Positron Emission Tomography*). Aquestes tècniques d'imatge mèdica permeten visualitzar processos fisiològics i bioquímics del cos humà *in vivo*, mitjançant la injecció d'un element radiotraçador. Els radiotraçadors són compostos químics, similars a les substàncies naturals del cos, en què un o més àtoms són substituïts per radionúclids emissors de fotons, per al seu ús en càmeres gamma i SPECT, o de positrons (l'antipartícula de l'electró) per PET.

La tècnica PET ha experimentat millores significatives en els últims 60 anys, establint-se en l'actualitat com una eina diagnòstica imprescindible en medicina. Per aquest motiu i per tal de millorar la qualitat diagnòstica, l'objectiu principal d'aquesta tesi doctoral ha estat el desenvolupament de nous detectors PET de gran eficiència.

L'obtenció de la imatge PET comença amb la injecció de l'element radiotraçador en el subjecte d'estudi. Allí es desintegra emetent positrons que viatgen a l'interior del cos del pacient a l'atzar fins que col·lisionen amb un electró cortical del teixit. Com a resultat d'aquesta col·lisió s'emeten dos raigs gamma de 511 keV, en direccions gairebé oposades, que són detectats en coincidència en l'escàner PET registrant un esdeveniment. La informació relativa a aquests esdeveniment és enviada a un ordinador, on finalment, algoritmes de reconstrucció són emprats per generar una imatge mostrant la distribució tridimensional del radiotraçador a l'interior del cos. La selecció del radiotraçador depèn de l'estudi que es va a realitzar. Per exemple, la 18F-fluoro-desoxi-glucosa (18F-FDG), que és el compost més utilitzat en PET, s'empra com un traçador de captació de glucosa ja que segueix una ruta metabòlica similar a la glucosa *in vivo*, l'única diferència és que roman atrapada dins del teixit sense metabolitzar en CO_2 i aigua. Això és d'especial interès en oncologia atès que les cèl·lules canceroses proliferants tenen una taxa metabòlica de glucosa superior a la mitjana, i capten la 18F-FDG.

La tècnica d'imatge PET s'empra fonamentalment en l'estudi de malalties oncològiques, cardiovasculars i neurològiques. Cal esmentar, però, la seua especial rellevància en l'estudi del cervell i de les seves malalties associades. De fet, el primer dispositiu d'imatge basat en la detecció en coincidències de positrons va ser construït el 1952 per Brownell i Sweet [69], i era un sistema dedicat a l'estudi del cervell. No va ser fins 1970-1973 quan Robertson i Thompson van construir el primer escàner PET complet, anomenat Positome [74].

La qualitat diagnòstica derivada del PET, està lligada a la qualitat de la imatge proporcionada, la qual depèn de l'eficiència dels blocs detectors que constitueixen l'escàner. Aquests blocs estan constituïts per tres components principals: el cristall centellejador, el fotosensor i la seua electrònica associada. El cristall centellejador és l'encarregat de frenar els raigs gammes de 511 keV emesos des de l'interior del pacient, generant fotons òptics de menor energia que seran detectats en el fotosensor. La informació recol·lectada es processa amb l'electrònica associada i s'envia a l'ordinador per a la seva posterior reconstrucció. Durant el procés de reconstrucció s'apliquen nombroses correccions tals com la correcció per atenuació, normalització o dispersió.

En l'actualitat, la majoria de sistemes PET comercials estan constituïts per blocs detectors basats en cristalls pixelats (matrius de petits cristalls) i tubs fotomultiplicadors (PMT, de l'anglès *Photomultiplier Tubes*). Els cristalls pixelats permeten estimar les coordenades (x, y) de l'impacte del fotó de manera senzilla, però, l'obtenció de la coordenada de profunditat d'interacció (z), imprescindible per corregir l'error de paral·laxi i obtenir una bona resolució espacial sobretot a als llindars del camp de visió de l'escàner, resulta una tasca difícil requerint l'ús de materials extres i per tant incrementant el preu total de l'escàner. A més a més, la resolució espacial d'aquests blocs està limitada per la mida del píxel; en el cas dels PMT la seua gran grandària i incompatibilitat amb camps magnètics limita el seu ús.

Una alternativa a la configuració anterior, és l'ús de blocs monolítics i fotodetectors de silici (SIPM, de l'anglès *Silicon Photomultiplier*). Aquests blocs de cristall monolític estan constituïts per una única peça de material centellejador que permet observar la distribució de fotons òptics generada. Aquesta informació és utilitzada per obtenir les coordenades 3D d'impacte del fotó (*x, y, z*) amb bona resolució sense necessitat de materials extra, damunt són més fàcils de produir i per tant més econòmics. Els SIPMs són detectors d'estat sòlid, el seu desenvolupament ha estat una contribució clau a les recents millores en PET ja que són més compactes que els PMT permetent la construcció d'escàners més robustos, tenen una major granularitat el que millora la recol·lecció de la llum de centelleig, presenten una gran quantitat de configuracions i a més, són compatibles amb camps magnètics. Els capítols 1 i 2 d'aquesta tesi doctoral descriuen en detall les tècniques d'imatge mèdica més rellevants en l'actualitat, així com els principis físics que regeixen les tècnica PET.

Els objectius d'aquesta tesi doctoral poden dividir-se en dues etapes. Una primera etapa que ha consistit en l'estudi, desenvolupament i millora de blocs PET basats en cristalls monolítics i SIPMs, i una segona etapa dedicada a la seua implementació en equips reals. Per complir els objectius establerts, s'ha estudiat des d'una perspectiva més teòrica la distribució de la llum de centelleig en el bloc monolític i les equacions que caracteritzen aquesta distribució. Des de la perspectiva experimental, s'ha investigat l'efecte del tractament aplicat a les cares del cristall millorant la determinació de les coordenades 3D d'interacció del fotó, el seu acoblament amb el fotosensor reduint perdudes òptiques i també els algoritmes utilitzats per comprendre i utilitzar la informació mesurada. Nombrosos tipus de cristalls, tractaments i fotosensors han estat estudiats i avaluats experimentalment. Com a resultat dels estudis realitzats, destaca el disseny de dos blocs detectors d'alta eficiència que s'han incorporat en dos escàners PET dedicats a l'estudi del cervell (ambdós finançats per la Unió Europea) i l'obtenció de sis publicacions en revistes d'alt interès en la comunitat científica. A continuació, es resumeixen els resultats obtinguts més rellevants.

El primer dels dissenys, està basat en l'ús d'un cristall LYSO monolític de dimensions de 50 × 50 × 15 mm^3, acoblat a un fotosensor de 12 × 12 SiPMs (SensL, C-Sèries, 35 um mida de cel·la). L'electrònica de readout inclou un sistema innovador de reducció del nombre de senyals que uneix les files i columnes centrals del fotosensor mantenint, per tant, una bona caracterització de la distribució de llum als límits del bloc. Cal esmentar que en cristalls monolítics la distribució de la llum es trunca a les zones properes als margens donant lloc un posicionament erroni de les coordenades d'interacció, per aquest motiu és imprescindible caracteritzar eficientment la llum en aquestes zones. El readout utilitzat, atès que manté un bon samplejat a les vores, permet detectar esdeveniments amb bona resolució en tot el volum sense necessitat d'un sistema electrònic complex. El sistema redueix 12 + 12 senyals a tan sols 8 + 8 per bloc detector. En el cas de CareMiBrain s'han reduït 912 senyals a an sols 768. El rendiment del bloc s'ha avaluat utilitzant fonts radioactives de ^{22}Na. Els resultats obtinguts mostren una resolució espacial mitjana de 1.8 mm (FWHM), una resolució en DOI de 3.7 mm (FWHM) el que permet diferenciar els esdeveniments en funció de la seva profunditat d'interacció en fins a 4 capes, i una resolució energètica del 13% (FWHM). A més, el bloc ha mostrat un millor rendiment caracteritzant esdeveniments propers a la vora en comparació a un fotosensor estàndard de 8 × 8 SiPMs de SensL (J-Sèries, 35 um mida de cel·la). Aquests resultats es troben a la publicació *"Detector bloc performance based on a Monolithic LYSO crystal using a novell signal multiplexing method"* [3] inclosa en la tesi.

Destaca el fet que, a causa del bon rendiment obtingut, aquest disseny ha estat el seleccionat per a la construcció d'un equip PET dissenyat dins d'un projecte nacional pertanyent al programa de recerca i innovació Horitzó 2020 de la Unió Europea liderat per l'empresa Oncovisión. El seu objectiu ha estat el desenvolupament d'un sistema PET, anomenat CareMiBrain, dirigit a unitats de trastorns mentals i de medicina nuclear d'hospitals a Europa, EUA i Japó. El sistema està dedicat a la detecció primerenca de la malaltia d'Alzheimer i altres causes de deteriorament cognitiu.

Cal esmentar, però, que tot i que la tècnica PET és un dels mètodes d'imatge més utilitzats en l'àmbit clínic ja que proporciona imatges altament específiques i quantitatives, l'absència d'informació anatòmica dificulta, en alguns casos, la interpretació de la distribució del radiotraçador, conduint a interpretacions errònies de les imatges. Per ajudar el personal mèdic a localitzar i avaluar millor les lesions, molts algoritmes fusionen les imatges funcionals PET amb les imatges anatòmiques proporcionades per un escàner de tomografia computeritzada (CT, de l'anglès *Computerized Tomography*) o de ressonància magnètica (MR, de l'anglès *Magnetic Resonance*).

En alguns casos de l'àmbit neurològic, com per exemple en el diagnòstic de l'esquizofrènia i la depressió, està fusió té vital importància. D'una banda, la MR proporciona informació anatòmica molt detallada però que no pot ser utilitzada de manera eficient per diagnosticar clínicament aquests trastorns mentals, sinó que únicament permet diferenciar l'esquizofrènia ja diagnosticada dels controls sans sobre una base estadística. D'altra banda, l'obtenció d'imatges PET és extremadament útil per comprendre el tractament farmacològic d'aquestes malalties i ha ajudat a desenvolupar la generació més recent de medicaments efectius. No obstant això, la seua utilitat per al diagnòstic clínic d'aquests trastorns mentals està limitada per: l'alt cost, la complexitat de la infraestructura requerida per generar radiofàrmacs i la limitada sensibilitat i resolució dels escàners actuals.

Amb l'objectiu de fusionar la informació proporcionada per la MR amb la del PET de manera eficient per a l'estudi d'aquestes malalties, va sorgir el projecte europeu MINDVIEW. És un projecte de naturalesa multidisciplinària amb l'objectiu principal de dissenyar i construir un innovador escàner PET d'alta sensibilitat i resolució, compatible amb tots els escàners de ressonància magnètica del món. El sistema està dedicat a l'examen cerebral i l'estudi de trastorns psiquiàtrics, concretament al diagnòstic i control de l'esquizofrènia. L'escàner PET requereix un bloc detector eficient, compatible amb camps magnètics i de baix cost facilitant així la seva transferibilitat. Amb aquest objectiu va sorgir el disseny del segon bloc detector desenvolupat en aquesta tesi doctoral. Aquest detector està constituït per un cristall monolític LYSO de dimensions 50 x 50 x 20 mm^3, acoblat a una matriu de 12x12 fotosensors de SensL (MindView-Series). Per millorar l'eficiència del bloc, s'han estudiat dos tractaments de la superfície del cristall: i) pintar totes les cares de negre (excepte la que està en contacte amb el fotosensor) i, ii) pintar les cares laterals de negre i acoblar una làmina retroreflectora a la cara d'entrada del cristall. Aquesta làmina retroreflectora reflecteix la llum en la mateixa direcció d'incidència, incrementant la quantitat de llum que arriba al fotosensor però sense trencar la forma de la distribució de la llum, això és de vital importància per poder obtenir de manera eficient les coordenades d'interacció del fotó. Nombroses làmines amb diferents configuracions han estat avaluades. Així mateix, s'han investigat dos tractaments per a acoblar la làmina al cristall, l'ús d'aire i greix òptic. Els millors resultats s'han obtingut usant greix òptic i làmines petites (rang submil·limètric), observant-se una millora de fins a un 25% en l'eficiència global del bloc detector en termes de resolució espacial i energètica. Els valors obtinguts són resolucions espacials de 1.5 mm, resolucions en DOI de 4 mm i una resolució energètica homogènia al llarg de tot el cristall del 13%. Una explicació detallada dels experiments realitzats i de l'obtenció de la coordenada de profunditat d'interacció es troba a la publicació *"Performance Study of a Large Monolithic LYSO PET Detector With Accurate Photon DOI Using retroreflector Layers"* [1].

Durant la tesi s'ha acoblat i validat el primer prototip de l'escàner MINDView, que ja inclou aquest bloc detector. L'equip està instal·lat a l'hospital Klinikum Recht der ISAAR a Munic i on s'estan realitzant proves de validació i diagnòstiques amb pacients. Els resultats preliminars obtinguts amb l'equip es troben resumits en l'article científic *"Initial Results of the MINDView PET Insert Inside the 3T MMR"* [2]. L'equip està compost per 3 anells amb 20 blocs detectors cadascun. Té un diàmetre de 33 cm i un camp de visió de 152 mm, el que permet la visualització completa de les estructures cerebrals. L'escàner ha estat validat dins d'un camp magnètic de 3T (Siemens Biograph MMR) mostrant una alta eficiència i sense observar-se deteriorament en els resultats del PET a adquisicions simultànies. A les imatges reconstruïdes s'ha inclòs la correcció per DOI, el que ha donat lloc a resolucions espacials de 1.7 mm (FWHM) al centre de l'escàner, degradant a només 3 mm (FWHM) a 100 mm del centre. Quan la DOI no s'inclou aquest valor degrada fins a 7 mm. En l'avaluació inicial s'ha obtingut una sensibilitat del 7% per a un rang energètic de 350-650 keV. En general, les imatges obtingudes suggereixen una resolució més gran que la proveïda pels escàners actuals de cos complet que es fan servir en els hospitals per a estudis neurològics, demostrant la rellevància de l'escàner.

Tant el CareMiBrain com el MINDView són escàners PET dedicats a l'estudi del cervell. Com ja ha sigut descrit en la secció 3.4 d'aquesta tesi, els equips dedicats presenten certs avantatges en comparació als sistemes de PET de cos sencer utilitzats en estudis neurològics, com ara una resolució més gran, sensibilitat més gran, un preu competitiu (fins a tres vegades menor), necessitats d'instal·lacions hospitalàries més petites i menor dosi de radiotraçador per al pacient el que condueix a un menor cost per al sistema de salut. Amb tots aquests avanços s'espera una detecció primerenca de les malalties neurològiques, millorant el pronòstic del pacient. Actualment, aquests equips han superat les proves de certificació i els primers pacients ja han estat escanejats.

El següent objectiu abordat en la tesi, ha estat la investigació de blocs detectors PET basats en cristalls centellejadors BGO, amb la finalitat de millorar el seu rendiment. Els cristalls de BGO van ser introduïts durant els anys 1970-1980, i van ser l'opció preferida per construir escàners PET. No obstant això, va ser finalment substituït per nous cristalls més ràpids i eficients com ara LSO i LYSO. El principal inconvenient que presenten els cristalls centellejadors de BGO és el seu baix *Light Yield*, és a dir, l'eficiència de conversió de l'energia dipositada pel raig gamma de 511 keV en fotons òptics. Això es tradueix en un pitjor rendiment del bloc en termes de resolució energètica i temporal.

En una primera aproximació estudiem el rendiment de blocs BGO pixelats obtenint molt bons resultats en termes de resolució espacial i energètica, obtenint una determinació discreta de la profunditat d'interacció [184]. Després d'això, per tal de treure partit a tots els avantatges que presenten els blocs monolítics, vam estendre el nostre estudi a aquests blocs. En aquest cas, per millorar la transferència de llum al fotosensor, investiguem l'ús d'estructures de nanopattern. Aquestes estructures s'imprimeixen a la cara de sortida del cristall (la que està en contacte amb el fotosensor) i, a causa de principis de difracció i d'acoblament dels índexs de reflexió permet augmentar de manera aleatòria l'extracció de fotons. Igual que en els dissenys anteriors, el bloc inclou una làmina retroreflectora acoblada a la cara d'entrada i els laterals pintats de negre [1][4]. A més, s'han estudiat dues configuracions de la matriu de fotosensors, la primera és una agrupació de 12 x 12 SiPMs (SensL C-Sèries, 52% àrea activa) mentre que la segona està basada en una agrupació de 16 × 16 SiPMs (SensL J-Sèries, 92% àrea activa). Donada la seva major àrea activa, millors resultats han estat obtinguts amb la configuració de 16 × 16 SiPMs. Pel que fa als tractaments avaluats, la millor resolució energètica (~ 20%) ha estat obtinguda utilitzant l'estructura de nanopattern. No obstant això, aquesta estructura, donat que l'extracció de fotons es produeix de manera aleatòria canviant la seva trajectòria, trenca lleugerament la forma de la distribució de la llum empitjorant, per tant, la resolució espacial i DOI. D'aquesta manera, si tenim en compte els tres paràmetres més rellevants a l'hora de caracteritzar un bloc detector, resolució espacial energètica i DOI, millor rendiment global ha estat obtingut per al fotosensor de 16 × 16 SiPMs i el tractament incloent la làmina retroreflectora però sense l'estructura de nanopattern. En aquest cas, s'ha obtingut una resolució DOI de 5.3 mm, el que ens ha permès distingir tres capes d'interacció al cristall, obtenint resolucions espacials de 2.5 mm a l'entrada del cristall (15-10 mm des de la fotosensor) , 2.2 mm (10-5 mm) i 1.6 mm (5-0 mm). Veure l'article *"Highly improved operation of Monolithic BGO-PET blocks"* [4] inclòs en la tesi. Aquests resultats suggereixen que els blocs monolítics BGO acoblats a SiPMs són uns bons candidats per construir escàners PET d'alta sensibilitat que requereixen grans volums de material centellejador. Un exemple és l'actual equip EXPLORER, que està sent construït i en el qual el volum de material requerit és molt gran [91].

L'últim bloc detector PET dissenyat i validat en aquesta tesi és un bloc híbrid que a més permet ser utilitzat de manera simultània amb equips de ressonància magnètica. Aquest disseny combina l'ús de blocs de cristalls pixelats i monolítics, beneficiant-se dels avantatges presents a cada un d'ells. D'una banda, el cristall pixelat dota el bloc detector d'una resolució espacial homogènia, determinada per la grandària del píxel emprat, en tot el detector. D'altra banda, el bloc monolític augmenta la sensibilitat del detector i permet una caracterització contínua de la DOI. En el disseny proposat hem situat el bloc monolític en contacte amb el fotosensor de manera que, el raig gamma travessa primer el bloc pixelat. D'aquesta manera, la major part de la llum de centelleig es transfereix al fotosensor a través del cristall monolític, que actua com una guia de llum, sense pèrdues significatives i per tant la bona resolució energètica i de posicionament del cristall pixelat són preservades. En aquest estudi, hem utilitzat píxels de tan sols 0.8 × 0.8 mm^2, que han pogut resoldre completament. Al cristall monolític hem obtingut una resolució espacial mitjana de 1.6 mm (FWHM). A més, aquest bloc híbrid proporciona dues informacions DOI diferents, una discreta de 4-5 mm i una altra contínua (gràcies al bloc monolític) en el rang de 2-3 mm (FWHM). A més, la bona resolució energètica obtinguda juntament amb la resolució DOI permet diferenciar els esdeveniments en funció de la capa d'interacció. Aquest concepte híbrid pot estendre a més de dos components i proveeix una bona resolució tridimensional de les coordenades d'interacció alhora que una bona eficiència de detecció a un cost raonable. Per a més detalls veure l'article *"A Scintillator geometry suitable for very small PET gantries"* [5].

Tant la proposta del bloc BGO com la híbrida, mostren una prova de concepte de dos blocs detectors innovadors que presenten una bona eficiència. El disseny híbrid podria emprar-se en equips de petits animals obtenint imatges d'alta resolució. El disseny BGO, donat el seu reduït cost, seria un molt bon candidat per construir equips PET de cos sencer on el volum de material centellejador requerit és elevat.

L'últim objectiu abordat en la tesi ha estat l'estudi de la resolució temporal dels blocs PET basats en cristalls monolítics. Aquest objectiu està motivat pel fet d'incloure informació temporal de la interacció del fotó al cristall durant la reconstrucció permetent acotar la línia de resposta i millorar substancialment la imatge final. Atès que l'electrònica que hem emprat en el desenvolupament dels blocs detectors presentats prèviament no és òptima per obtenir bones resolucions temporals, per a aquest estudi hem utilitzat ASICs. En concret, hem estudiat i implementat el PETsys TOF-PET ASIC acoblat a un fotosensor de 8 × 8 MPPC (Mod. S12642-0808pb) d'Hamamatsu Photonics amb 3 × 3 mm^2 d'àrea activa. En un primer acostament a l'ús d'aquests ASICs i amb la finalitat de caracteritzar el bloc detector vam fer ús de cristalls LYSO pixelats obtenint una resolució temporal, avaluada a través del CRT, de 370 ps. Després d'aquests experiments, vam començar a validar el sistema amb dos blocs LYSO monolítics de 24.5 × 24.5 mm^2, i 10 mm i 5 mm d'altura respectivament. Atès que la resolució temporal està directament relacionada amb la quantitat de llum que arriba al fotosensor, amb la finalitat d'incrementar aquesta quantitat de llum les cares del cristall van ser cobertes amb material reflectant ESR. En aquest cas es va demostrar l'habilitat per obtenir una bona resolució DOI i espacial utilitzant ASICs. Es van investigar nombrosos mètodes per obtenir la marca temporal de cada impacte, obtenint el millor resultat amb el mètode *averaged weighting for the sigma average*, es va obtenir un CRT de 1.2 ns. Els detalls del mètode estan descrits en *"Pilot tests of a PET detector using the TOF-PET ASIC based on Monolithic crystals and SiPMs"* [6].

Aquest valor no és òptim, per aquest motiu a fi de millorar-lo, es va implementar i estudiar la segona generació de l'ASIC, juntament amb l'ús de làmines retroreflectores. Una millora en el rendiment del bloc va ser obtinguda aconseguint valors de resolució temporal de 585 ps en un bloc LYSO monolític de 15 mm [171]. Actualment estem investigant mètodes per millorar aquest valor i poder incloure aquesta informació en equips de geometria oberta amb limitacions angulars.

En conclusió, en aquesta tesi doctoral hem dissenyat i avaluat el rendiment de blocs detectors PET basats en cristalls centellejadors monolítics i fotodetectors de SiPMs. En general, s'ha obtingut una bona caracterització dels perfils de la distribució de la llum de centelleig generada al bloc monolític. Aquesta informació ha estat utilitzada per estimar les coordenades d'impacte del fotó, incloent la coordenada de profunditat d'interacció, obtenint una bona resolució espacial, energètica i de DOI. S'ha observat un gran deteriorament en la qualitat de la imatge quan la informació relativa a la profunditat d'interacció no s'ha inclòs en la reconstrucció demostrant, per tant, la rellevància d'aquesta coordenada. Actualment estem investigant mètodes per calibrar la posició d'interacció del fotó en funció de la profunditat d'interacció, el que podria millorar la resolució espacial al llarg de l'eix axial de l'escàner.

Així mateix, s'ha demostrat que augmentant el nombre de fotons de centelleig col·lectats augmenta el rendiment del bloc detector. Al llarg de la tesi s'han avaluat nombrosos tractaments de les superfícies dels cristalls, sempre augmentant aquesta recol·lecció. Cal esmentar, que sempre s'ha intentat preservar tot el possible la forma de la distribució de la llum ja que els algoritmes de posicionament empleats, *CoG*, *RTP* i *E/I* requereixen la seva conservació. Per aquest motiu el tractament que millor resultat general ha proporcionat és l'ús de làmines retroreflectores acoblades a la cara d'entrada del cristall centellejador. No obstant, si utilitzéssim altres mètodes de posicionament que no requereixin preservar la forma de la distribució de la llum, com ara xarxes neurals o algoritmes basats en el *machine learning* permetrien l'aplicació d'altres tractaments com ara làmines reflectores, ESR, en totes les cares proporcionant bons resultats. El següent pas en la nostra investigació és millorar la resolució temporal obtinguda amb els cristalls monolítics acoblats a l'ASIC per millorar la imatge final obtinguda i aplicar aquest coneixement a sistemes en els quals la geometria és oberta.

Com a resultat de les investigacions dutes a terme, dos dels blocs detectors dissenyats han estat utilitzats en la construcció de dos sistemes PET dedicats a l'estudi del cervell, per tant, s'ha aconseguit la traslació de la nostra investigació a l'àmbit clínic. A més, un dels sistemes ha estat reeixidament testejat sota la influència de camps magnètics demostrant el potencial dels fotosensors SiPMs. Molt bons resultats han estat obtinguts per aquests equips PET, fins i tot treballant simultàniament amb seqüències de ressonància molt intenses com ara l'EPI o UTE. La fusió de PET i ressonància magnètica proporcionaran imatges funcionals del cervell molt precises millorant per tant el diagnòstic clínic.

En conclusió, els avanços en instrumentació són clau per al continu desenvolupament i millora dels escàners PET i per tant de la qualitat diagnòstica de determinades malalties. Amb aquest objectiu, aquesta tesi doctoral aborda l'estudi, disseny i implementació de nous blocs detectors d'alta eficiència. Els resultats obtinguts durant la tesi donen suport experimental als conceptes i les línies d'investigació seguides pel grup i, a més, motiven el continu desenvolupament i millora d'aquests blocs, motivant també el continu avanç en la investigació per millorar el diagnòstic clínic i per tant la qualitat de vida dels pacients.

Bibliography

[1] A. Gonzalez-Montoro, et al., "Performance study of a large monolithic LYSO PET detector with accurate photon DOI using retroreflector layers,". IEEE Trans. Rad. Plasma. Med. Sci., Vol. 1, 2017.

[2] A. J. Gonzalez, et al., "Initial Results on the MINDView PET Insert Inside the 3T mMR," IEEE Trans. Rad. Plasma. Med. Sci., In press, 2018.

[3] A. González-Montoro, et al., "Detector block performance based on a monolithic LYSO crystal using a novel signal multiplexing method," Nucl. Inst. Meth. A. In press, 2018, https://doi.org/10.1016/j.nima.2017.10.098.

[4] A. Gonzalez-Montoro, et al., "Highly improved operation of monolithic BGO-PET blocks," J. Instrum., Vol. 12, C11027, 2017.

[5] A. J. Gonzalez, et al., "A scintillator geometry suitable for very small PET gantries,". J. Instrum., Vol. 12, C12018, 2017.

[6] A. Aguilar, et al., "Pilot tests of a PET detector using the TOF-PET ASIC based on monolithic crystals and SiPMs," J. Instrum., Vol. 11, C12033, 2016.

[7] J. Hsieh, "Computed Tomography: Principles, Design, Artifacts, and Recent Advances," 2nd ed. Bellingham, WA: SPIE; 2009.

[8] A. M. Blamire, "The technology of MRI—the next 10 years?," Br. J. Radiol., Vol. 81, 2008.

[9] A. P. Dhawan, "Medical Image Analysis," Wiley–Interscience, New York. 2003.

[10] A. Sarvazyan, et al., "Overview of elastography–an emerging branch of medical imaging," Curr. Med. Imaging Rev., Vol. 7, 2011.

[11] W. C. Roentgen, "On a New Kind of Rays," Nature., Vol. 53, 1896.

[12] S. A. Huettel, A.W. Song, G. McCarthy, "Functional Magnetic Resonance Imaging," Massachusetts: Sinauer, ISBN 978-0-87893-286-3, 2009.

[13] J. A. Detre, et al., "Applications of arterial spin labeled MRI in the brain," J. Magn. Reson. Imaging., Vol. 35, 2012.

[14] H. Rahbar and S. C. Partridge, "Multiparametric MR Imaging of Breast Cancer," Magn. Reson. Imaging Clin. N. Am., Vol. 24, 2016.

[15] M. Scialpi, et al., "Pancreatic tumors imaging: An update," Int. J. Surg., Suppl. 1, 2016.

[16] C. Mari Aparici, "Introducción a la Imagen Molecular.," Rev. Española de Medicina Nuclear e Imagen Molecular., Vol. 6, 2007.

[17] J. K. Willmann, et al., "Molecularimaging in drug development," Nat. Rev. Drug. Discov., Vol. 7, 2008.

[18] M. L. James and S. S. Gambhir, "A Molecular Imaging Primer: Modalities, Imaging Agents, and Applications," Physiol. Rev., Vol. 92, 2012.

[19] http://miil.stanford.edu/research/target_molecular_signals.html.

[20] H. O. Anger, “Scintillation camera with multichannel collimators,” J. Nucl. Med., Vol. 5, 1964.

[21] C. Molinos, “Aplicación de un fotomultiplicador de silicio en el diseño de una sonda intraoperatoria inalámbrica para la detección de radiación gamma en medicina nuclear,” PhD thesis, Universitat de València, 2009.

[22] H. Wieczorek and A. Goedicke, “Analytical model for SPECT detector concepts,” IEEE Trans. Nucl. Sci., Vol. 53, 2006.

[23] R. M. Capote, et al., “Optimization of convergent collimators for pixelated SPECT systems,” Med. Phys., Vol. 40, 2013.

[24] K. Ogawa and M. Muraishi, “Feasibility study on an ultra-high-resolution SPECT with CdTe detectors,” IEEE Trans. Nucl. Sci., Vol. 57, 2010.

[25] SPECT at the US National Library of Medicine Medical Subject Headings (MeSH).

[26] J. LeBlanc, et al., “C-SPRINT: a prototype Compton camera system for low energy gamma ray imaging,” IEEE Trans. Nucl. Sci., Vol. 45, 1998.

[27] J. Krimmer, et al., “Development of a Compton camera for medical applications based on silicon strip and scintillation detectors,” Nucl. Inst. Meth. A., Vol. 787, 2015.

[28] F. Roellinghoff, et al., “Design of a compton camera for 3d prompt- imaging during ion beam therapy,” Nucl. Inst. Meth. A., Vol. 648, Supplement 1:S20 – S23. NIMA 4th International Conference on Imaging techniques in Subatomic Physics, Astrophysics, Medicine, Biology and Industry, 2011.

[29] G. Kanbach, et al., “The MEGA project,” New Astron. Rev., Vol. 48, 2004.

[30] S. E. Boggs, “The Advanced Compton Telescope mission,” New Astron. Rev., Vol. 50, 2006.

[31] S. Watanabe, et al., “A Si/CdTe semiconductor Compton camera,” IEEE 2nd ed., ser. Trans. Nucl. Sci., Vol. 52, 2005.

[32] R. S. Holt, “Compton imaging,” Endeavour. Vol. 9, 1985.

[33] E. Yoshida, et al., “Simulation study of a DOI-based PET-Compton imaging system for positron emitters,” IEEE Nucl. Sci. Symposium and Med. Imaging Conference (NSS/MIC), 2015.

[34] University of California - Berkeley. "Lifelong brain-stimulating habits linked to lower Alzheimer's protein levels." ScienceDaily, 2012. <www.sciencedaily.com/releases/2012/01/120123163348.htm>.

[35] L. Yu, et al., “Radiation dose reduction in computed tomography: techniques and future perspective,” Imaging Med., Vol. 1, 2009.

[36] G. E. Gold, et al., “Recent advances in MRI of articular cartilage,” Am. J. Roentgenol., Vol. 193, 2009.

[37] M. G. Pomper and J. S. Lee, “Small animal imaging in drug development,” Curr. Pharm. Des., Vol. 11, 2005.

[38] B. Zitová and J. Flusser, “Image registration methods: a survey,” Image Vis. Compu., Vol. 21, 2003.

[39] J. S. Lee, et al., “Development and applications of a software for Functional Image Registration (FIRE),” Comput. Meth. Prog. Biomed., Vol. 78, 2005.

[40] G. W. Goerres, et al., “Respiration-induced attenuation artifact at PET/CT: technical considerations,” Radiology, Vol. 226, 2003.

[41] M. M. Ter-Pogossian, S. R. Bergmann, and B. E. Sobel, “Influence of cardiac and respiratory motion on tomographic reconstructions of the heart: implications for quantitative nuclear cardiology,” J. Comput. Assist. Tomogr., Vol. 6, 1982.

[42] Y. Seo Y, C. Mari C and B. H. Hasegawa, “Technological development and advances in single-photon emission computed tomography/computed tomography,” Semin. Nucl. Med., Vol. 38, 2008.

[43] T. Beyer, et al., “A combined PET/CT scanner for clinical oncology,” J. Nucl. Med., Vol. 41, 2000.

[44] D. W. Townsend, “Dual-modality imaging: combining anatomy and function,” J. Nucl. Med., Vol. 49, 2008.

[45] T. Beyer, et al., “Magnetomflash,” Siemens, Vol.3, 2010.

[46] J. Cochrane, “PET/CT in Oncology,” Radiology Rounds, Massachusetts General Hospital Department of Oncology, Vol. 10, 2012.

[47] H. P. A. C. on Technology, “PET/MRI integrated hybrid scanners,” Tech. Rep. Technology Brief, Queensland Governmemt - Health Department, Queensland, 2012.

[48] N. L. Christensen, et al., “Positron emission tomography within a magnetic field using photomultiplier tubes and light guides,” Phys. Med. Biol., Vol. 40, 1995.

[49] C. Catana, et al., “Simultaneous in vivo positron emission tomography and magnetic resonance imaging,” Proc. Nat. Acad. Sci., Vol. 105, 2008.

[50] S. Vandenberghe and P. K. Marsden, “PET-MRI: a review of challenges and solutions in the development of integrated multimodality imaging,” Phys. Med. Biol., Vol. 60, 2015.

[51] C. Rischpler, et al., "Hybrid PET/MR imaging of the heart: potential, initial experiences, and future prospects," J. Nucl. Med., Vol. 54, 2013.

[52] E. Dimou, et al., "Amyloid PET and MRI in Alzheimer's disease and mild cognitive impairment," Curr. Alzheimer Research. Vol. 6, 2009.

[53] A. Martinez-Möller, et al., "Workflow and scan protocol considerations for integrated whole-body PET/MRI in oncology," J. Nucl. Med., Vol. 53, 2012.

[54] Can hybrid PET/MRI improve the diagnostic accuracy of brain glioma? (https://blog.medisin.ntnu.no/can-hybrid-petmri-improve-the-diagnostic-accuracy-of-brain-glioma/)

[55] A. Del Guerra, et al., “TRIMAGE: A dedicated trimodality (PET/MR/EEG) imaging tool for schizophrenia,” Eur. Psychiatry., Vol. 50, 2018.

[56] Y. Seo, H. Jiang and B.L. Franc, “Preclinical SPECT and SPECT/CT,” Recent Results Cancer Res., Vol. 187, 2013.

[57] V. Schulz, et al., "SiPM based preclinical PET/MR insert for a human 3T MR: first imaging experiments," Nucl. Sci. Symposium and Med. Imaging Conference (NSS/MIC), IEEE: 4467–4469, 2001.

[58] D. A. Rich, “A brief history of positron emission tomography,” J. Nucl. Med. Technol., Vol. 25, 1997.

[59] G. L. Brownel, “A history of positron imaging,” Physics Research Laboratory Massachusetts General Hospital, 1999.

[60] M. N. Croll., “Nuclear medicine instrumentation. Historic perspective,” Semin. Nucl. Med., Vol. 24, 1994.

[61] T. Jones and D. Townsend, “History and future technical innovation in positron emission tomography,” J. Med. Imaging., Vol. 4, 2017.

[62] A. J. Gonzalez, F. Sanchez and J.M. Benlloch, “Organ-Dedicated Molecular Imaging Systems,” IEEE Trans. Rad. Plasma. Med. Sci., Vol. 2, 2018.

[63] P. A. M. Dirac, “A theory of electrons and protons,” Proc. Camb. Soc., Vol. 26, 1929.

[64] C. D. Anderson, “The Positive Electron,” Phys. Rev., Vol.43, 1933.

[65] S. Ruben, M. D. Kamen and W. Z. Hassid, “Photosynthesis with radioactive carbon. II. Chemical properties of the intermediates,” Jam. Chern. Soc., Vol. 62, 1940.

[66] J. F. Volker, et al., “The absorption of fluoride by enamel, dentine, bone and the hydroxyapatite as shown by the radioactive isotope,” J. Bioi. Chern., Vol. 134, 1940.

[67] J. H. Wills, “Secretion of intravenously injected fluorine in the submaxillary saliva of cats,” J. Dent. Res., Vol. 19, 1940.

[68] M. M. Ter-Pogossian and W. E. Powers, “The use of radioactive oxygen-IS in the determination of oxygen content in malignant neoplasms,” Radioiosotopes in scientific research, vol 3. Proc. of the 1st UNESCO International Conference, Paris, 1957.

[69] C. A. Tobias, et al., “The elimination of carbon monoxide from the human body with reference to the possible conversion of carbon monoxide to carbon dioxide,” Am. J. Physiol., Vol. 194, 1945.

[70] F. R. Wrenn, M. L. Good, P. Handler, “The use of positron-emitting radioisotopes for the localization of brain tumors,” Science., Vol. 19, 1951.

[71] G. L. Brownell and W. H. Sweet, “Localization of brain tumors with positron emitters,” Nucleonics., Vol. 1955.

[72] S. Rankowitz, et al., “Positron scanner for locating brain tumors,” Proc. IRE lnt. Com. Rec., New York, NY; 1962.

[73] H. O. Anger and A. Gottschalk, “Localization of brain tumors with the positron scintillation camera,” J. Nucl. Med., Vol. 4, 1963.

[74] H. O. Anger and D.C. Van Dyke, “Human bone marrow distribution shown in vivo by iron-52 and the positron scintillation camera,” Science., Vol. 144, 1964.

[75] C. J. Thompson, Y. L. Yamamoto, and E. Meyer, “A Position Imaging System for the Measurement of Regional Cerebral Blood Flow,” Appl. Opt. Inst. Med. V., Vol. 96, 1976.

[76] M. E. Phelps, et al., “Application of annihilation coincidence detection to transaxial reconstruction tomography,” J. Nucl. Med., Vol. 16, 1975.

[77] M. M. Ter-Pogossian, et al., “Positron emission transaxial tomograph for nuclear imaging (PETT),” Radiology., Vol. 114, 1975.

[78] C. W. Williams, M. C. Crabtree and S. G. Burgiss, “Design and performance characteristics of a positron emission computed axial tomograph—ECAT®-II,” IEEE Trans. Nucl. Sci. Vol. 26, 1979.

[79] E. J. Hoffman, et al., “ECAT III—basic design considerations,” IEEE Trans. Nucl. Sci. Vol. 30, 1983.

[80] D. W. Townsend, et al., “A rotating PET scanner using BGO block detectors: design, performance and applications,” J. Nucl. Med. Vol. 34, 1993.

[81] T. J. Spinks, et al., “Physical characteristics of the ECAT EXACT 3D positron tomograph,” Phys. Med. Biol., Vol. 45, 2000.

[82] Z. H. Cho, J. K. Chan and L. Eriksson, “Circular ring transverse axial positron camera for three-dimensional reconstruction of radionuclides distribution,” IEEE Trans. Nucl. Sci., NS-23, 1976.

[83] Z. H. Cho and M. R. Farukhi, “Bismuth germanate as a potential scintillation detector in positron cameras,” J. Nucl. Med., Vol. 18, 1977.

[84] N. A. Mullani, et al., “Dynamic imaging with high resolution time-of-flight PET camera- TOFPET I,” IEEE Trans. Nucl. Sci., NS-31, 1984.

[85] M. M. Ter-Pogossian, et al., “Photon time-of-flight assisted positron emission tomography,” J. Comput. Assist. Tomogr., S:227- 239, 1981.

[86] T. Ido, et al., “Labeled 2-deoxy-D-glucose analogs. Fluorine-18-labeled 2-deoxy-2-fluoro- D-glucose. 2-deoxy- 2-fluoro-D-man- nose, and C-14-2-fluoro-D-glucose,” J. Lab. Compd. Radiopharm., Vol. 14, 1978.

[87] M. E. Casey and R. Nutt, “A multicrystal two dimensional BGO detector system for positron emission tomography,” IEEE Trans. Nucl. Sci. Vol. 33, 1986.

[88] P. M. Bloomfield, et al., “Three-dimensional performance of a small-diameter positron emission tomograph,” Phys. Med. Biol. Vol. 42, 1997.

[89] S. R. Cherry, et al., “MicroPET: a high resolution PET scanner for imaging small animals,” IEEE Trans. Nucl. Sci. Vol. 44, 1997.

[90] Q. Bao, et al., “Performance evaluation of the inveon dedicated PET preclinical tomograph based on the NEMA NU-4 standards,” J. Nucl. Med. Vol. 50, 2009.

[91] S. R. Cherry, et al., “Total-Body PET: Maximizing Sensitivity to Create New Opportunities for Clinical Research and Patient Care," J. Nucl. Med., Vol. 59, 2018.

[92] De Burdette, et al., "Temporal lobe central benzodiazepine binding in unilateral mesial temporal lobe epilepsy," Neurology., Vol. 45, 1995

[93] I. Kanno, et al., "Measurements of cerebral blood flow using bolus inhalation of C15O2 and positron emission tomography: description of the method and comparison with C15O2 continuous inhalation method," J. Cereb. Blood Flow Metabol., Vol. 4,1984.

[94] O. Warburg, "The metabolism of tumors," New York: Richard Smith;129-161, 1931.

[95] S. C Huang, et al., "Quantitative measurement of local cerebral blood flow in humans by positron emission tomography and 15O-water," J. Cereb. Blood Flow Metabol., Vol. 3, 1983

[96] R. D. Evans, “The Atomic Nucleus,” McGraw-Hill, New York, LCCCN 55-7275, 1955.

[97] D. W. Rickey, R. Gordon and W. Huda, "On lifting the inherent limitations of positron emission tomography by using magnetic fields (MagPET)," Automedica., Vol. 14, 1992.

[98] C. S. Levin, “Calculation of positron range and its effect on the fundamental limit of positron emission tomography system spatial resolution,” Phys. Med. Biol., Vol. 44, 1999.

[99] C. S. Wu and S. A. Moskowski, “Beta Decay,” New York: Interscience., 1966.

[100] H. Daniel, “Shapes of beta-ray spectra,” Rev. Mod. Phys., Vol. 40, 1968

[101] K. S. Krane, “Introductory Nuclear Physics,” John Wiley and sons, 1995.

[102] H. Hirayama., Lecture Note on Photon Interactions and Cross Sections. KEK High Energy Accelerator Research Organization Oho Tsukuba Ibaraki Japan

[103] A. H. Compton, “A Quantum Theory of the Scattering of X-rays by Light Elements,” Phys. Rev., Vol. 21, 1923

[104] W. R. Leo, “Techniques for Nuclear and Particle Physics Experiments: A How-to Approach,” Springer Science & Business Media, 2012.

[105] R. Ford and W. Nelson., SLAC-210, UC-32, 1978.

[106] G. F. Knoll, “Radiation detection and measurement,” John Wiley & Sons, 2010.

[107] A. Ros, “Optimización de cristales centelleadores para la determinación de la DOI en tomografía de rayos gamma”. PhD thesis, Universitat de València, 2012.

[108] B. S. Gopal, “Basics of PET imaging,” Physics. Chemistry, and Regulations, Springer, 2010.

[109] S. R. Cherry, J. A. Sorenson and M.E. Phelps, “Physics in nuclear medicine,” Phyladelphia, Pa: Saunders/Elsevier Science, ISBN 0-7216-8341-X, 2003.

[110] A. J. Gonzalez, et al 2016 “A PET design based on SiPM and monolithic LYSO crystals: performance evaluation,” IEEE Trans. Nucl. Sci., Vol. 63, 2015.

[111] M. N. Wernick and J. N. Aarsvold, “EMISSION TOMOGRAPHY: THE FUNDAMENTALS OF PET AND SPECT,” Elsevier, Imprint: Academic Press, Inc., ISBN: 0-12-744482-3, 576, 2004.

[112] G. Zen, “Medical image reconstruction,” Springer, 2010.

[113] S. Surti and J. S. Karp, “Design considerations for a limited-angle, dedicated breast, TOF PET scanner,” IEEE Nucl. Sci. Symposium Conf. Record., Vol. 5, 2007.

[114] J.S. Karp, et al., “Benefit of Time-of- Flight in PET: Experimental and Clinical Results,” J. Nucl. Med., Vol. 49, 2008.

[115] S. Vanderberghe, et al., “Recent developments in time-of-flight PET,” Eur. J. Nucl. Mol. Med. Imaging., Vol. 3, 2016

[116] P. Lecoq, “Pushing the Limits in Time-of-Flight PET Imaging,” IEEE Trans. Rad. Plasma Med. Sci., Vol. 1, 2017.

[117] Siemens Healthineers Headquarters, “Biograph Vision,” available at: https://siemens.com/vision.

[118] M. Defrise, et al., “Time-of-flight PET data determine the attenuation sinogram up to a constant”, Phys. Med. Biol., Vol. 57, 2012.

[119] P. E. Kinahan and J. G. Rogers, “Analytic 3D image reconstruction using all detected events,” IEEE Trans. Nucl. Sci., Vol. 36, 1989.

[120] G. Brix, et al., “Performance Evaluation of a Whole-Body PET Scanner Using the NEMA Protocol,” J. Nucl. Med., Vol. 38, 1991.

[121] T. J. Spinks, et al., “The effect of activity outside the direct field of view in a 3D-only whole-body positron tomograph,” Phys. Med. Biol., Vol. 43, 1998.

[122] A. C. Kak and M. Slaney, “Principles of Computerized Tomographic Imaging,” IEEE Press, 1988.

[123] M. E. Daube-Witherspoon and G. Muehllehner, “Treatment of axial data in three- dimensional PET,” J. Nucl. Med., Vol. 28, 1987.

[124] V. Sossi, et al., “The performance of the single-slice rebinning technique for imaging the human striatum as evaluated bp phantom studies,” Phys. Med. Biol., Vol. 39, 1994.

[125] R. M. Lewitt, G. Muehllehner, J. S. and Karp, “3D image reconstruction for PET by multi-slice rebinning and axial filtering,” IEEE Nucl. Sci. Symposium Med. Imaging Conference, 1991.

[126] M. Defrise, et al., “Exact and approximate rebinning algorithms for 3-D PET data,” Medical Imaging, IEEE Trans. Med. Imaging., Vol. 16, 1997.

[127] S. Matej, et al., “Performance of the Fourier rebinning algorithm for PET with large acceptance angles,” Phys. Med. Biol., Vol. 43, 1998.

[128] M. Yavuz, and J. A. Fessler, "Statistical Tomographic Recon methods for randoms- precorrected PET scans," Med. Imaging Analysis., Vol. 2, 1998.

[129] L. A. Shepp and Y. Vardi, “Maximum likelihood reconstruction for emission tomography,” IEEE Trans. Ned. Imaging., Vol. 1, 1982.

[130] H. M. Hudson and R. S. Larkin, “Accelerated image reconstruction using ordered subsets of projection data,” IEEE Trans. Med. Imaging., Vol. 13, 1994.

[131] C. Bleckmann, et al., “Effect of attenuation correction on lesion detectability in FDG PET of breast cancer,” J. Nucl. Med., Vol. 40, 1999.

[132] J. T. Bushberg, et al., “The Essential Physics of Medical Imaging,” Wolters kluwer, 2002.

[133] H. Zaidi and K. F. Koral, “Scatter modeling and compensation in emission tomography,” Eur. J. Nucl. Med. Mol. Imaging., Vol. 31, 2004.

[134] D. L. Bailey and S. R. Meikle, “A convolution-subtraction scatter correction method for 3D PET,” Phys. Med. Biol., Vol. 39, 1994.

[135] M. Bentourkia, et al., “Assessment of scatter components in high-resolution PET: correction by nonstationary convolution subtraction,” J. Nucl. Med., Vol. 36, 1995.

[136] J. M. Ollinger, “Model-based scatter correction for fully 3D PET,” Phys. Med. Biol., Vol. 41, 1996.

[137] C. C. Watson, “New,faster,image-based scatter correction for 3DPET,” IEEE Trans. Nucl. Sci., Vol. 47, 2000.

[138] C. S. Levin, M. Dahlbom and E. J. Hoffman, “A Monte Carlo correction for the effect of Compton scattering in 3-D PET brain imaging,” IEEE Trans. Nucl. Sci., Vol. 42, 1995.

[139] F. Sánchez, et al., “Design and test of a portable mini gamma camera,” Med. Phys., Vol. 31, 2004.

[140] C. S. Levin, “Detector design issues for compact nuclear emission cameras dedicated to breast imaging,” Nucl. Inst. Meth. A., Vol. 497, 2003.

[141] H. Sabet H, et al., “A sub-mm spatial resolution LYSO:Ce detector for small animal PET,” IEEE Nucl. Sci. Symposium Med. Imaging Conference, NSS/MIC, 2016.

[142] H. Sabet, et al., “Novel laser-processed CsI:Tl detector for SPECT,” Med. Phys., Vol. 43, 2016.

[143] M. Ito, S. J. Hong and J. S. Lee, “Positron emission tomography (PET) detectors with depth-of-interaction (DOI) capability,” Biomed. Eng. Letters., Vol. 1, 2011.

[144] H. Liu, el al., "Development of a depth of interaction detector for gamma-rays," Nucl. Inst. Meth. A., Vol. 459, 2001.

[145] T. K. Lewellen, "Recent developments in PET detector technology," Phys. Med. Biol., Vol. 53, 2008.

[146] L. Eriksson, et al., "Phoswich solutions for the PET DOI problem," Nucl. Inst. Meth. A., Vol. 648, 2011.

[147] J. H. Jung, et al., "Optimization of LSO/LuYAP phoswich detector for small animal PET," Nucl. Instr. and Meth. A., Vol. 571, 2007.

[148] M. Rafecas, et al., "A Monte Carlo study of high-resolution PET with Granulated dual-layer detectors," IEEE Trans. Nucl. Sci., Vol. 48, 2001.

[149] C. S. Levin, "Design of a high-resolution and high-sensitivity scintillation crystal array for PET with nearly complete light collection," IEEE Trans. Nucl. Sci., Vol. 49, 2000.

[150] K. Shimizu, et al., "Development of 3-D detector system for positron CT," IEEE Trans. Nucl. Sci., Vol. 35, 1988.

[151] Y. Shao, H. Li and K. Gao, "Initial experimental studies of using solid-state photomultiplier for PET applications," Nucl. Inst. Meth. A., Vol. 580, 2007.

[152] R. S. Miyaoka and T. K. Lewellen, "Design of a depth of interaction(DOI) PET detector module," IEEE Trans. Nucl. Sci., Vol. 45, 1998.

[153] M. Ito, et al., "Design and simulation of a novel method for determining depth-of-interaction in a PET scintillation crystal array using a single-ended readout by a multi-anode PMT," Phys. Med. Biol., Vol. 55, 2010.

[154] H. Du, et al., "Continuous depth-of-interaction encoding using phosphor-coated scintillators," Phys. Med. Biol., Vol. 54, 2009.

[155] T. Niknejad, et al., "Development of high-resolution detector module with depth of interaction identification for positron emission tomography," Nucl. Inst. Meth. A., Vol. 845, 2017.

[156] Saint-Gobain "LYSO scintillation material" data sheet. https://www.crystals.saintgobain.com/sites/imdf.crystals.com/files/documents/lyso-material-data-sheet_0.pdf

[157] S. Gundacker, et al., "Measurement of intrinsic rise times for various L(Y)SO and LuAG scintillators with a general study of prompt photons to achieve 10 ps in TOF-PET," Phys. Med. Biol., Vol. 61, 2016.

[158] J. W. Cates and C. S. Levin, "Evaluation of a clinical TOF-PET detector design that achieves ≤ 100 ps coincidence time resolution," Phys. Med. Biol., Vol. 63, 2018.

[159] J. R. Stickel, "High-resolution PET detector design: modelling components of intrinsic spatial resolution," Phys. Med. Biol., Vol. 50, 2005.

[160] W. Lehnert, "Analytical positron range modelling in heterogeneous media for PET Monte Carlo simulation," Phys. Med. Biol., Vol. 57, 2011.

[161] J. Joung, R. S. Miyaoka and T. K. Lewellen, “cMiCE: a high resolutionanimal PET using continuous LSO with a statistics based positioning scheme,” Nucl. Inst. Meth. A., Vol. 489, 2002.

[162] I. Vilardi, et al., “Optimization of the effective light attenuation length of YAP:ce and LYSO:Ce crystals for a novel geometrical PET concept,” Nucl. Inst. Meth. A., Vol. 564, 2006.

[163] P. Bruyndonckx, et al., “Study of spatial resolution and depth of interaction of APD-based PET detector modules using light sharing schemes,” IEEE Trans. Nucl. Sci., Vol. 50, 2003.

[164] R. Pani, et al., “A Novel Method for γ-photons Depth-of- Interaction Detection in Monolithic Scintillation Crystals,” IEEE Trans. Nucl. Sci., Vol. 63, 2016.

[165] E. Preziosi, et al., “Performance study of a PET scanner based on monolithic scintillators for different DoI-dependent methods,” J. Instrum., Vol. 11, C12076, 2016.

[166] E. Preziosi, et al., “A crystal identification method for monolithic phoswich detectors based on scintillation light distribution,” J. Instrum., Vol. 11, P12009, 2016.

[167] P. Conde, et al., “Noise rejection in Monolithic PET detectors,” IEEE Nuclear Science Symposium, (NSS/MIC/RTSD), 2016.

[168] E. Roncalki and S.R. Cherry, “Simulation of light transport in scintillators based on 3D characterization of crystal surfaces,” Phys. Med. Biol., Vol. 58, 2013.

[169] G. Borghi, et al., “Towards monolithic scintillators based TOF-PET systems: practical methods for detector calibration and operation,” Phys. Med. Biol., Vol. 61, 2016.

[170] E. Lamprou, et al., “PET detector block with accurate 4D capabilities”, Nucl. Inst. Meth. A., in press 2017. https://doi.org/10.1016/j.nima.2017.11.002.E.

[171] E. Lamprou, et al., “Characterization of TOF-PET Detectors Based on Monolithic Blocks and ASIC-Readout”. arXiv:1806.08715v1

[172] N. Giokaris, et al., “Partially slotted crystals for a high-resolution γ-camera based on a position sensitive photomultiplier,” Nucl. Inst. Meth. A., Vol. 550, 2005.

[173] S-O. Flyckt and C. Marmonier, “PHOTOMULTIPLIER TUBES principles & applications,” Phonis, Brive, France, 2002.

[174] C. S. Levin, “Promising new photon detection concepts for high resolution clinical and preclinical PET,” J. Nucl. Med., Vol. 53, 2012.

[175] A. Stoykov and R. Scheuermann, "Silicon Avalanche Photodiodes," Laboratory for Muon Spin Spectroscopy, Paul Scherrer Institut, 2004.

[176] N. Dinu, “Instrumentation on silicon detectors: from properties characterization to applications,” Université Paris Sud-Paris XI, 2013.

[177] A. J. González, et al., “Design of the PET-MR system for head imaging of the DREAM project,” Nucl. Inst. Meth. A., Vol. 702, 2013.

[178] M. Motoyoshi, “Through-Silicon Via (TSV),” Proceeding of the IEEE., Vol 97, 2009.

[179] T. Frach, et al, “The Digital Silicon Photomultiplier – Principle of Operation and Intrinsic Detector Performance”. IEEE Nucl. Sci. Symposium conference record, 2009.

[180] D. R. Schaart, et al., “Advances in digital dSiPMs and their application in biomedical imaging,” Nucl. Inst. Meth. A., Vol. 809, 2015

[181] V. Stolin, et al., “Evaluation of imaging modules based on SensL array SB-8 for nuclear medicine applications,” IEEE Trans. Nucl. Sci., vol. 61, 2014.

[182] T. Niknejad, et al., “TOFPET2: a high-performance ASIC for time and amplitude measurements of SiPM signals in time-of-flight applications,” J. Instrum., Vol. 11, 2016.

[183] A. J. Gonzalez, et al., “Next Generation of the Albira Small Animal PET Based on SiPM Detectors and Continuous Crystals,” Albira White Paper.

[184] A. J. Gonzalez, et al., “Performance of large BGO arrays coupled to SiPM photosensors – Continued study,” IEEE Nucl. Sci. Symposuim Med. Imaging Conference, 2016.

[185] G. Landi., “Properties of the center of gravity as an algorithm for position measurements,” Nucl. Inst. Meth. A., Vol. 485, 2002.

[186] R. Pani, et al., “Preliminary evaluation of a monolithic detector module for integrated PET/MRI scanner with high spatial resolution,” J. Instrum, Vol. 10, C06006, 2015.

[187] R. Pani, et al., “Position algorithm for monolithic scintillation crystals based on charge projection readout,” J. Intrum., Vol. 11, C01061, 2016.

[188] C. W. Lerche, et al., “Dependency of energy, position and depth of interaction resolution on scintillation crystal coating and geometry,” Trans. Nucl. Sci., Vol. 55, 2008.

[189] De Berg, et al., “Computational Geometry,” Springer-Verlag, Berlin, Germany; 1997.

[190] H. Semmaoui, et al., IEEE MIC-NSS Conference Proceeding, 2015.

[191] Y. Li, et al., IEEE International Workshop on Multidimensional (nD) systems, 2007.

[192] S. Moehrs, et al., “A detector head design for small-animal PET with silicon photomultipliers (SiPM),” Phys. Med. Biol., Vol. 51, 2006.

[193] M. Morrocchi, et al., “Development of a PET detector module with Depth of Interaction capability,” Nucl. Instrum. in Phys. Res. A., Vol. 732, 2013.

[194] T. Ling, et al., “Parametric positioning of a continuous crystal PET detector with depth of interaction decoding,” Phys. Med. Biol., Vol. 53, 2008.

[195] P- Garcia de Acilu, et al., “Study and optimization of positioning algorithms for monolithic PET detectors blocks,” J. Instrum., Vol. 7, C06010, 2012.

[196] P. Conde, et al., “Determination of the Interaction Position of Gamma Photons in Monolithic Scintillators Using Neural Network Fitting,” IEEE Trans. Nucl. Sci., Vol. 63, 2016.

[197] P. Bruyndonckx et al., “Performance study of a PET detector module based on a continuous scintillator,” IEEE Trans. Nucl. Sci., Vol. 53, 2006.

[198] H. H. Barrett, et al., “Maximum-likelihood methods for processing signals fromg-ray detectors,” IEEE Trans. Nucl. Sci., Vol. 56, 2009.

[199] M. Gerven and S. Bohte, "Artificial Neural Networks as Models of Neural Information Processing,” Front. Comput. Neurosci., Vol. 11, 2017.

[200] P. Bruyndonckx, et al., “ Neural network-based position estimators for PET detectors using monolithic LSO blocks,” IEEE Trans. Nucl. Sci., Vol. 51, 2004.

[201] J. M. Benlloch, et al., “The MINDVIEW project: First results,” Eur. Psychiatry., Vol. 50, 2018.

[202] A. J. Gonzalez, A. Gonzalez-Montoro, et al., “A method to reduce the number of signals to be read out in a detector,” EP17382769.2, 14th Nov. 2017.

Appendix A. Contributions published during the development of the PhD thesis

Peer-reviewed publications

In addition to the peer-reviewed articles that have been selected for the thesis compendium five more articles have been published during the development of this PhD thesis. The complete list, including the selected ones, is depicted below sorted in chronological order.

1. A.J. González, S. Berr, G. Cañizares, A. González-Montoro, A. Orero, C. Correcher, S. Majewski, A. Ahmadreza, J. Nuyts, F. Sanchez, and J. M. Benlloch. "Feasibility study and pilot results of a PET system based on a single LYSO tube," Front. Med., In press, 2018.
   DOI: 10.3389/fmed.2018.00328

2. A. J. Gonzalez, A. Gonzalez-Montoro, J. Barbera, L. F. Vidal, L. Moliner, F. Sanchez, C. Correcher, E. J. Pincay, G. Cañizares, E. Lamprou, S. Sanchez, J. V. Catret, S. Jiménez-Serrano, S. Aussenhofer, J. Cabello, M. Schwaiger, A. Iborra, D. Visvikis, T. Merlin, and J. M. Benlloch.
   "Initial Results of the MINDView PET Insert Inside the 3T mMR," IEEE Trans. Rad. Plasma. Med. Sci., In press, 2018.
   DOI: 10.1109/TRPMS.2018.2866899

3. A. González-Montoro, F. Sanchez, R. Marti, L. Hernández, Aa. Aguilar, J. Barbera, J.V. Catret, G. Cañizares, P. Conde, E. Lamprou, F. Martos, S. Sanchez, L.F. Vidal, J. M. Benlloch, and A.J. González.
   "Detector block performance based on a monolithic LYSO crystal using a novel signal multiplexing method," Nucl. Inst. Meth. A., In press, 2018.
   DOI:10.1016/j.nima.2017.10.098

4. E. Lamprou, A. Aguilar, A. González-Montoro, J. M. Monzo, G. Cañizares, S. Iranzo, L. F. Vidal, L. Hernandez, P. Conde, S. SAnchez, F. Sanchez, A.J. González, and J. M. Benlloch.
   "PET detector block with accurate 4D capabilities," Nucl. Inst. Meth. A., In press, 2017.
   DOI: 10.1016/j.nima.2017.11.002

5. A. González-Montoro, F. Sanchez, S. Majewski, S. Zanettini, J. M. Benlloch, and A.J. González.
   "Highly improved operation of BGO-PET blocks," J. Instrum, Vol. 12, 2017.
   DOI: 10.1088/1748-0221/12/11/C11027

6. A.J. González, A. González-Montoro, A. Aguilar, G. Cañizares, R. Marti, S. Iranzo, E. Lamprou, S. Sanchez, F. Sanchez, and J. M. Benlloch.
   "A scintillatior geometry suitable for very small PET gantries," J. Instrum, Vol. 12, 2017.
   DOI: 10.1088/1748-0221/12/12/C12018

7. A. González-Montoro, A. Aguilar, G. Cañizares, P. Conde, L. Hernández, L.F. Vidal, M. Galasso, A. Fabbri, F. Sánchez, J. M. Benlloch, and A.J. González.
   "Performance Study of a Large Monolithic LYSO PET Detector with Accurate Photon DOI Using Retroreflector Layers," IEEE Trans. Rad. Plasma. Med. Sci., Vol. 1, 2017.
   DOI: 10.1109/TRPMS.2017.2692819

8. J. M. Monzo, A. Aguilar, A. González-Montoro, E. Lamprou, A. J. Gonzalez, L. Hernandez, D. Mazur, R. J. Colom, and J. M. Benlloch.
   "PETIROC2 based readout electronics optimization for Gamma Cameras and PET detectors," J. Instrum, Vol. 12, 2017.
   DOI: 10.1088/1748-0221/12/02/C02059

9. A. Aguilar, A. González-Montoro, A.J. González, L. Hernández, J.M. Monzó, R. Bugalho, L. Ferramacho, and J. M. Benlloch.
   "Pilot tests of a PET detector using the TOF-PET ASIC based on monolithic crystals and SiPMs ," J. Instrum, Vol. 11, 2016.
   DOI: 10.1088/1748-0221/11/12/C12033

10. E. Preziosi, S. Sanchez, A. J. Gonzalez, L. Hernandez, R. Pani, C. Borrazzo, M. Bettiol, M. J. Rodriguez-Alvarez, A. Gonzalez-Montoro, L. Moliner, and J. M. Benlloch.
    "Performance study of a PET scanner based on monolithic scintillators for different DoI-dependent methods," J. Instrum, Vol. 11, 2016.
    DOI: 10.1088/1748-0221/12/02/C02059

11. P. Conde, A. J. González ∗, A. González-Montoro, L. Hernández, P. Bellido, E. Crespo, A. Iborra, L. Moliner, J. P. Rigla, M. J. Rodríguez- Álvarez, F. Sánchez, M. Seimetz, A. Soriano, L. F. Vidal, and J. M. Benlloch.
    "Statistical moments of the scillation light distribution analysis with dSiPM and monolithic crystals," IEEE Trans. Rad. Nucl. Sci., Vol. 65, 2015.
    DOI: 10.1109/TNS.2015.2473695

Conference Proceedings

1. A. Gonzalez-Montoro, E. Lamprou, A. Perez, L. Hernandez, G. Canizares, M.Freire, L. F. Vidal, E. J. Pincay, J. Barrio, S. Sanchez, F. Sanchez, J. M. Benlloch, A. J. Gonzalez.
   "Reduction signals method preserving spatial and temporal capabilities," 21st IEEE Real Time Conference, Conference Record. Williamsburg, USA (2018).
   arXiv:1806.08646

2. E. Lamprou, A. Gonzalez-Montoro, G. Canizares, V. Ilisie, J. Barrio, F. Sanchez, A. J. Gonzalez, J. M. Benlloch.
   "Characterization of TOF-PET detectors Based on Monolithic Blocks and ASIC-Readout," 21st IEEE Real Time Conference, Conference Record. Williamsburg, USA (2018).
   arXiv:1806.08715

3. A. González-Montoro, F. Sanchez, P. Bruyndoncx, G. Cañizares, A. Aguilar, S. Iranzo, E. Lamprou, R. Marti, S. Sanchez, J. M. Benlloch, and A.J. González.
   "A method to measure the intrinsic detector resolution on monolithic crystals," IEEE NSS-MIC Conference Record. Atlanta, USA (2017).

4. A. González-Montoro, F. Sanchez, S. Majewski, S. Zanettini, J. M. Benlloch, and A.J. González.
   "PET detector block with DOI capabilities based on a large monolithic BGO crystals," IEEE NSS-MIC Conference Record. Atlanta, USA (2017).

5. A. Aguilar, E. Lamprou, A. González-Montoro, J.M. Monzo, G. Cañizares, L.F. Vidal, L. Hernandez, S. Iranzo, R. Marti, S. Sanchez, A.J. González, and J. M. Benlloch.
   "Progress Report of an Accurate 4D PET Detector Based on SiPMs and TOFPET ASIC," IEEE NSS-MIC Conference Record. Atlanta, USA (2017).

6. A.J. González, A. González-Montoro, A. Aguilar, P. Conde, G. Cañizares, L. Herández, A. Iborra, L. Moliner, L.F. Vidal, S. Sánchez, F. Sánchez, R. Garcia, J. Barberá, C. Correcher, S. Aussenhofer, D. Gareis, M. Galasso, A. Fabbri, E. Preciozi, D. Visvikis, J. Bert, A. Autret and J. M. Benlloch..
   "A brain PET insert MR compatible: Final design and first results," IEEE NSS-MIC Conference Record. Strasbourg, France (2016).